INTERACTIONS OF CdSe NANOPLATELETS

An interplay of ligand shell, solvent restructuring, and solvation forces

Dissertation zur Erlangung des Grades
„Doktor der Naturwissenschaften“
am Fachbereich Physik, Mathematik und Informatik
der Johannes Gutenberg-Universität in Mainz

Knuth Nanning Petersen
geboren in Niebüll

Mainz,
November 2023

Arbeitskreis Theorie der Polymere
Max-Planck-Institut für Polymerforschung, Mainz

1. Gutachter: [redacted]

2. Gutachter: [redacted]

Tag der Einreichung: 30.11.2024

Tag der Prüfung: 16.04.2024

Abstract

CdSe nanoplatelets show extraordinary (optical) properties. Therefore, they are candidates for applications in light-emitting devices, solar cells, field effect transistors, and lasers. They are usually synthesized with colloidal methods, and sterically stabilized in n-alkane solvents. The properties of CdSe nanoplatelets have been investigated in many studies. However, little attention has been paid to the interactions between the nanoplatelets. The lack of knowledge has made the interpretation of experimental results difficult. For example, it has been unclear why CdSe nanoplatelets assemble into stacks in pure n-alkane solvents, which influences their steric stability. In this thesis, we consider the interplay of the effects that contribute to the interaction of CdSe nanoplatelets. Unlike metallic nanocrystals, the core-core van der Waals interaction between semiconducting CdSe nanoplatelets is weak. Also, the dipole-dipole interaction is weak. Thus, either of these two interactions cannot explain why the nanoplatelets form stacks. Here, we follow the hypothesis that solvation forces cause a strong attraction between the nanoplatelets, leading to the formation of stacks, and influencing their steric stability.

At the interface between a surface and a solvent, the solvent often restructures into layers. As two surfaces approach each other, the solvent layering intensifies, and strong solvation forces can appear. However, nanocrystals often have highly curved surfaces. Due to the curvature, the ligand packing density of these nanocrystals decreases with the distance to their surface. Therefore, the ligand shell and the solvent mix, no significant layer formation occurs, and solvation forces are usually negligible. Thus, the traditional continuum model that is often used to describe the effects of the ligand shell neglects solvation forces. However, the ligand shell of nanocrystals with extended flat facets can be very dense, so that solvent layer formation and solvation forces crucially influence their interaction.

We show that CdSe nanoplatelets are an ideal model system for the study of solvation forces. The ligand grafting density is very high. Furthermore, they can be synthesized with very large base facet areas. We show in molecular dynamics simulations that the solvent restructures into well-defined layers away from the ligand-solvent interface. Strong solvation forces occur between the base facets of the nanoplatelets. These forces cause an attraction that can lead to the stacking of the nanoplatelets. The strength of the attraction depends on the size and geometry of the nanoplatelets, the ligand shell, and the solvent type.

We anticipate that our research results are applicable to other systems. In general, we expect that solvation forces will play a crucial role in the interactions of nanocrystals with extended flat facets, large ligand densities, and well-defined, even ligand-solvent interfaces.

Zusammenfassung

CdSe-Nanoplättchen besitzen außergewöhnliche (optische) Eigenschaften. Mögliche Einsatzgebiete sind LEDs, Solarzellen, Feldeffekttransistoren und Laser. Üblicherweise werden kolloidale Methoden genutzt, um sie zu synthetisieren. Danach werden sie oft für Anwendungen oder die weitere Verarbeitung in unpolaren Lösungsmitteln sterisch stabilisiert. Die anwendungsbezogenen Eigenschaften von CdSe-Nanoplättchen sind in vielen Studien untersucht worden, jedoch wurde der Wechselwirkung zwischen den Nanoplättchen dabei wenig Aufmerksamkeit geschenkt. Das dadurch fehlende Wissen hat bisher die Interpretation von experimentellen Ergebnissen erschwert. So war etwa bisher unklar, warum CdSe-Nanoplättchen in reinen unpolaren Lösungsmitteln Stapel bilden – eine Eigenschaft, welche ihre sterische Stabilität beeinflusst.

Sowohl die Van-der-Waals-Wechselwirkung, als auch die Dipol-Dipol-Wechselwirkung zwischen den Nanokristallen selbst sind zu schwach, um die Stapelbildung zu erklären. In dieser Arbeit wird der Hypothese nachgegangen, dass Lösungsmittelkräfte die maßgebliche Ursache der Stapelbildung sind.

Lösungsmittelmoleküle neigen dazu, sich an Grenzflächen und Oberflächen in Schichten anzuordnen. Wenn sich zwei Grenzflächen einander nähern, verstärkt sich die Schichtung und es können starke Lösungsmittelkräfte auftreten. Bei sterisch stabilisierten Nanokristallen bildet die Oberfläche der Ligandenhülle die Grenzfläche. Die meisten in der Vergangenheit synthetisierten Nanokristalle ähneln jedoch einer Kugel. Ihre Ligandenhülle wird aufgrund ihrer Geometrie nach außen hin dünner. Daher vermischen sich die Liganden und das Lösungsmittel. Es kommt zu keiner nennenswerten Schichtbildung, und die Lösungsmittelkräfte sind in der Regel vernachlässigbar klein. Daher vernachlässigt das traditionelle Kontinuumsmodell, welches häufig zur Beschreibung der Wechselwirkung von Nanopartikeln mit Ligandenhüllen verwendet wird, die Lösungsmittelkräfte. Allerdings kann die Ligandenhülle von Nanokristallen mit ausgedehnten flachen Facetten sehr dicht sein, sodass es zur Bildung von Lösungsmittelschichten kommt und starke Lösungsmittelkräfte auftreten.

CdSe-Nanoplättchen sind ein ideales Modellsystem für die Untersuchung von Lösungsmittelkräften sind, da sie über ausgedehnte Facetten verfügen und über eine sehr dichte Ligandenhülle. In Molekulardynamiksimulationen wird gezeigt, dass sich das Lösungsmittel nahe der Ligandenhülle in wohldefinierte Schichten anordnet. Insbesondere zwischen den Basisfacetten der Nanoplättchen treten starke Lösungsmittelkräfte auf. Die Simulationen zeigen, dass die Stärke der Anziehungskraft zwischen den Plättchen von der Größe und Geometrie der Nanoplättchen, der Ligandenhülle und dem Lösungsmitteltyp abhängt.

Es ist zu erwarten, dass sich diese Ergebnisse auch auf andere Systeme übertragen

lassen. Zu erwarten ist, dass Lösungsmittelkräfte eine herausragende Rolle in der Wechselwirkung von Nanokristallen mit ausgedehnten flachen Facetten und dichten Ligandenhüllen spielen. Dies ist insbesondere dann der Fall, wenn die Ligandenhüllen eine gut definierte, gleichmäßige Grenzfläche zum Lösungsmittel aufweisen,

Contents

Curriculum vitae

Chapter 1

Introduction

Nowadays, the prefix “nano-”, as used in nanotechnology, nanostructures, nanocrystals, etc., arouses strong emotions, hopes, and expectations. Just as the SI-prefix kilo stands for 10^3, nano stands for 10^{-9}. In the field of nanotechnology, the prefix refers to the size of the particles or structures, which are in the nanometer (nm) range. There have been major breakthroughs in the field of nanotechnology over the last four decades, which have led to innovative applications. The lotus effect is used to make surfaces water and dirt resistant. [1, 2]. Silver (Ag) nanocrystals are used, e.g., in textiles, because of their antibacterial and fungicidal properties [2]. Nanotechnology is also used in modern electronics. For example, semiconducting nanocrystals improve the color gamut of liquid-crystal displays (LCDs) [3]. Since the effects on which the applications are based are often intuitively not tangible, they appear almost magical. Therefore, “nano-” is associated with futuristic technologies. This goes so far that it is often associated with science fiction, where it is used as a synonym to explain unique, according to our knowledge, impossible technologies.

In fact, the prefix “nano-” does not only evoke positive associations. There is also a public discussion about the dangers of nanotechnologies. Like other materials, nanoparticles can have a negative impact on our health. One example is titanium dioxide (TiO_2) nanocrystals, which are used in sun creams, cosmetics, and food. Originally, they were considered harmless. Recently, however, there has been a discussion about the risks to human and environmental health, both in the public and in the science community [4]. Another example is nanocrystals in the fine dust of car exhaust gases, which cause health concerns [5]. However, the discussion can also drift into the absurd, when in science fiction nanites, small nano-scale robots, become an existential threat to mankind.

Following these impressions of the prefix “nano-”, we could get the idea that the use of nanotechnology, in particular of nanocrystals, is something new, probably becoming part of our life in the last decades, where scientific, and technological progress was fast. However, this impression is wrong. In fact, as summarized by Montanarella and Kovalenko [6], applications of nanotechnology have been with us for thousands of years, even though their usage was purely empirical and unwitting.

In Cyprus and Greece, nanoporous clay was used during the fifth millennium BC to bleach wool and fleece [7, 6]. Another example is from the ancient Mayas. From ca. 300 BC to the 17th century, they have used pigments made from natural dyes that are added to nanostructured clay [8]. The Moorish Damascus steel, used at the time of the Crusaders, is a further example. Its excellent properties are based on embedded carbon nanotubes [9, 10]. The coloring of glass and ceramics is one area where nanocrystals have been used already in the Bronze Age, and are still being used [6]. In northern Italy found glasses from around 1200–1000 BC, chromophoric elements like Cu, Co, Fe, and Mo were used for coloring. For example, metallic copper nanocrystals have been used for a red color [11, 12]. An extraordinary example of coloring with nanocrystals is the Lycurgus cup created by the Romans in the fourth century AD, which can be viewed in the British Museum. It has the fascinating property that its color depends on the direction of the light falling on it. If light shines through the glass, it appears red, while in reflection, it appears green. This behavior stems from light absorption and scattering of alloyed Ag/Au metallic nanocrystals and other components, which are dispersed in the glass [13, 14, 6].

Systematic studies of nanocrystals set in at the beginning of the 20th century, creating a link between the nanocrystal size and their unique properties. In the 1980s, Alexei I. Ekimov and Louis E. Brus intentionally and independently synthesized semiconductor nanocrystals in glass and water. They finally created an unambiguous link between the size dependent properties of nanocrystals and the quantum confinement effect (see Section 3.2) [15, 6]. The properties of a solid are usually given independently of its size. However, for nanocrystals with dimensions in the range of a few nm, the electronic structure depends on the size of the nanocrystals [16, 15]. For instance, the band gap of semiconductor nanocrystals such as CdSe nanoplatelets increases when their size is reduced. Therefore, by the nanocrystal size, we can tune the absorption and emission spectra. Coincidentally, while writing this thesis, the Nobel Prize in Chemistry 2023 was awarded “for the discovery and synthesis of quantum dots” [17]. The award winners are Louis E. Brus and Alexei I. Ekimov, together with Moungi G. Bawendi, who developed a highly reliable colloidal synthesis method known as “hot injection” for monodisperse colloidal nanocrystals [6].

The use of wet colloidal methods for the synthesis of nanocrystals is widespread [18]. Colloids are fluids that contain dispersed polyatomic particles, like nanocrystals [19]. An important property of such colloids is the colloidal stability. Depending on whether the nanocrystals precipitate after some time or remain in the solution permanently, we define the colloid to be metastable or stable. The colloidal stability of nanocrystals in a solvent depends on the balance of several free energy contributions (see Chapter 2). Contributions to the free energy are either of enthalpic or entropic origin. The core-core van der Waals interaction, the dipole-dipole interaction, electrostatic contributions like the electric double layer, and depletion forces, as well as the translational and rotational entropy of nanocrystals, are usually important (see Figure 1.1).

There are well-developed frameworks for the description of each of these contributions to free energy [20]. In older studies, contributing forces have usually been described by continuum approaches, where the different contributions are summed up in a second step [21]. However, the forces acting on nanocrystals are not necessarily independent of each other, or well described in their discrete nature by continuum approaches [22]. In recent studies, the discrete nature of the nanoparticle surface, surfactant molecules, and the solvent have come into focus.

To give a few examples: Polyvinylpyrrolidon (PVP) covered triangular Ag nanoplates in water tend to attach by their side facets, and not by their base facets [23, 24]. This is

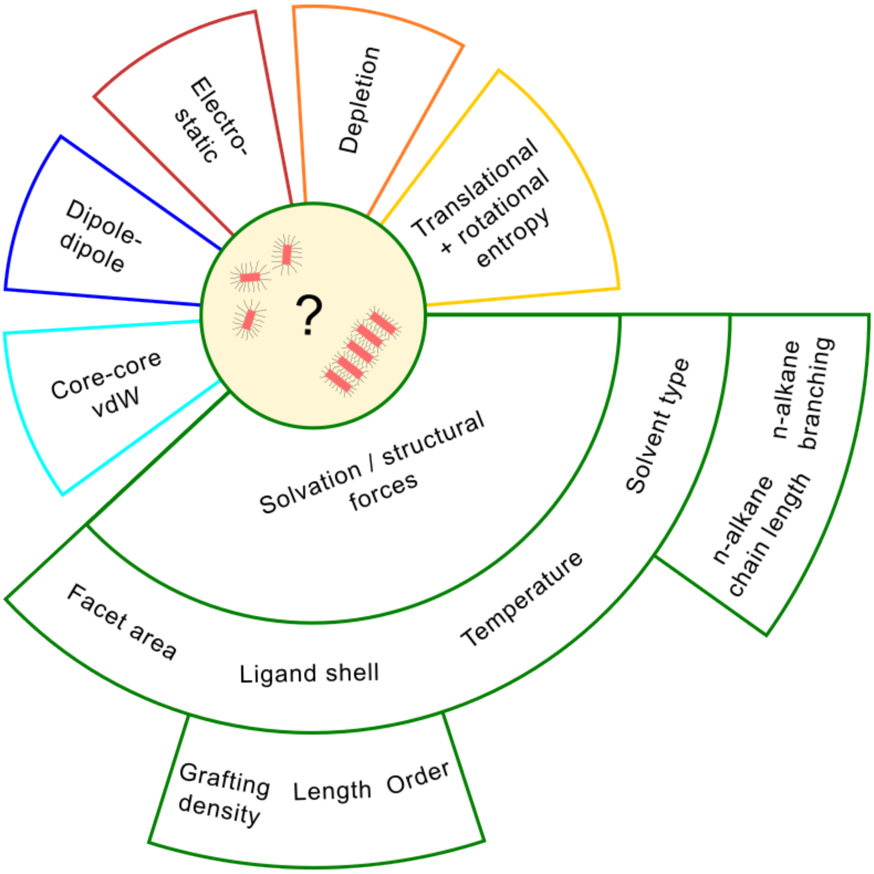

Figure 1.1: Schematic sketches to illustrate free energy contributions that determine the (dis-) assembling of nanocrystals. In the case of ligand passivated CdSe nanoplatelets dispersed in an apolar alkane solvent, solvation forces are crucial. The strength of solvation forces depends on the interacting facet area, the ligand shell, the solvent type, and the temperature. The packing density of the ligand shell depends on the ligand grafting density, the ligand length, and the ligand ordering. The solvent restructuring that causes solvation forces is more pronounced in n-alkane solvents with a longer chain length, and changes its shape in isomers of alkanes.

surprising, as at first glance the attraction between the base facets is larger. Balankura *et al.* have revealed the mechanism with computer simulations [25]. The PVP is only loosely bound to the plate surface. As two facets attach, the PVP molecules have to vacate the facet. As there are more PVP molecules to move on the base facet than on the side facet, the free energy barrier is higher.

Similarly, oriented attachment of gibbsite particles in water is influenced by the structure of the crystal surface [26]. The highest energy barrier in the attachment of gibbsite particles is the removal of the last water layer. Therefore, the particles have time to rearrange in the state with one water layer in between, before assembling. Rotation or translational motion may occur. Ho *et al.* have shown that such motions are connected with significant changes in the free energy, which depend on the surface crystal structure. After the removal of the last layer of water, the particles are fixed in their configuration.

In apolar solvents, nanocrystals are usually sterically stabilized by ligands, surfactant molecules bound to the particle surface [27, 28, 29, 21]. Again, it is important to look at the details. For the interaction of hexadecanethiol passivated gold nanospheres dispersed in n-decane, Kister, Debora *et al.* have found a shell, and a core dominated interaction regime, dependent on the core diameter [30]. For smaller gold nanospheres, the agglomeration temperature and the interparticle spacing are dominated by the ordering of the ligand shells. The ligands form bundles of aligned ligands. The bundles attract each other and interlock. In contrast, the interaction of larger gold nanospheres is dominated by the core-core van der Waals attraction, which becomes eventually strong enough to compress the ligand shell.

Following upon this study, Kister, Debora *et al.* have considered the effect of different ligand length [31]. In the core dominated regime, increasing the ligand length, increases the range of repulsion between the ligand shells. Thereby, the core-core van der Waals attraction is reduced and the steric stability increases. However, in contrast to the classical model [29, 21, 28], in the shell dominated regime, the steric stability decreases with the ligand length. This is related to the ordering of the ligands. They have found that shorter ligands begin to order at lower temperatures than longer ligands.

The solvent also plays an important role [32]. According to the rule of thumb, “like dissolves like”, we would expect the hexadecanethiol ligands of gold nanospheres to mix better with n-hexadecane than with n-hexane. Therefore, intuitively, the steric stability should be higher in n-hexadecane than with n-hexane. However, the opposite is observed. Solvent molecules with a similar length than the ligand length are in favor of ordering, and bundle formation of the ligands. As the bundles increase the attraction, the steric stability decreases.

Due to the particle geometry, the density of the ligand shell of spherical nanoparticles is comparatively low in the outer region. However, this does not account for flat surfaces. Here, the change in the ligand packing density with the distance to the surface is small [27]. Therefore, the ligand shell is harder. On such a ligand-solvent interface, pronounced solvent restructuring can appear. This has already been demonstrated by Widmer-Cooper *et al.* for ligand coated Cadmium Sulfur (CdS) nanorods, where the n-hexane solvent forms layers at the interface [33, 34]. The solvent layering causes oscillating solvation forces between the facets of the nanorods that can dominate the interaction.

Recently, Cadmium Selenite (CdSe) nanoplatelets have gained a lot of attention due to their extraordinary optical properties (see Section 3.2) [35, 36, 37, 38]. Similar to perovskite nanoplatelets [39], they are candidates for applications in light-emitting devices [40], solar cells [41] and other devices [42, 43]. Like other nanocrystals, CdSe nanoplatelets are usually synthesized by colloidal methods [44, 45, 37]. After synthesis, we can sterically stabilize them in apolar solvents like n-hexane [45, 46, 37]. Jana *et al.* have studied the steric stability of CdSe nanoplatelets with different ligand types in n-hexane, as well as their precipitation [45, 46]. Within the precipitation process, nanocrystals typically agglomerate into larger clusters. Like other disk-shaped nanocrystals [47, 39], CdSe nanoplatelets self-assemble into stacks of various length [45]. In order to properly control the steric stability, it is helpful to understand why the nanoplatelets form stacks. We assume, there must be an attraction between the nanoplatelets that promotes stack formation.

Unlike metallic nanocrystals, the core-core van der Waals interaction between semiconducting nanocrystals is weak. For CdSe nanoplatelets with a base facet area of 225 nm, we estimate that it is below $1\,k_{\mathrm{B}}T$ (see Section 3.4). This is too weak to be the (only) cause of stack formation. Another possible attraction comes from permanent dipoles in the CdSe nanocrystals. Dozov *et al.* have measured the permanent dipoles by transient electric birefringence [48]. For a nanoplatelet with the dimensions $20\,\mathrm{nm} \times 9\,\mathrm{nm} \times 1.5\,\mathrm{nm}$, they estimated the interaction energy to be $G_{\text{dipole-dipole}} \approx 3\,k_{\mathrm{B}}T$. However, this assumes an optimal relative orientation of the dipoles. Additionally, thermal averaging will potentially further reduce the contribution.

In this thesis, we follow another hypothesis. We show that that solvation forces play a crucial role in the interaction of CdSe nanoplatelets, that they are the main cause of stack formation, and crucially influence the steric stability in apolar solvents. Indeed, it turns out that CdSe nanoplatelets are an excellent model system to study solvation forces between ligand passivated nanocrystals. There are three main reasons for this. First, there is the weak core-core van der Waals attraction, which does not mask the solvation forces. Second, there is the dense ligand shell of $5.4\,\mathrm{ligands/nm^2}$ [49, 50]. The denser the ligand shell, the stronger the solvent restructuring is, and the stronger the solvation forces are. Third, the large facet area to particle size relation. Among other nanocrystal shapes, the ratio of facet area to particle size is maximized in platelets. As with other interactions, such as the core-core van der Waals force, solvation forces scale with the facet area. However, the structure of the ligand shell is also important in the case of solvation forces. As we show in this work, the influence of the edges decreases with increasing facet size. As a result, the ligand density increases and the solvation forces are more pronounced.

The thesis is structured as follows. We begin with a discussion of the fundamental forces between colloidal nanocrystals in Chapter 2. In the following Chapter 3, we introduce the special properties of CdSe nanoplatelets, and discuss their precipitation behavior. Building on this, we summarize what is known about the interaction of CdSe nanoplatelets, estimate the van der Waals attraction, and argue why solvation forces can cause the observed behavior of CdSe nanoplatelets. In Chapter 4, we give an introduction to molecular dynamics simulations, force fields, and umbrella sampling. Thereafter, in Chapter 5, we describe the implementation of our model systems of infinite large ligand passivated facets and CdSe nanoplatelets, as well as the implementation of umbrella sampling for the calculation of free energy curves.

We present our simulation and calculation results in Chapter 6 and Chapter 7. Solvation forces are connected to the restructuring of the solvent at surfaces. For ligand passivated nanoparticles, the restructuring happens at the ligand-solvent interface. In Chapter 6, we consider infinite facets with a ligand brush. We compare different ligand shell properties, and how they influence the solvent restructuring. We also consider different alkane solvents, including the effects of chain length, and branching.

In Chapter 7, we show our main results. We design a coarse grained model system of CdSe nanoplatelets, and use multiple windows umbrella sampling to calculate free energy curves, that provide insight into the pair interaction. We find strong oscillating solvation forces between the base facets of the nanoplatelets. Thereby, we show that the interaction depends on the relative orientation of the nanoplatelets. The oscillation is strongest for a parallel, face-to-face approach, while it turns to monotonic attractive for a side shift of the platelets. The strength of the interaction depends on the softness of the ligand shell. We show that the strength reduces with the ligand length, while it increases with the ligand grafting density. Additionally, the facet size is of importance. We find that the strength of the interaction increases linearly with the facet area. Finally, we consider different alkane solvent lengths. We find that the attraction increases with the chain length. From our results, we conclude that solvation forces are crucial in the interaction of CdSe nanoplatelets, and for their steric stability. However, while our simulation results are in good agreement with previous experimental studies, we were looking for an experimental setup to confirm our conclusions. In Chapter 8, we present experimental results on the saturation concentration, where the nanoplatelets start to assemble. We compare different base facet areas, as well as different n-alkanes. The experiments confirm our simulation results. Finally, we summarize our results in Chapter 9.

In AppendixA, we present some additional results, while we present test calculations, and simulation details in Appendix B.

Chapter 2

Interaction and colloidal stability of nanocrystals

A variety of effects can contribute to the free energy of colloidal particles in a solution. The main contributions typically include van der Waals forces G_{vdW}, dipole-dipole interactions $G_{\text{dipole-dipole}}$, solvation forces $G_{\text{solvation forces}}$, and depletion forces $G_{\text{depletion}}$. In the case of ligand grafted particles, a mixing term G_{mix}, which describes the mixing of the ligand shell with the solvent, and a term describing the compression of the ligand shell at close particle separations G_{com} have to be considered. The translational entropy S_{trans}, and the rotational entropy S_{rot} of the particles also have an influence.

From the thermodynamic perspective, the balance between these free energy terms determines the colloidal stability of particles in a solution:

$$\Delta G = \sum_i G_i. \tag{2.1}$$

In the following sections, we discuss the most important contributions. Thereby, we limit ourselves to the main effects that influence (nano-) particles in apolar solvents, like n-hexane.

2.1 Electrostatic interactions

Since atoms, molecules, and nanocrystals are composed of a large number of charges, electrostatic interactions are always present. In this section, we will look at different aspects of electrostatic interactions. We begin by considering charge-charge interactions in Subsection 2.1.1. In particular, we consider the interaction of ions and charged surfaces. In this context, we also discuss how polar and apolar solutions differ. In Subsection 2.1.2, we then consider dipole-dipole interactions in general and between nanocrystals. Finally, we consider van der Waals interactions in Subsection 2.1.3.

2.1.1 Charge-charge interactions

Electrostatic interactions can be crucial for the interaction of colloidal particles.

Solvent	Dielectric constant ϵ	Bjerrum length λ_{B} (nm)
Water	80	0.7
Ethanol	26	2.1
Acetone	21	2.7
n-octane	1.84	30.3
n-dodecane	2.01	27.7
n-hexadecane	2.05	27.2
Cyclohexane	2.03	27.4

Table 2.1: Dielectric constants ϵ for different solvents [20], and calculated Bjerrum lengths of two elementary charges at 300 K.

It is helpful to distinguish between polar and apolar solvents. Polar solvents are water and aqueous solutions with high dielectric constants. In contrast, apolar solvents have low dielectric constants, like alkanes. In these two regimes, the behavior of charged particles differs significantly.

The interaction energy between two ions with the charges q_1 and q_2 can be calculated by the Coulomb interaction:

$$E_{\text{Coulomb}} = \frac{1}{4\pi\epsilon_0\epsilon}\frac{q_1 q_2}{r}, \tag{2.2}$$

where r is the distance between the charges, and ϵ the dielectric constant of the solvent.

To prevent the combining of dissolved ions, the thermal energy must be greater than the Coulomb attraction between the charges. The Bjerrum length λ_{B} describes the distance between two elementary charges e at which the thermal energy ($\sim k_{\mathrm{B}}T$) is equal to their Coulomb energy [51, 52]:

$$\lambda_{\mathrm{B}} = \frac{e^2}{4\pi\epsilon_0\epsilon k_B T}. \tag{2.3}$$

In Table 2.1, we list the dielectric constants of different solvents, as well as calculated Bjerrum lengths for the interaction of two elementary charges as found in the interaction of small ions like NaCl.

The Bjerrum length in water is small ($\lambda_{\mathrm{B}}^{\mathrm{H^2O}} = 0.7\,\mathrm{nm}$), while it is much larger in an apolar solvent like n-octane ($\lambda_{\mathrm{B}}^{\text{n-octane}} = 30.3\,\mathrm{nm}$) [51, 52]. This comparison indicates already that it is easier to solve ions in water, than in an apolar solvent. Additionally, water forms hydration shells around ions, which sterically contribute to the stabilization of small ions [51]. In contrast, while an apolar solvent like n-octane might restructure around an ion, the radius of the restructured region will be much smaller than the Bjerrum length. Therefore, it cannot significantly contribute to the stabilization.

In combination, the effects cause the solubility of NaCl and other small ions in water and their insolubility in apolar solutions. However, this does not mean that dissociated ions do not occur in apolar solutions. Ions in apolar media are typically either larger in size, or contained in a protective structure, like a micelle, or a polymer [51]. Nevertheless, in general, there are drastically fewer ions in an apolar than in a polar solvent.

However, just because there are fewer ions, does not mean that they have less impact on the colloidal stability of nanoparticles. A related quantity to the Bjerrum length λ_{B} is the Debye-Hückel length:

$$\lambda_\mathrm{D} = \left(4\pi\lambda_\mathrm{B}\sum_i n_i^0 z_i^2\right)^{-1/2}, \tag{2.4}$$

where z_i is the valency, and n_i^0 the mean number density of ion species i. The Debye-Hückel length arises in the context of the Poisson-Boltzmann equation [53], and quantifies the length scale, where a charged surface perturbates a counterion cloud [52].

The magnitude of the Debye length depends solely on the solution properties, and not on the surface properties [20]. In aqueous media, depending on the ion concentration, the Debye length ranges from a few tens of nm to a fraction of a nm. In contrast, it ranges between 1 to 100 µm in apolar solvents. Therefore, while there are fewer ions in an apolar solvent, the screening of charges is drastically lower.

The differences between the polar and the apolar regime have severe consequences for the interaction and colloidal stabilization of nanoparticles. Nanoparticles can be stabilized by surface charges in polar solvents. Counterions will screen the surface charges. An electric double layer (EDL) forms. As two particles approach, the electric double layers overlap. This induces local osmotic pressure between the surfaces, which results in a repulsion between the nanoparticles [28].

Similar to the Hamaker approach, we can formulate geometric dependent equations to describe the interaction energy by the double layer [20]. For example, the interaction energy of two flat surfaces is:

$$G_\text{EDL, flat} = \frac{1}{2\pi\lambda_\mathrm{D}} Z e^{\frac{-D}{\lambda_\mathrm{D}}}, \tag{2.5}$$

and for two spheres of radii R_1, and R_2 it is:

$$G_\text{EDL, spheres} = \frac{R_1 R_2}{R_1 + R_2} Z e^{\frac{-D}{\lambda_\mathrm{D}}}, \tag{2.6}$$

where D is the surface-surface distance. Z is an interaction constant, similar to the Hamaker constant A:

$$Z = 64\pi\epsilon_0\epsilon\left(\frac{k_\mathrm{B}T}{ze}\right)^2 \tanh^2\left(\frac{ze\psi_0}{4k_\mathrm{B}T}\right) \tag{2.7}$$

It depends on the surface potential ψ_0 of the isolated surface ($D \longrightarrow \infty$). For low potentials, we can approximate the surface potential ψ_0 by the charge density $\sigma = \epsilon_0\epsilon\psi_0$.

These effects can be described by the DLVO theory, named after Derjaguin, Landau, Verwey, and Overbeek [20]. This theory describes the colloidal stability by the balance between the van der Waals attraction, and the repulsion by the electric double layer:

$$\Delta G = G_\mathrm{vdW} + G_\mathrm{EDL}. \tag{2.8}$$

This model works well in the polar regime. However, as discussed, there are fewer charges, and a drastically smaller screening, in the apolar regime. That is why this model is not transferable to apolar solvents. Here, charges influence each other over large distances.

Thus, if nanoparticles have surface charges, this will have a major impact on their interaction.

The question remains whether surface charges occur on nanocrystals in apolar solvents. As we will discuss in Section 2.2, nanocrystals are usually sterically stabilized in an apolar solvent. Ligand molecules are grafted to their surfaces, forming a protective shell, and neutralizing the surface. Therefore, in the ideal case, the nanoparticles are neutral. In an ideal apolar system, electrostatic interactions due to surface charges do not appear. However, this does not completely exclude the occurrence of defects in real systems [52]. Unfortunately, there is a remarkable void in the literature concerning this issue.

2.1.2 Dipole-dipole interactions

Even in the ideal apolar system without ions and surface charges, electrostatic interactions play a major role. Any atom, molecule or nanocrystal possesses a large number of charges. According to the superposition principle, the electrostatic potential at a point P with the position vector $\vec{R} = (X, Y, Z)$ away from the center of a group of charges Q_i is the sum of the individual potentials:

$$\Phi\left(\vec{R}\right) = \frac{1}{4\pi\epsilon_0\epsilon} \sum_i \frac{Q_i}{|\vec{R} - \vec{r_i}|}, \tag{2.9}$$

where $\vec{r_i} = (x_i, y_i, z_i)$ is the position vector of the charges.

Assuming that the distance $|\vec{R}\,|$ from the center of the charge distribution is greater than the mean distance of the charges, a Taylor expansion can be carried out. The result is the multipole expansion:

$$\begin{aligned} \Phi(R) = \frac{1}{4\pi\epsilon_0\epsilon} \Bigg[& \frac{1}{|\vec{R}\,|} \sum_i Q_i + \frac{1}{|\vec{R}\,|^3} \sum_i (Q_i \vec{r_i}) \vec{R} \\ & + \frac{1}{|\vec{R}|^5} \sum_i \frac{Q_i}{2} \Big[\left(3x_i^2 - r_i^2\right) X^2 + \left(3y_i^2 - r_i^2\right) Y^2 + \left(3z_i^2 - r_i^2\right) Z^2 \\ & + 2\left(3x_i y_i XY + 3x_i z_i XZ + 3y_i z_i YZ\right) \Big] + \cdots \Bigg]. \end{aligned} \tag{2.10}$$

The first term describes the normal Coulomb potential, the second term electric dipoles ($\vec{\mu} = Q_i * \vec{r_i}$), and the third term electric quadrupoles. For neutral particles, the first term becomes zero ($\sum_i Q_i = 0$). However, this does not account for the other terms. Therefore, even if atoms, molecules, or nanocrystals are overall neutral, electrostatic interactions must be considered. This concerns in particular the dipole-dipole interaction. The influence of the quadrupoles and of multipoles of higher order is usually negligible.

In general, the interaction energy of two dipoles $\vec{\mu_1}$ and $\vec{\mu_2}$ with a distance $\vec{r}$ can be calculated by [20]:

$$U_{\text{diple-dipole}} = \frac{1}{4\pi\epsilon_0\epsilon} \frac{|\vec{\mu_1}|\,|\vec{\mu_2}| - 3(\vec{\mu_1} \cdot \hat{e}_r)(\vec{\mu_2} \cdot \hat{e}_r)}{|\vec{r}\,|^3}, \tag{2.11}$$

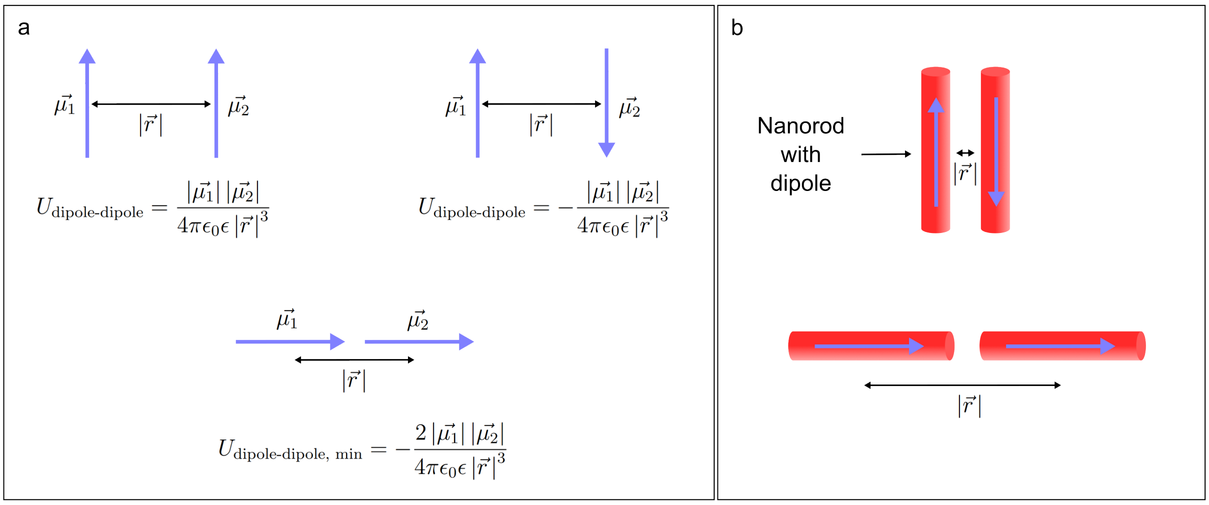

Figure 2.1: The interaction energy $U_{\text{diple-dipole}}(\vec{r})$ of two dipoles $\vec{\mu_1}$ and $\vec{\mu_2}$ with distance $|\vec{r}|$ depends on the relative orientation of the dipoles. **Panel a** shows sketches of different dipole orientations. For a fixed distance $|\vec{r}|$, the configuration where the dipoles point in-line in the same direction has the lowest energy. For dipoles in nanocrystals, the minimal distance depends on the nanocrystal shape, and therefore the minimal interaction energy. **Panel b** shows sketches of nanorods with dipoles. Here, the minimal dipole distance is smaller in the parallel configuration.

where $\hat{e}_r$ is a unit vector pointing along the line that connects the dipoles. The strength of the dipole-dipole interaction depends on the relative orientation of the dipoles (see Figure 2.1a). Dependent on the orientation, the dipole-dipole interaction can be attractive, or repulsive. For example, if two dipoles point in-line in the same direction, the attraction between the dipoles will be maximal for a given distance $|\vec{r}|$:

$$U_{\text{dipole-dipole, min}} = -\frac{2\,|\vec{\mu_1}|\,|\vec{\mu_2}|}{4\pi\epsilon_0\epsilon\,|\vec{r}|^3}. \tag{2.12}$$

There are a number of nanocrystal types with large permanent dipoles [54, 55, 56, 57, 52]. For nanocrystals, the dipole orientation with the lowest energy actually depends also on the position of the dipoles within the nanoparticles, the separation of the nanoparticles, and the shape of the nanoparticles. For example, consider nanorods with dipoles orientated along the central axis. A parallel orientation of the nanorods (antiparallel orientation of the dipoles) can enable a closer contact and a smaller distance $|\vec{r}|$ between the dipoles than a linear configuration of the nanorods (see Figure 2.1b). Thus, dependent on the system, a parallel nanorod configuration can result in a stronger attraction due to the dipole-dipole interaction than an in-line nanorod configuration [52].

Furthermore, thermal averaging of the relative orientations of the dipoles has to be considered in estimating the strength of the dipole-dipole interaction between colloidal nanocrystals (similar to the Keesom-interaction for freely rotating dipoles, see next section). Due to the thermal averaging, the actual attraction between nanocrystals due to the dipole-dipole interaction will generally be weaker than one would naively expect from Equation 2.11 [48].

2.1.3 Van der Waals forces

Van der Waals (vdW) forces appear between all atoms, molecules, and particles. Therefore, they are the most ubiquitous interaction between colloidal nanoparticles [58]. In general, we can differentiate three effects, which can contribute to the van der Waals forces [20]. All three contributions are essentially dipole-dipole interactions. However, they differentiate by the dipole type.

The first one is the Keesom-interaction, as the result of the interaction of two freely rotating permanent dipoles (or multipoles). The assumption of freely rotating dipoles is valid at large separations, or in media with a high dielectric constant ϵ, where the angle dependence of the free energy is smaller than $k_\mathrm{B}T$. A Boltzmann-average can be applied to the interaction, resulting in an interaction energy:

$$G_\mathrm{Keesom} \propto -\frac{1}{Tr^6}, \tag{2.13}$$

where r is the distance, and T is the temperature. Permanent dipoles do not occur in every material. Therefore, the Keesom-interaction does not appear in all materials. It should also be noted that large permanent dipoles can occur in nanocrystals [54, 55, 56, 57, 52]. For these dipoles, the assumption of free rotation is not applicable. They are not included in the Keesom interaction and must be treated individually (see previous subsection).

The second contribution to the van der Waals attraction is the Debye interaction. A permanent dipole in one molecule can polarize a second molecule, creating an induced dipole. The Debye interaction is caused by permanent dipole-induced dipole interactions. As this interaction is very similar to the first contribution, a similar proportionality applies here:

$$G_\mathrm{Debye} \propto -\frac{1}{r^6}. \tag{2.14}$$

However, a permanent dipole is not required to induce a dipole in an atom or molecule. Intuitively, we can understand this as follows. Suppose the time-averaged dipole moment of an atom or molecule is zero. Then at each instant there is still a finite dipole moment given by the instantaneous positions of the electrons and nuclear protons [20]. The electric field of this instantaneous dipole moment can induce a dipole in a neighboring atom or molecule. Then, the interaction of the induced dipole moments creates an attraction.

This induced dipole-induced dipole interaction is the third term contributing to the van der Waals attraction. The forces are called the London forces, dispersion forces, or charge fluctuation forces. London forces are always present, since charge fluctuations are present in every material. Here, similar to the first two contributions, the following proportionality applies:

$$G_\mathrm{London} \propto -\frac{1}{r^6}. \tag{2.15}$$

Overall, the interaction energy due to the van der Waals forces is:

$$G_{\mathrm{vdW}} = -\frac{C(T)}{r^6}, \tag{2.16}$$

where $C(T)$ is a material specific constant that can depend on the temperature.

Equation 2.16 describes the van der Waals interaction energy between two atoms or molecules. The interaction between larger objects, such as nanocrystals, can be described as the sum of the atomistic contributions. Often, the discrete nature of the materials is not relevant. Then, the Hamaker approach can be used [59, 20, 58]. In this continuum approach, the interaction energy between the atoms/molecules of the two colloidal particles is integrated over the particle volumes V_1 and V_2:

$$G_{\mathrm{vdW}} = -\int_{V_1} dV_1 \int_{V_2} dV_2 \, \frac{A}{\pi^2 r^6}. \tag{2.17}$$

A is the material dependent Hamaker constant:

$$A = \pi^2 C \rho_1 \rho_2, \tag{2.18}$$

where ρ_1 and ρ_2 are the number densities in the two particles.

One advantage of this approach is that the Hamaker constant of a material only needs to be calculated once. This greatly simplifies the calculation of the van der Waals interaction. In the literature, Hamaker constants are typically specified for interaction in vacuum. However, the Hamaker constant for the interaction between two particles in a solvent can be approximated, if the vacuum Hamaker constants of the material of the two particles A_{11} and of the solvent A_{22} are known [20]:

$$A_{121} \approx \left(\sqrt{A_{11}} - \sqrt{A_{22}}\right)^2. \tag{2.19}$$

Equation 2.17 has been solved for different geometries. For the interaction between two spheres of radius R_1 and R_2, it solves to:

$$G_{\mathrm{vdW}} = -\frac{A}{6d} \frac{R_1 R_2}{R_1 + R_2}, \tag{2.20}$$

under the condition that $R_1, R_2 \gg d$, where d is the surface-surface distance.

For the interaction between two flat surfaces, it solves to:

$$\frac{G_{\mathrm{vdW}}}{S} = -\frac{A}{12\pi d^3}, \tag{2.21}$$

where S is the surface area, and d the distance between the two surfaces.

The Hamaker method offers a good first-order approximation of the van der Waals interaction. However, it neglects many-body effects between the atoms of the two particles, and retardation effects, which are caused by the finite speed of light. Retardation effects can be important at larger distances. Additionally, it neglects effects that appear at short distances due to the discrete atoms. Although there are more accurate models for the approximation of the van der Waals interaction, like the Dzyaloshinskii-Lifshitz-Pitaevskii, and the discrete coupled-dipole method, the Hamaker model is widely used, because of its simplicity [58].

2.2 Ligand effects

Capping ligands, surfactant molecules grafted to the surface of nanocrystals, have a crucial impact on nanocrystal properties. For example, they can form permeation barriers, which influence nanocrystal growths, and can direct reactions [27].

Ligand shells also significantly influence the interaction between nanocrystals. Let us assume nanocrystals with a high attraction, e.g., due to van der Waals forces [21, 30]. If we surround this nanocrystal with a ligand shell, these will help to screen the attraction. More importantly, it will increase the distance between the nanocrystals. As the van der Waals attraction is short in range (see Equation 2.17), this significantly changes the attraction between the nanocrystals. This effect can be tuned well via the properties of the ligands. In apolar solvents, ligand shells are widely used to tune sterically the colloidal stability of nanoparticles [29, 21, 28].

Two contributions to the free energy are of importance. The first is the free energy of the mixing of the solvent with the ligands G_{mix}. According to the Flory-Krigbaum theory, we can describe the free energy of mixing of two chains tethered to a nanocrystal surface by the equation [28, 29]:

$$G_{\text{mix}} = 2k_B T \frac{v_s}{v_s} \left(\frac{1}{2} - \chi \right) \int_V \phi_1 \phi_2 \, dV, \tag{2.22}$$

where k_B is the Boltzmann constant, T the temperature, v_s the Kuhn segment volume, v_s the solvent molecular volume, and χ the Flory-Huggins chain-solvent interaction parameter. ϕ_1 and ϕ_2 are the segment densities of the ligand shells. Equation 2.22 can be adapted to different particle geometries, such as spherical nanoparticles or flat surfaces [29, 21].

In a good solvent ($\chi < 1/2$), the ligands of a nanoparticle will expand and mix with the solvent, while they will shrink in a bad solvent ($\chi > 1/2$). For example, ligands with an aliphatic tail will reject mixing with water, while they like to mix with an apolar solvent like n-hexane. In other words, in a good solvent the mixing of the ligands with the solvent reduces the free energy, while the mixing in a bad solvent will increase the free energy. As two particles approach to separations d, closer than two times the expanded ligand length L ($d < 2L$), solvent molecules will be pushed out of the ligand shells. In a good solvent, this increases the free energy of the system ($G_{\text{mix}} > 0$), and G_{mix} therefore contributes to the repulsion between the colloidal particles. On the other hand, in a bad solvent, this leads to a reduction of the free energy($G_{\text{mix}} < 0$), and G_{mix} contributes to the attraction [28]. Therefore, nanoparticles coated with ligands with an aliphatic tail will have a lower colloidal stability in water than in n-hexane [60].

The second contribution is the compression of the ligand chains at small separations. In the classical approach via the Flory model, it is assumed that the ligand density is small, and that the compression of the ligands starts at distances $d < L$. The approach describes the compression as [61, 29]:

$$G_{\text{com}} = 2k_{\text{B}} T \nu \left[\frac{\delta^2 - 1}{2} - \ln \delta \right], \tag{2.23}$$

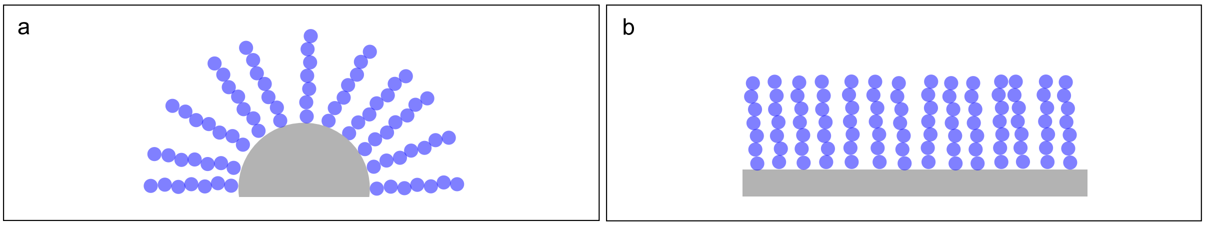

Figure 2.2: Schematic sketches to illustrate the arrangement of the ligands in the ligand shell on a curved/spherical surface (**panel a**) and on a flat surface (**panel b**). The ligand packing density is reduced at a curved surface.

where δ is the compression ratio, and ν is the total number of ligands per unit area of the nanoparticle.

As the ligand shells are compressed, the ligands can occupy less volume. Therefore, their configurational entropy reduces. This causes a repulsion, and an increase in the free energy G_{com} [29, 21]. In general, the repulsion will depend on the ligand density, the elastic properties of the ligands, and the degree of interpenetration of the ligand shells.

In a good solvent, both terms create a repulsion at small particle distances. It is usually possible to use different molecules as ligands, e.g., carboxylic acids with different length [45]. Therefore, it is relatively easy to control the minimal distance between colloidal particles by the ligand shell, thereby tuning the attraction, and their colloidal stability.

In this context, an understanding of the key properties of ligand shells is helpful. A key aspect is the ligand packing density. The packing density of a ligand shell will increase with the ligand grafting density. However, an increase in the packing density can also be achieved by using ligands that occupy more space, like dendrimers [62].

It is important to be aware of the influence of surface curvature. In comparison, the ligand shell of a particle with a curved surface and linear ligands will be dilute, while the ligand shell of a particle with flat facets will be dense (see Figure 2.2).

We can address this by an empirical model [63, 27]. We define the ligand packing density $\lambda_0(r)$ by

$$\lambda_0(r) = \frac{A_C(r)}{A_S}, \tag{2.24}$$

where $A_C(r)$ is the cross-sectional area per ligand, and A_S the surface area per ligand. For a curved surface, the ligand packing density $\lambda_0(r)$ will be smaller at larger distances r to the surface. For a sphere, we can describe it as:

$$\lambda_{0,\text{sphere}}(r) = \frac{R^2}{(r+R)^2}\,\lambda_{0,\text{sphere}}(0), \tag{2.25}$$

where R is the radius of the sphere. In contrast, for an extended flat surface, we get:

$$\lambda_{0,\text{flat}}(r) = \lambda_{0,\text{flat}}(0). \tag{2.26}$$

Although it should be noted that the facets of nanoparticles are finite, this nevertheless demonstrates the greater packing density on flat surfaces. The empirical model highlights the crucial influence of the surface curvature on the packing density of the ligands, which has to be considered in the discussion of the impact of ligand shells.

Concerning the continuum approach, we should mention that the model assumes dilute ligand shells [29, 21]. However, this is not always an adequate description. For example, CdSe nanoplatelets with 5.4 ligands/nm^2 have a rather dense ligand shell. Whereby, the interpenetration of two approaching ligand shells is quite limited [45]. Furthermore, there are several effects that are not covered due to the continuum approach. In a bad solvent [32], or at a low temperature [64, 33, 30], the tendency of the ligands to mix with the solvent molecules is strongly reduced. In such a regime, it is more favorable for the ligands to form bundles due to the van der Waals attraction between the chains [65, 28, 27]:

$$G_{\text{lig-lig}} = -A \frac{3\pi}{8l^2} \frac{L}{x^5}, \tag{2.27}$$

where L is the chain length, l the carbon-carbon bond length, A the Hamaker constant, and x the backbone separation. As a result, the structure of the ligand shell significantly affects the interaction between nanoparticles [33, 30, 31].

In this context, it is worth taking a look at dried superlattices of nanoparticles. Such a superlattice can be generated via evaporation of the solvent, in which the nanoparticles have been synthesized, or dispersed. A typical assumption for simulations and calculations is that the superlattice symmetry does not depend on the dynamics in the solvent. Therefore, in simulations, and calculations of such a superlattice, usually only the dried up state, without any solvent, is considered. For the prediction of nanoparticle separations, and of superlattice symmetries (bcc, fcc, etc.), geometrical models were developed [28]: the optimal packing model (OPM) [66], the overlap cone model (OCM) [67], and the orbifold topological model (OTM) [68]. The OTM model is stands out. It treats ligand shell deformations as a set of topological defects, such as vortices and declination lines [68, 69]. For the future, it seems worth considering such concepts to improve the description of the ligand shell of dispersed nanoparticles.

Finally, the introduced continuum approach neglects the effect of solvation, and depletion forces, which we will introduce in the following two sections. These forces depend strongly on the properties of the interface of the colloidal particle with the solvent, and such on the ligand shell. This is a main aspect of this thesis.

2.3 Solvation forces

When a surface is brought into contact with a liquid, the structure of the liquid near it changes [20]. Often, the liquid molecules restructure into layers, as depicted for spherical molecules in Figure 2.3a. In these cases, the layer formation is evident from an oscillation in the liquid density, which decreases in amplitude with distance from the surface. How strong the change in the boundary layer is depends on the nature of the surface, as well as the liquid type. At rough, uneven, or soft surfaces the liquid density oscillation is reduced. This also applies to bulky liquid molecules, which poorly form layers.

In turn, when two surfaces approach each other in a liquid, the layering can be amplified (Figure 2.3b). Dependent on the distance D, well-defined liquid layers appear

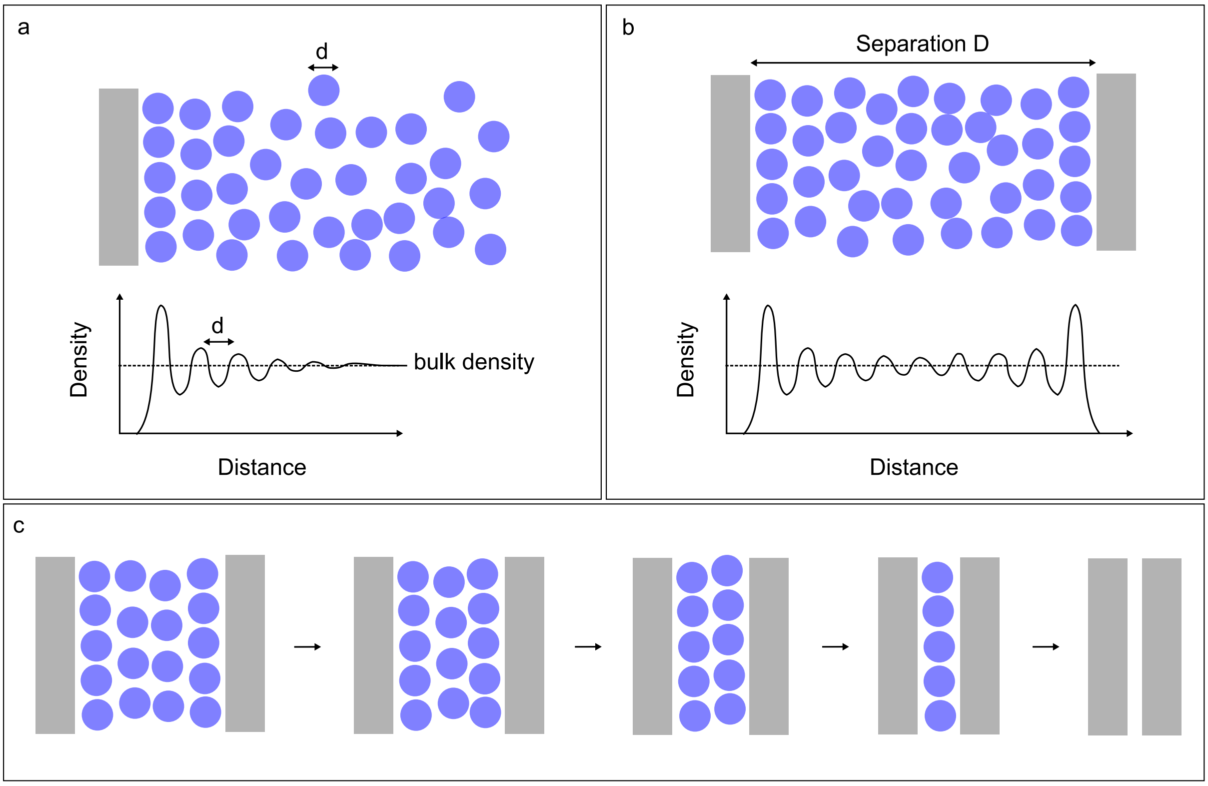

Figure 2.3: Schematic sketches to illustrate the liquid layering and density changes of spherical molecules at a surface (**panel a**), and the changes as two surfaces approach each other (**panels b**, and **c**).

(Figure 2.3c). These layers are energetically or entropically favored [70]. When the distance is varied, oscillatory forces appear. These forces are called solvation, or structural forces. In the case of aqueous solutions, where hydrogen bonds are of large importance, these forces are also referred to as hydration forces.

The oscillation also manifests itself in the free energy. States with well-defined layers correspond to minima in the free energy, whereas free energy maxima are located at the transitions between the states. Typically, the free energy oscillates with a periodicity equal to the mean diameter d of the liquid molecules [71]. In a first approximation, the free energy can be described by an exponentially decaying cosine function [20, 70]:

$$G_{\text{solvation forces}} \approx G_0 \cos\left(\frac{2\pi D}{d}\right) e^{-\frac{D}{d}}, \tag{2.28}$$

where G_0 is the value of the first free energy minimum. In the first minimum, the two surfaces are in contact ($D \approx 0$). Usually, the oscillation decays on separations of 5 to 10 molecular diameters [72]. It is worth noting, that the restructuring of the liquid does not only create solvation forces. Due to the density changes in the liquid, it also influences the van der Waals attraction between the two surfaces. Therefore, solvation forces can be seen as van der Waals forces at small distances, with inclusion of the discrete structure of the fluid [70]. However, the relationship between solvation forces and van der Waals forces could also be considered as an example of the nonadditivity of intramolecular and (nano-) particle interactions, in the sense that the different forces are not independent of each other [22].

Solvation forces have been intensely studied for extended surfaces. Israelachvili summarizes the essential aspects of different properties in his book [20]. We reproduce them here in abbreviated form.

- **Magnitude.** The oscillatory solvation force in general exceeds the van der Waals force at separations below 5 to 10 molecular diameters.

- **Inert, spherical, rigid solvent molecules.** The periodicity of the oscillatory solvation forces at room temperature is typically close to the mean molecule diameter. For example, this is the case for tetrachloromethane, benzene, cyclohexane, and OMCTS [71].

- **Linear and branched solvent molecules.** Christenson *et al.* have measured the solvation forces between molecularly smooth mica surfaces in different n-alkane solvents [72]. Independent of the length of the linear alkane molecules, they have found oscillating solvation forces at separations below around 5 nm, that decay with the distance between the mica surfaces. In contrast to liquids with rigid spherical molecules [71], the length of the n-alkane molecules does not influence the periodicity, which is comparable to the width of the alkane molecules. However, the strength of the solvation forces increases with the alkane length. Branching of alkanes disrupts the liquid layering. Therefore, it can reduce the amplitude of solvation forces, and in the extreme case change it from oscillatory to monotonic [71, 73].

- **Water, and immiscible polar components in apolar liquids.** Even a trace amount of water in an apolar liquid can have a dramatic effect on the solvation force between hydrophilic surfaces. When water molecules adsorb to the hydrophilic surfaces, they cause a disruption in the ordering of the solvent layering. Typically, this leads to a shift of the oscillatory forces to lower, more adhesive energies.

- **Surface structure and roughness.** Between two completely smooth surfaces, the liquid molecules will order in layers (out-of-plane ordering). However, there is little inducement for ordering within planes (in-plane ordering). On the other hand, if the surfaces have a crystalline periodic lattice structure, this will induce in-plane, “epitaxial” ordering [74]. In contrast, if the surface is randomly structured or rough, the oscillatory solvation force can vanish, and be replaced by a monotonic force.

- **Surface curvature.** As long as the curvature of a surface is regular, or uniform, ordering of the liquid, and therefore solvation forces can occur. This is a consequence of the Derjaguin approximation. This relationship has often been used in the measurement of solvation forces [72]. However, it is worth noting that if the surface properties change together with the curvature, the Derjaguin approximation can lose its validity.

It is to assume that the above listed fundamental behavior of solvation forces does not differ from the appearance of oscillatory solvation forces between nanoparticles. However, the appearance of solvation forces depends on the geometry and surface structure of the interacting objects. Therefore, only detailed studies of nanoparticle systems can provide insight into the solvation forces that actually occur.

While there are various studies considering the role of solvation forces in the interaction of nanoparticles with hard and smooth surfaces [75], especially of hydration forces in aqueous environments [76, 77, 78], there are fewer studies considering solvation forces between ligand coated nanoparticles in apolar solvents.

The interaction of ligand coated nanoparticles is of great significance, as nanoparticles in apolar solvents typically are sterically stabilized by ligands. In general, a surface that is coated with ligands will be softer than the solid surface. Therefore, it is counterintuitive to expect large solvent restructuring at the ligand-solvent interface, and large solvation forces. This is particular true, if the solvent is a good or a theta solvent for the ligand shell, or if the surface the ligands are bound to is curved (see Figure 2.2) [63, 27].

Studies of ligand coated spherical nanoparticles in explicit apolar solvent, support these arguments [30, 31, 32, 60]. Due to the soft ligand shells, solvent layering and solvation forces are insignificant. However, for similar ligand grafting densities, the ligand packing density at the ligand solvent interface is larger on flat surfaces than on curved surfaces (see Figure 2.2) [63, 27]. Widmer-Cooper *et al.* have studied ligand coated nanorods with large, but narrow, flat facets. As they have shown by molecular dynamics simulations, in these systems solvation forces have a crucial impact on the effective interaction [33, 34]. The solvent layering, and the solvation forces, depend on the temperature. At lower temperatures, the ligands form bundles that support solvent layering, causing significant oscillatory solvation forces. In contrast, at higher temperatures, the ligands become disordered, and the interaction changes to a monotonic repulsion [33]. They have also shown that the solvent layering and the solvation force becomes weaker for lower ligand grafting densities. Additionally, they have studied different facet widths. Since the facet width influences the space available to the ligands, as well as the ordering of the ligands, it influences the shape and strength of the solvation forces. The effect of the facet width is most pronounced at low ligand grafting densities, where the interaction is monotonic repulsive for narrower facets, and oscillatory for broader facets [34].

2.4 Depletion forces

The presence of smaller particles can cause an attraction between colloidal particles that is of entropic origin [52, 58, 20]. The acting force is commonly known as the depletion force, and the particles that cause it as depletants. Depletants can be polymer coils, micelles, and smaller solid particles.

For a dilute concentration of depletants, the mechanism was first described by Asakura and Oosawa [79]. Let us consider two colloidal particles, and spherical depletants. We can define a volume around the colloidal particles that the center of the depletants cannot enter, as depicted in Figure 2.4a for two platelets. As the two platelets assemble, this excluded volume reduces by ΔV (Figure 2.4b). The increase in available volume V is connected to an increase in the entropy of the depletants, and thus to a reduction of the free energy [58]. The free energy by the translation entropy of the depletants is:

$$G_{\text{depletants, translational}} = -Nk_BT\ln V, \tag{2.29}$$

where N is the number of depletants. Assuming that V_0 is the original volume, and ΔV the volume change, we can rewrite this to:

$$G_{\text{depletants, translational}} = -Nk_BT\ln\left(V_0 + \Delta V\right) = -Nk_BT\left[\ln V_0 + \ln\left(1 + \frac{\Delta V}{V_0}\right)\right]. \tag{2.30}$$

We can approximate the second term via the Taylor series around the expansion point of value 1:

$$\ln\left(1 + \frac{\Delta V}{V_0}\right) \approx \frac{\Delta V}{V_0} - \frac{\left(\frac{\Delta V}{V_0}\right)^2}{2} + \cdots \tag{2.31}$$

Nk_BT/V_0 is the osmotic pressure p_{osmotic}. Therefore, taking only the first term of the Taylor series into account, the depletion force effects the free energy by:

$$G_{\text{depletion}} \approx -\, p_{\text{osmotic}}\,\Delta V. \tag{2.32}$$

As the strength of the depletion force depends on the excluded volume, it is typically stronger between colloidal particles with flat facets, like platelets, than between particles with a curved surface like spheres (Figure 2.4b, c).

In the Asakura-Oosawa model, we assume that outside of the depletion zone, the depletants are uniformly distributed. For a low depletant concentration, this is a good approximation. However, at higher depletant concentrations, this approximation breaks down, and the depletants form layers around the larger colloidal particles.

Crocker *et al.* have done a study that demonstrates this point well [80]. They have probed the effect of the depletion force between two PMMA (polymethylmethacrylate) spheres in a line optical tweezer. The PMMA spheres have diameters of about (1100 ± 15) nm. As depletants, they have used 83 nm PS (polystyrene) spheres. For low depletant volume fractions, they have measured free energy curves that are monotonically attractive, and in good agreement with the Asakura-Oosawa model. However, in slightly larger volume fractions, they have found a repulsive barrier at separations of about the diameter of the depletants. Finally, for volume fractions ≥ 0.25, they have measured oscillating free energy curves. Crocker *et al.* explain this by the more pronounced layering of the depletants.

It becomes apparent that there are large similarities in the behavior of depletion and solvation forces, as both of which are caused by the layer formation of particles, and are largely a result of entropy changes. Thus, the free energy curves of Crocker et al. for large volume fractions and the free energy curves describing solvation forces between colloidal particles are very similar (compare with results in Chapter 7). Therefore, for this work, which is mainly concerned with solvation forces, it is worthwhile to take a closer look at the behavior of depletion forces.

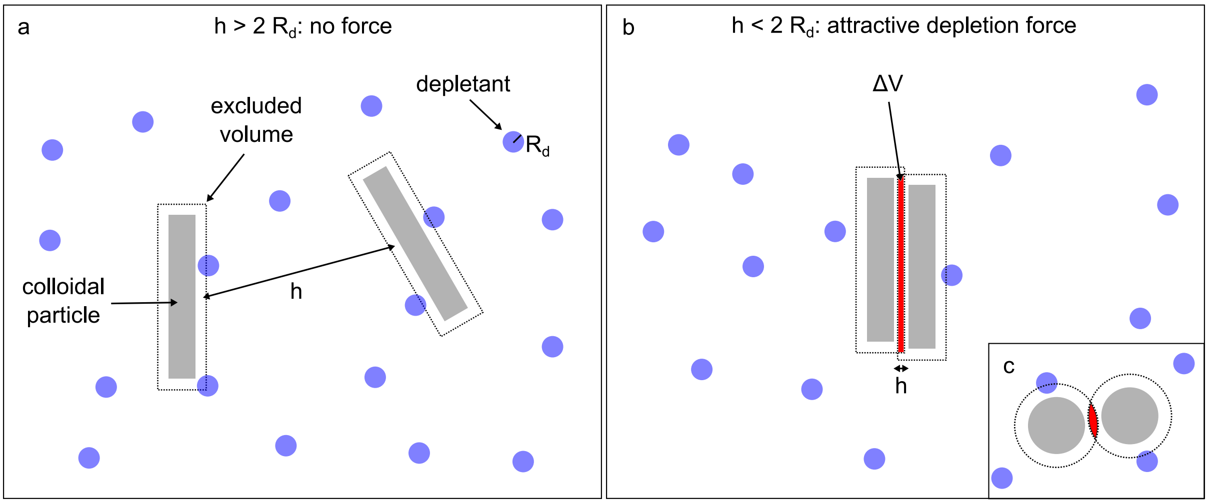

Figure 2.4: Schematic sketch to illustrate the Asakura-Oosawa model of the interaction of colloidal particles in a dilute depletant solution. We can define an excluded volume around each colloidal particle that the center of the depletants cannot enter (**panel a**). As two particles approach, the change in excluded volume ΔV leads to an attraction between the particles (**panel b**). For similarly sized particles, the excluded volume ΔV is smaller between particles with a curved surface than between particles with a flat surface (**panel c**).

Mason has studied the depletion interaction caused by nanometer-sized micelles between micron-sized disks and spheres of wax in mixed aqueous dispersions [81]. In agreement with the Asakura-Oosawa model, he has found that the depletion force can be controlled by the micelle concentration. Thereby, he has shown that the micelle concentration at which the micron-sized particles start to aggregate depends on their orientation, shape, and size. Assembling of disks occurs at much lower concentrations than that of disks with spheres of similar sizes. Again, the aggregation of spheres with each other happens at even higher micelle concentrations.

For disks, the change in excluded volume at an approach depends on the relative orientation. Accordingly, the attraction is stronger in the base facet-to-base facet orientation than in the side facet-to-side facet orientation. Therefore, Mason has found that, dependent on the micelle concentration, disks form stacks. At higher micelle concentrations, these stacks form bundles, attracting each other side by side.

Chapter 3

CdSe nanoplatelets as model system

Solvation forces are caused by the restructuring of the solvent between surfaces or interfaces. Thereby, the restructuring is more pronounced between hard surfaces. As illustrated in Figure 2.2, the ligand shell on a flat surface is denser than on a curved surface. Therefore, we expect stronger solvation forces between nanoparticles with flat facets than between nanoparticles with curved surfaces. Among the different shapes of nanocrystals, nanoplatelets possess a maximized facet to particles size ratio. Therefore, nanoplatelets are an optimal model system to study solvation forces.

We use CdSe nanoplatelets as a model system. They have several properties, which are advantageous. They typically have a rectangular shape, where their thickness can be controlled with atomistic precision. They possess optical properties that we can exploit by charge carrier measurements to learn about their agglomeration behavior (see Chapter 8). Additionally, the magnitude of the van der Waals force between the CdSe nanoplatelets is small. This is helpful, as a weak van der Waals attraction will not dominate over the solvation forces.

This chapter is structured as follows. In Section 3.1, we discuss the synthesis of CdSe nanoplatelets. Thereafter, we discuss the unique (optical) properties of CdSe nanoplatelets in Section 3.2, as well as their precipitation behavior in Section 3.3. In the following Section 3.4, we discuss the interaction between CdSe nanoplatelets, and how the different contributions to the interaction influence the colloidal stability. We show that the van der Waals attraction is too weak to be the cause of the nanoplatelet stack formation. Finally, we discuss, how other contributions can be the cause of stack formation, and the role of solvation forces.

3.1 Synthesis of CdSe nanoplatelets – atomistic precision

Zincblende CdSe nanoplatelets typically have a rectangular platelet-like shape. They can be synthesized by a colloidal approach [44, 45, 37]. Typically, a long-chain Cd(carboxylate)$_2$ like Cd(myristate)$_2$ is used as a precursor. It is heated together with Se powder in a non-coordinating solvent like 1-octadecene. Then, a short-chain Cd(carboxylate)$_2$ is added. The nanoplatelet thickness is controlled by the addition temperature, while the lateral size of depends on the reaction time [82]. As resulting nanoparticles are typically not uniform, usually a series of selective precipitation and centrifugation steps are performed [45, 37].

The key feature of CdSe nanoplatelets is that the thickness can be controlled with atomistic precision, independent of the lateral size. The thickness is usually expressed in the number of monolayers m (m Se layer, and $m+1$ Cd layers).

3.2 Special electronic and optical properties of CdSe nanoplatelets

The electronic and optical properties of bulk solids usually do not depend on their size. However, this changes when we consider solids with at least one dimension smaller than a few nanometers [16]. Here, intriguing quantum confinement effects appear that significantly change material properties.

In an atom or molecule, the electronic structure is characterized by discrete states. In contrast, in a bulk material, the energies of the electronic states form continuous bands (see Figure 3.1a). Semiconductor nanocrystals can be placed between these cases. As we reduce the nanocrystal size in at least one dimension to the nanometer regime ($\leq 2-50\,\text{nm}$ dependent on the material), fewer atoms contribute with their orbitals to the combined electronic states. More discrete energy levels appear, and the energy band gap increases (see Figure 3.1b) [84]. Thus, we can control the band gap by the nanocrystal dimensions. This effect is known as the quantum confinement effect.

We can understand this effect also from a different perspective. As we promote one electron from the valance band to the conduction band, we create a hole located in the valence band. If the attraction is strong enough, they can form an exciton. In an exciton, the hole and the electron are bound to each other.

First, we consider the binding energies and the binding radius of an exciton in a bulk material, where the exciton can expand and move freely in any direction. We can describe the exciton analog to the approach for a hydrogen atom [85]. The Hamiltonian includes the kinetic terms for the hole, and the electron, as well as the term for the Coulomb energy:

$$H = -\frac{\hbar^2}{2m_e^*}\nabla_e^2 - \frac{\hbar^2}{2m_h^*}\nabla_h^2 - \frac{e^2}{\epsilon\,|r_e - r_h|}, \tag{3.1}$$

where m_e^* and m_h^* are the effective masses, and ϵ is the material specific dielectric constant. We transform the Hamiltonian to relative coordinates and center of mass coordinates (cm):

$$H = H_{\text{cm}} + H_{\text{rel}}, \tag{3.2}$$

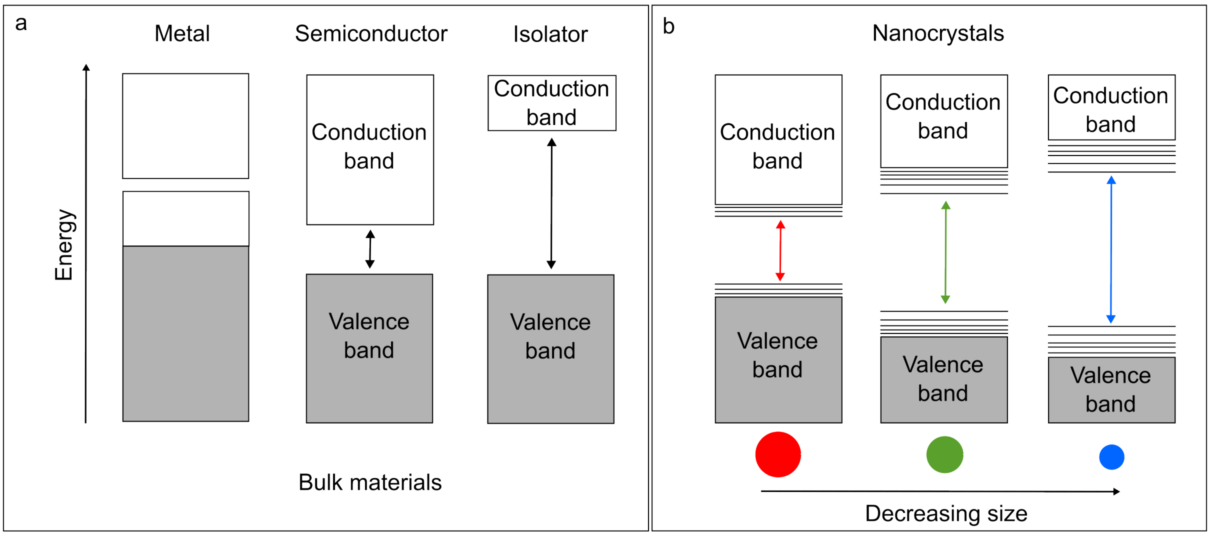

Figure 3.1: Schematic sketch of the electronic energy states respectively bands in different materials to illustrate the quantum confinement effect. In **panel a**, we sketch band structures of bulk materials. In bulk materials, the energy states combine to continuous bands. In metals, the highest energy electrons occupy a partially filled band. In semiconductors and insulators, a gap occurs between the valence band and the conduction band. Thereby, semiconductors have a smaller band gap than insulators. As illustrated in **panel b** for quantum dots, the number of states in semiconductor nanocrystals reduces with their size. If one or more dimensions of the nanocrystals becomes small enough, the quantum confinement effect appears, and the band gap is tuned. Therefore, the absorption and emission spectrum of nanocrystals can be controlled by the nanocrystal size and shape. Panel b is inspired by figures in [83, 84].

assuming a wave function of the form:

$$\Psi(r_e, r_h) = \Psi_{\text{cm}}(R)\Psi_{\text{rel}}(r), \tag{3.3}$$

where $r = r_e - r_h$, and $R = (m_e * r_e + m_h * r_h)/(m_e * + m_h *)$. We introduce the reduced mass $\mu = (m_e^* m_h *)/(m_e * + m_h *)$. Finally, we obtain:

$$H_{\text{rel}} = -\frac{\hbar^2}{2\mu}\nabla_r^2 - \frac{e^2}{\epsilon r}. \tag{3.4}$$

The resulting eigenvalues for the exciton binding energies are:

$$E_n = (-13.6\,\text{eV})\frac{\mu}{m_e \epsilon^2 n^2}, \text{ with } n = 1,\ 2,\ 3,\ ..., \tag{3.5}$$

and the exciton Bohr radius:

$$a_{\text{B}} = \frac{m_e}{\mu} a_0, \tag{3.6}$$

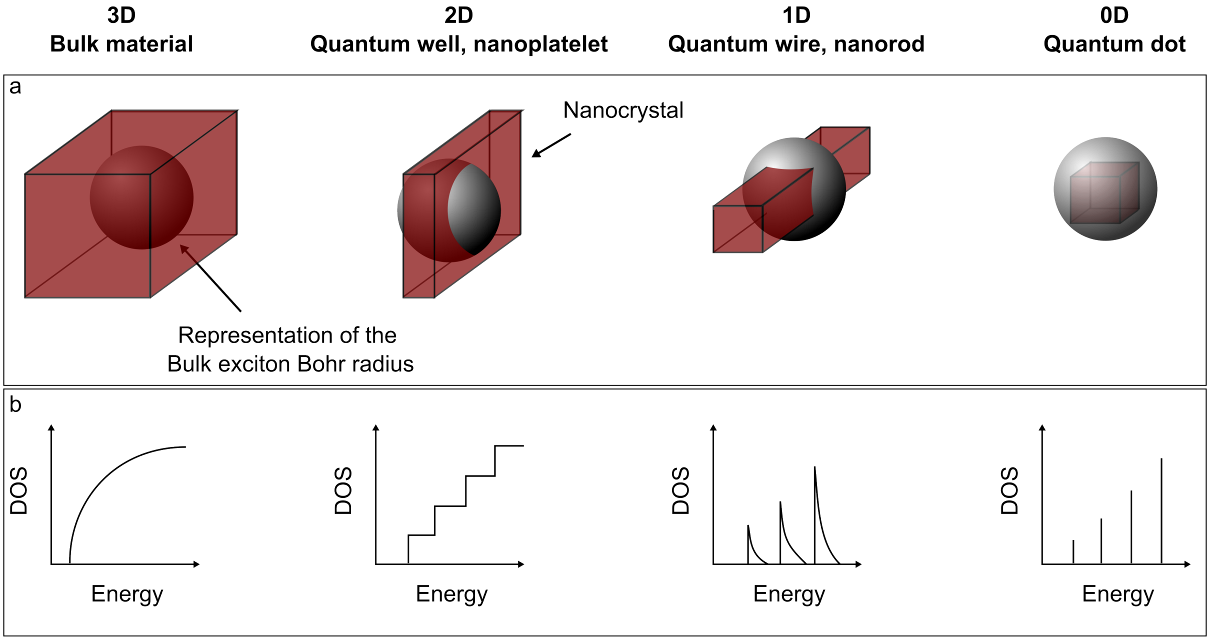

Figure 3.2: **Panel a** shows sketches of nanocrystals with different shapes and sizes. A sphere is also shown. It represents the bulk exciton Bohr radius. **Panel b** shows the idealized density of states (DOS) for one band of a semiconductor [16]. The DOS depends on the dimensions of the material. For example, the energy levels are continuous in the case of a bulk semiconductor, while they become discretized in a 1D nanorod or 0D quantum dot. The Figure is inspired by illustrations in [16, 84].

where a_0 is the Bohr radius. For the different energetic states results:

$$\langle r_n \rangle = a_\mathrm{B} n^2. \tag{3.7}$$

Typical exciton Bohr radii in bulk materials are e.g., (4-6) nm in CdSe, 29 nm in InAs, and 104 nm in PbTe [86, 87].

Often, the dimensions of nanocrystals are close to the bulk exciton Bohr radius or smaller (see illustration in Figure 3.2a). In such a nanocrystal, the exciton can no longer expand and move freely.

We can consider this situation to resemble the standard particle in the box problem. We can describe the box by potential walls, for example, in the case of a confinement in one dimension by

$$\begin{aligned} V &= 0, \qquad 0 \leq x \leq L \\ V &= \infty, \ \ x < 0, L < x, \end{aligned} \tag{3.8}$$

where L is the box size, and x the coordinate. This approach results in discretized energy states [88]:

$$E_l^\mathrm{conf} = l^2 \frac{\pi^2 \hbar^2}{2m^* L^2}, \qquad l = 1,\, 2,\, 3,\, \dots\ , \tag{3.9}$$

where m^* is the effective mass of the confined particle.

Depending on the size of the nanocrystal, we can either treat the whole exciton as a confined particle, or the electron and the hole separately [15]. In both cases, the energy increases by a term similar to $E_1^{\mathrm{conf}} \propto L^{-2}$, and thus the band gap. It should be noted that the Coulomb interaction between the hole and the electron also changes, which in turn leads to a term that reduces the band gap and partially counteracts the quantum confinement effect. However, the Coulomb term typically scales with $\propto L^{-1}$. Thus, the Coulomb term is more important in larger nanocrystals [15]. Of course, this is a very simplified description, for a more detailed description, please refer to [84, 15].

The quantum confinement effect depends on the dimensions of a semiconductor. We can differentiate between semiconductors where the quantum confinement appears in one (quantum wells, nanoplatelets), two (nanowires, nanorods), or three dimensions (quantum dots) (see Figure 3.2a). Thereby, the shape and size of a nanocrystal also influences the density of states (DOS) (see Figure 3.2b) [16]. While the DOS is typically proportional to the root of the energy E in bulk semiconductors (DOS $\propto E^{\frac{1}{2}}$), it shows a step-like shape in 2D semiconductors, such as quantum wells or nanoplatelets. Thereby, the energy is constant between steps (DOS $\propto E^0$). In 1D semiconductors, such as nanorods or quantum wires, the DOS also shows a step-like behavior. However, between steps, the DOS decreases (DOS $\propto E^{-\frac{1}{2}}$). Finally, the DOS becomes quantized in 0D quantum dots.

The first known quantum wells were grown epitaxial on surfaces. Semiconducting nanoplatelets, such as CdSe nanoplatelets, are the colloidal equivalent [52]. Here, the quantum confinement is created by the finite thickness of the nanoplatelets, as it is smaller than the exciton Bohr radius. In the case of CdSe nanoplatelets, the thickness can be controlled with atomic precision. Thereby, the lateral size can be chosen independently of the quantum confinement effect. Usually, the absorption cross-section of a nanocrystal grows with its size. The variable lateral size, allows tuning of the absorption cross-section [35]. This is an advantage over spherical quantum dots, where the absorption cross-section is in competition with the required quantum confinement effect. As this is not the case in nanoplatelets, large absorption cross-section can be combined with sharp emission peaks. A typical, absorption and emission spectra can be found in Figure 8.1e. Due to their optical properties [52], CdSe nanoplatelets are candidates for the usage in light-emitting devices [40], field effect transistors [42], solar cells [41], and lasers [43].

In Chapter 8, we show that the optical properties can be used to experimentally measure the saturation concentration, where the nanoplatelets start to assemble. We use the method to compare different nanoplatelets sizes, and solvent types. The results allow us to draw conclusions about the nature of the interaction between the nanoplatelets.

3.3 Precipitation behavior and nanoplatelet stacking

When dispersed nanoparticles precipitate, they typically agglomerate into larger objects. Similar to other disk or platelets shaped nanoparticles [39, 47], Jana *et al.* have found that CdSe nanoplatelets form stacks [45]. Thereby, the nanoplatelets self-assembly base facet to base facet. Interestingly, they have shown that for saturated surfactant ligands

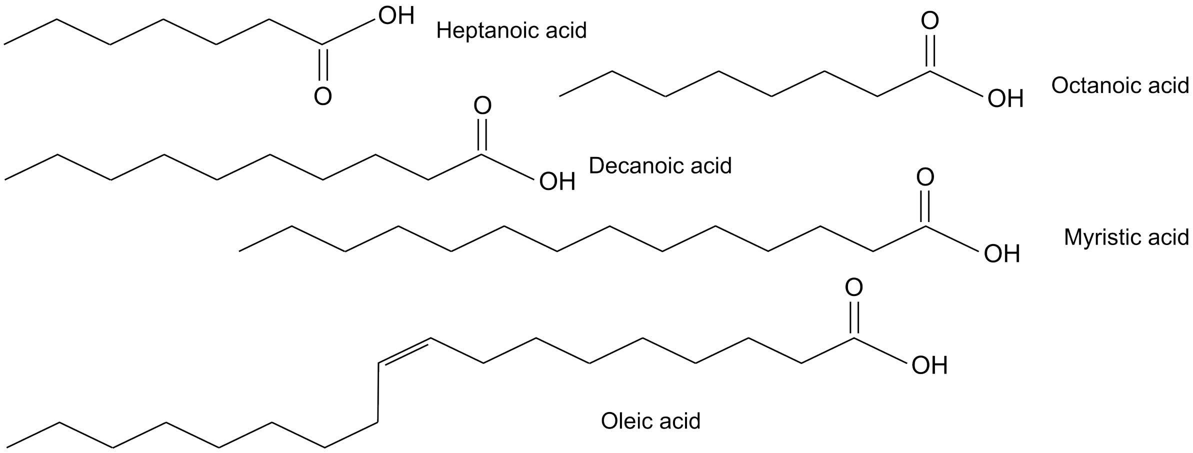

Figure 3.3: Typical ligands used for passivation and steric stabilization of CdSe nanoplatelets.

like myristic acid, there is nearly no interdigitation between the ligand shells. Only for oleic acid ligands, they have found some degree of interdigitation. This shows that the continuum approach, which is often used to describe the interaction between ligand shells, is not suitable (see Section 2.2).

In general, CdSe nanoplatelets are metastable in apolar solvents. Dependent on the concentration, the stacking, and therefore the precipitation time varies between hours, days, and months. Jana *et al.* have studied the colloidal stability of CdSe nanoplatelets in n-hexane. As expected, the flocculation is faster for higher nanoplatelet concentrations [89, 90]. This is expected because the collision rate of nanocrystals increases with nanocrystal concentration. Furthermore, the translational entropy decreases with the nanoplatelet concentration, since the translational entropy depends on the accessible volume per particle. Therefore, the balance of the contributions to the free energy shifts towards assembling.

The flocculation rate and the colloidal stability also depends on the ligand length. They varied the ligands between heptanoic acid, octanoic acid, decanoic acid, myristic acid, and oleic acid (see Figure 3.3). Independent of the nanoplatelet concentration, they have found that the colloidal stability increases with the ligand length from heptanoic to decanoic acid. The difference between decanoic and myristic acid is negligibly small. Nanoplatelets with oleic acid are dramatically more stable in the dispersion. We assume that this is due to the double bond in oleic acid that changes the ordering of the ligands.

For the nanoplatelets with oleic acid ligand shells, they studied different concentration of oleic acid in the dispersion. Increasing the oleic acid concentration, they first have observed an increase in the steric stability. They attribute it to an increase in the ligand shell density. After an optimal stability, they have observed a decrease in the steric stability. Presumably, oleic acid acts as a depletant. In a consecutive study [46], they have used the oleic acid concentration to control the length of the nanoplatelet stacks. They have shown that the CdSe nanoplatelet stacks behave similar to living polymers [91, 92].

As Abecassis *et al.* have shown, the stack formation can also be controlled by the addition of a bad solvent to the ligands like ethanol [93]. They have created superparticles. These superparticles consist out of parallel assembled nanoplatelet stacks.

3.4 Interaction of CdSe nanoplatelets

To control the steric stability, it is desirable to get an understanding of the fundamental forces that drive the nanoplatelets to form stacks. As described in the previous Chapter, the steric stability of a colloidal nanoparticle depends on the balance of different free energy terms.

Let us consider first the ligand effects. Typical ligands used for CdSe nanoplatelets are heptanoic acid, octanoic acid, decanoic acid, myristic acid, and oleic acid (see Figure 3.3) [45, 46, 37]. Typical solvents are n-hexane, and other alkane solvents [45, 46, 37]. The solvent and ligand molecules are chemically similar. Therefore, unmixing of the ligand shell and the solvent at close contact will create a repulsion ($G_{\text{mix}} > 0$, see Section 2.2). Of course, the compression term also leads to repulsion at close distances ($G_{\text{com}} > 0$).

However, in the attempt to understand stack formation, it is even more important to explain the attraction between the nanoplatelets. The core-core van der Waals attraction is always present. However, its strength depends on the nanocrystal material. In Section 2.1.3, we described how the Hamaker approach can be used to estimate the van der Waals interaction energy.

We use the Hamaker approach to estimate the core-core van der Waals attraction between CdSe nanoplatelets. The core-core van der Waals interaction is influenced by the ligand shells at small nanoplatelet separations, and by the ligand shells plus the solvent at larger separations. For all three media, we need the Hamaker constants. According to Rabani, the Hamaker constant of CdSe is $\mathrm{A}_{\text{CdSe}} = 6.216\ 10^{-20}$ J [94]. From Hough and White [95], we adopt the Hamaker constants of n-alkanes with different length A_{Alkane}. They are listed in Table 3.1. The description of the ligand shell is more problematic. To our knowledge, there is no Hamaker constant to describe it. However, the ligand tails and n-alkanes are chemical similar. Therefore, the Hamaker constant of the ligand shell should be close to that of n-alkanes.

We calculate the van der Waals attraction between two flat CdSe crystals in different n-alkane solvents. We use Equation 2.19, to calculate the Hamaker constant of CdSe interacting through n-alkane solvents. With the resulting Hamaker constant and Equation 2.21, we estimate the interaction energies between two nanoplatelet facets. It is worth noting that equation 2.21 assumes two infinitely thick flat surfaces. Therefore, we can assume that it overestimates the strength of the van der Waals attraction.

For nanoplatelets with $225\,\text{nm}^2$ facet areas, we compare the face-to-face interaction energy in different n-alkane solvents (Figure 3.4a). This is the base facet area Jana *et al.* have used [45]. The strength of the van der Waals interaction decreases with increasing n-alkane chain length.

In the next step, we compare the van der Waals attraction between different facet areas (Figure 3.4b). As we do not know which n-alkane solvent describes the interaction best,

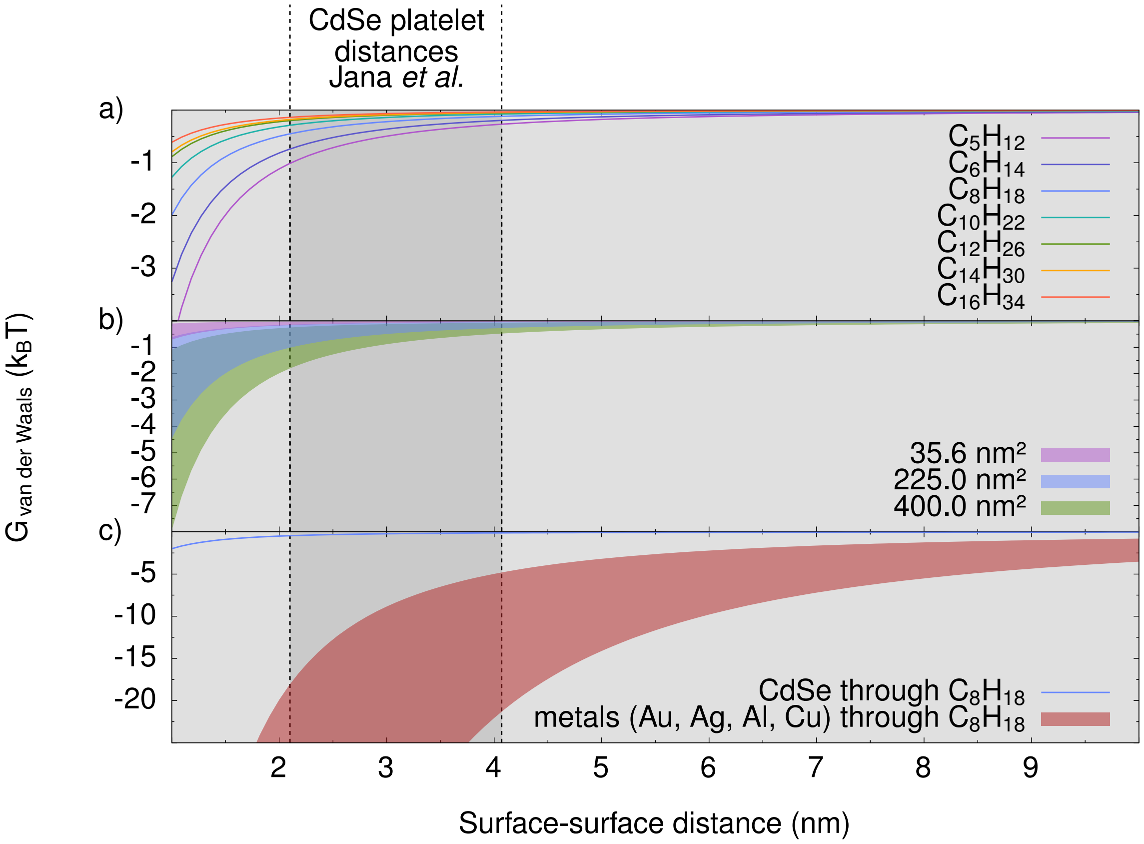

Figure 3.4: Estimation of the core-core van der Waals interaction energy between CdSe nanoplatelets [96]. In **panel a**, we compare the interaction energy in different n-alkane solvents. Here, the base facet area is 225 nm^2. The attraction reduces with the n-alkane chain length. In **panel b**, we compare different nanoplatelet base facet areas. Thereby, we use broader curves to illustrate the effect of the different n-alkanes (n-propane to n-hexadecane). The colors of the curves change, as they overlap. In **panel c**, we compare the van der Waals interaction energy of CdSe nanoplatelets through n-octane with the interaction energy of hypothetical nanoplatelets consisting of metal. Again, the base facet area is 225 nm^2. Jana *et al.* have measured for different ligands the surface-surface distance of stacked nanoplatelets [45]. The distance varies between 2.1 and 4.1 nm. In all panels, we mark the range with a gray rectangle.

Alkane chain length	Hamaker constant (10^{-20} J)
5	3.75
6	4.07
7	4.32
8	4.50
9	4.66
10	4.82
11	4.88
12	5.04
13	5.05
14	5.10
15	5.16
16	5.23

Table 3.1: Hamaker constants of different n-alkane solvents at 20°C from Ref. [95]. The value increases with the molecule length.

we illustrate the effect of the different solvents by broader curves. The strength of the attraction increases with the facet area.

If the platelets were very close to each other, then the van der Waals attraction would be strong enough to explain the observed stack formation. However, due to the ligand shell, this is not the case. For face-to-face stacked nanoplatelets, Jana *et al.* have measured the distance between neighboring nanoplatelets. Dependent on the ligand length, they have found surface-surface distances between 2.1 nm for heptanoic acid ligands, and 4.1 nm for oleic acid ligands. For these distances, we estimate that the attractive van der Waals interaction energy for $225\,\mathrm{nm}^2$ is around or below $1\,k_\mathrm{B}T$. In Chapter 8, our experimental collaborators use CdSe nanoplatelets up to $400\,\mathrm{nm}^2$. As the van der Waals interaction increases with the facet are, in this case the interaction energy is around or below $2\,k_\mathrm{B}T$.

We do not know which alkane solvent best describes the ligand shell. Nevertheless, from our estimations, we conclude that the van der Waals attraction between the CdSe crystals is too weak to be (alone) responsible for the nanoplatelet stack formation.

This may come as a surprise, as the stability of colloidal (nano-) particles in apolar solution is often described as the balance between the attractive van der Waals interaction G_vdW, the mixing of the ligand shell with the solvent G_mix, and the compression of the ligand shell G_com [29, 21, 28]. However, the strength of the core-core van der Waals attraction strongly depends on the materials. The Hamaker constants of metals are large (20 to 50 10^{-20} J) [20, 97] compared to CdSe. In Figure 3.4, we compare the interaction of CdSe nanoplatelets through n-octane with the interaction of metallic nanoplatelets through n-octane. The attraction between metallic nanoplatelets is drastically larger.

As the van der Waals attraction between the CdSe cores does not appear to be responsible for the stack formation, other contributions to the interactions have to be considered. A possibility is that there are permanent dipoles in the CdSe nanoplatelet crystals (see Section 2.1.2). Dozov *et al.* have measured the dipoles in CdSe nanoplatelets by transient electric birefringence [48]. The average dimensions of the nanoplatelets are, 20 nm×9 nm×1.5 nm. They have found a permanent dipole that is larger than 300 D. Whereby, the in-plane component is larger than 245 D, and the component along the nanoplatelets thickness (out-of-plane) is around 80 D. The interaction energy of two dipoles in neighboring nanoplatelets depends on the relative orientation of the dipoles, respectively their components. They calculated for facet-to-face oriented nanoplatelets at a separation of about 4 nm a maximal interaction energy of $G_{\text{dipole-dipole}} \approx -3k_{\mathrm{B}}T$. However, as Dozov *et al.* discuss, in reality the relative orientation of the dipoles might not be optimal. Additionally, thermal averaging should be considered. Such effects would weaken the attraction. It is likely that the dipole-dipole interaction contributes to the stack formation. However, it seems unlikely that they are the driving force. In any case, it would be worthwhile to investigate the dipole-dipole interaction in CdSe nanoplatelets further, considering different nanoplatelet facet areas as well as thicknesses.

In this thesis, we follow a different hypothesis. With large flat facets, and a very dense ligand shell, we expect that solvation forces are crucial for the interaction, stack formation and steric stability of CdSe nanoplatelets. In the following Chapters, we use molecular dynamics simulations to study solvation forces between ligand passivated CdSe nanoplatelets.

Chapter 4

Methods: molecular dynamics simulation, force fields, and umbrella sampling

For the description of complex systems, analytical models are often not sufficient. In such a case, simulations can be applied. In this chapter, we give a brief introduction to molecular dynamics (MD) simulations, force fields, and umbrella sampling. The introduction to MD simulations is inspired by the book of Frenkel and Smit [98].

4.1 Molecular dynamics simulations

A molecular dynamics simulation has features similar to an experiment [98]. In a real experiment, we prepare a sample. We assign a measurement instrument, e.g., a thermometer, to the sample. Then we run the measurement over a defined time. When we perform a molecular dynamics simulation, we follow the same concept. First, we define a model system with N particles. For each particle, we assign a mass m_i, and a position vector r_i. Then we solve Newton's equation of motion:

$$m_i \frac{d^2 r_i}{dt^2} = f_i = -\frac{\partial}{\partial r_i} U(r_1, ..., r_N), \tag{4.1}$$

where f_i is the force acting on the particle i, and $U(r_1, ..., r_N)$ is the potential energy. $U(r_1, ..., r_N)$ results from the interactions between the individual particles (see next section). After the implementation, we relax the system into the thermodynamic equilibrium. Then we perform our actual measurement.

Several algorithms exist, to solve the equation of motion for each particle r_i. All of them have in common that they solve the originally continuous equation of motion with discrete time steps Δt. The Verlet algorithm is one of the simplest. It results from a Taylor expansion of the particle position r_i around the time t. We start the derivation with

$$r_i(t+\Delta t) = r_i(t) + v_i(t)\Delta t + \frac{f_i(t)}{2m_i}\Delta t^2 + \frac{\Delta t^3}{3!} + \mathcal{O}(\Delta t^4), \tag{4.2}$$

and

$$r_i(t - \Delta t) = r_i(t) - v_i(t)\Delta t + \frac{f_i(t)}{2m_i}\Delta t^2 - \frac{\Delta t^3}{3!} + \mathcal{O}(\Delta t^4), \tag{4.3}$$

where $v_i(t)$ is the velocity vector of the ith particle, and $f_i(t)$ the force acting on it. We sum up the two equations, and get:

$$r(t + \Delta t) + r(t - \Delta t) = 2r_i(t) + \frac{f_i(t)}{m_i}\Delta t^2 + \mathcal{O}(\Delta t^4). \tag{4.4}$$

Finally, we get:

$$r_i(t + \Delta t) \approx 2r_i(t) - r(t - \Delta t) + \frac{f_i(t)}{m}\Delta t^2. \tag{4.5}$$

Iteratively solving Equation 4.5 for each particle in each time step, we progress our simulation. Thereby, the velocity is not used. However, it can be calculated via:

$$v_i(t) = \frac{r_i(t + \Delta t) - r_i(t - \Delta t)}{2\Delta t} + \mathcal{O}(\Delta t^2). \tag{4.6}$$

An alternative algorithm that uses the velocities is the velocity-Verlet algorithm:

$$r_i(t + \Delta t) = r_i(t) + v_i(t)\Delta t + \frac{f_i(t)}{2m_i}\Delta t^2, \tag{4.7}$$

$$v_i(t + \Delta t) = v_i(t) + \frac{f_i(t + \Delta t) + f_i(t)}{2m_i}\Delta t. \tag{4.8}$$

Both algorithms conserve the number of particles N, the volume V, and the energy E (NVE ensemble).

The algorithms satisfy two properties that are crucial for long-term stability. They are time-reversible and symplectic [99]. The algorithms solve the equations of motion of a system in discrete steps. Thus, time reversibility means that if we take the initial condition $r_i(t + \Delta t)$, $v_i(t + \Delta t)$ and step $-\Delta t$ backwards in time, we will end up with $r_i(t)$, $v_i(t)$. Furthermore, the symplectic algorithms have the property that they solve exactly the discrete "shadow" Hamiltonian $\tilde{H}(r_i, \Delta t)$, which is an approximation of the true Hamiltonian $H(r_i)$ of a system. This auxiliary Hamiltonian remains close to the true Hamiltonian, such that $H(r_i) = \tilde{H}(r_i, \Delta t)$ for $t \to 0$. Due to these important properties, system properties such as the potential energy are conserved.

4.2 Thermostats and barostats

We do not always want to limit ourselves to the NVE ensemble. Often we prefer to perform the simulation at constant pressure P and temperature T. Several thermostats and barostats exist to achieve this goal. First, we introduce the Berendsen thermostat and barostat, which follows a very intuitive approach. Then we introduce the more sophisticated Nosé-Hoover thermostat. Finally, we discuss the Martyna-Tobias-Klein thermostat barostat, which is based on the Nosé-Hoover thermostat. We use the Martyna-Tobias-Klein thermostat barostat in most of our NPT simulations. Additionally, we introduce the Dissipative Particle Dynamics (DPD), which we employ in some of our simulations as a thermostat.

4.2.1 Berendsen thermostat and barostat

We can calculate the temperature at each time step via the velocities [98]:

$$T(t) = \sum_{i=1}^{N} \frac{m_i |v_i|^2(t)}{k_{\mathrm{B}} N_f}, \tag{4.9}$$

where N_f is the number of degrees of freedom. Therefore, we can control the temperature by manipulating the velocities. We couple the system to an external bath with temperature T_0. The Berendsen thermostat [100, 101] is doing this by a scaling factor to the velocities:

$$\lambda(t) = \left[1 + \frac{\Delta t}{\tau_T}\left(\frac{T_0}{T(t)} - 1\right)\right]^{\frac{1}{2}}, \tag{4.10}$$

where $T(t)$ the instantaneous temperature, and τ_T is a coupling parameter. τ_T essentially controls how strong the bath is coupled to the simulation system. The velocity-Verlet algorithm changes in the following way:

$$r_i(t + \Delta t) = r_i(t) + v_i(t)\Delta t + \frac{f_i(t)}{2m_i}\Delta t^2, \tag{4.11}$$

$$\tilde{v}_i(t + \Delta t) = v_i(t) + \frac{f_i(t + \Delta t) + f_i(t)}{2m_i}\Delta t, \tag{4.12}$$

$$v_i(t + \Delta t) = \lambda(t)\ \tilde{v}_i(t + \Delta t). \tag{4.13}$$

Similarly, the pressure can be controlled by a barostat that scales the coordinates and the box volume $V(t)$:

$$r(t) = \chi(t)\tilde{r}(t), \tag{4.14}$$

$$V(t) = \chi^3(t)\tilde{V}(t). \tag{4.15}$$

The scaling factor is:

$$\chi(t) = \left[1 - \beta_T \frac{\Delta t}{\tau_P}(P_0 - P(t))\right]^{\frac{1}{3}}, \tag{4.16}$$

where β_T is the isothermal compressibility, P_0 is the desired pressure, $P(t)$ the instantaneous pressure of the system, and τ_P is the coupling constant.

The Berendsen thermostat and barostat are very robust. They are particularly useful for transferring a system from one state to another. However, they do not reproduce the true canonical (NVT), or isothermal isobaric (NPT) ensemble [102].

4.2.2 Nosé-Hoover thermostat

A more sophisticated approach is the Nosé-Hoover thermostat. It is based on a clever extension of the Lagrangian, where additional artificial coordinates and velocities are introduced [98, 101]. The additional degree of freedom allows controlling the system. The following equations of motion result:

$$\dot{r}_i = p_i / m_i, \tag{4.17}$$

$$\dot{p}_i = f_i(r_1, ..., r_N) - \lambda p_i, \tag{4.18}$$

$$\dot{\lambda} = \frac{1}{Q}\left[\sum_{i=1}^{N} \frac{p_i^2}{m_i} - N_f k_{\mathrm{B}} T_0\right], \tag{4.19}$$

where r_i and p_i are the position and the momentum of a particle, T_0 is the desired temperature, N_f the number of degrees of freedom, λ the thermostat variable, and Q the "mass" of the thermostat. Q can be tuned to adjust the response of the thermostat.

In contrast to the Berendsen thermostat, deviations from the desired temperature T_0 drives the time derivative of the velocity scaling factor, and not the scaling factor itself [101]. The Nosé-Hoover thermostat reproduces the correct ensembles.

4.2.3 Martyna-Tobias-Klein thermostat barostat

The Martyna-Tobias-Klein thermostat barostat is an extension of the Nosé-Hoover approach [103, 99]. The approach consists of the following equations of motion:

$$\dot{r}_i = \frac{p_i}{m_i} + \chi r_i, \tag{4.20}$$

$$\dot{p}_i = f_i(r_1, ..., r_N) - \left(1 + \frac{3}{N_f}\right) \chi p_i - \lambda p_i, \tag{4.21}$$

$$\dot{\lambda} = \frac{N_f k_{\mathrm{B}}}{Q}(T(t) - T_0) + \frac{W\chi^2 - k_{\mathrm{B}} T_0}{Q}, \tag{4.22}$$

$$\dot{\chi} = \frac{3}{W} V(t)(P(t) - P_0) + \frac{3}{W} k_{\mathrm{B}} T(t) - \chi\lambda, \tag{4.23}$$

$$\dot{V} = 3\chi V. \tag{4.24}$$

W is the introduced "mass" of the barostat. In analog to the Berendsen thermostat barostat, Q and W can be expressed through relaxation times τ_T and τ_P:

$$Q = N_f k_{\mathrm{B}} \tau_T^2, \tag{4.25}$$

$$W = N_f k_{\mathrm{B}} \tau_P^2. \tag{4.26}$$

Also the Martyna-Tobias-Klein thermostat barostat reproduces the correct ensembles. We use the Martyna-Tobias-Klein thermostat barostat in most of our NPT simulations.

4.2.4 Dissipative Particle Dynamics

The idea of Dissipative Particle Dynamics (DPD) stems from the description of the Brownian motion of colloidal particles [98]. The Brownian motion of uncharged particles does not depend on the molecular details of the solvent, but just at temperature, density, and viscosity. Therefore, DPD was designed to reproduce hydrodynamic behavior, and thermal fluctuations that can drive Brownian motions.

The idea is, to introduce a dissipative $f^{\mathrm{D}}(r_{ij})$, and a random force $f^{\mathrm{R}}(r_{ij})$:

$$f_i = \sum_{i \neq i} \left[f^{\mathrm{pair}}(r_{ij}) + f^{\mathrm{D}}(r_{ij}) + f^{\mathrm{R}}(r_{ij}) \right], \tag{4.27}$$

where $r_{ij} = |r_i - r_j|$, and $f^{\mathrm{pair}}(r_{ij})$ stems from the pair interaction between particle i, and j. The dissipative force acts like a frictional force that depends on the positions and velocities of the particles:

$$f^{\mathrm{D}}(r_{ij}) = -\gamma \, \omega^{\mathrm{D}}(r_{ij}) \, (v_{ij} \cdot \hat{r}_{ij}) \hat{r}_{ij}, \tag{4.28}$$

where $v_{ij} = |v_i - v_j|$, and $\hat{r}_{ij}$ is the unit vector in the direction of r_{ij}. The strength of the friction force is controlled by the friction coefficient γ, while $\omega^{\mathrm{D}}(r_{ij})$ describes the variation of the friction coefficient with the distance. The particles would eventually stop moving if there were only f^{pair} and f^{D}.

The random force provides the continuous kicks that keep the system in thermal motion [104]. It is defined in the following way:

$$f^{\mathrm{R}}(r_{ij}) = -\sigma \, \omega^{\mathrm{R}}(r_{ij}) \, A_{ij} \, \hat{r}_{ij}, \tag{4.29}$$

where σ determines the strength of the random force, and $\omega^{\mathrm{R}}(r_{ij})$ describes the variation with the distance. A_{ij} is a Gaussian distributed random variable.

The two forces are not independent of each other. P. Español and P. Warren have shown that DPD conserves the momentum of the particles, when the force parameters are chosen according to the fluctuation-dissipation theorem for the DPD method [104]:

$$\begin{gathered} \omega^{\mathrm{D}}(r_{ij}) = (\omega^{\mathrm{R}}(r_{ij}))^2 \\ \sigma^2 = 2 k_{\mathrm{B}} T \gamma. \end{gathered} \tag{4.30}$$

Note that the temperature is introduced in Equation 4.30. DPD can be used as a thermostat, which we do in some simulations.

4.3 Force fields

Besides the algorithm to solve the equations of motion, the definition, and calculation of the forces is of large importance. Force fields are an approximation of the particle interaction. A force field unites a set of interaction potentials, and the corresponding force description (see Equation 4.1) [105].

Usually, we differentiate between nonbonded and bonded interactions. It is very common to describe the nonbonded pair interaction energy of two particles i and j by a 12-6 Lennard-Jones potential, together with a Coulomb term to describe the interaction of their charges q_i, q_j [106]:

$$U^{\mathrm{pair}}_{\mathrm{nonbonded}}(r_{ij}) = 4\epsilon_{ij} \left[\left(\frac{\sigma_{ij}}{r_{ij}} \right)^{12} - \left(\frac{\sigma_{ij}}{r_{ij}} \right)^{6} \right] + \frac{q_i q_j}{4\pi\epsilon_0 \epsilon r_{ij}}, \tag{4.31}$$

where ϵ_{ij} defines the depth of the Lennard-Jones potential, and σ_{ij} the range of the Lennard-Jones potential. σ_{ij} defines the distance at which the Lennard-Jones potential passes through zero, and it defines the position of the potentials minimum ($r_{ij}^{\text{min}} \approx 1.12\,\sigma_{ij}$). The first term of the Lennard-Jones potential describes the repulsion, while the second term describes the attraction.

The shape of the repulsion of the Lennard-Jones potential is not explicitly physically motivated. The main reason to use the exponent "12" is computational convenience. After the calculation of $(\sigma_{ij}/r_{ij})^6$, it requires just an additional multiplication to calculate $(\sigma_{ij}/r_{ij})^{12}$ The exponent "6" of the second term of the Lennard-Jones potential can be justified by the van der Waals interaction (see Section 2.1.3).

The total nonbonded interaction energy results from summing up the particle pairs:

$$U_{\text{nonbonded}}^{\text{total}}(r_1, ..., r_N) = \sum_{i=1}^{N} \sum_{j>i}^{N} U_{\text{nonbonded}}^{\text{pair}}(|r_i - r_j|) \tag{4.32}$$

Within a molecule, we have to describe bonds, angles, and dihedral angles. A typical set of terms to describe the bonded interactions is [107]:

$$\begin{aligned} U_{\text{bonded}}(r_1, ..., r_N) = &\sum_{\text{bonds}} \frac{1}{2}\kappa_b (r_b - r_0)^2 \\ &+ \sum_{\text{angles}} \frac{1}{2}\kappa_\theta (\theta_a - \theta_0)^2 \\ &+ \sum_{\text{dihedrals}} \left(c_0 + c_1\left[1 + \cos(\Phi)\right] + c_2\left[1 - \cos(2\Phi)\right] + c_3\left[1 + \cos(3\Phi)\right]\right), \end{aligned} \tag{4.33}$$

where the first line describes the bond potential, and the second line describes the angle potential, both by a harmonic potential. Here, κ_b, and κ_θ are the force constants of the bond and angle potential, whereby r_0, and θ_0 are the equilibrium values. The third line describes the dihedral angles, where the parameters c_x are the force constants, and Φ is the torsion angle. The exact form of the nonbonded and bonded interaction terms depends on the selected force field.

So far, we have implicitly assumed that we are describing the interaction of atoms. This is not necessarily the case. Depending on the considered system, it may be beneficial to adjust the resolution. For example, an all-atomistic description allows us to relate macroscopic properties to the microscopic in a straightforward way. However, computer simulations with a large number of particles are demanding. Accordingly, the system size and the time that can be simulated is limited. In contrast, macroscopic systems tend to be large, and macroscopic effects often occur on long time scales. Therefore, to describe macroscopic properties, it is often beneficial to reduce the resolution. We can switch to a description where we simulate larger coarse-grained beads instead of single atoms.

To create a coarse-grained model, several challenges have to be overcome. The coarse-grained beads must be defined, the shape of the force field specified, and interaction parameters determined. In general, there are two approaches to defining such a coarse-grained model: the bottom-up approach, and the top-down approach [108]. In a bottom-up approach, the force field is constructed to reproduce the properties and statistics of

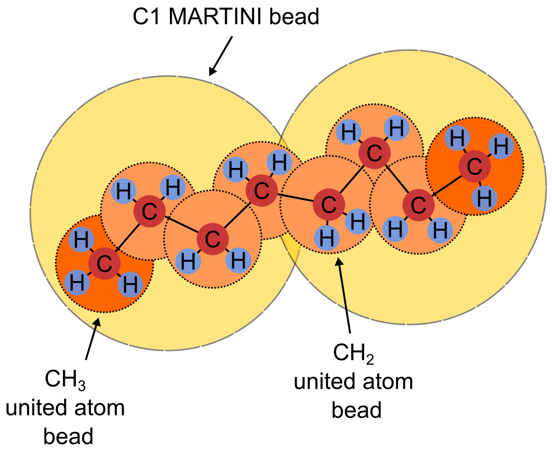

Figure 4.1: Sketch to demonstrate the coarse-graining. Depicted is an n-octane molecule in the all-atomistic representation. In the united atom description, heavy atoms, such as carbon atoms C, are combined with the hydrogen atoms H bonded to them, and described by a single bead. In the TraPPE-UA atom force field, the bead type depends on the number of hydrogen atoms. In the sketch, two bead types are depicted, the CH_3 and CH_2 bead type. The MARTINI force field is more coarse-grained. Here, four CH_x groups are mapped in one C1 MARTINI bead.

a fine-grained representation, like an all-atomistic one. Typically, such a force field is developed in relation to reference simulations in such a way that it reproduces the correct coarse-grained equations of motions. This includes an adequate description of equilibrium and certain nonequilibrium processes [108]. In contrast, in a top-down approach, the interactions are typically evaluated empirically by reproducing and comparing with experimental results, such as vapor-liquid coexistence curves, critical temperatures, and densities [107].

A coarse-grained model has several benefits. The decrease in the number of particles and in the degrees of freedom significantly speeds up simulations [109]. Moreover, the energy landscape is smoother in a coarse grained simulation. Overall, dynamics are faster, and larger time steps compared to all-atom simulations can be used [110]. At the cost of lower accuracy and resolution, coarse-grained simulations can represent time and length scales that are not feasible with all atomistic simulations. In this thesis, we use two top-down force fields with a different level of coarse graining (see Figure 4.1).

TraPPE-UA is a united atom force field [107, 111]. In a united atom force field, heavy atoms, such as O, or C, are combined with the hydrogen atoms bonded to them, and mapped to a single bead. Therefore, this force field comes with its resolution very close to an all-atomistic representation. The nonbonded, angle, and dihedral potentials are described by the terms given in the Equations 4.31 and 4.33. In the original version of TraPPE-UA, bonds have a fixed length. However, we extend the force field in our setup by a harmonic bond stretching term [112], as in Equation 4.33.

There are two important details to note. First, the TraPPE-UA force field handles the nonbonded Lennard-Jones potential with a cutoff of $r_{\text{cutoff}} = 1.4\,\text{nm}$. The interaction energy $U^{\text{pair}}_{\text{nonbonded}}(r)$ is calculated only up to the cutoff distance. However, while the interaction potential is small at the cutoff distance or larger distances, the potential is not zero. To correct the appearing deviation in the potential energy $U^{\text{total}}_{\text{nonbonded}}(r_1, ..., r_N)$, an analytical tail correction is used:

$$\Delta U^{\text{tail}}_{\text{nonbonded}} = 2\pi N\rho \int_{r_{\text{cutoff}}}^{\infty} U^{\text{pair}}_{\text{nonbonded}}(r) r^2 dr, \tag{4.34}$$

where N is the number of particles, and ρ the particle number density. As the HOOMD version (2.6), which we use, does not include an analytical tail correction, we instead increase the cutoff to $r_{\text{cutoff}} = 1.8\,\text{nm}$. Secondly, the nonbonded interaction is not calculated for beads within a single molecule that are separated by less than four beads.

The second force field is the coarse-grained **MARTINI force field**. In the MARTINI force field, four CH_x groups are mapped in one MARTINI bead [109]. Therefore, compared to the TraPPE-UA force field, the resolution is lower. For example, n-octane is described by only two C1-MARTINI beads, while it is described by eight beads in the TraPPE-UA force field: on each end of the chain one CH_3 bead, and six CH_2 beads in the middle of the chain. Although the resolution in the MARTINI model is reduced considerably, the computing effort is also reduced. Therefore, we use the TraPPE-UA force field where we need a higher resolution, and the MARTINI force field where we handle a large system or scan many parameters.

Again, there are several details on the MARTINI force field worth mentioning. As the TraPPE-UA force field, the nonbonded interactions are described by a 12-6 Lennard-Jones potential. However, instead of an analytical tail correction, the potential is shifted [106]:

$$\begin{aligned}
U^{\text{pair}}_{\text{nonbonded}}(r_{ij}) &= U_{\text{LJ}}(r_{ij}) + \Delta U(r_{ij}) && r_{ij} < r_{\text{cutoff}}, \\
U^{\text{pair}}_{\text{nonbonded}}(r_{ij}) &= 0 && r_{ij} \geq r_{\text{cutoff}}, \\
\Delta U(r_{ij}) &= -U_{\text{LJ}}(r_{\text{cutoff}}) - (r_{ij} - r_{\text{cutoff}}) \frac{\partial U_{\text{LJ}}(r_{\text{cutoff}})}{\partial r_{ij}}, \\
U_{\text{LJ}}(r_{ij}) &= 4\epsilon_{ij} \left[\left(\frac{\sigma_{ij}}{r_{ij}} \right)^{12} - \left(\frac{\sigma_{ij}}{r_{ij}} \right)^{6} \right].
\end{aligned} \tag{4.35}$$

The bonds and angles are also represented by harmonic potentials. However, dihedrals are not included.

A feature of coarse grained systems is that the underlying energy landscape is smoother than in an all atomistic simulation. Therefore, dynamics are faster. This is the main reason why the interpretation of time scales is not straightforward. With the MARTINI force field, the effective time is roughly four times the simulation time [109]. We use this estimation. However, the true conversion factor may differ.

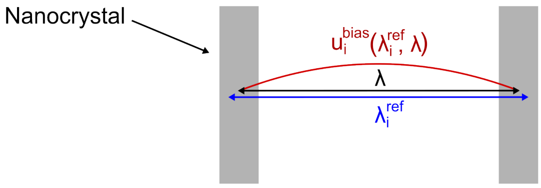

Figure 4.2: Sketch of an umbrella sampling setup. The reaction coordinate is the center-center distance λ between the nanocrystals. The umbrella sampling calculation is separated into several windows. In each window, a bias potential $u_i^{\text{bias}}(\lambda, \lambda_i^{\text{ref}})$ is added, which acts on the distance between the nanocrystals, for example a harmonic potential as in Equation 4.43. In the sketched time step of window i, the center-center distance λ is smaller than the reference value λ_i^{ref}. Therefore, the umbrella potential pushes the two nanocrystals apart. This is indicated by the curvature in the drawing of the potential.

4.4 Umbrella sampling

While we can determine the potential energy and the temperature directly from the molecular dynamics simulation, this does not apply to the interaction free energy. Therefore, we have to use other methods here. One of these methods is umbrella sampling. Umbrella sampling allows calculating the free energy along one or multiple reaction coordinates. In this section, we summarize the technique. Thereby, we follow the derivation J. Kästner describes in his review [113].

For simplicity, we derive the formalism in the canonical ensemble (NVT), with a constant number of particles N, a constant volume V, and a constant temperature T. The Helmholtz free energy is:

$$A = U - ST, \tag{4.36}$$

where U is the internal energy, and S the entropy. We can also describe the free energy via

$$A = -\frac{1}{\beta} \ln Q, \tag{4.37}$$

where $\beta = 1/(k_\mathrm{B}T)$, and Q is the Helmholtz partition function:

$$Q = -\int e^{-\beta U(r)} d^N r, \tag{4.38}$$

with the potential energy $U(r)$.

Let us now consider a Cartesian reaction coordinate λ, that is a defined by a mapping function $\lambda(r)$ that depends on the coordinates r. For example, λ can be the distance between two nanocrystals (see Figure 4.2). We define the partition function as a function of the reaction coordinate [99, 113]:

$$Q_\lambda = \int \delta[\lambda(r) - \lambda]\, e^{-\beta U(r)} d^N r, \tag{4.39}$$

where the delta function $\delta[\lambda(r)-\lambda]$ is introduced to select the states, where the mapping function $\lambda(r)$ has the value λ.

With the two partition functions, we can calculate the free energy along the reaction coordinate:

$$A(\lambda) = -\frac{1}{\beta} \ln \frac{Q_\lambda}{Q}, \tag{4.40}$$

where $q(\lambda) = \frac{Q_\lambda}{Q}$ is the probability distribution corresponding to the reaction coordinate λ. Hence, $q(\lambda)d\lambda$ is the probability of finding the system in the interval $d\lambda$ around λ.

We do not get the probability distribution $q(\lambda)$ right away in simulations. However, an ergodic system visits all states during an infinite simulation. If this is the case, the time average

$$p(\lambda) = \lim_{t\to\infty} \frac{1}{t} \int_0^t \rho[\lambda(t)]dt \tag{4.41}$$

becomes equal to the ensemble average $q(\lambda)$. Thereby, $\rho[\lambda(t)]$ is the number density of the occurrence of $\lambda(t)$.

Thus, in principle, we can obtain the free energy curve $A(\lambda)$ directly from a molecular dynamics simulation. However, in practice this mostly does not work, as simulation time is limited. According to Boltzmann-statistics, the probability α of sampling a state with the energy E is proportional to the Boltzmann-factor $\propto \exp\left(-E/k_\mathrm{B}T\right)$. Therefore, high-energy states are sampled only rarely, if at all. Furthermore, states separated from the rest by high energy barriers may also not be sampled during a finite long simulation.

Umbrella sampling is a technique that allows to increase the sampling rate. An artificial bias potential $u_i^\mathrm{bias}(\lambda)$ dependent on the reaction coordinate is added:

$$U^\mathrm{bias}(r) = U(r) + u_i^\mathrm{bias}(\lambda). \tag{4.42}$$

For example, this can be a harmonic potential:

$$u_i^\mathrm{bias}(\lambda) = \frac{\kappa_i}{2}\left(\lambda - \lambda_i^\mathrm{ref}\right)^2, \tag{4.43}$$

where κ_i defines the strength of the potential, and λ_i^ref is the reference reaction coordinate. The bias can be applied to a single simulation, or to multiple independent simulations (windows) along the reaction coordinate. The index "i" refers to the window for which the potential is defined. With the bias, the probability distribution changes to:

$$q_i^\mathrm{bias} = \frac{\int \delta[\Lambda(r)-\lambda]\, e^{-\beta[U(r)+u_i^\mathrm{bias}(\Lambda(r))]} d^N r}{\int e^{-\beta[U(r)+u_i^\mathrm{bias}(\Lambda(r))]} d^N r}. \tag{4.44}$$

Since u_i^bias depends solely on λ, we can rewrite it:

$$q_i^\mathrm{bias} = e^{-\beta u_i^\mathrm{bias}(\lambda)}\, \frac{\int \delta[\Lambda(r)-\lambda]\, e^{-\beta U(r)} d^N r}{\int e^{-\beta[U(r)+u_i^\mathrm{bias}(\Lambda(r))]} d^N r}. \tag{4.45}$$

This we can connect to the unbiased probability distribution:

$$\begin{aligned} q_i &= \frac{\int \delta[\Lambda(r) - \lambda]\, e^{-\beta U(r)} d^N r}{\int e^{-\beta U(r)} d^N r} \\ &= q_i^{\text{bias}} e^{\beta u_i^{\text{bias}}(\lambda)} \, \frac{\int e^{-\beta[U(r) + u_i^{\text{bias}}(\Lambda(r))]} d^N r}{\int \delta[\Lambda(r) - \lambda]\, e^{-\beta U(r)} d^N r} \\ &= q_i^{\text{bias}} e^{\beta u_i^{\text{bias}}(\lambda)} \, \left\langle e^{-\beta u_i^{\text{bias}}(\lambda)} \right\rangle . \end{aligned} \tag{4.46}$$

With it, we can calculate the free energy:

$$\begin{aligned} A_i(\lambda) &= -k_{\mathrm{B}} T \ln \left(q_i^{\text{bias}}(\lambda)\right) - u_i^{\text{bias}}(\lambda) - k_{\mathrm{B}} T \ln \left\langle e^{-\beta u_i^{\text{bias}}(\lambda)} \right\rangle \\ &= -k_{\mathrm{B}} T \ln \left(q_i^{\text{bias}}(\lambda)\right) - u_i^{\text{bias}}(\lambda) + F_i, \end{aligned} \tag{4.47}$$

where F_i is independent on λ. With an appropriate chosen umbrella potential, we achieve a sufficient sampling in each window. In a single window, Equation 4.47 is sufficient to calculate the free energy curve. However, in multiple windows umbrella sampling, we have to calculate the F_i's to connect the free energy curves obtained in each window. We cannot obtain them directly from the simulation, as they are connected to the unbiased probability distribution:

$$\begin{aligned} e^{-\beta F_i} &= \left\langle e^{-\beta u_i^{\text{bias}}(\lambda)} \right\rangle \\ &= \int q(\lambda) e^{-\beta u_i^{\text{bias}}(\lambda)} d\lambda \\ &= \int e^{-\beta(A(\lambda) + u_i^{\text{bias}}(\lambda))} d\lambda. \end{aligned} \tag{4.48}$$

In this thesis, we use the Weighted Histogram Analysis Method (WHAM) to calculate the F_i's. The idea is, to form the total distribution from the weighted sum of the distributions of the individual windows:

$$q(\lambda) = \sum_i x_i q_i(\lambda), \tag{4.49}$$

where the weights x_i follow the condition $\sum_i x_i = 1$. The weights are chosen in such a way, that the statistical error of $q(\lambda)$ is minimized:

$$\frac{\partial \sigma^2(q(\lambda))}{\partial x_i} = 0. \tag{4.50}$$

With $x_i = a_i / \sum_i a_i$, this leads to the condition:

$$a_i(\lambda) = N_i e^{-\beta u_i^{\text{bias}}(\lambda) + \beta F_i}, \tag{4.51}$$

where N_i is the number of sampled points for the window i. With this condition, we can calculate $q(\lambda)$ with Equation 4.49, and the F_i's with Equation 4.48. However, as the F_i's enter Equation 4.49, we have to do this iteratively.

Chapter 5

Implementation: model systems, density, and free energy calculation

To study the effects of solvent restructuring and solvation forces on the CdSe nanoplatelet interaction, we create two model systems. Of each model system, we create two versions, where we describe the interactions either with the TraPPE-UA or the MARTINI force field (see Section 4.3).

The first model system describes infinite large ligand passivated facets (Figure 5.1). This setup allows us to study the solvent restructuring at the ligand-solvent interface (see Chapter 6a,b). Thereby, we expect that this setup replicates the ligand structure in the middle of the base facets of large nanoplatelets, where effects of the edges should be negligible. The second model system describes finite nanoplatelets (Figure 5.2a,b). With it, we study the solvation forces between of CdSe nanoplatelets (see Chapter 7).

In the following two sections, we describe the setups in detail. In the third section, we discuss the choice of the ligand grafting density in the setups with the MARTINI force field. In the fourth section, we discuss our implementation of umbrella sampling for the calculation of free energy curves.

5.1 Infinite large facets

The restructuring of the solvent at surfaces, in our case the ligand-solvent interface, causes solvation forces. We create ligand passivated platelets with infinite large facets to study the solvent restructuring at the ligand-solvent interface.

Figure 5.1 displays our setups. Panel a shows our setup with the TraPPE-UA force field, and panel b our setup with the MARTINI force field (see Section 4.3). In both setups, we implicitly describe the platelet surface by surface beads. These surface beads are used as grafting points for the ligand shell. Replicating the surface of CdSe nanoplatelets, the ligand grafting points are arranged in a face centered grid [114, 49]. The ligands are inseparably bound to the surface beads. On the top and the bottom of the platelet, the solvent is placed. We use periodic simulation boxes. Since the box length in x and y direction is kept constant, the setups describe infinite large facets.

There are four subtleties to the TraPPE-UA setup. Partly, we have already discussed them in Section 4.3. Firstly, TraPPE-UA describes the nonbonded interaction by a 12-6

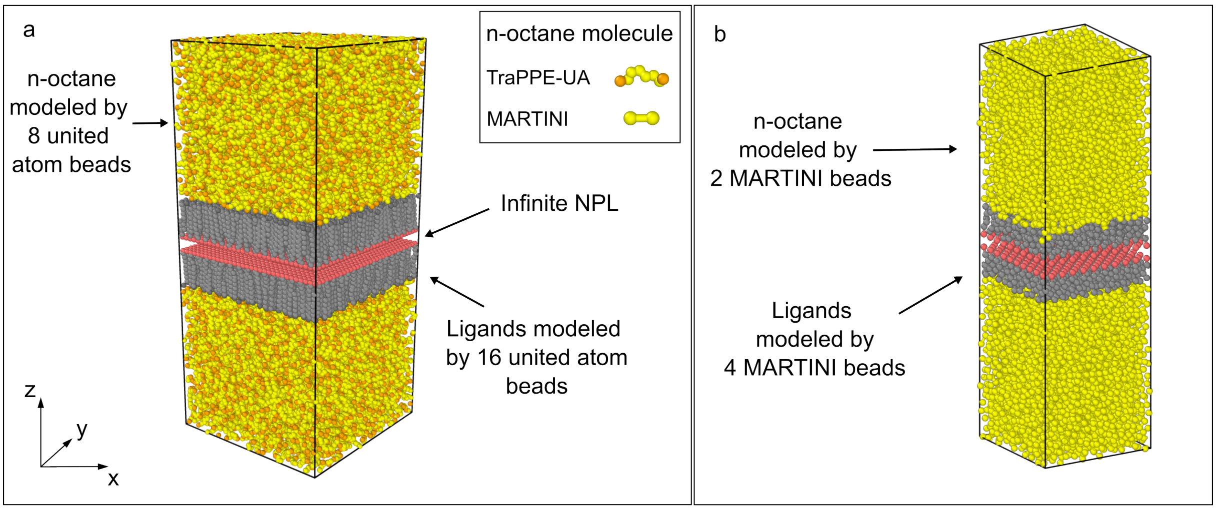

Figure 5.1: System setup for the simulation of infinite large ligand coated facets. **Panel a** shows the setup with the TraPPE-UA force field, while **panel b** shows the setup with the MARTINI force field. In both cases, the facet surface is modeled by surface beads (red). The surface beads are used as grafting points for the ligands (gray). On the top and the bottom, solvent molecules are placed (yellow). In the shown cases, it is octane (**see inset**). In **panel a**, the ligand and octane molecules consist of CH_2, and CH_3 united atom beads. For the CH_3 beads, a darker color has been chosen. In **panel a**, we add additional surface beads between the ligand grafting points to prevent ligand molecules entering the center of the platelet. In **panel b**, we describe the ligand and solvent molecules by C1 MARTINI beads. We use periodic simulation boxes. Therefore, the setup describes infinite large ligand passivated facets.

Lennard-Jones potential, including a tail correction. As the HOOMD version (2.6) we use does not include a tail correction, we instead increase the cutoff to $r_{\text{cutoff}} = 1.8$ nm. Secondly, in the TraPPE-UA force field, the nonbonded interaction is not calculated for beads within one molecule that are separated by less than four beads. In our simulations, this includes the surface beads, which we use as grafting points for the ligands. Without this interaction, beads of the ligands can enter the inside of the platelets. To solve this technical issue, we add surface beads in between the ligand grafting points to the TraPPE-UA setup. Thirdly, the TraPPE-UA force field does not include interaction parameters for CdSe. To describe the interaction with the surface beads, we choose parameters which actually describe the interaction with CdS (Table 5.1) [33]. This approximation is reasonable, as we are interested in the ligand-solvent interface. The interaction with the surface has only a minor effect on the behavior at the interface. Fourthly, in the original version of TraPPE-UA, bonds have a fixed length. However, we extend the force field by a bond stretching term [112].

Concerning the MARTINI force field, there is no representation of CdSe or similar materials. We chose the most repelling interaction of the interaction table between the surface beads and the ligand / solvent beads ($\varepsilon = 2.0\,\text{kJ/mol}$, $\sigma = 0.62\,\text{nm}$) [109].

TraPPE-UA force field

	CdSe	
	ϵ in kJ/mol	σ in nm
CH_3	0.599	0.354
CH_2	0.466	0.354
CH	0.466	0.354

MARTINI force field

	CdSe	
	ϵ in kJ/mol	σ in nm
C1	2.0	0.62 nm

Table 5.1: Interaction parameter for the interaction with the surface beads in the TraPPE-UA setup and the MARTINI setup

The theoretical ligand grafting density for carboxylic ligands on the {001}-CdSe surface is 5.4 ligands/nm^2 [49]. This value results from the assumption that the ligands bind to the Cd atoms, considering a face centered surface lattice and the experimental CdSe lattice constant 0.608 nm. Experimental measurements have confirmed this value [49, 50]. Unless otherwise stated, we use these values in the TraPPE-UA setup. However, MARTINI beads are large. At a high ligand grafting density, the MARTINI beads have not enough space. This can lead to unrealistic behavior. Therefore, we use in the MARTINI setups a lattice constant of 0.746 nm, corresponding to a ligand grafting density of 3.6 ligands/nm^2 (see Section 5.3 for a detailed discussion).

Unless otherwise stated, we employ ligands with a length of 16 CH_x beads in the TraPPE-UA setup, and accordingly 4 C1 beads in the MARTINI setup. The standard solvent is in both cases n-octane.

To run our molecular dynamics simulations, we use the HOOMD package (v2.6.0) [115, 116, 117]. In both setups, simulations are performed at a constant pressure of 1 atm and a constant temperature of 300 K. We control the temperature by a Dissipative Particle Dynamics (DPD) thermostat [118], and the pressure by a Martyna-Tobias-Klein barostat [103] (see Section 4.2.4, and 4.2.3). In the simulations with the TraPPE-UA setup, we use time steps of 2 fs, while we use 20 fs with the MARTINI setup (×4 for effective time, see Section 4.3). Further simulation parameters are summarized in Section B.1.1.

5.2 Nanoplatelets

We create a model system to describe ligand passivated CdSe nanoplatelets in our simulations (Figure 5.2). As already discussed in Section 3.4, the core-core van der Waals interaction and the dipole-dipole interaction between CdSe nanoplatelets are weak. Therefore, we neglect them in our model of the nanoplatelets. Furthermore, we assume that the core of the nanoplatelets is rigid, and that the nanocrystal itself does not change in any way during the simulation. Therefore, we do not have to represent the nanocrystal core in detail. This also applies to the nanocrystal surface. The interaction is mainly influenced by the ligand and the solvent molecules.

Again, we create a variation where we describe the interactions with the TraPPE-UA force field (panel a), and a variation where we describe the interactions with the MARTINI force field (panel b). We model the nanoplatelets by surface beads. These surface beads give the platelets their shape. In experiments, CdSe nanoplatelets usually have a square or rectangular shape (see Figure 8.1) [45, 46, 37]. We model nanoplatelets with square base facets. The surface beads serve as ligand grafting points. Replicating the surface of CdSe nanoplatelets, the surface beads are arranged in a face centered grid [114, 49].

In HOOMD [115, 116, 117], the simulation code we use, we define the nanoplatelets as rigid objects. Rigid objects are composed of a single central bead and several constituent beads. In our case, the constituent beads are the surface beads. The mass and momentum of the nanoplatelet are assigned to the central bead. During the simulation, the total forces and torques from the constituent beads are transferred to the central bead. Then, the equations of motion are solved for the central bead.

The syntax to setup a rigid object is complicated. Therefore, we use HOOBAS [119] to generate the nanoplatelets as rigid objects in HOOMD. HOOBAS is a molecular building tool that simplifies the creation of complex objects in molecular dynamics simulations. Depending on the size of the nanoplatelet, we calculate the nanoplatelet mass via the mass density of CdSe $\rho = 5.7\,\mathrm{g/cm^3}$.

A variety of molecules can be used as ligands for CdSe nanoplatelets, such as heptanoic acid, octanoic acid, or myristic acid [45]. In the case of CdSe nanoplatelets, the ligands are strongly bound to the nanocrystal surface. We expect that it is a very rare event that the ligands separate from the surface. Therefore, we describe the ligands as aliphatic tails that are inseparably bound to the surface beads of the rigid nanoplatelet.

To run our molecular dynamics simulations, we use the HOOMD package (v2.6.0) [115, 116, 117]. Simulations are performed at a constant pressure of 1 atm, and a constant temperature of 300 K. We use cubic periodic simulation boxes.

In simulations with the TraPPE-UA setup, we control the temperature by a Dissipative Particle Dynamics (DPD) thermostat [118], and the pressure by a Martyna-Tobias-Klein barostat [103] (see Section 4.2.4, and 4.2.3). In simulations with the MARTINI setup, we use the standard HOOMD NPT integrator as a thermostat and barostat. It is based on the Martyna-Tobias-Klein equations of motion [103, 120, 121]. In the simulations with the TraPPE-UA setup, we use time steps of 2 fs, while we use 20 fs with the MARTINI setup (×4 for effective time, see Section 4.3).

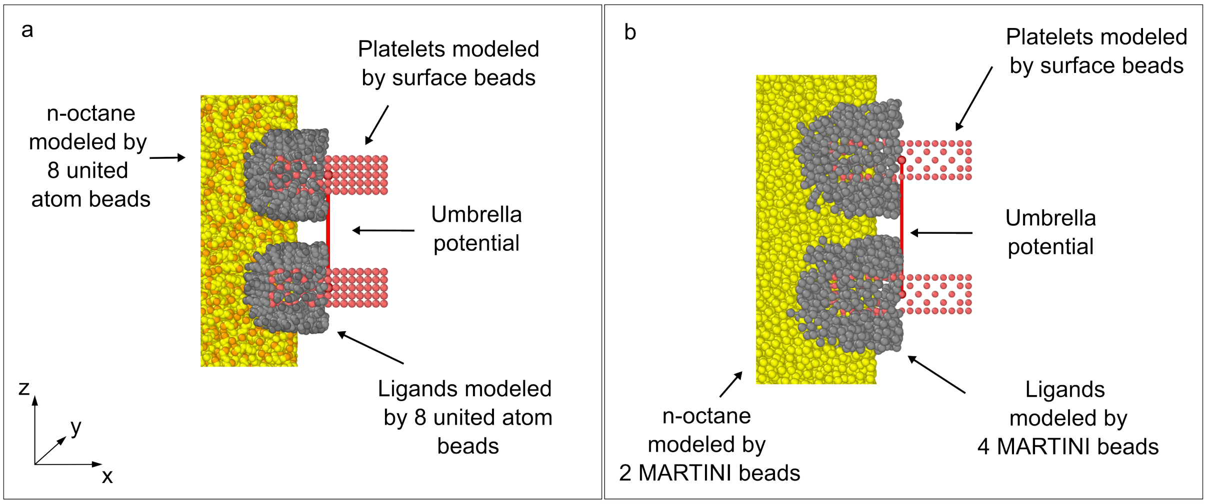

Figure 5.2: Model system setup for CdSe nanoplatelets. **Panel a** shows the setup with the TraPPE-UA force field, while **panel b** shows the setup with the MARTINI force field. In both cases, the nanoplatelets are modeled by surface beads (red). The surface beads are used as grafting points for the ligands (gray). Around the nanoplatelets, solvent molecules are placed (yellow). In the shown cases, it is n-octane. In **panel a**, the ligand and octane molecules consist of CH_2, and CH_3 united atom beads. For the CH_3 beads, a darker color has been chosen. In **panel a**, we add additional surface beads between the ligand grafting points to prevent ligand molecules entering the center of the nanoplatelet. In **panel b**, we describe the ligand and solvent molecules by C1 MARTINI beads.

5.3 Ligand grafting density in the MARTINI setups

The theoretical ligand grafting density for carboxylic ligands on the {001}-CdSe surface is 5.4 ligands/nm^2, corresponding to the experimental CdSe lattice constant 0.608 nm [49]. Experimental measurements have confirmed this value [49, 50]. While we in general use 5.4 ligands/nm^2 in the setups with the TraPPE-UA force field, we use a smaller value in the setups with the MARTINI force field. The reason is that C1 MARTINI beads are large (σ= 0.47 nm). At the CdSe lattice constant, they have not enough space available. Hence, their ordering in the ligand shell changes. The infinite setup shows this well. In the infinite facet setup, we already find a change in the ligand structure at 4.2 ligands/nm^2. Some ligands shrink, while other ligands' extent (see snapshots in Figure A.2 and sketches in Figure 5.3). As a result, the ligand-solvent interface gets uneven, and the solvent restructuring gets disturbed (see Section A.1.1 for further discussion).

At finite nanoplatelets, we find an edge effect. The ligands at the edges can occupy more space. This also reduces the confinement of the ligands further away from the edges. Accordingly, the properties of the ligand shell changes compared to an infinite facet. We find that for nanoplatelets with 27.3 nm^2 base facet area, a grafting density of 4.2 ligands/nm^2 is still reasonable (see Section 7.2.4). However, for larger ligand grafting

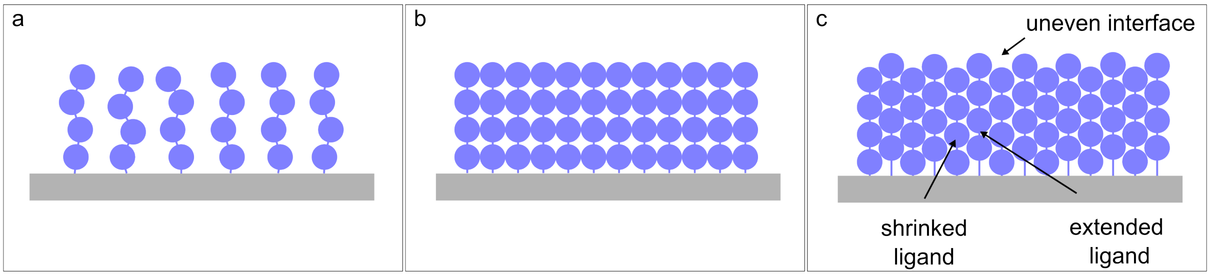

Figure 5.3: The sketches show ligand shells with different ligand grafting densities. **Panel a** shows a low ligand grafting density, where the ligands have more than enough space. **Panel b** shows a larger ligand grafting density. Here, the ligands have just enough space. Finally, **panel c** shows an unrealistic large ligand grafting density. With an unrealistic large ligand grafting density, some ligands shrink, while others extend. The result is an uneven ligand-solvent interface.

densities this is not the case. The use of the experimental 5.4 ligands / nm^2 results in a too large ligand packing density, and in strong tensions in the ligand shell. In our test simulations, artifacts occur. We observe that some ligand bonds are very compressed or overstretched. In addition, the surface at the interface to the solvent is altered.

Despite the problems in the description of the ligand shell, the MARTINI model is suitable for the representation of the ligand shell of the nanoplatelets. In general, solvation forces between interfaces are strongly correlated with the solvent restructuring [20]. In our simulations with the infinite facet setups, we find that the magnitude of the amplitudes of the oscillation in the solvent density at the ligand-solvent interface depends on the ligand grafting density (see Section 6.2.2 and Section A.1.1). However, the overall shape of the solvent density oscillation does not depend on the ligand grafting density. Therefore, we assume that the MARTINI setup with a smaller ligand grafting density is a good description of the CdSe nanoplatelets to study the main properties of the interaction.

The idea that the MARTINI setup with a lower ligand grafting density is a good description is confirmed in our characterization of the pair interaction between two nanoplatelets. We calculate free energy curves to characterize the pair interaction. For the face-to-face interaction of the nanoplatelets, we find that the free energy oscillates with the distance between the platelets. For reasonable small ligand grafting densities, the amplitudes of the free energy oscillation depend on the ligand grafting density, while the general shape is independent (Section 7.2.4). Only, if the ligand grafting density is too small, the effects flatten out. Therefore, we expect that general trends for other parameters are largely unaffected by the ligand grafting density, e.g., ligand length, facet size.

Unless otherwise stated, we use a lattice constant of 0.746 nm in the MARTINI setup, corresponding to a ligand grafting density of 3.6 ligands/nm^2. At this lattice constant, the distance between two neighboring grafting sites matches the distance of the minimum in the 12-6 Lennard-Jones interaction potential of two ligand beads (see Figure 5.4).

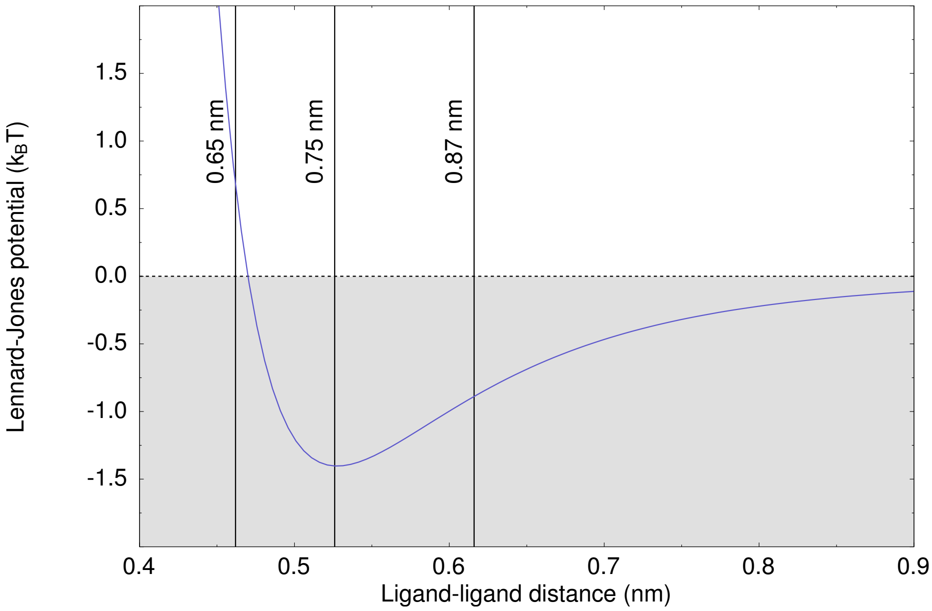

Figure 5.4: Distance between ligand grafting sites in comparison to the nonbonded Lennard-Jones interaction potential between ligand beads in the MARTINI force field [96].

5.4 Density calculations

We calculate ligand and solvent densities at various parts of the manuscript. In general, we assume that the beads of the ligand and solvent molecules are point-like particles. To each bead, we assign the corresponding mass. We calculate the densities by creating a histogram of the masses and averaging over the corresponding volume in each bin of the histogram. Additionally, we average over many snapshots from the simulation.

We create one-dimensional density curves and two-dimensional density heatmaps. In Figure 5.5a-c, we show cross-sectional snapshots of different setups, where we illustrate typical histogram bins. In panel a, we show the snapshot of an infinite facet setup, where we create one-dimensional density curves (e.g., Figure 6.3). In all infinite facet setups,

Setup	Force field	Dimension	# of snapshots	production run (ns)
Infinite facet	TraPPE-UA	1D	5000	200
	MARTINI	1D	5000	8000
Nanoplatelet	TraPPE-UA	1D	600	2.4
	MARTINI	1D	5000	800
	MARTINI	2D	3000	800

Table 5.2: List of the minimal number of snapshots used in the density calculations of each setup, and the corresponding minimal production run length.

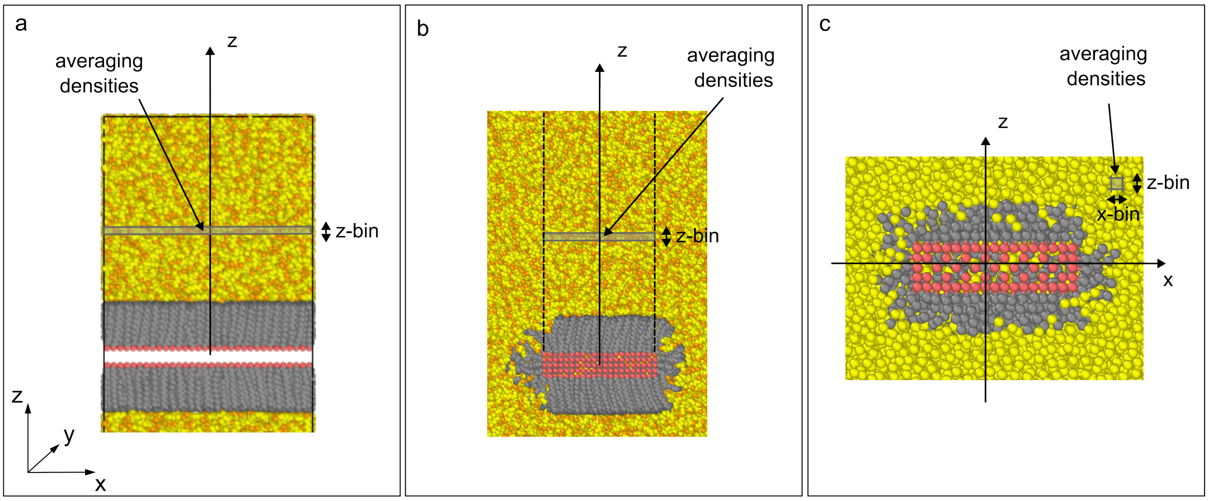

Figure 5.5: Cross-sectional simulation snapshots of different setups with sketched histogram bins. **Panel a** and **b** depict setups to calculate one-dimensional density curves. **Panel a** shows a snapshot from an infinite facet setup. In this setup, the densities at each z-distance are averaged over the bin volume that is created by the z-bin and the whole xy-plane. **Panel b** shows the snapshot of a single nanoplatelet. In such simulations, the densities in each z-distance are averaged over the bin volume that is created by the z-bin and the facet area in the corresponding xy-plane. Finally, **panel c** shows a snapshot, where a two-dimensional density heatmap is calculated. The densities are averaged over the bin volume that is crated by a xz-bin and the side length of the nanoplatelet in y-direction.

we divide the z-direction into z-bins of 0.01 nm size, and average the ligand and solvent densities over the bin volume that is created by the z-bin and the whole xy-plane. In panel b, we show a snapshot of a single nanoplatelet, where we calculate the densities away from the base facet (e.g., Figure 6.9). In such setups, we average the densities in each bin over the bin volume that is created by the z-bin and the base facet area in the corresponding xy-plane. In panel c, we present a snapshot from a single nanoplatelet, where we create two-dimensional ligand and solvent density heatmaps (e.g., Figure 7.2.2d)). In such two-dimensional density calculations, we divide the z-direction into z-bins, and the x-direction into x-bins. Each bin volume is created by the corresponding z-bin, x-bin, and the side length of the nanoplatelet in y-direction.

In all one-dimensional density calculations, we use z-bins of 0.01 nm size. In Section B.1.2, we discuss test calculations with different bin sizes. We also use this bin size in the calculation of two-dimensional density heatmaps (z-bin $=$ x-bin $= 0.01$ nm).

We average the densities over many snapshots. In Table 5.2, we list the minimal number of snapshots and the corresponding minimal production run length, which we use in the density calculations in each setup.

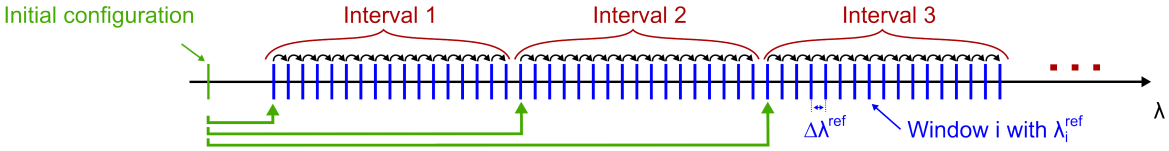

Figure 5.6: Sketch of the division of the reaction coordinate λ into windows i with λ_i^{ref}, and intervals. The first window of each interval is started from the initial configuration. Other windows of each interval are initiated and run sequentially.

5.5 Free energy calculation

To get a deeper understanding of the CdSe nanoplatelet pair interaction, we calculate free energy curves for selected nanoplatelet approaches using multiple windows umbrella sampling simulations (see Section 4.4) [113].

We focus primarily on the interaction in a face-to-face orientation of the nanoplatelets in z-direction, as depicted in Figure 4.2, and shown in the snapshots in Figure 5.2a,b. Thereby, we do not allow a rotation of the nanoplatelets. We achieve this by disabling anisotropic integration in HOOMD. As the nanoplatelets are the only rigid objects in the simulation, this only affects the nanoplatelets. In addition, we constrain the nanoplatelets with built-in HOOMD commands to prevent a sideways movement of the platelets. However, it turns out that numerical noise causes errors in the position of the nanoplatelets, which add up in longer simulations. Therefore, we additionally apply a custom plugin, which resets the x and y coordinates as well as the corresponding velocities to zero. We only allow movements of the nanoplatelets toward or away from each other in the z-direction.

To control the distance, we apply a harmonic umbrella potential between the center beads of the two nanoplatelets:

$$u_i^{\text{bias}}(\lambda) = \frac{1}{2}\kappa\left(\lambda - \lambda_i^{\text{ref}}\right)^2, \tag{5.1}$$

where λ is the distance along the z coordinate, and λ_i^{ref} is the preferred distance targeted by the umbrella potential in each window i. We use a force constant of $\kappa = 50000\,\text{kJ/mol}$.

Our workflow is outlined in Figure 5.6. First, we create an initial configuration, positioning the two nanoplatelets at a small distance, where the ligand shell is already compressed. We equilibrate the initial system. We divide the reaction coordinate in different windows with λ_i^{ref}. Thereby, we change λ_i^{ref} by steps of $\Delta\lambda^{\text{ref}} = 0.005$ nm or $\Delta\lambda^{\text{ref}} = 0.0025$ nm, dependent on the platelet size / simulation box size (see Tables B.9-B.18). Applying $\Delta\lambda^{\text{ref}} = 0.005$ nm, an umbrella simulation from a distance of 4.75 nm to 10.0 nm include 1050 windows.

We combine the windows into intervals. We start the first window of each interval from the initial configuration. Again, we equilibrate the system. Then, we collect the center-center distances in a production run. Subsequently, starting from each preceding window, the simulations in the other windows of each interval are performed in a sequence.

In most of the simulations with the MARTINI setup (Figure 5.2b), the production run in each window has a length of 40 ns. In this 40 ns, we collect the center-center distances from 250 snapshots (see Section B.2.1.4 for test of number of snapshots). In the simulations with a solvent molecule chain lengths of three and four beads, we increase the length of the production run to 80 ns, where we collect the center-center distances from 500 snapshots. We do this because of the higher viscosity of the solvent, and slower movement of the nanoplatelets (see Section B.2.1.5). In the simulations with the TraPPE-UA setup (Figure 5.2a), the production run in each window has a length of 2 ns, where we collect the center-center distances from 500 snapshots.

Independent of the used force field, we calculate the free energy curves from the probability distributions of the center-center distances in each window. For this, we use the Weighted Histogram Analysis Method (WHAM), as described in Section 4.4 [122, 123, 113]. We perform the WHAM analysis with the tool of D. Bauer [124]. Two parameters determine the accuracy of the WHAM calculation. The first parameter is the number of bins in which the tool divides λ. We use 305 bins/nm (see parameter tests in Section B.2.1.1). The second parameter is the tolerance. The tolerance is the abortion criteria for the WHAM calculation. The WHAM calculation stops when the difference between the free energy values of the newest step $F_{\text{new}}(\lambda)$, and the free energy values of the previous step $F_{\text{old}}(\lambda)$ is smaller than the tolerance ($|F_{\text{new}}(\lambda) - F_{\text{old}}(\lambda)| <$ tolerance). We use a tolerance of 10^{-6} kJ/mol. The error of the free energy values is estimated via Bayesian bootstrapping [125]. In this thesis, we always do ten bootstrapping runs to calculate the error.

When the outcome of umbrella sampling is affected by the initial conditions, it may indicate that the simulations are not sufficiently converged [126]. Therefore, for selected systems, we also perform test simulations where we move from large to small distances. The results do not differ (see Section B.2.1.2 in the appendix). However, we find a finite size effect for too small simulation boxes (see Section B.2.1.3 in the Appendix). Accordingly, we vary the number of solvent molecules, and such the box size, dependent on the nanoplatelet dimensions, and the solvent type (see Tables B.7-B.18).

Chapter 6

Solvent restructuring at ligand brushes

At the interface between a surface and a solvent, the solvent typically restructures. Often, the solvent restructures into layers. In particular, solvent layering has been demonstrated for nanoparticles [127, 128]. The strength and shape of this perturbation has a major influence on the interaction of nanoparticles, especially on the manifestation of solvation forces. Therefore, before we deal with the pair interaction of CdSe nanoplatelets in the next chapter, we consider here the solvent restructuring on the ligand-solvent interface.

The dimensions of CdSe nanoplatelets depend on the synthesis (see Section 3.1). The base facet area can be small, or very large (see Figure 8.1). Therefore, we consider the solvent restructuring at the base facets of small nanoplatelets, and on infinite facets. Thereby, we assume that the infinite facets represent very large nanoplatelets. Furthermore, we vary the ligand grafting density, the ligand length, the solvent type, and the temperature.

6.1 Model system

Snapshots of our setups are shown in Figure 6.1. **Panel a** shows the setup of a single nanoplatelet, while **panel b** shows the setup of an infinite facet. We model the nanoplatelet / facet surface with surface beads, which we use as grafting points for the ligands. Between the ligand grafting points, we add additional surface beads to prevent ligands beads entering the center between the two facets. Unless otherwise stated, we use in this chapter 5.4 ligands/nm^2, ligands with a length of 16 CH$_\mathrm{x}$ beads, and the solvent n-octane. We use periodic simulation boxes. Therefore, the setup in **panel b** describes infinite large ligand passivated facets.

The simulations in this chapter are less computationally demanding. Therefore, we use here the TraPPE-UA force field, with its higher resolution. Additional results from the MARTINI setup can be found in the appendix (Section A.1.1), and in Chapter 7. We describe the setups in more detail in Section 5.1, and in Section 5.2. In Section 4.3, we describe the force fields. In Section B.1.1, we list additional simulation parameters.

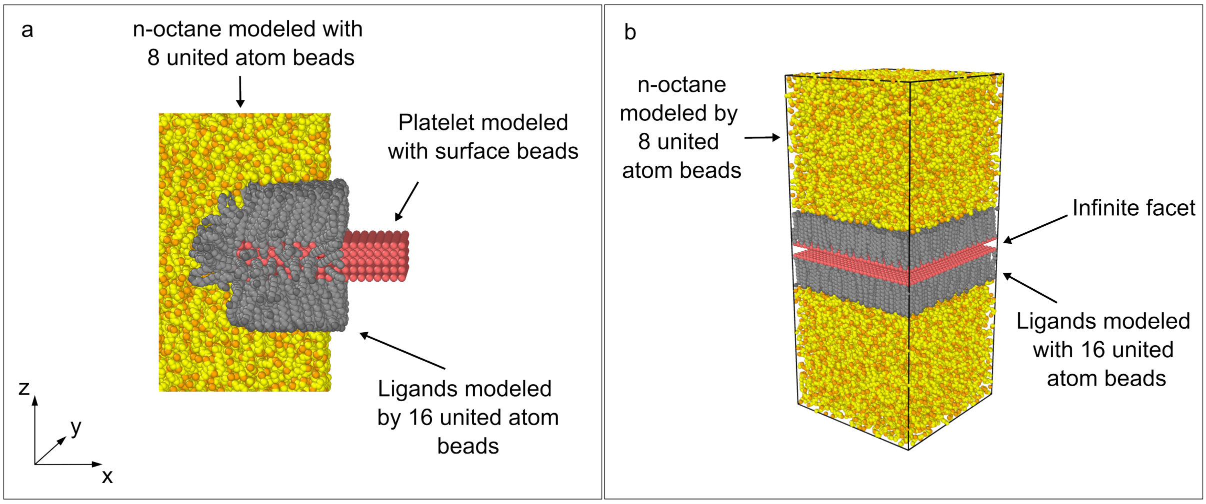

Figure 6.1: System setups. **Panel a** shows a snapshot from a single nanoplatelet, while **panel b** shows a snapshot of an infinite facet setup. The nanoplatelet / facet surface is modeled with surface beads (red). The surface beads are used as grafting points for the ligands (gray). The solvent is n-octane (yellow/orange). The ligand and octane molecules consist of CH_2, and CH_3 united atom beads. For the CH_3 beads, a darker color has been chosen. Additional surface beads between the ligand grafting points prevent ligand molecules entering the center of the platelet. We use periodic simulation boxes. Therefore, the setup in **panel b** describes infinite large ligand passivated facets.

6.2 Results

We run simulations, where we apply the described setups. For each parameter combination, we first equilibrate the system. Then we carry out a production run. With the particle positions from the production run, we calculate the densities of the ligands and the solvent. For each distance z from the facet surface, we average the densities over the corresponding xy-plane, and perform a time average (see Section 5.4 for a detailed description).

6.2.1 Solvent restructuring and facet area

In Figure 6.2, we show the density profiles away from the base facets of single nanoplatelets with different facet areas and away from an infinite facet. The solvent is n-octane, and the ligands have a length of 16 CH_x beads.

Regardless of the facet area, the ligand and solvent densities show the same characteristics. We find that the ligand density is oscillating with the distance away from the facet surface. This is due to the arrangement of the ligand beads, where one end of the ligand molecule is fixed to the surface, and the available space is limited. It is noticeable that the ligand density away from the infinite facet is constant when averaged over a larger range

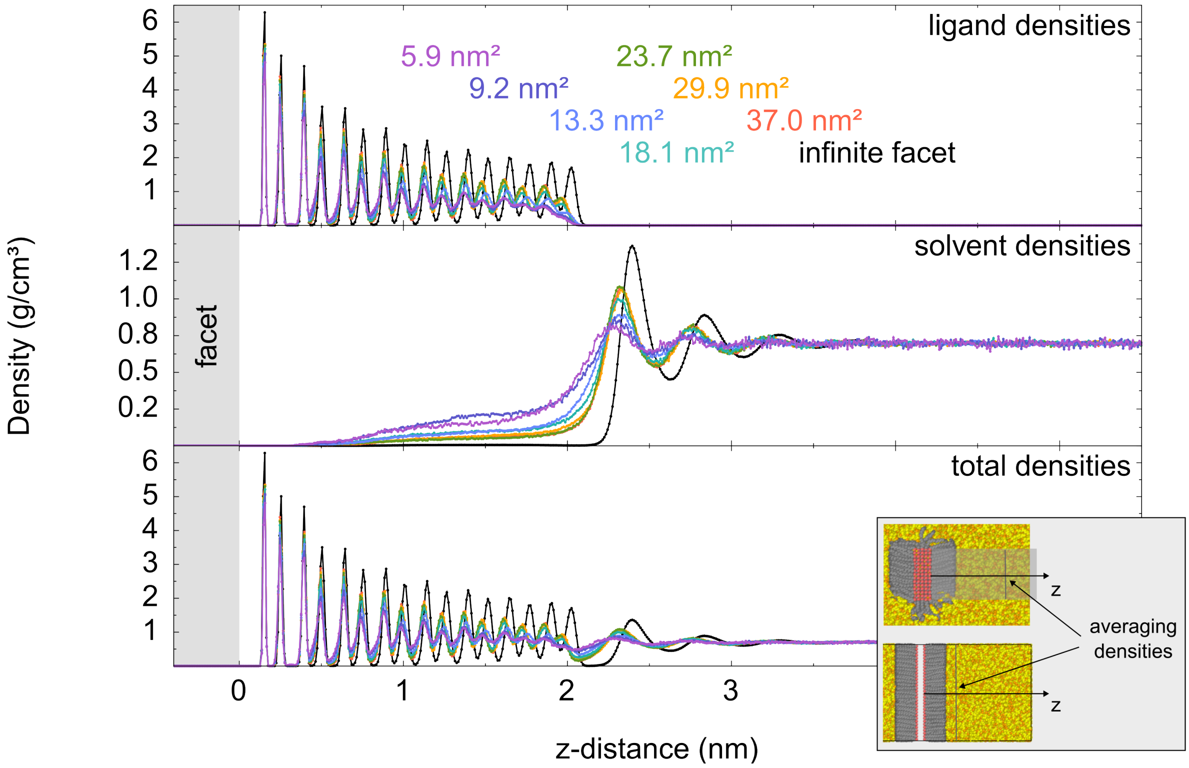

Figure 6.2: Effect of the facet area. We compare densities away from the base facets of single nanoplatelets with different base facet areas in the TraPPE-UA setup. The platelet thickness is 1.2 nm. For comparison, the densities away from the infinite facet setup is also shown. The top panel shows the ligand, the middle panel the solvent, and the bottom panel the total densities. As depicted in the inset, the densities at each distance in the z-direction result from the averaging over the corresponding xy-plane, and from time averaging. For clarity, the data points are connected with straight lines.

(see Section B.1.2 in the Appendix). This is in agreement with simplified models, where it is assumed that the ligand density is constant in a ligand shell on a flat surface [27].

We find that the ligand-solvent interface causes the solvent to restructure. Close to the interface, the solvent density oscillates. Thereby, the spacing between two extrema is constant. In agreement with previous results, it is close to the thickness of the solvent molecules, and not to their length [72]. The amplitude of the oscillation decreases with the distance to the interface.

We find that the densities depend on the facet area. For smaller facet areas, the oscillations in the ligand and solvent densities are less pronounced, and more solvent enters the ligand shell. As the facet area increases, the oscillations increase, and less solvent enters the ligand shell. With increasing facet area, the densities away from the finite nanoplatelets approach the densities away from the infinite facet.

We assume that the edges of the base facets of the finite nanoplatelets are responsible for the changes. The ligands have more space at the edges. Therefore, the ligands arrange themselves differently on a small facet than on a large or an infinite facet (see Figure 5.4a, b). The ligand density at the ligand-solvent interface increases with the facet area, and the surface of the ligand shell becomes harder. Therefore, the solvent restructuring increases. This is a general trend we observe. The higher the density of the ligand shell, the harder the surface is, the more pronounced is the solvent restructuring (see also Section 7.2.3, where we compare nanoplatelets with and without a ligand shell).

6.2.2 Ligand grafting density

5.4 ligands per nm^2 is the expected ligand grafting density for carboxylic ligands on the $\{001\}$-CdSe surface [49]. This value results from the assumption that the ligands bind to the Cd atoms, considering a face centered surface lattice and the experimental CdSe lattice constant 0.608 nm. Experimental measurements have confirmed this value [49, 50].

Here, we compare different ligand grafting densities at finite nanoplatelets, and at an infinite facet to improve our understanding of how the ligand grafting density affects the solvent restructuring. The base facet area of the finite nanoplatelets is 37.0 nm^2. We control the ligand grafting density in our setup with the lattice constant. Therefore, we vary the thickness of the nanoplatelets together with the ligand grafting density (see Table 6.1).

In Figure 6.3, we show the calculated densities. In both setups, we find similar trends. The higher the ligand grafting density, the higher is the ligand packing density. This means that less space is available for the ligand molecules / beads, as it is evident from the sharper peaks. Vice versa, the available space increases as the grafting density decreases.

Accordingly, we find that the amount of solvent in the ligand shell decreases with the ligand grafting density. For example, we find no solvent in the ligand shell of the infinite facet with 6.7 ligands per nm^2. This confirms that the ligand shell can fulfill the function of a permeation barrier, which shields the surface of the nanocrystal from the components of the solvent [27]. Additionally, we find that the restructuring of the solvent is more pronounced with higher ligand grafting densities.

In the previous subsection, we have discussed that the edges of the facets affect the densities. We observe this here as well. For small nanoplatelets, significantly larger ligand grafting densities must be chosen than in the infinite facet setup to produce a similarly large solvent oscillation. For example, 5.4 ligands per nm^2 at the finite nanoplatelet creates a similar strong solvent density oscillation than 3.8 ligands per nm^2 at the infinite facet.

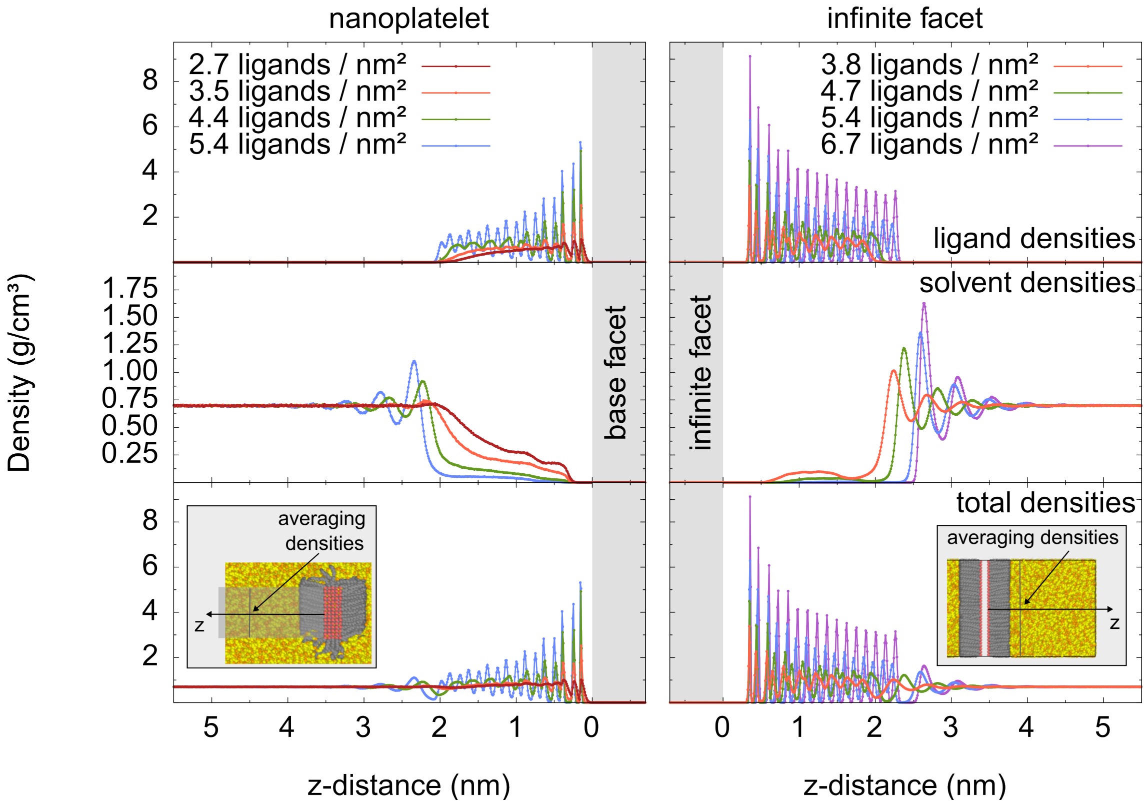

Figure 6.3: Effect of the ligand grafting density on the solvent restructuring. The left column shows the densities away from the base facet of single nanoplatelets, while the right column shows the densities away from an infinite facet. The top row shows the ligand, the middle row the solvent, and the bottom row the total densities. As depicted in the insets, the densities at each distance in the z-direction result from the averaging over the corresponding xy-plane, and from time averaging. For clarity, the data points are connected with straight lines.

ligand grafting density (ligands / nm^2)	lattice constant (nm)	thickness (nm)
2.7	0.869	1.7
3.5	0.76	1.5
4.4	0.676	1.4
5.4	0.608	1.2

Table 6.1: Connection between ligand grafting density, lattice constant and nanoplatelet thickness

6.2.3 Ligand length

We vary the ligand length, and compare the solvent restructuring at the ligand-solvent interface (Figure 6.4). We use a ligand grafting density of 5.4 ligands/nm^2. In this case, the ligand shell is very dense and hard. However, the mobility of the ligand beads increases with the distance to the surface. In both setups, this is visible in the decrease in the amplitude of the ligand density oscillation. As a consequence, the surface of the ligand shell becomes softer with increasing ligand length, and we find that the amplitudes of the solvent oscillation at the interface decrease.

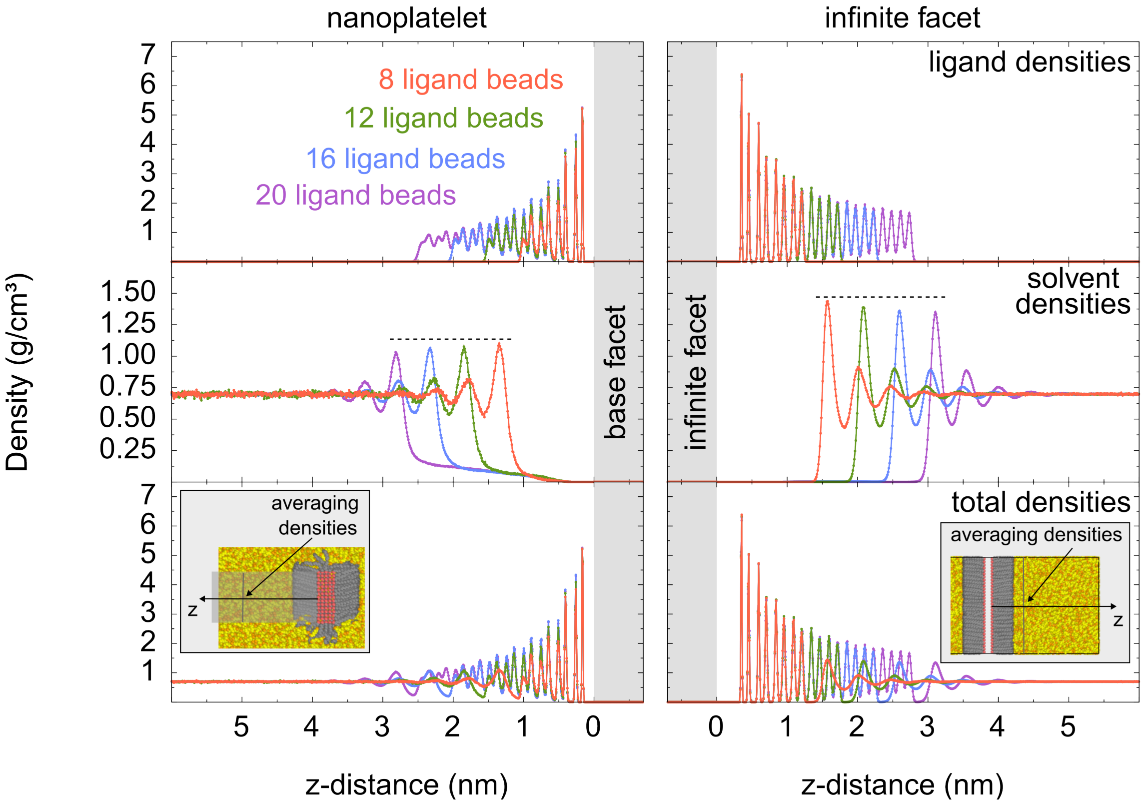

Figure 6.4: Effect of the ligand length on the solvent restructuring at the ligand-solvent interface. The left column shows the densities away from the base facet of a single nanoplatelet with 18.1 nm^2 facet area, while the right column shows the densities away from an infinite facet. The top row shows the ligand, the middle row the solvent, and the bottom row the total densities. As depicted in the insets, the densities at each distance in the z-direction result from the averaging over the corresponding xy-plane, and from time averaging. For clarity, the data points are connected with straight lines.

6.2.4 Solvent type

The restructuring of the solvent not only depends on the properties of the ligand shell, but also on the solvent type. In Figure 6.5, we compare linear n-alkane solvents with different length in the infinite facet setup. With increasing alkane length, the bulk solvent density is increasing. Thereby, the amplitudes of the solvent density oscillation increases significantly. However, these differences become smaller with increasing chain length.

From various studies on solvation forces, it is known that the distance between the extrema depends on the solvent molecule [71, 20, 129]. Linear alkanes can align fully stretched parallel to the surface. The density, or in the case of solvation force measurements, the force, oscillates with the thickness of the molecules. Therefore, the distance between the extremes in n-alkanes is always the same, regardless of the n-alkane length [72]. We observe this here as well. The spacing s between two extrema of the same kind of the solvent density is independent of the alkane length (Figure 6.5).

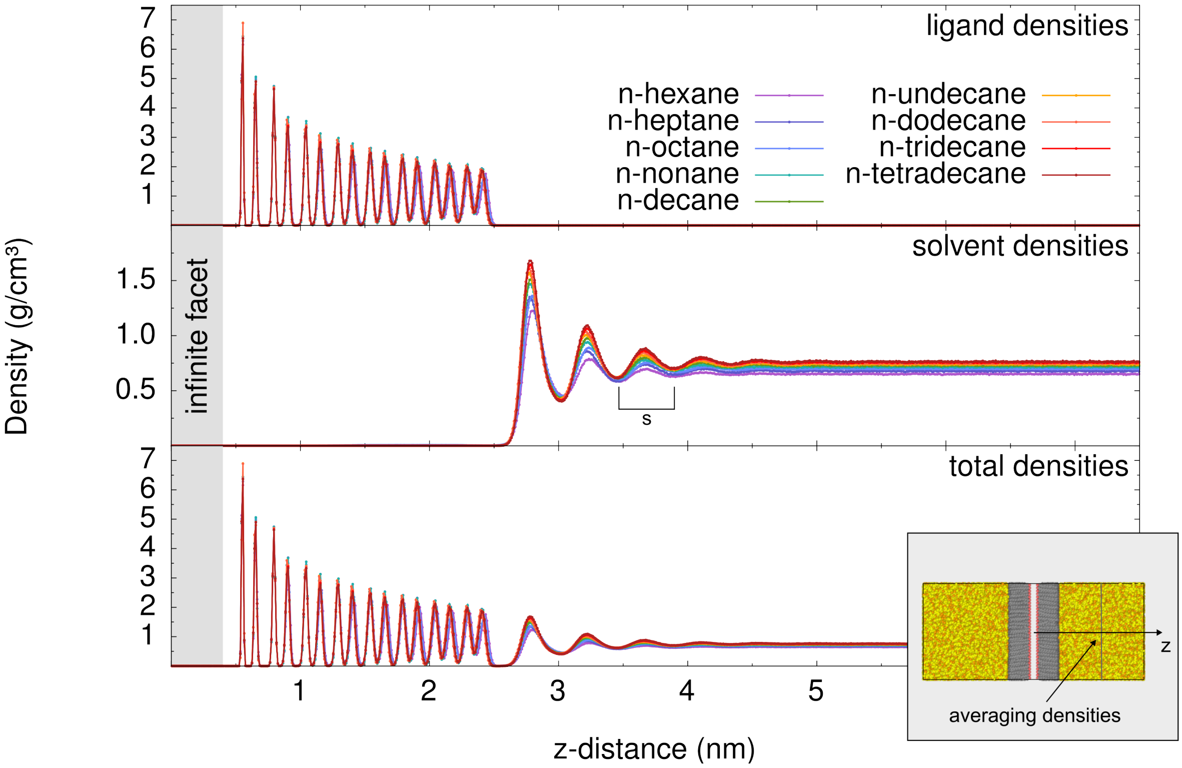

Figure 6.5: Effect of alkane solvent length. The top panel shows the ligand, the middle panel the solvent, and the bottom panel the total densities. As depicted in the inset, the densities at each distance in the z-direction result from the averaging over the entire xy-plane, and from time averaging. For clarity, the data points are connected with straight lines.

However, the spacing s between two extrema can be tuned by increasing the cross-section of the solvent molecules. As an example, we plot in Figure 6.6 the densities of different isomers of octane. The isomers are characterized by different degrees of branching. From n-octane, to 2-methylheptane, to 3,4-dimethylhexane, to iso-octane the increase in branching is increasing the cross-section of the molecules. The molecules become more voluminous, and the spacing s is increasing. It is worth noting that the change in s between 3,4-dimethylhexane and iso-octane is small, while the amplitudes of the solvent oscillation increase. We assume that the increase in the amplitudes is a result of the increased rigidity.

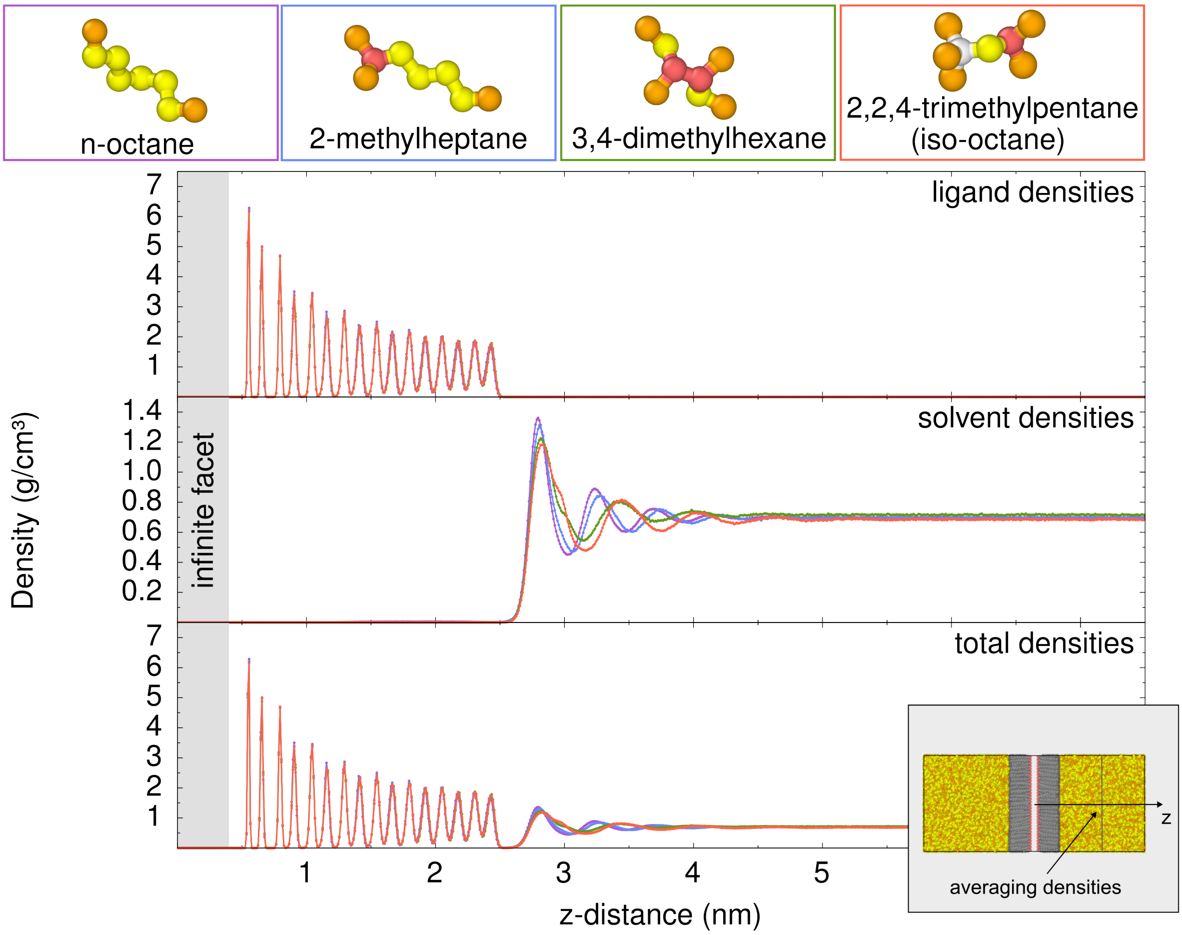

Figure 6.6: Comparison of octane isomers in the infinite facet setup. Selected snapshots of the isomers are shown above the plot. The bead colors correspond to the different bead types: CH_3 is shown in orange, CH_2 in yellow, CH_1 in red, and CH_0 in white. The color of the frames around the snapshots corresponds to the corresponding density curves. The top panel of the plot shows the ligand, the middle panel the solvent, and the bottom panel the total densities. As depicted in the inset, the densities at each distance in the z-direction result from the averaging over the entire xy-plane, and from time averaging. For clarity, the data points are connected with straight lines.

Finally, we added one and two double bonds to the solvent molecules. In Figure 6.7, we compare n-octane with 1-octene, and 1,7-octene. Here, we find changes in the ligand shell. In 1-octene, the ligand shell shrinks compared to n-octane. Interestingly, this does not account for 1,7-octene. Here, the density curves of the ligand shells overlap completely. Regarding the solvent, it should first be noted that the alkenes have a higher bulk density. Apart from that, the double bonds influence the restructuring of the solvent less than the branching of the isomers. We find that the amplitude of the solvent density oscillations decreases with the number of double bonds. As a result of the changes in the ligand shell, the first minimum of 1-octene shifts slightly towards the surface, which is not the case for 1,7-octene. However, as can be seen in the comparison of n-octane and 1,7-octene, there is a minor change in the spacing between the extrema.

The presented results demonstrate that the solvent restructuring sensitively depends on the solvent type. This is true, even between, at first glance, very similar solvents molecules. At the end of the next chapter, we study how the differences influence the interaction between CdSe nanoplatelets (see Section 7.2.9, and Section 7.2.10).

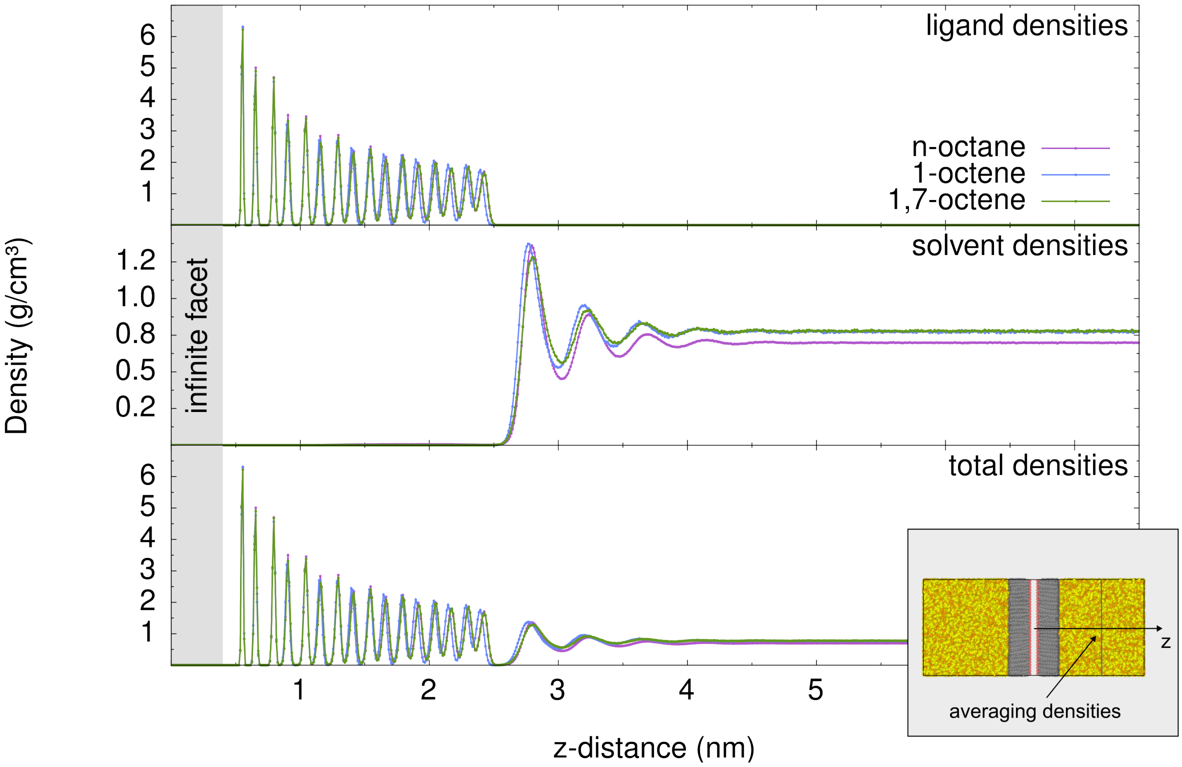

Figure 6.7: Effect of double bonds. In the infinite facet setup, we compare n-octane with 1-octene, and 1,7-octene. The top panel shows the ligand, the middle panel the solvent, and the bottom panel the total densities. As depicted in the inset, the densities at each distance in the z-direction result from the averaging over the entire xy-plane, and from time averaging. For clarity, the data points are connected with straight lines.

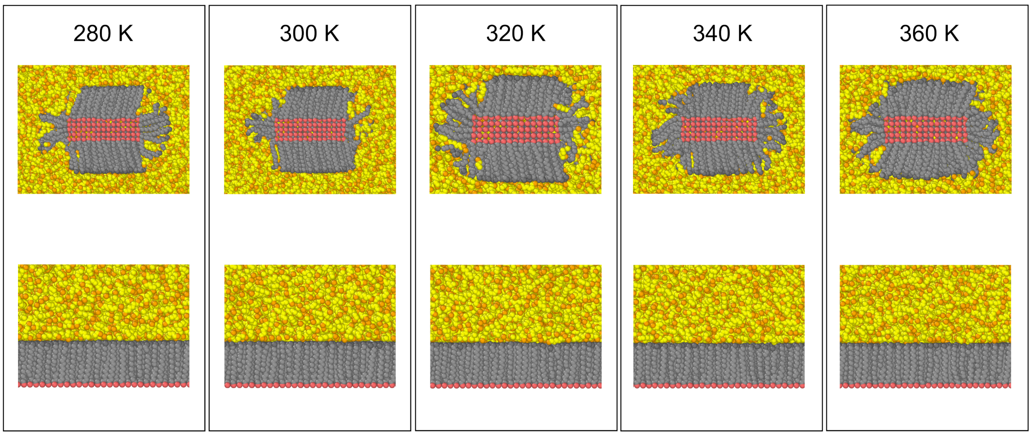

Figure 6.8: Effect of the temperature on the ligand configuration. The top row displays cross-sectional snapshots of a small nanoplatelet at different temperatures. In the bottom row, snapshots of the infinite facet setup at different temperatures are shown. At 280 K, the ligands of the small nanoplatelet form well-defined bundles at the base and side facets. With increasing temperature, the bundles loosen their cohesion, until the ligand shell takes a space-filling shape around the nanoplatelet. While there are visible changes in the ligand shell of the small nanoplatelet, there are no obvious changes in the ligand shell of the infinite facet.

6.2.5 Temperature dependence

As Widmer-Cooper *et al.* have shown for CdS nanorods, the temperature can influence the ordering of the ligands, and the solvent restructuring [33, 52]. In their system, the ligands form into bundles at lower temperature, which induce a more pronounced solvent restructuring. In contrast, at higher temperatures, the ligands occupy the available space. In this case, the ligand shell is soft, and solvent restructuring is reduced. This effect has the consequence that the solvation forces at low temperatures are significantly stronger than at high temperatures.

When we compare the CdS nanorods with our CdSe nanoplatelets, the main differences are the facet dimensions, and the ligand grafting densities. The facets of the nanorods are long, but not wide ($\leq 8\,\mathrm{nm}$) [33, 34]. Additionally, the ligand grafting density is only $3.6\,\mathrm{ligands/nm^2}$. In contrast, we consider CdSe nanoplatelets with side length of up to around 20 nm, and a ligand grafting density of $5.4\,\mathrm{ligands/nm^2}$.

We have already compared different ligand grafting densities in Section 6.2.2. A higher ligand grafting density reduces the freedom of the ligands, and increases the solvent restructuring. Therefore, we expect a more pronounced solvent restructuring on the base facets of CdSe nanoplatelets than on the facets of CdS nanorods.

Here, we focus on the dimensions of the facet area. On a small facet, the ligands have more space that they can occupy due to the edges. Furthermore, the facet edges can be seen as declination lines that disrupt the ligand ordering [68, 69]. Therefore, the ligand ordering on a small facet will be different from that on a large facet. We expect that

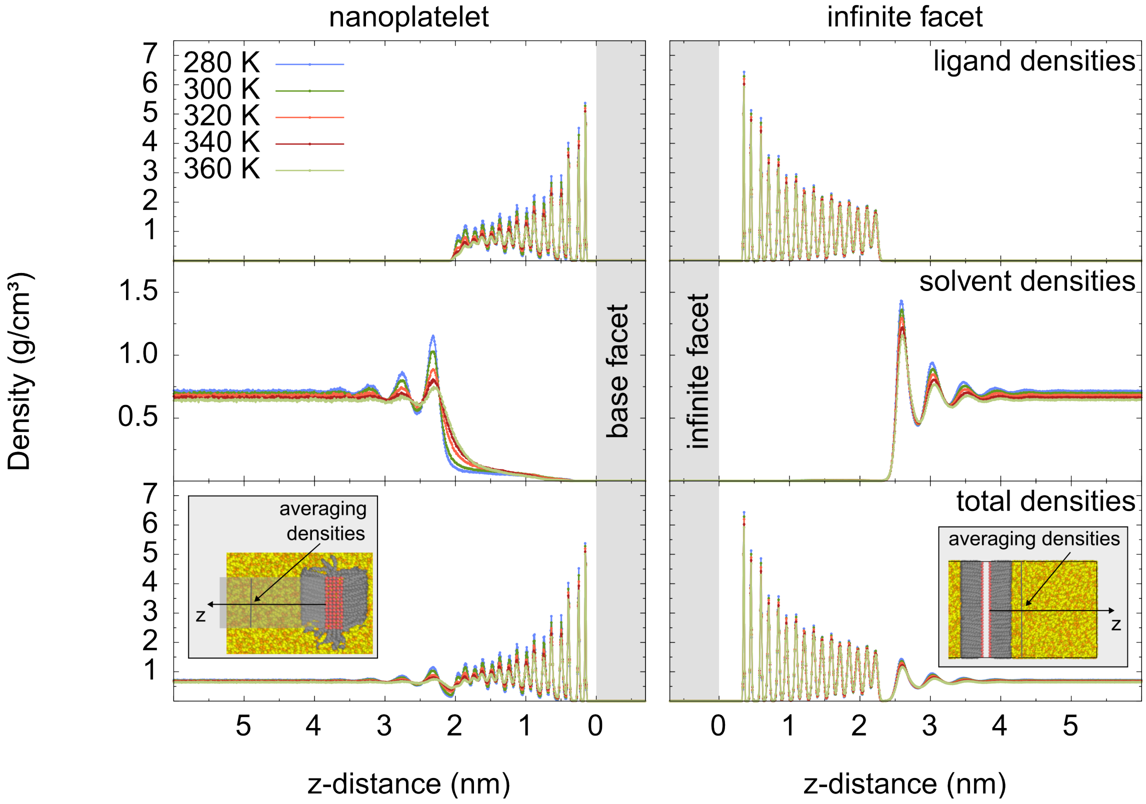

Figure 6.9: Effect of the temperature on the solvent restructuring. The left column shows the densities for the base facet of a small nanoplatelet, while the right column shows the densities for an infinite facet. The top row shows the ligand, the middle row the solvent, and the bottom row the total densities. For clarity, the data points are connected with straight lines. For lower temperatures, the solvent restructuring is more pronounced, as the ligand shell is harder. The effect is stronger on the ligand-solvent interface of the small nanoplatelet, as the ligands can occupy more space due to the edges.

the temperature has a less significant impact on the solvent restructuring at large CdSe nanoplatelets. To test this, we compare the ordering of the ligand shell, and the solvent restructuring around a small nanoplatelet with that at our infinite setup. Again, the solvent is n-octane. The small nanoplatelet has a facet area of $18.1\,\mathrm{nm}^2$ and a thickness of $1.2\,\mathrm{nm}$. In Section 5.2, we describe the setup of the nanoplatelet in detail.

First, let us compare cross-sectional snapshots from both systems at different temperatures (Figure 6.8). Here, we find strong temperature dependent differences in the ligand shell of the small nanoplatelet. At 280 K, the ligands form sharp defined bundles at the base facets of the nanoplatelet. With increasing temperature, the bundles loose cohesion, until the ligand shell takes a space-filling shape around the nanoplatelet. In contrast, there are no obvious visible temperature dependent changes in the snapshots of the infinite setup. The ligand shell is densely packed. Therefore, the ligand beads are quite confined to their positions.

In the next step, we calculate the ligand and solvent densities. We compare the densities in Figure 6.9. For all temperatures, we find that the ligand density is smaller in the nanoplatelet setup. As a result, also the solvent restructuring is less pronounced. As expected, the bulk solvent density decreases with increasing temperature. Additionally, we find that the ligand density decreases with the temperature. However, the temperature dependent change is much more pronounced at the small nanoplatelet. In agreement with our findings from the snapshots, we find that the temperature dependent changes in the solvent restructuring are also much more pronounced at the small nanoplatelet.

In summary, the ligand ordering, and the solvent restructuring decrease with the temperature. However, this effect will be more pronounced for small facets, and less pronounced for large facets.

6.3 Summary and discussion

We find that the solvent restructuring at the ligand-solvent interface depends on various parameters. The denser and harder the ligand-solvent interface is, the more pronounced is the solvent restructuring. Therefore, an increase in the ligand grafting density, or a reduction of the ligand length, leads to an increase in the amplitude of the solvent density oscillation.

Likewise, the restructuring of the solvent compared to the bulk depends strongly on the solvent type. In agreement with previous studies on hard surfaces, we find an increase in the amplitude of the solvent density oscillation for longer n-alkanes [72]. As we demonstrate for isomers of octane, the spacing between the extrema of the solvent density oscillation can be tuned by the cross-section of the solvent molecules. The cross-section is in turn dependent on the branching. Furthermore, the amplitudes of the solvent oscillation depend on the branching.

In addition, the temperature can influence the solvent restructuring. Thereby, it depends on the properties of the ligand shell how much the temperature affects it. On small facets, such as on a small nanoplatelet, the ligands have more available space. At low temperatures, they form bundles on the base facets, which amplify the solvent oscillation. As the ligands are more confined, the effect is smaller on extended facets.

Although the solvation forces have their origin in the restructuring of the solvent, no simple proportionality can be established between the density oscillation in different solvents and the solvation forces. For this purpose, it would be necessary to take a closer look at the free energy costs associated with density fluctuation in the various solvents. Nevertheless, these results already give an impression of the interaction. In solvents with strong density oscillations, we can expect free energy extrema that are separated by the same distance as the extrema of the solvent oscillation.

We also refer to the additional results for the infinite facet simulations with the MARTINI setup in the appendix, where the general trends are reproduced, while some differences become clear (see Section A.1.1). As already discussed in detail in Section 5.3, the ligand grafting density in the MARTINI setup has to be chosen wisely. This effect can be seen particularly well in these simulations.

In the next chapter, we discuss the pair interaction between nanoplatelets. Since these simulations are more complex, we reduce the resolution, and use in most cases the more coarse-grained MARTINI force field to describe the interactions. Thereby, we use the united atom simulations as a reference, to confirm that the results are reliable.

Chapter 7

CdSe nanoplatelets pair interaction

In Chapter 3, we have discussed the special properties of ligand passivated CdSe nanoplatelets. Like other disk- or platelet-shaped nanocrystals [39, 47], CdSe nanoplatelets show the tendency to form stacks [45, 46, 37]. The stack formation influences their steric stability. Furthermore, we have discussed the different interactions, that can cause the stack formation. We have estimated the core-core van der Waals attraction, and discussed the dipole-dipole interaction. We concluded that both contributions to the attraction between the CdSe nanoplatelets are too weak to explain (alone) the stack formation. In this chapter, we pursue the hypothesis that solvation forces crucially influence the interaction, and are the cause of stack formation. In agreement with this hypothesis, we have already shown in the previous chapter that ligand passivated surfaces can cause a strong restructuring in the solvent at the ligand-solvent interface. Here, we use molecular dynamics simulations to study full nanoplatelets with different properties in different apolar solvents. For example, we vary the facet area, the ligand grafting density, and the ligand length.

After shortly introducing our model system again in Section 7.1, we present our simulation and calculation results in Section 7.2. In Section 7.3, we present a summary and discuss our conclusions.

The majority of the results we report in this chapter have already been published in Nano Letters [96].

7.1 Model system

As described in detail in Section 5.2, we create a model system of CdSe nanoplatelets (see Figures 5.2a,b, and Figure 7.1). We describe the nanoplatelets as rigid objects. Thereby, we model the surface of the nanoplatelets by surface beads. We use these surface beads as grafting points for the ligands, which we permanently bind to the surface.

Depending on the nanoplatelet size, and the number of nanoplatelets, we use between 100k and 500k molecules to describe the solvent. Therefore, the computational cost is significantly higher than in the previous chapter. To still be able to consider a large variety of parameters, we therefore decrease the resolution in most of the simulations in this chapter, and use the setup with the MARTINI force field (see Figure 5.2b, and

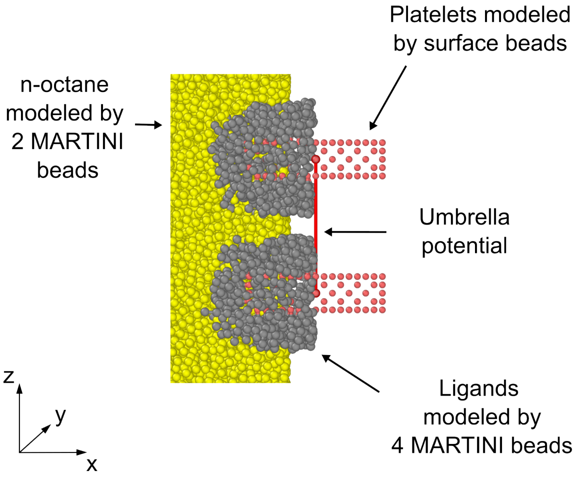

Figure 7.1: System setup with the MARTINI force field. CdSe Nanoplatelets are modeled by surface beads (red), which are used as ligand grafting points. The ligand molecules are modeled by four C1 MARTINI beads (gray), and the n-octane solvent molecules by two C1 MARTINI beads (yellow).

Figure 7.1). Only in Section 7.2.8 and Section 7.2.10, we use the setup with the TraPPE-UA force field (see Figure 5.2a). In Section 7.2.8, we consider different temperatures, and in Section 7.2.10 we compare different isomers of octane. Therefore, a higher resolution is required to describe the ligand shell and the solvent in more detail.

Unless otherwise specified, we consider in all simulations with the MARTINI force field nanoplatelets with 35.6 nm^2 base facet area, and 1.5 nm thickness. Thereby, we model the ligands with four MARTINI beads, equivalent to an alkyl length of 16 carbon atoms. The standard solvent in our simulations is n-octane, which we model with two C1 MARTINI beads.

7.2 Results

In the following subsections, we present our results on the nanoplatelet interaction. We start our analysis with the characterization of the stability of nanoplatelet stacks in Subsection 7.2.1. Thereafter, we analyze in Subsection 7.2.2 the pair interaction of two nanoplatelets in detail. We apply multiple windows umbrella sampling to calculate free energy curves for different approach paths, and compare the results with the changes in the solvent densities. In Subsection 7.2.3, we compare nanoplatelets without and with a ligand shell, and the solvent orientation in both systems. Thereafter, we consider the effects of the ligand grafting density and the ligand length on the pair interaction in the Subsections 7.2.4 and 7.2.5. Furthermore, the facet area and thickness affect the nanoplatelet interaction. We consider the facet area in Subsection 7.2.6, and the thickness in Subsection 7.2.7. In Subsection 7.2.8, we consider the effect of the temperature. Finally, we consider the effect of the solvent type in Subsection 7.2.9, and Subsection 7.2.10.

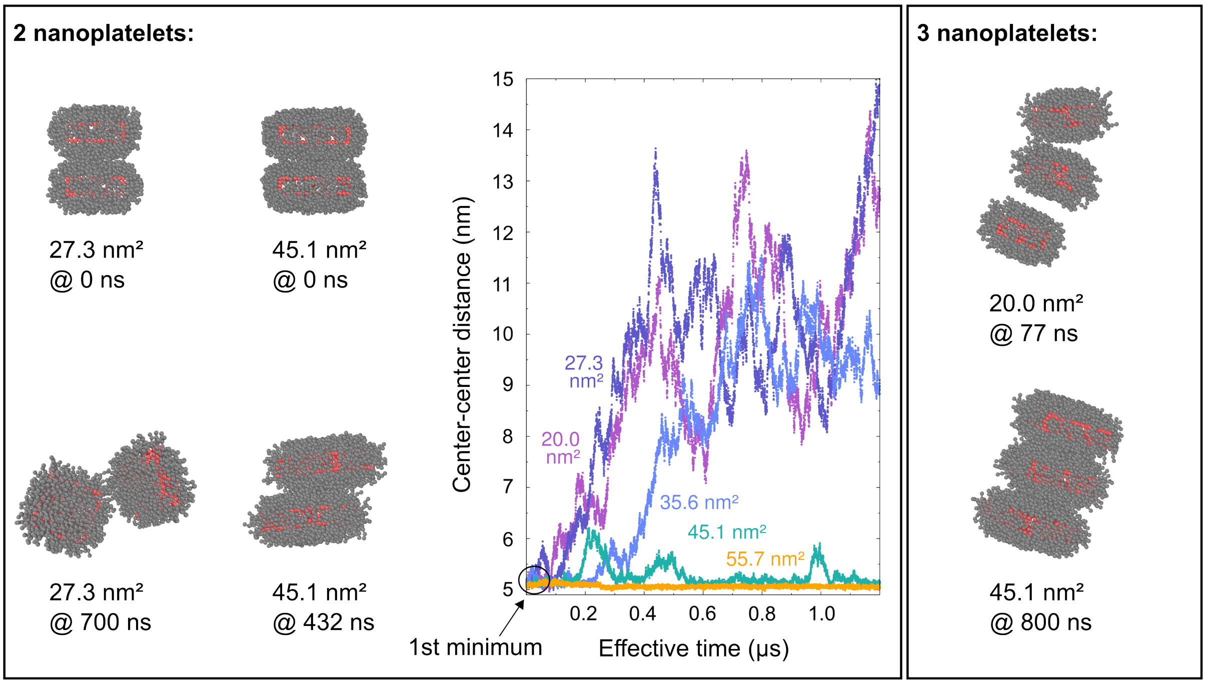

Figure 7.2: Simulations of free moving CdSe nanoplatelets [96]. Snapshots from simulations with initially stacked nanoplatelets. The solvent is not shown. Below each snapshot, the base facet area and the corresponding simulation time are specified. Additionally, the time series of the center-center distances of the simulations with two nanoplatelets are plotted.

7.2.1 Characterization of nanoplatelet stacks

We begin our considerations with the characterization of nanoplatelet stack. We form small nanoplatelet stacks, and observe their behavior in the simulations.

We consider nanoplatelets with a thickness of 1.5 nm, and base facet areas between 20 nm^2 and 55.6 nm^2 (see Tables B.7 and B.8 for simulation details). We examine stacks consisting of two or three nanoplatelets. In each simulation, the nanoplatelets are placed at a close distance in the simulation box. First, we equilibrate each system setup. Thereby, we allow the nanoplatelets only to move along the z-direction, and do not allow a rotation of the nanoplatelets, or a movement to the side. The nanoplatelets move into the global minimum in the face-to-face orientation (later called first minimum, vide infra). In Figure 7.2, we show for simulations with two nanoplatelets snapshots of the resulting configuration (@ 0 ns).

After the start conditions have been reached, we begin the actual simulation. Now, the nanoplatelets can move freely. We run the simulation for an effective simulation time of 1.2 µs. For the simulations with two platelets, we show the time series of the center-center distances for different base facet areas in Figure 7.2. The time series of the simulations with three nanoplatelets are shown in Figure A.6. Videos of selected simulations are available in our publication [96].

We observe that the nanoplatelet behavior depends on the base facet area. Stacks of nanoplatelets with small facet areas ($\leq 35.6\,\mathrm{nm}^2$) rapidly disassemble. On the other hand, if the nanoplatelets have larger facet areas, the platelets stick together, and the stacks are stable. For facet areas larger than $45.1\,\mathrm{nm}^2$, both for stacks with two, and for stacks with three platelets, we do not observe a separation.

We observe that the nanoplatelets rotate around the main axis of the stack. Additionally, we observe small lateral displacements. These results are in agreement with the experimental results of Jana et al. [46]. Complementary, we find here that the sideways movements decrease with facet size. This is reflected in the center-center distances. In the trajectory of the stack with $45.1\,\mathrm{nm}^2$ nanoplatelets, the center-center distance fluctuates due to these movements, while this effect is greatly weakened at $55.7\,\mathrm{nm}^2$.

This kind of movements of the nanoplatelets within the stack are very typical for stacks consistent of disk- or platelet shaped particles. For example, similar behavior has been observed in in experiments with micrometer-sized discs. Those micrometer-sized discs can form stacks under the influence of depletion forces [81]. This illustrates the similarity between solvation and depletion forces.

We also carry out simulations for unattached nanoplatelets. We initially position the platelets around 10 nm apart. Each simulation we run for at least 8 µs (see Figures A.5, A.7, A.8, and A.9 in Section A.2.1). Here, we do not observe an assembling of the nanoplatelets. In the simulations, it looks like as if the nanoplatelets repeatedly encounter barriers when they come too close to each other.

We only include the interaction between the ligands and the solvent molecules in the simulations. Therefore, both the attraction between the nanoplatelets and the barriers indicate the existence of solvation forces.

7.2.2 Interaction mechanism

Now, we take a closer look at the interaction between CdSe nanoplatelets. We calculate free energy curves for three selected assembling pathways. To calculate the free energy curves, we use multiple windows umbrella sampling combined with WHAM (see Section 4.4 and Section 5.5).

In Figure 7.3, we present the free energy curves. Next to each curve, we display a snapshot, where we indicate the corresponding approach path by an arrow. First, we consider an approach of the side facets (panel a). In this orientation, we find no significant attraction between the nanoplatelets. We only find a repulsion by the ligand shell at close distances. However, there is significant attraction and repulsion between the base facets (panel b). Here, we find that the free energy is oscillating with the distance between the facets.

We can clearly attribute the oscillation in the free energy to solvation forces. In Figure 7.3d, we show heatmaps of the solvent and ligand densities around a single nanoplatelet. The solvent restructures at the ligand-solvent interface and solvent layers are visible. The solvent restructuring increases the free energy of the solvent, compared to the bulk solvent. As two nanoplatelets approach each other, the solvent layering changes, causing the oscillation in the free energy. At the free energy minima, we find an integer number of solvent layers between the nanoplatelets (Figure 7.3e), and no solvent layer at the first minimum. At the first minimum, there are just a few solvent molecules in the soft ligand shell.

For a closer look, we create one-dimensional plots of the ligand and solvent densities away from the base facet. As depicted in the inset of Figure 7.4, we average the densities at each distance in z direction over the whole facet in each xy-plane, and over 6200 snapshots from a trajectory of 1 µs.

In Figure 7.4, we compare the ligand and solvent densities at the first, and second free energy minimum. Shown are the averaged densities away from the base facets. We can divide the densities into two regions. The densities away from the base facets, which are oriented towards the solvent, do not change at the transition between the second and the first minimum. The changes in the densities that cause the appearance of solvation forces take place between the nanoplatelets. We find that the amplitude of the density ligand peaks slightly increases in the first free energy minimum, compared to the second minimum. We hypothesize that the amplitude of the ligand density peaks increases due to the decrease in available volume for the ligand beads. The increased confinement of the ligand beads reduces the entropy of the ligands. Therefore, this effect will slightly increase the free energy. However, the ligand density is higher than the solvent density. Therefore, we expect that the van der Waals ligand-ligand attraction contribute to the reduction of the free energy in the transition from 2nd minimum to the 1st minimum. In the second free energy minimum, we find a strong peak of the solvent density between the ligand shells. This peak disappears in the first minimum. The corresponding number of solvent molecules are no longer confined between the nanoplatelets, and can freely orient themselves and move in the bulk solvent. This change, increases the entropy of the solvent, and decreases the free energy of the nanoplatelet pair interaction. Since these effects are coupled, they cannot be cleanly separated from each other.

We assume that the solvent layering, and therefore the oscillations in the free energy, are most pronounced for the face-to-face approach of two facets. However, the solvation forces also depend on the relative orientation of the facets. To illustrate this, we calculate the free energy curve for a lateral shift of two nanoplatelets (Figure 7.3c). Thereby, we fix the face-to-face distance between the nanoplatelets to the first minimum from Figure 7.3b (5.11 nm), and vary the side shift, as depicted in the snapshot of Figure 7.3c.

For the side shift of two nanoplatelets, we find no barriers in the free energy curve (Figure 7.3c). The solvent forms no significant layers on this path, which would cause a barrier by solvation forces. However, there is still an attraction between the facets, as the area of the ligand-solvent interface is reduced. We should note that there will be a contribution due to the reduction of the rotational entropy of the nanoplatelets, which we do not calculate here.

These results for the pair interaction explain the observed behavior of the nanoplatelets in the previous subsection, and the stack formation of CdSe nanoplatelets in general. The solvation forces provide the crucial attraction between the nanoplatelets. The attraction ensures that the stacks with the larger nanoplatelets are stable. In Subsection 7.2.6, we will compare how the facet size affects the interaction. We point out in advance that the attraction scales with the facet area, which explains that stacks with smaller nanoplatelets

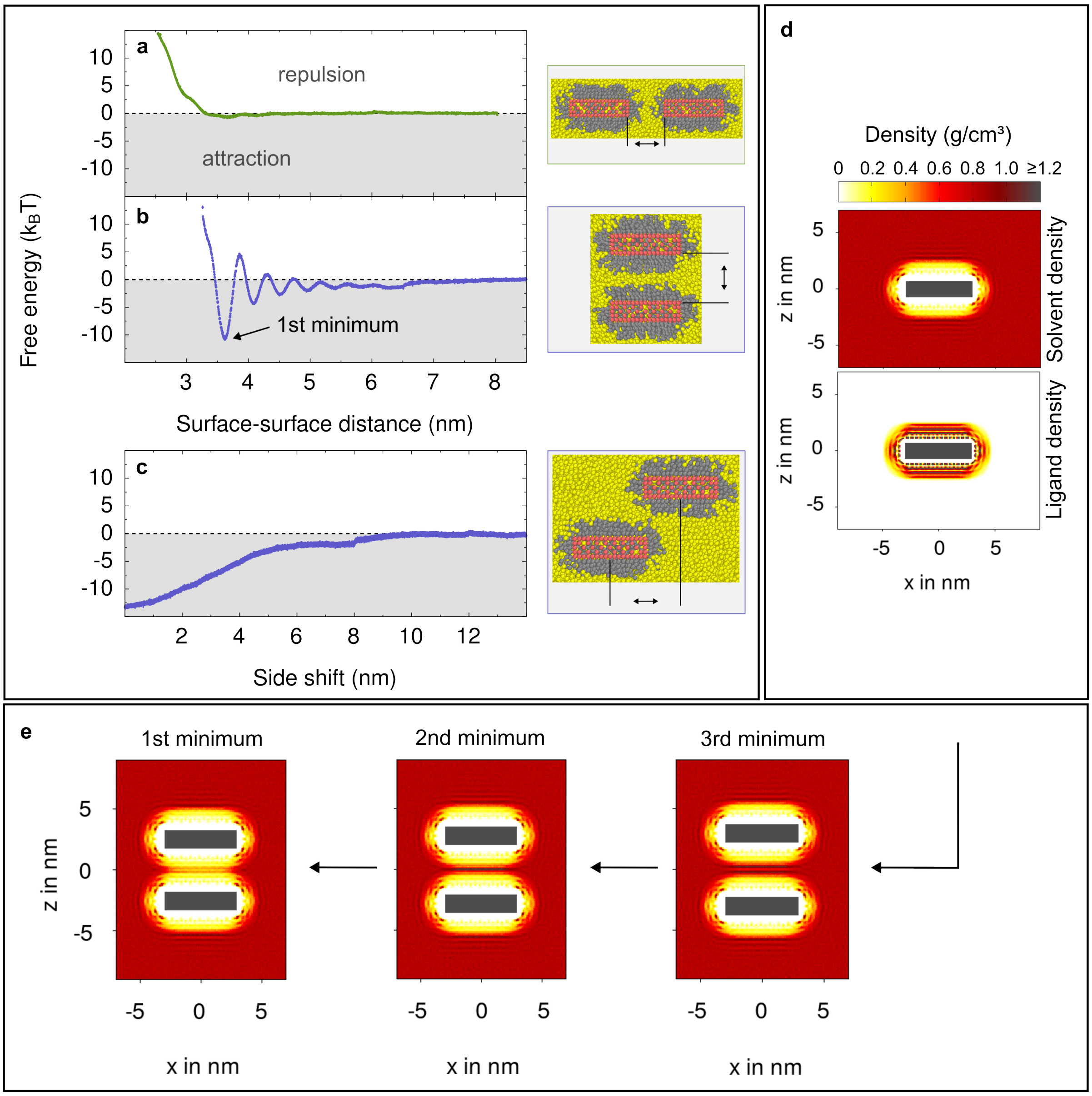

Figure 7.3: Interaction mechanism [96]. **Panel a-c** show free energy curves describing the approach/separation of two nanoplatelets in different orientations. **Panel a** shows the approach/separation by the side facets, and **panel b** an approach/separation by the base facets. In **panel c**, the face-to-face distance between the nanoplatelets is kept constant, while the nanoplatelets approach/separate via lateral displacement. The ligand and solvent densities around a single nanoplatelet are shown in **panel d**. For the base facet-to-base facet approach, the solvent density around the nanoplatelets at the first three minima are depicted in **panel e**. In Figure A.10, we present a larger version of the heatmap of the 3rd minimum.

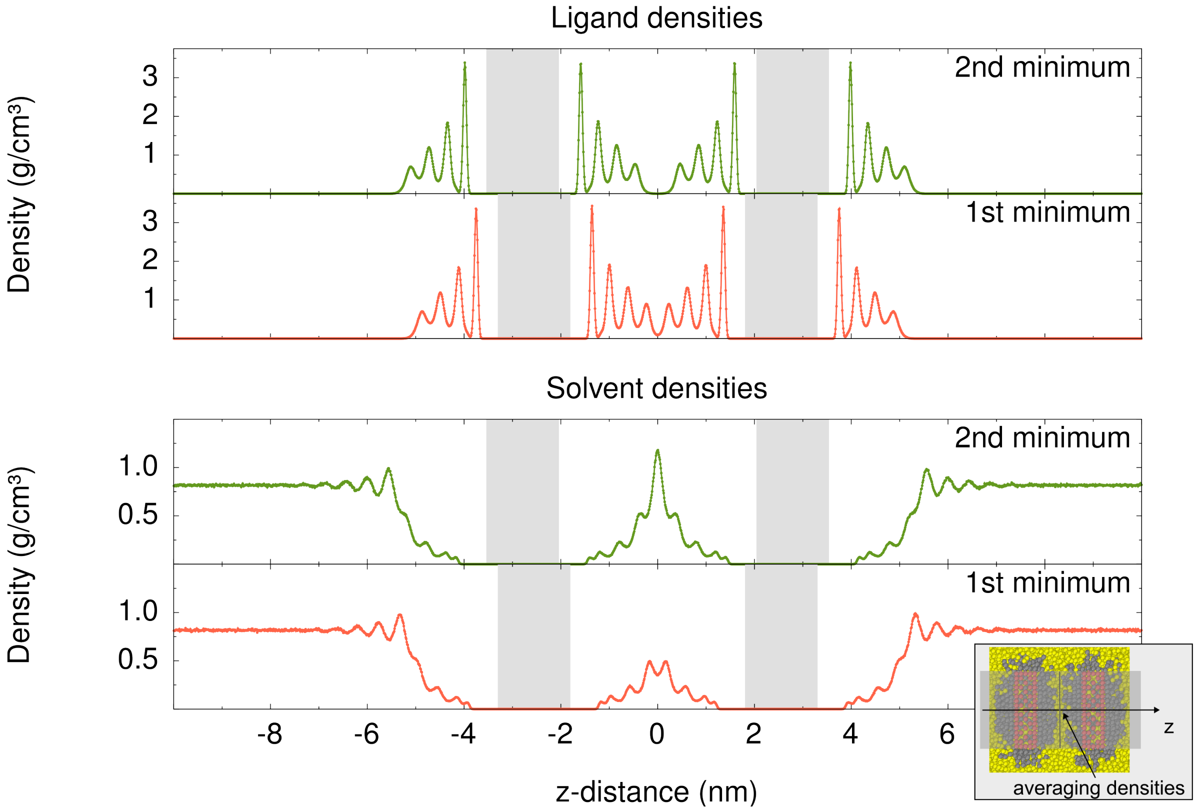

Figure 7.4: Comparison of the ligand and solvent densities at the first and the second minimum of the base facet-to-base facet interaction. As depicted in the inset, the densities at each distance in z-direction are averaged over the whole base facet area in the corresponding xy-plane, and are time averaged. For clarity, the data points are connected with straight lines. The positions of the nanoplatelets are marked with gray boxes.

are not stable. Furthermore, the free energy barriers prevent an immediate self-assembly of CdSe nanoplatelets when they come close. This explains why we do not observe self-assembling within our limited simulation time (ns to µs). Moreover, this explains why a dispersion of CdSe nanoplatelets in n-alkane solvent is in general metastable. As quantified by Jana *et al.*, the precipitation time depends on the concentration, and varies between hours, days, and months [45]. As in the experiments, we expect that we would observe self-assembling in much longer simulations.

7.2.3 Influence of the ligand shell, and solvent orientation

We examine the orientation of the solvent molecules between the nanoplatelets. In this context, it is useful to compare nanoplatelets without and with a ligand shell. Therefore, we combine these two aspects here.

We calculate the free energy curve for the face-to-face approach of two nanoplatelets without a ligand shell. The bare nanoplatelets consist only out of the surface beads.

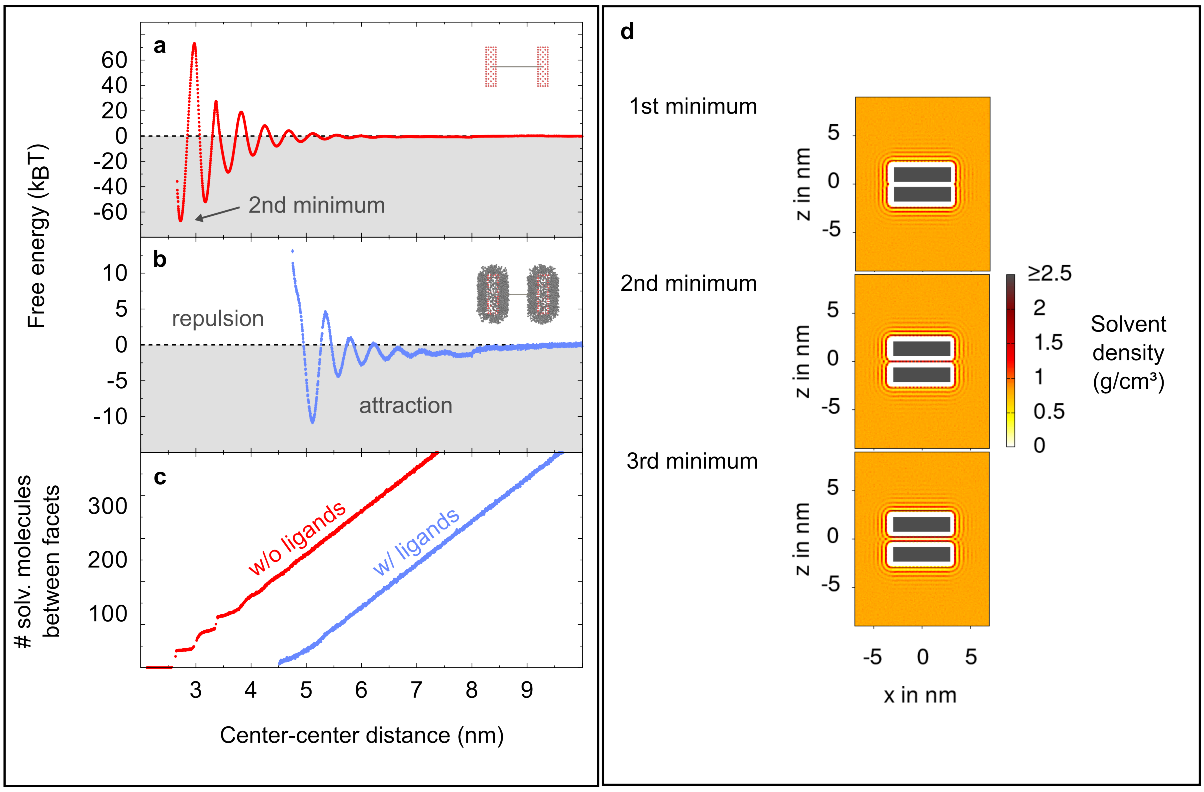

Figure 7.5: Effect of a ligand shell [96]. **Panel a** displays the free energy curve for the base facet-to-base facet interaction between two nanoplatelets without a ligand shell. For comparison, the free energy curve for the interaction with a ligand shell from Figure 7.2.2b is shown again in **panel b**. Note that the scale of the ordinate axis is different in **a** and **b**. In **panel c**, we plot the number of solvent molecules between the base facets for both calculations. Heatmaps of the solvent density around the nanoplatelets without a ligand shell are shown in **panel d**.

Thereby, the interaction between the surface and solvent beads is drastically more repulsive than between the solvent beads among themselves. Additionally, the surface is drastically harder, as the surface beads do not move independently. A side effect of the hard, flat, parallel oriented facet surfaces is that it is difficult to sample the transition between the first and the second minimum properly. Therefore, we do not include the 1st minimum in the free energy calculation, which lies at a distance of 2.14 nm. Therefore, the free energy curve in Figure 7.5a starts at its 2nd minimum. For comparison, we show again the free energy curve for the face-to-face approach of nanoplatelets with a ligand shell from the previous subsection (Figure 7.5b). In Figure 7.5c, we compare the number of solvent between the base facets of the nanoplatelets in both systems at different distances. Additionally, we present solvent density heatmaps of the system without a ligand shell for the first free energy minima in Figure 7.5d.

In the bare setup, the solvent restructuring at the interface is more pronounced (Figure 7.5d), and the amplitude of the free energy oscillation is larger (Figure 7.5a). Another aspect that stands out is that the curve without ligand shell oscillates "symmetrically" around the zero line, while in the system with ligand shell, there is a dip at 8 nm. We assume that this is due to the softer surface. The penalty at the transition between two minima is lower because the ligand shell can give way. This can be visualized by plotting the number of solvent molecules between the facets (Figure 7.5c). Here, steps appear in the bare setup, while they disappear in the setup with a ligand shell.

There are also large differences in the orientation of the solvent molecules in the two setups. To quantify the solvent orientation, we calculate the nematic order parameter as a function of the distance d between the nanoplatelets:

$$S(d) = \left\langle \frac{3\cos^2(\theta) - 1}{2} \right\rangle_{\text{solvent molecules}} , \tag{7.1}$$

where θ is the angle between a bond of a solvent molecule and the normal of the facet area (z-axis), and $\langle \dots \rangle$ indicates an ensemble average over all the solvent molecules between the base facets of two nanoplatelets. $S = 1$ would indicate that all solvent bonds are orientated perpendicular to the base facet surface, $S = 0$ a random orientation, and $S = -0.5$ a parallel orientation. We calculate the nematic order parameter for the bare setup and the setup with a ligand shell. Thereby, we calculate the average center-center distance d in each window from the umbrella sampling, as well as the average nematic order parameter $S(d)$. For computational speed and memory availability, we only save all particle data every 4 ns during a simulation. Therefore, we average over ten snapshots from a period of 40 ns per window. In Figure 7.6, we present the resulting curves.

In the bare setup, the orientation strongly depends on the distance between the nanoplatelets. We find that S oscillates in a similar fashion as the free energy curve. Thereby, the amplitudes of the nematic order parameter decay with the nanoplatelet distance. The reason for the oscillation becomes clear by comparison with the free energy curve and the solvent layering. Around the second free energy minimum, there is one layer of solvent molecules between the two facets. Therefore, the solvent molecules are forced to align themselves parallel to the surface ($S \longrightarrow -0.5$). Around the third free energy minimum, there are two layers of solvent molecules between the facets. Here, the solvent molecules have greater freedom. The two beads of the solvent molecules can arrange themselves in either one or in both layers. Some solvent molecules will align themselves parallel to the facet surfaces, and others perpendicular (see snapshot in Figure 7.6b). In the latter case, one bead will be in one layer and the other bead in the other layer. Of course, there are also configurations in between. The increased freedom reduces the nematic order.

As can be seen from the marked free energy minima in Figure 7.6a, there is an offset between the free energy minima and the minima of the nematic order parameter. A possible explanation is the rotational entropy of the solvent molecules. A reduction in the rotational freedom ($S \longrightarrow -0.5$) leads to a reduction of the rotational entropy of the solvent molecules, and an increase in the free energy. Therefore, the minima of the free energy are not found in the configuration that has the strongest alignment.

Furthermore, there is a peak close to a separation of 3 nm that indicates a preference for a solvent orientation perpendicular to the nanoplatelet facet surfaces. We assume that

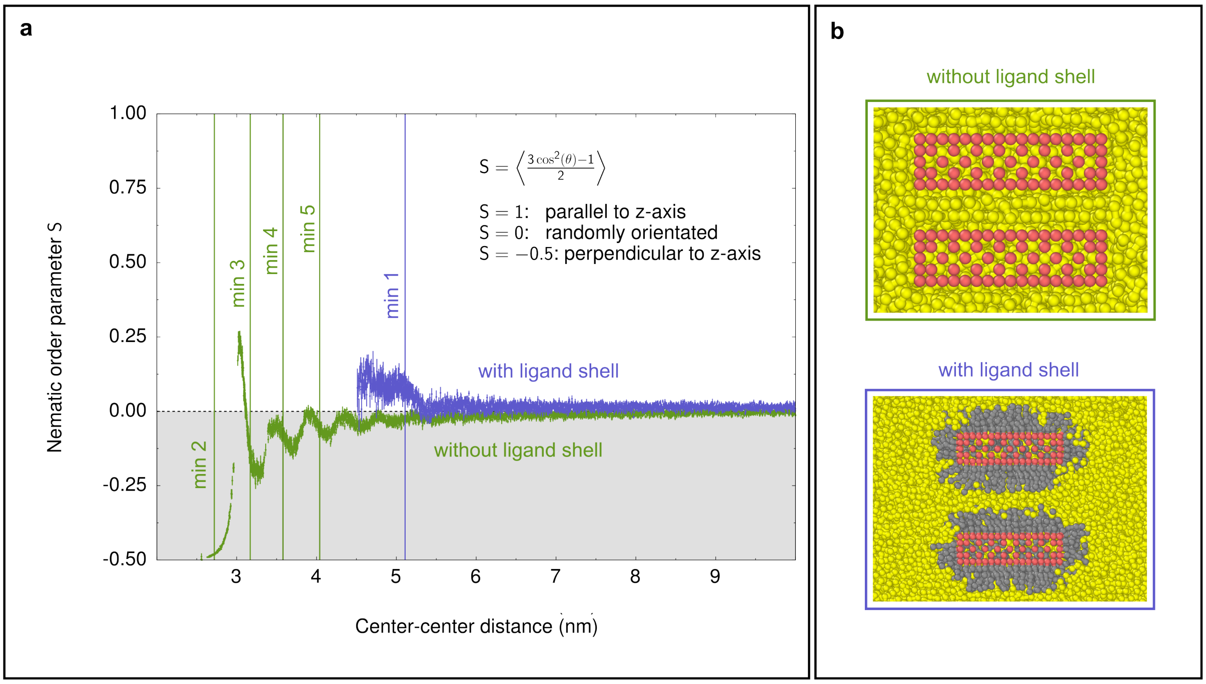

Figure 7.6: Solvent orientation [96]. **Panel a** shows the calculated nematic order parameters for the solvent molecules between the nanoplatelets without and with a ligand shell. The nanoplatelets have a base facet area of 35.6 nm, and a thickness of 1.5 nm. The positions of selected free energy minima from Figure 7.5a, b are marked. **Panel b** displays cross-sectional snapshots from the third free energy minima.

this peak is a result of some solvent molecules being restricted in their motion by the surface beads.

In the setup with a ligand shell, the behavior changes completely. As indicated by the nematic order parameter, the solvent molecules are mostly randomly orientated. Only around the marked first free energy minimum, the solvent molecules slightly tend to align themselves perpendicular to the facets. However, this is due to a few solvent molecules remaining between the nanoplatelets even though the two ligand shells are already in contact (see Figure 7.5c, Figure 7.3e, and Figure 7.4). We assume that they slightly tend to align themselves to the orientation of the ligands.

In summary, the solvent restructuring is more pronounced at a bare surface, and weakens with a ligand shell. This is reflected in the solvent orientation, which is significant in the bare setup, and vanishes in the setup with the ligand shell. Furthermore, the free energy oscillation is less pronounced with a ligand shell.

7.2.4 Ligand grafting density

The properties of the ligand shell are also important for the appearance of solvation forces. In Chapter 6, we have found that the solvent restructuring is more pronounced at higher ligand grafting densities. Here, we consider the effect of the ligand grafting density on the interaction of finite nanoplatelets.

As discussed in Section 5.3, the ligand grafting density in the MARTINI setup has to be chosen wisely. We vary the ligand grafting density between values that we consider reasonable: 2.7, 3.6, and 4.2 ligands/nm^2. In our setup, we use the surface beads of the nanoplatelet as ligand grafting points. We vary the ligand grafting density by changing the lattice constant of the surface beads. Thereby, we keep the base facet area constant at 27.3 nm^2. A side effect is that the thickness of the nanoplatelet cores changes (see Table 7.1, and snapshots in Figure 7.8b).

First, we consider the averaged ligand and solvent densities at different distances in z-direction from the base facets of single nanoplatelets (Figure 7.7). Here, we find similar trends as in the TraPPE-UA setups (Figure 6.3). As the ligand grafting density decreases, the thickness of the ligand shell decreases slightly, while the solvent restructuring decreases strongly and solvent can penetrate the ligand shell more easily.

The changes are clearly visible in the snapshots in Figure 7.8b. At a ligand grafting density of 4.2 ligands/nm^2, the ligand shell is very dense, and forms a hard shell around the nanoplatelets. We can see solvent ordering directly in the snapshot. On the other hand, at a ligand grafting density of 2.7 ligands/nm^2, the ligand shell becomes fluffy and soft. The solvent can easily penetrate into the ligand shell. Here, the solvent layering is strongly reduced.

The changes in densities are reflected in the nanoplatelet pair interaction. In Figure 7.8a, we compare the calculated free energy curves for the facet-to-face approach. Essentially, the ligand grafting density influences the free energy curves in three ways: by a change in the repulsion at close distances, by a shift in the position of the extrema, and by a change in the interaction strength.

All three effects can be attributed to changes in the densities. Denser ligand brushes are harder, less flexible, and thus lead to a stronger repulsion. For smaller ligand grafting densities, the positions of the extrema shift to smaller distances, as a softer ligand shell is thinner, and the interdigitation increases slightly. Finally, as the solvent restructuring decreases on a softer ligand shell, the amplitude of the free energy oscillation does the same. For a too small ligand grafting density, the free energy curve flattens out. Except from that, the shape of the free energy curve does not change qualitatively.

ligand grafting density (ligands / nm^2)	lattice constant (nm)	thickness (nm)
4.2	0.65	1.3
3.6	0.75	1.5
2.7	0.87	1.7

Table 7.1: Connection between ligand grafting density, lattice constant and nanoplatelet thickness

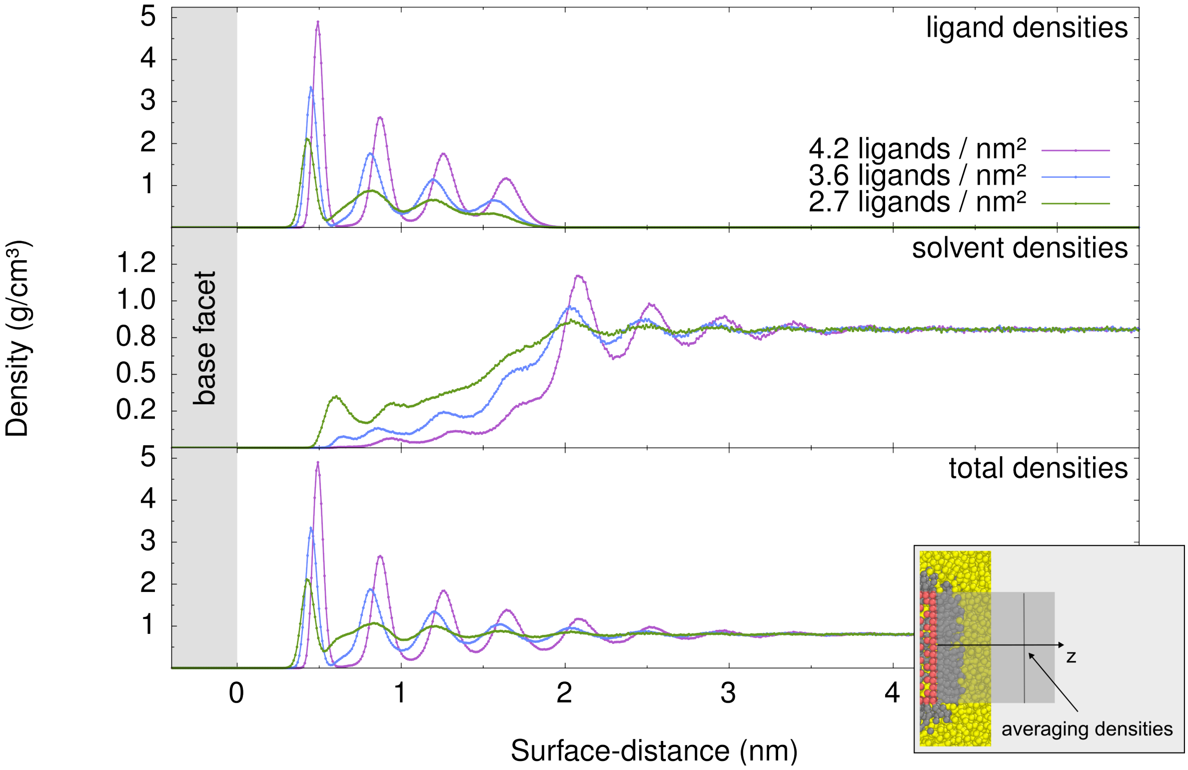

Figure 7.7: Effect of the ligand grafting density on the densities away from the base facet of a single nanoplatelet. The top panel shows the ligand, the middle panel the solvent, and the bottom panel the total densities. As depicted in the inset, the densities at each distance in z-direction are averaged over the whole base facet area in the corresponding xy-plane, and are time averaged. For clarity, the data points are connected with straight lines.

All three discussed ligand grafting densities are reasonable choices to describe the ligand shell on finite nanoplatelets. As discussed in Section 5.3, we use 3.6 ligands/nm^2 in all further simulations with the MARTINI setup.

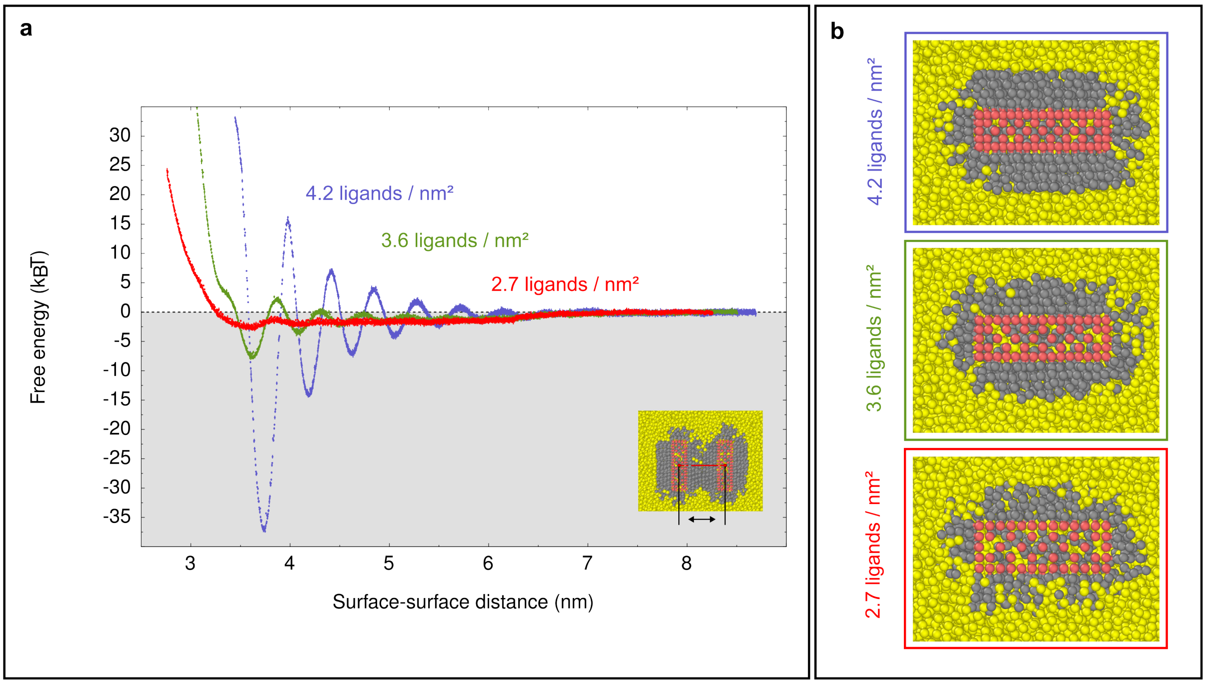

Figure 7.8: Effect of the ligand grafting density [96]. **Panel a** shows free energy curves of the base facet to base facet interaction (error bars included). The base facet area is in all three cases 27.3 nm^2, while the platelet thickness changes depending on the ligand grafting density / lattice constant (see Table 7.1). **Panel b** shows cross-sectional snapshots of the nanoplatelets. CdSe surface beads are shown in red, ligand beads in gray, and solvent beads in yellow.

7.2.5 Ligand length

Jana *et al.* have found that the steric stability of CdSe nanoplatelets increases with the ligand length [45]. We infer that the attraction between the nanoplatelets is reducing with the ligand length. To verify this, we compare the interaction between nanoplatelets with different ligand lengths. We compare ligands with three, four, and five C1 MARTINI beads. In all other simulations of this chapter with the MARTINI setup, We use four MARTINI C1 beads to describe the ligands. In Figure 7.9a, we show calculated free energy curves for the face-to-face approach of the nanoplatelets. Since the thickness of the ligand shell changes with the length of the ligands, the distances at which the extrema are located shift. Thereby, the separations between the extrema do not change. Moreover, the amplitudes of the free energy oscillation decrease with the ligand length.

We compare these findings with the averaged ligand and solvent densities at different distances from a base facet of single nanoplatelets. As depicted in the inset of Figure 7.10, we average the densities at each distance in z-direction over the whole base facet area in the corresponding xy-plane, and time average them.

As shown in Figure 7.10, we find that the ligand densities decrease with the distance to the base facets. Thereby, the curves are very similar until they each break off when the

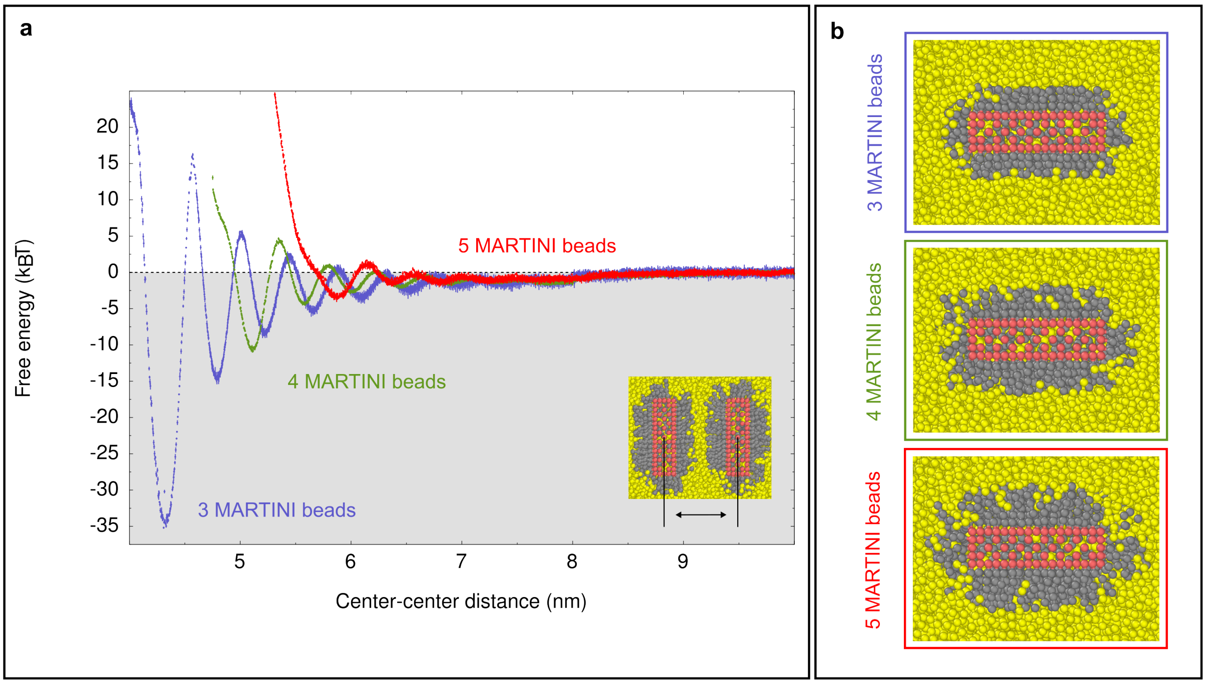

Figure 7.9: Effect of the ligand length on the face-to-face interaction [96]. The ligand length is varied between three and five MARTINI C1 beads. **Panel a** shows calculated free energy curves, while **panel b** shows cross-sectional snapshots of the nanoplatelets with different ligand length. CdSe surface beads are shown in red, ligand beads in gray, and solvent beads in yellow.

ligand length is reached. Hence, the ligand packing density at the ligand-solvent interface becomes less pronounced with the ligand length. The solvent densities reflect this. For longer ligands, we find that the solvent reaches deeper into the ligand shell. Moreover, the density oscillations in the solvent decreases with the ligand length. In Figure 7.9b, we show a snapshot of each setup. Here, the changes are clearly visible. The ligand shell in the setup with three ligand beads is very dense. The interface to the solvent is well-defined, and the solvent layering is visible in the snapshot. In contrast, the interface of the ligand shell in the setup with five ligand beads is uneven and looks fluffy. It is obvious that the solvent layer formation at such an interface is reduced.

In summary, we find that the solvent restructuring is less pronounced with longer ligands. Therefore, the solvation forces become weaker. This result is consistent with the observation of Jana *et al.* that the steric stability of CdSe nanoplatelets decreases with the ligand length [45].

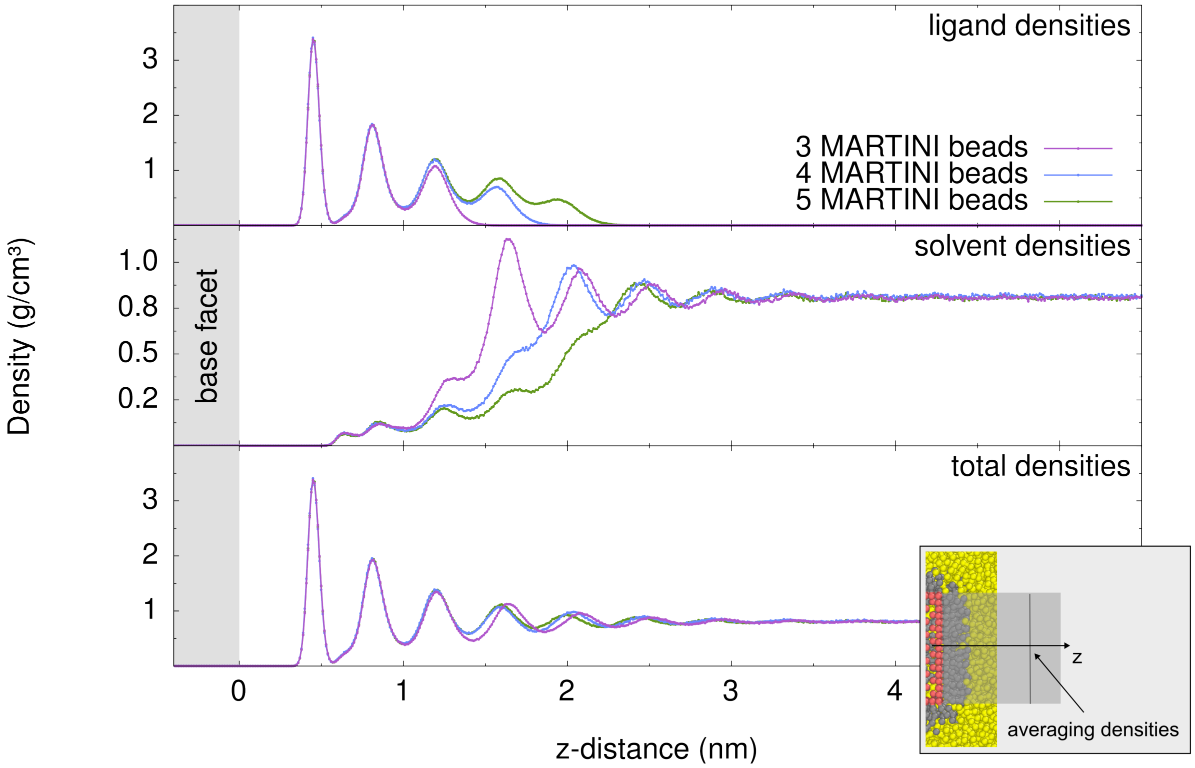

Figure 7.10: Effect of the ligand length on the solvent restructuring on the base facet of single nanoplatelets. The top panel shows the ligand, the middle panel the solvent, and the bottom panel the total densities. As depicted in the inset, the densities at each distance in z-direction are averaged over the whole base facet area in the corresponding xy-plane, and are time averaged. For clarity, the data points are connected with straight lines.

7.2.6 Facet area

Due to the computational cost, it is common to concentrate on smaller model systems when simulating colloidal (nano-) particles [25]. So do we. We consider CdSe nanoplatelets with base facet areas up to 55.7 nm^2, while they can be larger in experiments. For example, Jana *et al.* have used CdSe nanoplatelets with a base facet area of around 225 nm^2 [45], while Momper *et al.* have used base facet areas of around 130 nm^2 [37]. Moreover, in the experiments of our co-workers, which we report in Chapter 8, the base facet areas are varied between 25 nm^2, and 400 nm^2. For the evaluation of our results, it is therefore important to discuss the facet area. Especially, we have to discuss, to what extent our results can be extrapolated to nanoplatelets with larger facets.

We calculate free energy curves for the face-to-face interaction between nanoplatelets with base facet areas between 2.2 nm^2 and 55.7 nm^2, with a fixed nanoplatelet thickness of 1.5 nm. In Figure 7.11, we show the calculated free energy curves, together with cross-sectional snapshots. As shown in the corresponding snapshot, the nanoplatelet with

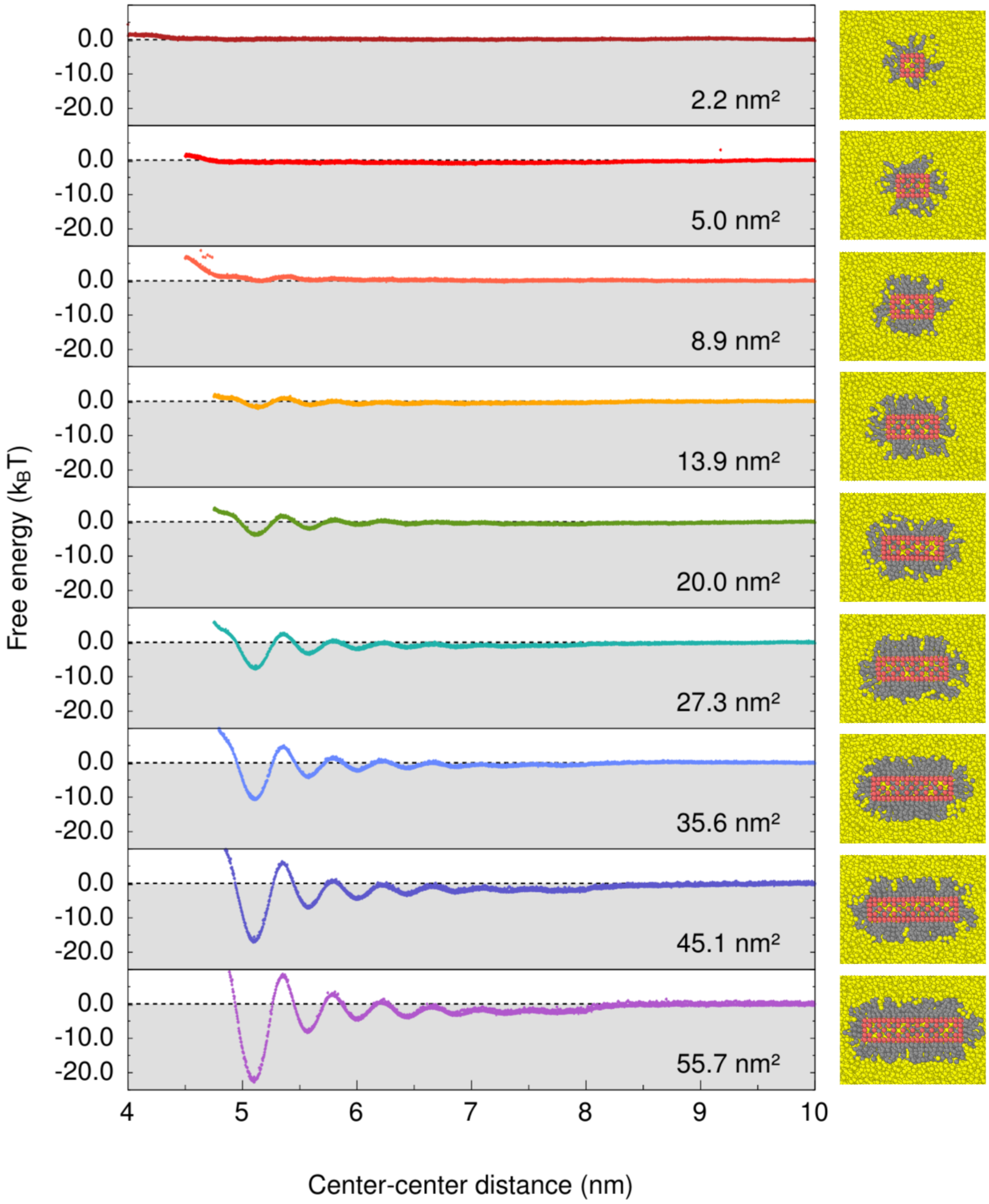

Figure 7.11: Dependence of the face-to-face interaction on the base facet area [96]. Shown are free energy curves for nanoplatelets with the same thickness, but different base facet areas (error bars included). To the right of each curve, a cross-sectional snapshot of a single nanoplatelet with the corresponding base facet area is shown. Surface beads are red, ligand beads gray, and solvent beads yellow.

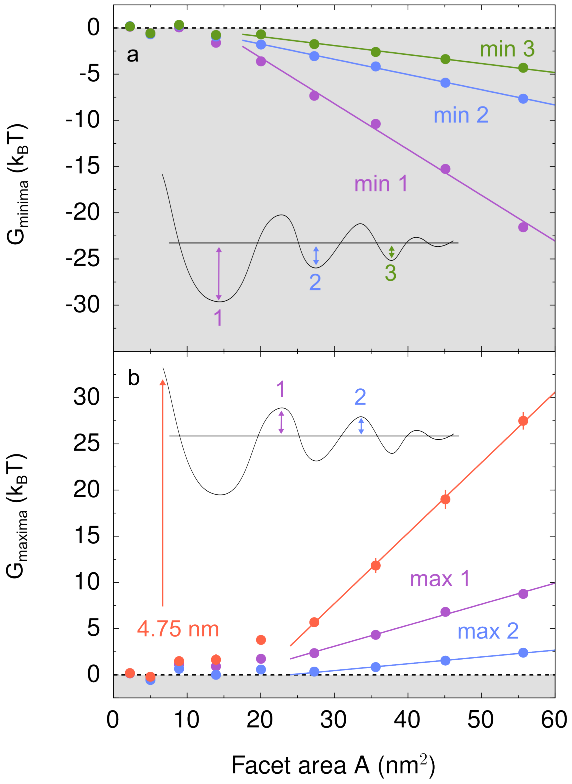

Figure 7.12: The attraction and repulsion between nanoplatelets depends on the facet area [96]. Free energy values relative to the free energy at infinite separations of selected extrema are plotted, see insets. In **panel a**, the dependence of the free energy values of the first three minima are shown. Linear fits are attached to points at facet areas equal to and larger than 20 nm^2. In **panel b**, the height of the free energy maxima, as well as the free energy at a distance of 4.75 nm, are displayed. Here, linear fits are attached to points at facet areas equal to and larger 27.3 nm^2.

2.2 nm^2 is essentially a small cube with a fluffy ligand shell. The ligand shell is similar to that of a small spherical particle. With increasing facet area the particles form into proper nanoplatelets, with extended base facet areas, and corresponding ligand shells. The change of the base facet area significantly influences the free energy curves. For the two smallest base facet areas (2.2 nm^2, and 5.0 nm^2), the free energy curves flattening out, and there is no significant attraction between the nanoplatelets. From around 8.9 nm^2 onwards, all free energy curves show qualitatively the same shape. Thereby, the positions of the extrema change only slightly, since the thickness of the ligand shell changes only little. However, the strength of the interaction continues to increase with the facet area.

To investigate this further, we plot the free energy values of the minima and maxima. In addition, we plot the free energy at a distance of 4.75 nm. At this distance, there is already a significant repulsion between the ligand brushes (Figure 7.12). We find that the magnitude of the attraction at the minima, as well as the magnitude of the repulsion at

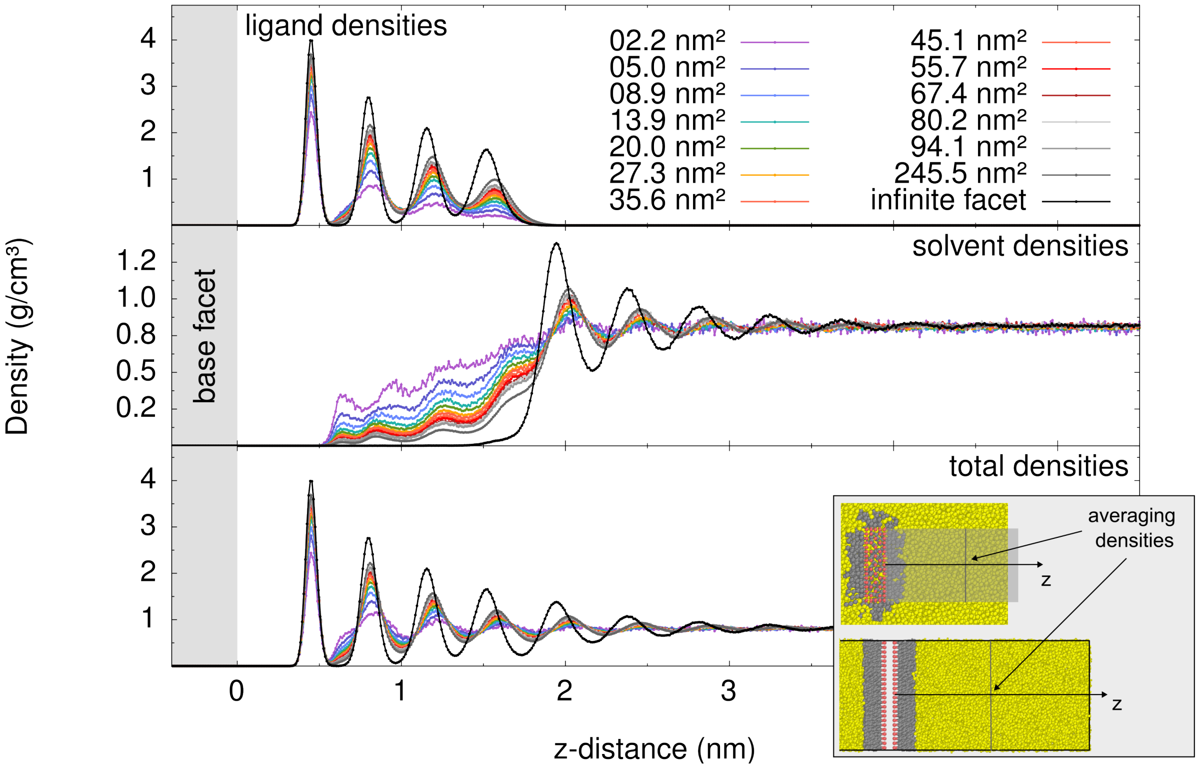

Figure 7.13: Effect of the facet area on the solvent restructuring. The top panel shows the ligand, the middle panel the solvent, and the bottom panel the total densities. As depicted in the inset, the densities at each distance in z-direction are averaged over the whole base facet area in the corresponding xy-plane, and are time averaged. For clarity, the data points are connected with straight lines.

the maxima, increase with the facet area. Thereby, the slope depends on the separation at which an extremum is located. For the minima and maxima at smaller nanoplatelet separations, the slope is steeper than for the minima and maxima at larger separations. Also, the magnitude of the repulsion at 4.75 nm increases with the facet area. We observe two different regimes. With smaller facet areas, the free energy values are small, and there is no clear trend. However, with larger facet areas, we observe linear slopes. The linear behavior starts at around 20 nm^2 for the minima, and at around 27.3 nm^2 for the maxima and the free energy value at 4.75 nm.

The difference between the two regimes can again be explained by the ligand densities, and the solvent restructuring at the ligand-solvent interface. In Figure 7.13, we plot the ligand and solvent densities away from the base facets of single nanoplatelets. Thereby, we average the densities over the whole facet area in the corresponding xy-plane, and time average (see inset of Figure 7.13). We find that both the ligand density oscillation and the solvent density oscillation become more pronounced as the facet area increases. Furthermore, with increasing facet area, less solvent stays within the ligand shell. However, the changes are clearly greater between the smaller facets.

As in the simulations with the TraPPE-UA setup in Section 6.2.1, we attribute the changes to the effect of the facet edges on the ligand ordering. The ligands near the edges have more space. Therefore, the ligands will arrange differently on a small facet than on a large or infinite facet, which directly affects the ligand density, and the solvent restructuring.

At the nanoplatelets with the smallest facet areas, the edges determine the ligand density. The ligand shell is soft, and solvent layering is very weak. Accordingly, the free energy curves for the interaction between the nanoplatelets with $2.2\,\mathrm{nm}^2$, and $5.0\,\mathrm{nm}^2$ facet area is flattening out, as solvation forces are tiny.

However, with increasing facet area, the ligand density in the center of the facets is increasing. The ligand shell gets harder, and solvent layering increases. Therefore, with increasing facet area, the solvation forces are getting stronger. Starting from $8.9\,\mathrm{nm}^2$, we find the typical oscillation in the free energy curves.

Finally, the changes in the densities for the facet areas between $20\,\mathrm{nm}^2/\ 27\,\mathrm{nm}^2$ and $55.7\,\mathrm{nm}^2$ are small. The small changes explain why the free energies appear to scale linearly with the facet area A:

$$G_{\mathrm{extrema}}^{\mathrm{small}\ \Delta A} \approx c\,A + d, \tag{7.2}$$

where c, and d are constants.

To extrapolate our results, we also consider the densities away from the base facets of single nanoplatelets with larger facet areas ($67.4\,\mathrm{nm}$, $80.2\,\mathrm{nm}$, $94.1\,\mathrm{nm}$, and $245.5\,\mathrm{nm}$). We do not calculate the free energy curves for these facet areas because of the computational costs. Furthermore, we add the density curves from the infinite setup to Figure 7.13 (see Section A.1.1). We find that the trends in the densities continue. As we increase the facet area, the amplitudes of the ligand density oscillation become larger, the amount of solvent in the ligand shell decreases, and the solvent restructuring becomes more pronounced. The density curves slowly converge to the curves of the infinite setup.

Again, the changes in the densities are tiny for small facet area changes ΔA, for example between $80.2\,\mathrm{nm}^2$ and $94.1\,\mathrm{nm}^2$. However, the changes in the densities are large for large facet area changes ΔA, for example between $27.3\,\mathrm{nm}^2$ and $245.5\,\mathrm{nm}^2$.

Therefore, we expect the amplitudes of the free energy oscillations to grow faster than linearly for large facet area changes ΔA:

$$G_{\mathrm{extrema}}^{\mathrm{large}\ \Delta A} \geq c\,A + d. \tag{7.3}$$

We assume that our results for small nanoplatelets are generally transferable to larger ones, since the essential features in the ligand and solvent densities, as well as the features of the free energy curves, do not change. Even though, we expect stronger solvation forces between larger facets.

7.2.7 Nanoplatelet thickness

In the face-to-face interaction of CdSe nanoplatelets, solvation forces derive from the solvent restructuring between the facets that depends on the separation. Therefore, it seems reasonable to assume that the interaction is independent of the thickness of the nanoplatelets.

To verify this, we compare three nanoplatelets with different thicknesses (1.5 nm, 2.2 nm, and 3.0 nm). In Figure 7.14, we show the free energy curves. It turns out that the overall attraction increases with the thickness. However, a closer look reveals that the first part of the free energy curves are identical, and just shifted. The changes in the shape of the curves appear between ∼4.75 nm distance and ∼8 nm. As discussed in Subsection 7.2.2, the shape of the free energy curve depends on the approach pathway. Therefore, we can split the problem into two parts: the question of why the attraction in the first minimum increases, and the question of why the shape of the free energy curves changes.

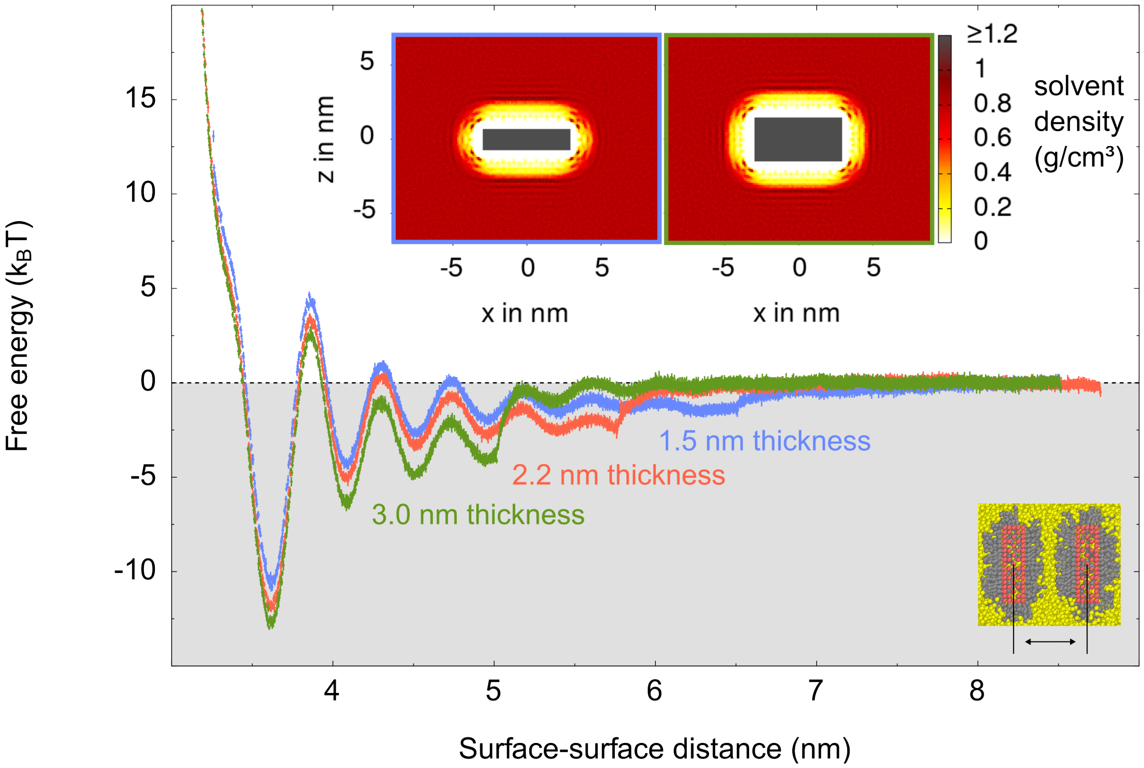

Figure 7.14: Effect of nanoplatelet thickness. Shown are free energy curves of the face-to-face interaction (error bars included) [96]. The platelets have 35.6 nm^2 base facet area. The thickness is varied between 1.5 nm, 2.2 nm, and 3.0 nm. The attraction between the thicker nanoplatelets increases. Also shown are heatmaps of the solvent density around single nanoplatelets with 1.5 nm (left), and 3.0 nm thickness (right). The main changes in the solvent density appear away from the side facets and the edges.

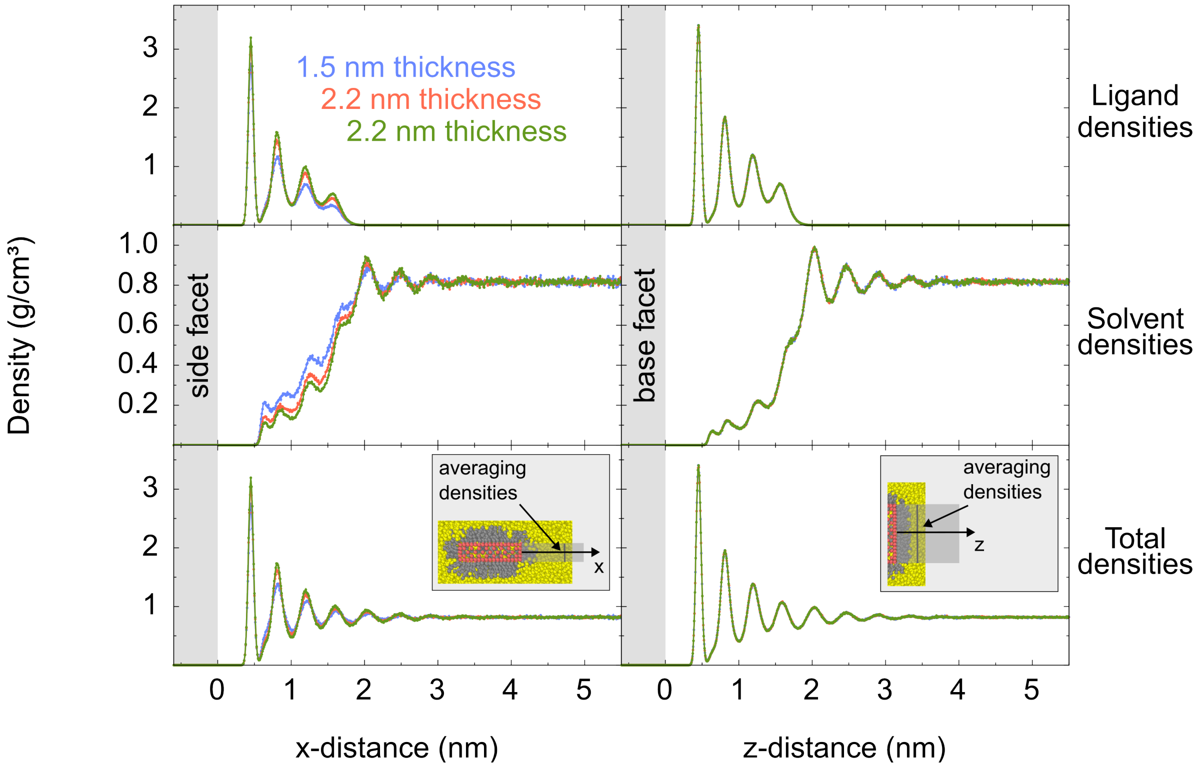

Figure 7.15: Effect of the nanoplatelet thickness on the ligand and solvent densities. The left column shows the densities away from the side facets, while the right column shows the densities away from the base facet. The top panel shows the ligand, the middle panel the solvent, and the bottom panel the total densities. The densities at each distance in x/z-direction are averaged over the whole facet area in the corresponding zy/xy-plane, and are time averaged. For clarity, the data points are connected with straight lines.

The densities provide some insights. We compare the densities away from the side facets and the base facets. In Figure 7.15, we present the densities for single nanoplatelets. In agreement with the previous subsection, we find that the ligand density oscillations at the side facets increase with the thickness. Furthermore, there is less solvent in the ligand shell of the thicker nanoplatelet. Additionally, the solvent layering is more pronounced. However, concerning the base facets, we find no changes in the densities between the two setups.

It gets interesting when we compare how the densities change as two nanoplatelets approach each other. The densities at the side facets are not influenced by the separation, and do not change. In contrast, the densities between the approaching base facets depend on the separation (Figure A.13). Independent of the separation, we find no differences between the two setups in the densities between the base facets.

We conclude that the configuration at the edges between the facets must change with distance, and that this change must be dependent on the system. This is the case because

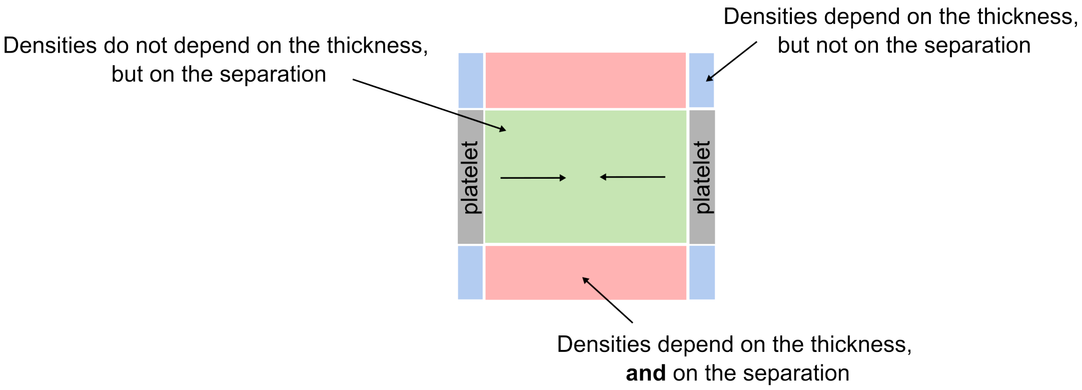

Figure 7.16: Sketch of the different regions around the nanoplatelets. Marked is, if the ligand and solvent densities depend on the nanoplatelet thickness, the facet surface separation, or on both.

the configurations of the ligand and solvent molecules at the edges are confined by the constant configuration at the side facets and the changing configurations at the base facets. We depict the different regions in Figure 7.16. We can assume that the density oscillations at the edges are more pronounced in the setup with thicker nanoplatelets. Therefore, we can also assume that the separation dependent changes in the density oscillations are larger in the setup with thicker nanoplatelets. These results and conclusions explain why the attraction increases with thickness. Larger changes in the density oscillations away from the edges will cause a larger attraction.

We can only address superficially the second question of why the shape of the free energy curves changes. The solvent restructuring away from the edges is different in the two setups. As two nanoplatelets approach, the solvent density oscillations interfere. Since the solvent oscillations are different in the two setups, also the result of the interference is different. We assume that the separation dependent changes in the densities are reflected in the different shapes of the free energy curves.

Finally, we can conclude that the interaction does indeed depend to some extent on the thickness of the nanoplatelets, and in general on the ligand and solvent structure at the edges of interacting facets.

7.2.8 Temperature dependence

The temperature can affect the interaction between nanocrystals in many ways. For example, entropic effects, such as the translational entropy (see following Chapter 8, Equation 8.1), become more prominent with increasing temperature, and energetic barriers become easier to cross. Furthermore, the ordering of the ligand and solvent molecules can change.

Widmer-Cooper *et al.* have shown that the interaction of nanocrystals can depend sensitively on the arrangement of the ligands in the ligand shell [33, 34]. They have found that the ligands of CdS nanorods form bundles at low temperatures. These bundles strengthen the layer formation of the solvent, and thus strengthen the solvation forces. Furthermore, they have found that the bundles dissolve at higher temperatures, and the layer formation of the solvent becomes negligible. Therefore, the interaction between the nanorods becomes purely repulsive.

We have discussed in Section 6.2.5 how the solvent restructuring at the ligand-solvent interface of CdSe nanoplatelets depends on the temperature. The ligand shell of CdSe nanoplatelets is denser than the ligand shell of CdS nanorods. Therefore, ligand bundle formation is of less importance. The dense ligand shell of CdSe nanoplatelets still supports pronounced solvent layering at higher temperatures. This is especially true when we consider the base facets of larger nanoplatelets, since the influence of the edges becomes smaller.

In this section, we consider the face-to-face interaction between CdSe nanoplatelets at different temperatures. The MARTINI model is poorly suited to describe the arrangement of the ligands in the ligand shell due to its low resolution. We therefore divide our consideration of temperature into two parts. In the first part, we will discuss simulations with the MARTINI setup, and in the second part, we will discuss simulations with the TraPPE-UA setup.

7.2.8.1 MARTINI setup

We consider the effect of the temperatures on the face-to-face interaction of CdSe nanoplatelets in the MARTINI setup. In Figure 7.17a, we show the calculated free energy curves.We find that the attraction between the nanoplatelets decreases as the temperature increases. The amplitudes of the free energy oscillation decrease, while the extrema move slightly to larger separations. However, Jana *et al.* have found that the interaction between CdS nanorods becomes repulsive at higher temperatures. In contrast to the result of Jana *et al.*, the effect of the temperature on the interaction of CdSe nanoplatelets is small. Qualitatively, the interaction between the CdSe nanoplatelets does not change.

We find explanations for the small influence of temperature in the arrangement of the ligands and in the densities of the ligands and the solvent. In Figure 7.17b, we show snapshots of one of the nanoplatelets at different temperatures. Here, we do not observe ligand bundling, or any obvious other order-disorder transition. Furthermore, we do not find qualitative changes in the ligand and solvent densities away from the base facets of the nanoplatelets (Figure 7.18). The amplitudes of the ligand density oscillation decrease at

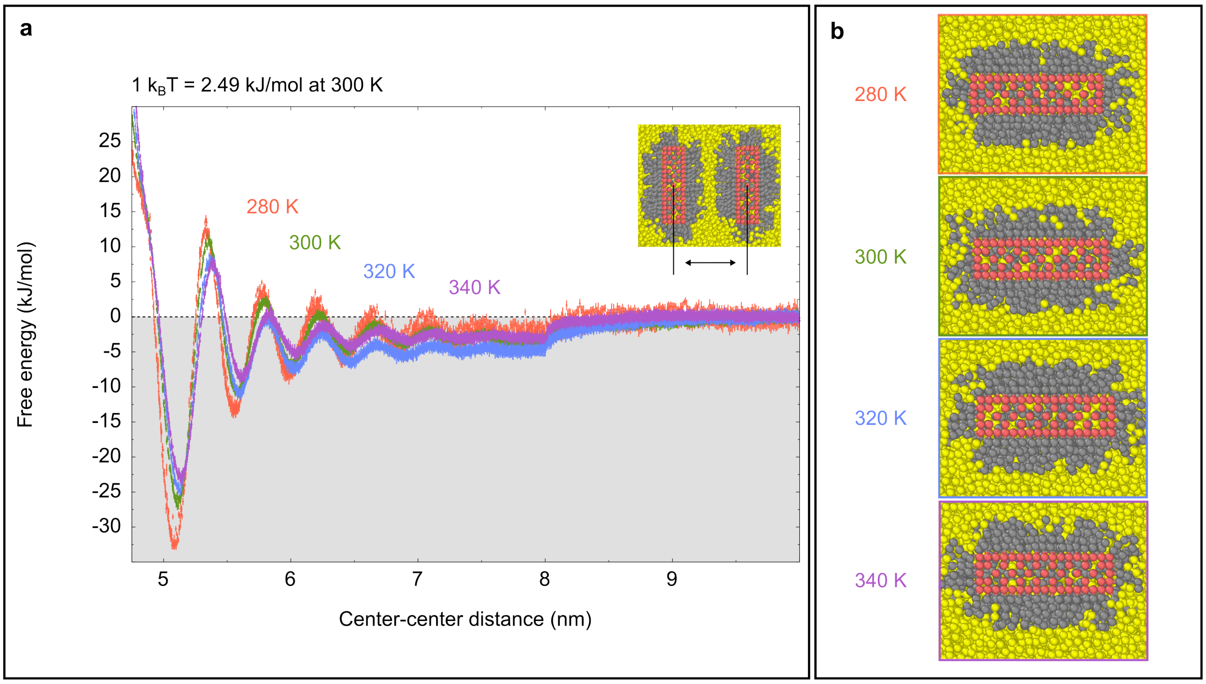

Figure 7.17: Effect of the temperature on the face-to-face interaction in the MARTINI setup. **Panel a**, shows free energy curves for different temperatures. Here, the free energy is given in kJ/mol. In most other figures of this chapter, the free energy is plotted in k_BT ($1\,k_BT$ = 2.49 kJ/mol at 300 K). The free energy oscillations are more pronounced at lower temperatures. **Panel b**, shows cross-sectional snapshots of nanoplatelets at different temperatures.

higher temperatures, the solvent layering becomes less pronounced, and the bulk solvent density becomes larger. However, the characteristics of the curves do not change.

7.2.8.2 TraPPE-UA setup

The TraPPE-UA setup may be better suited to look at the temperature effect. However, the TraPPE-UA force field quadruples the number of beads in the simulation box. To still obtain acceptable simulation durations, we can therefore only treat small nanoplatelets. We use nanoplatelets with 18.1 nm^2 base facet area, 1.2 nm thickness, and short ligands.

The nanoplatelets used in experiments are usually larger. Therefore, we select a configuration that resembles the ligand shell of larger nanoplatelets. We use ligands with a length corresponding to eight carbon atoms, describing octanoic acid ligands (see Figure 3.3). It is one of the ligand types Jana *et al.* have used in their experiments [45]. The length of the octanoic ligands is smaller than the dimensions of the base facets. Accordingly, they form a dense, well-ordered ligand shell on the base facets (see snapshots in Figure 7.19). As in the infinite facet setup in Figure 6.9, we do not observe bundle formation of the ligands on the base facets. However, we find that the ligands on the side facets form bundles at low temperatures. We attribute the absence of bundle formation

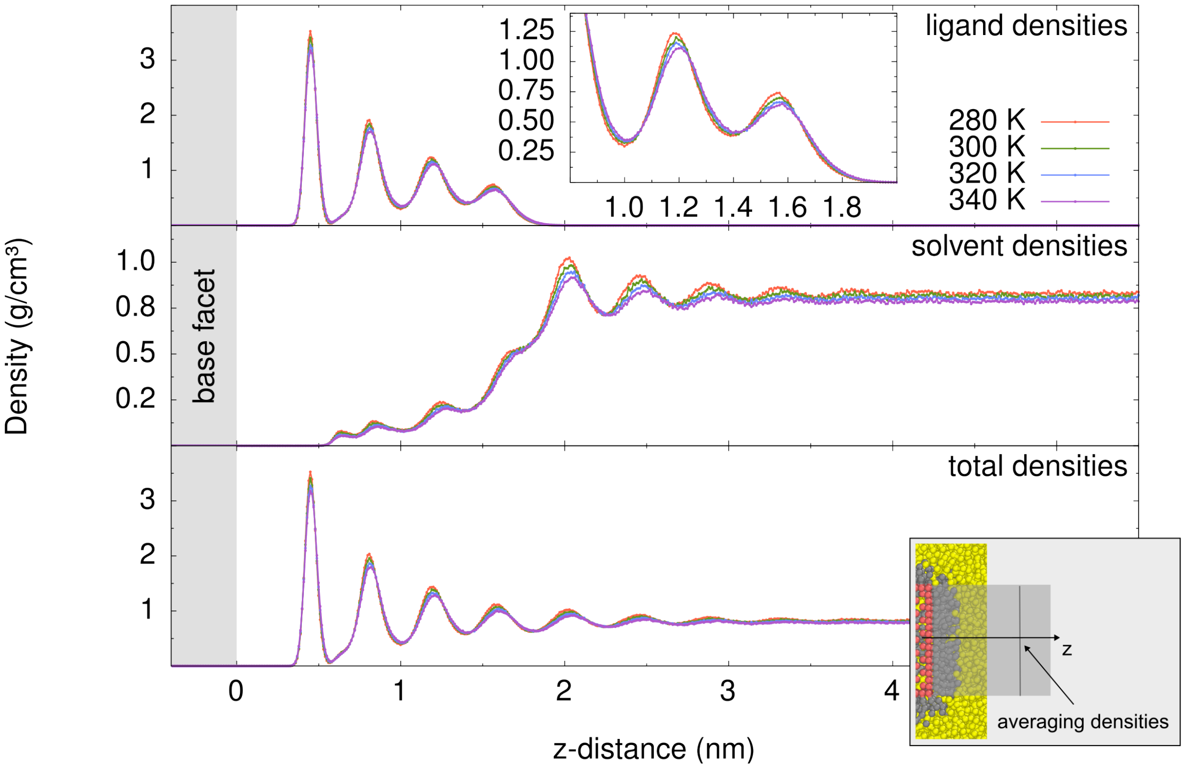

Figure 7.18: Temperature dependence of the solvent restructuring away from the base facet of single nanoplatelets in the MARTINI setup. The top panel shows the ligand, the middle panel the solvent, and the bottom panel the total densities. The inset in the top panel shows a zoom of the ligand shell density. As depicted in the bottom right inset, the densities at each distance in z-direction are averaged over the whole base facet area in the corresponding xy-plane, and are time averaged. For clarity, the data points are connected with straight lines.

at the base facets to the stronger confinement of the ligands, which is associated with shorter ligands (see Section 6.2.3).

In Figure 7.19, we show the calculated free energy curves. Because of the higher computational cost, we have limited ourselves to the first part of the free energy curves. Therefore, we place the zero-point of the free energy in the 1st free energy minimum. The free energy curves are very similar to those from the MARTINI setup. The free energy oscillation is more pronounced at lower temperatures. However, qualitatively, the curves do not change.

Overall, we conclude that the TraPPE-UA setup describes the properties of the ligand shell better than the MARTINI setup. However, the MARTINI setup is sufficient to study the general trends for other parameters, since it reproduces similar densities and free energies. Furthermore, we conclude that the temperature affects the interaction of large CdSe nanoplatelets, or CdSe nanoplatelets with short ligands, less than the interaction

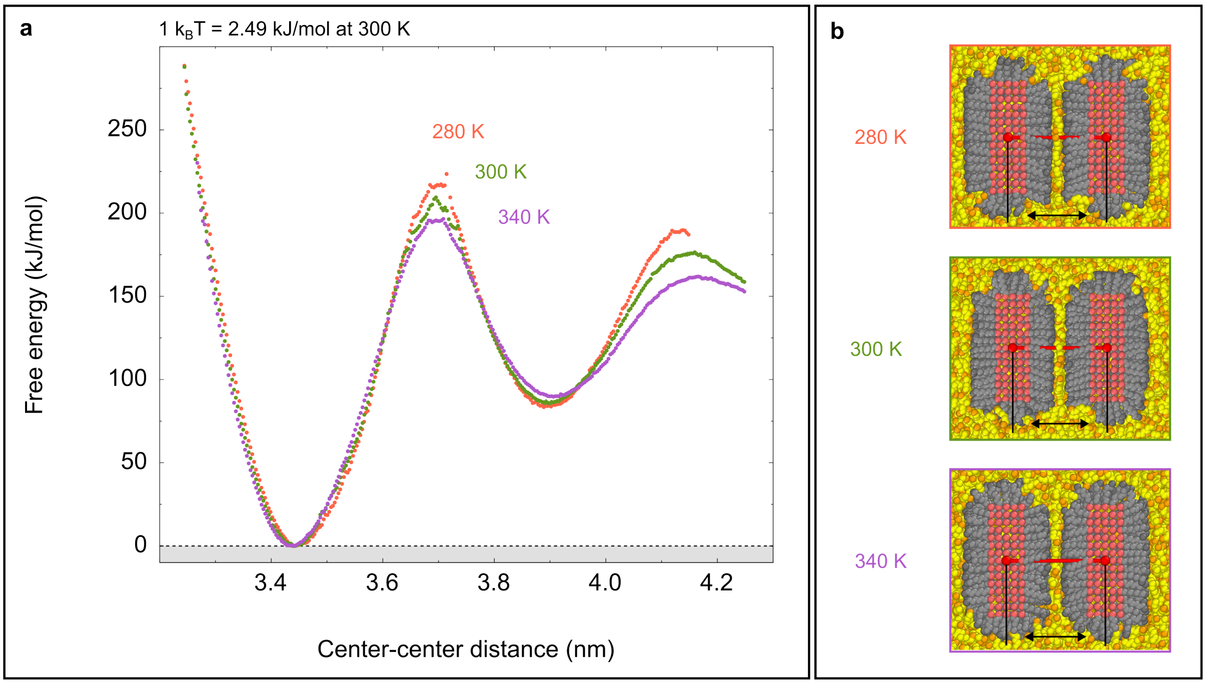

Figure 7.19: Effect of the temperature on the face-to-face interaction in the TraPPE-UA setup. **Panel a**, shows free energy curves for different temperatures. Here, the free energy is given in kJ/mol. In most other figures of this chapter, the free energy is plotted in $k_B T$ ($1\,k_B T = 2.49$ kJ/mol at 300 K). The free energy oscillations are more pronounced at lower temperatures. **Panel b**, shows cross-sectional snapshots of the nanoplatelets at different temperatures.

of CdS nanorods. However, even though the effect is smaller, changing the temperature is a way to control the attraction between CdSe nanoplatelets.

7.2.9 n-alkane solvent molecule length

In Section 6.2.4, we have found that the solvent restructuring at the ligand-solvent interface depends on the solvent type. For linear n-alkane molecules, the amplitude of the solvent oscillation increases with the n-alkane length. Here, we consider the influence of the n-alkane length on the pair interaction of CdSe nanoplatelets.

We consider solvent molecules with a length between one and four MARTINI C1 beads. This covers the range between n-hexane and n-tetradecane. In Figure 7.20, we show the ligand and solvent densities away from the base facets of single nanoplatelets. We observe similar trends as in the infinite facet TraPPE-UA setup (see Figure 6.5). With increasing alkane length, the bulk solvent density is increasing, and the amplitude of the solvent density oscillation increases. Additionally, we find that these differences become smaller with increasing chain length. Furthermore, it is evident that the positions of the extrema move slightly towards the base facet as the chain length increases (see inset with zoom).

We calculate the free energy curve for solvent molecules with up to four C1 MARTINI

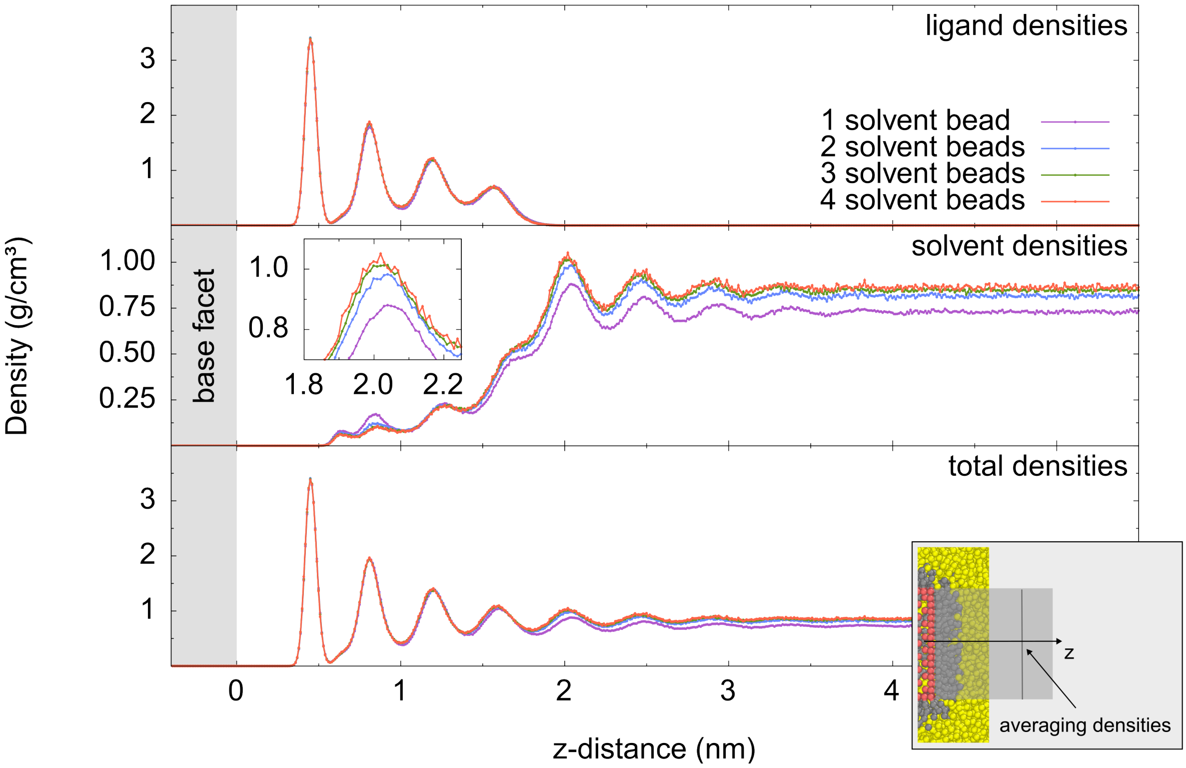

Figure 7.20: Effect of the alkane solvent length on the solvent restructuring. The top panel shows the ligand, the middle panel the solvent, and the bottom panel the total densities. A zoom of the largest maximum of the solvent density oscillation is shown in the inset in the second row. As depicted in the inset with the sketch, the densities at each distance in z-direction are averaged over the whole facet area in the corresponding xy-plane. For clarity, the data points are connected with straight lines.

beads. We find that we have to increase the number of solvent molecules and the simulation box size drastically for three and four solvent beads to avoid self interaction of the nanoplatelets (Table B.17). Additionally, the viscosity increases, and the nanoplatelets move slower. Therefore, we have to equilibrate the systems for longer periods, and have to double the production run to 80 ns (see Section B.2.1.5). Altogether, the computational cost for the simulations increases drastically with the solvent length. Therefore, we consider in the calculation with four solvent beads only separations up to 6.3 nm distance (see Figure B.10 for convergence).

In Figure 7.21, we show the calculated free energy curves. Since we have only calculated the first part of the free energy curve with four solvent beads, we place the zero point of the free energy in the 1st free energy minimum. In accordance with the results for the solvent restructuring, we find that the strength of the interaction increases with the n-alkane length. We find that the extrema slightly shift with increasing chain length to smaller separations. Furthermore, a new minimum at around 4.8 nm appears in the

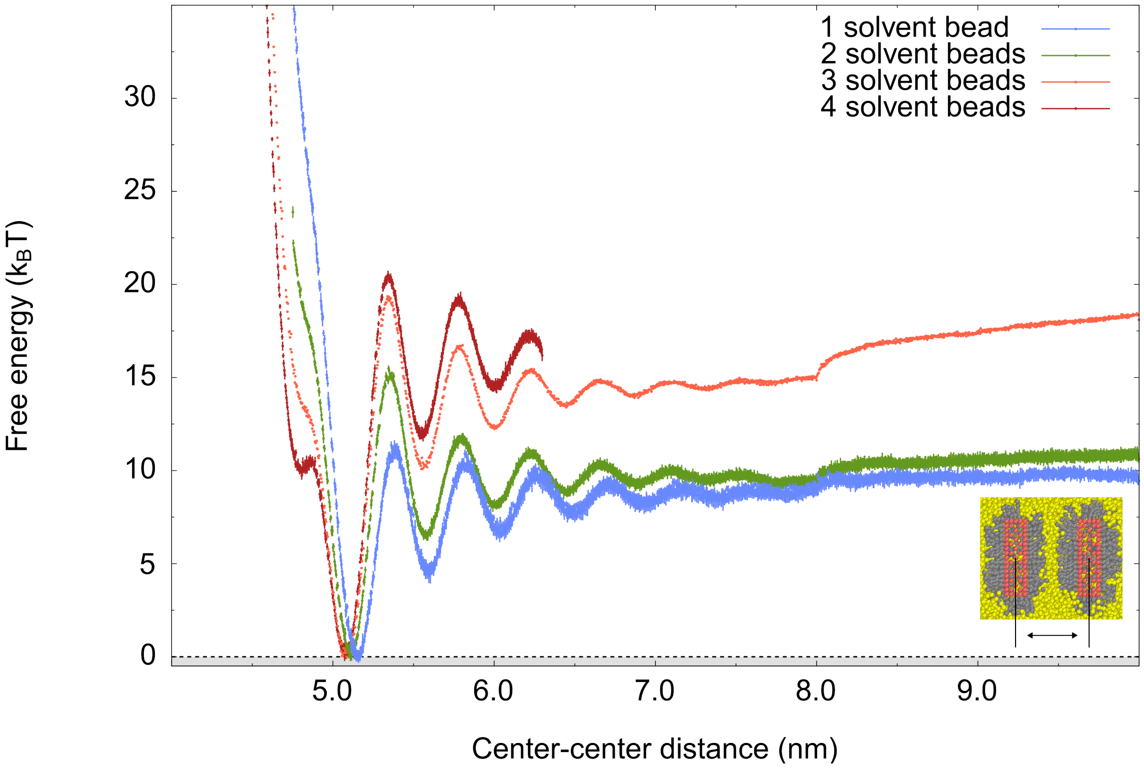

Figure 7.21: Effect of alkane solvent length on the free energy curves that describe the face-to-face interaction. The solvent length is varied between one and four C1 MARTINI beads. The zero point of the free energy is placed in the first minimum. The strength of free energy oscillation increases with the solvent length.

free energy curve for four solvent beads, whose characteristics we already find in the other curves. We assume that it results from the reorganizing and interdigitation of the ligands, which is more pronounced due to the increased attraction. As already observed in the densities, we find that with increasing solvent molecule length, the extrema shift slightly towards smaller separations.

In summary, we conclude that the attraction between CdSe nanoplatelets in n-alkane solvents with a longer chain length is larger. Therefore, we expect that the steric stability of CdSe nanoplatelets decreases in longer n-alkanes.

7.2.10 Isomers of octane in higher resolution

The isomers of a solvent molecule have all the same composition of atoms. However, they differ in their arrangement and branching. The magnitude and shape of the solvation forces can be different in different isomers of a solvent. For example, Wang *et al.* have shown that solvation forces between flat, uncoated surfaces are stronger in n-decane than in 2,2-dimethyloctane due to differences in the solvent restructuring [73].

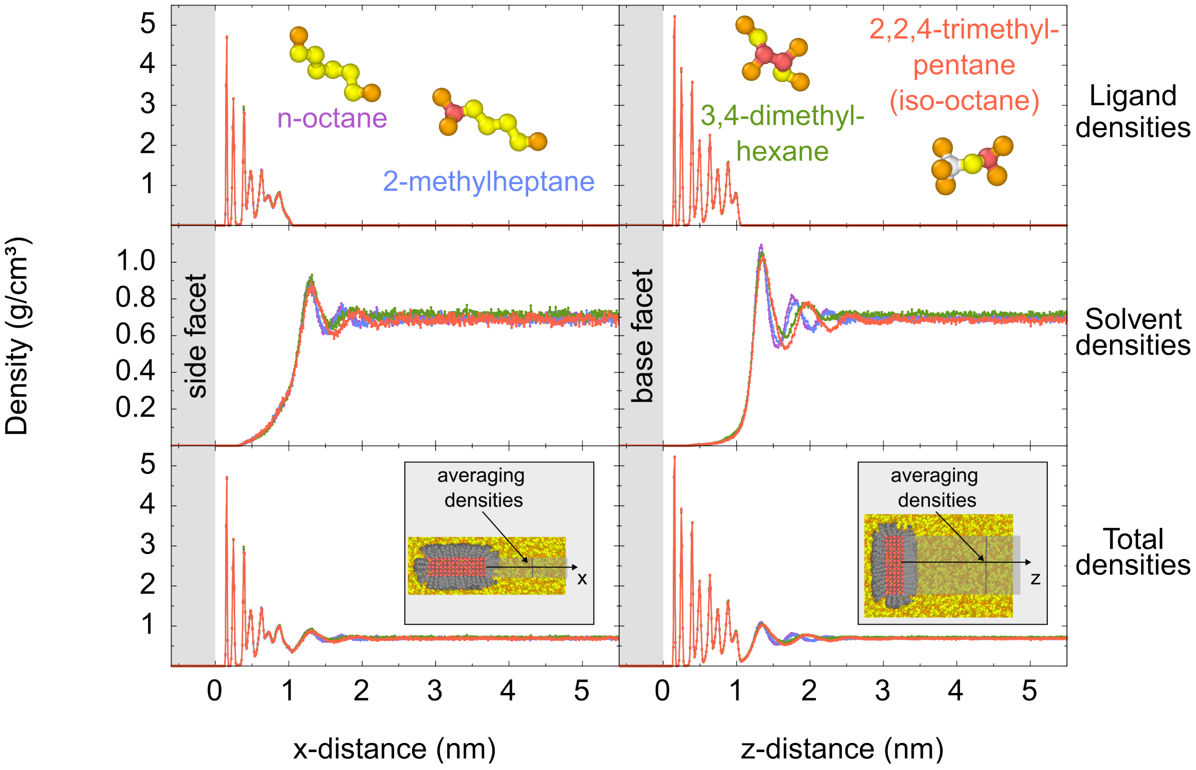

Figure 7.22: Ligand and solvent densities away from the side and base facets of single nanoplatelets in several isomers of octane. The top panel shows the ligand, the middle panel the solvent, and the bottom panel the total densities. As depicted in the insets, the densities at each distance in x/z-direction are averaged over the whole facet area in the corresponding zy/xy-plane. For clarity, the data points are connected with straight lines. Shown are also snapshots of single solvent molecules. The bead colors in the snapshots correspond to the different bead types: CH_3 is shown in orange, CH_2 in yellow, CH_1 in red, and CH_0 in white.

We systematically compare the face-to-face interaction in several isomers of octane. Since the resolution of the MARTINI model is not sufficient to describe the isomers, we use here the TraPPE-UA setup (see Figure 5.2). We use the same nanoplatelet setup as in Subsection 7.2.8.2. We use nanoplatelets with 18.1 nm^2 base facet area, 1.2 nm thickness, and with a length corresponding to eight carbon atoms.

In Figure 7.23, we present the calculated free energy curves. Because of the higher computational cost, we have limited ourselves to the first part of the free energy curves. Therefore, we place the zero-point of the free energy in the 1st free energy minimum. All free energy curves show qualitatively a very similar shape as those we have calculated with the MARTINI setup. This result again confirms our assessment that the MARTINI model is suitable for describing CdSe nanoplatelets. However, the higher resolution of the TraPPE-UA setup allows us to differentiate the features of the isomers. We find that

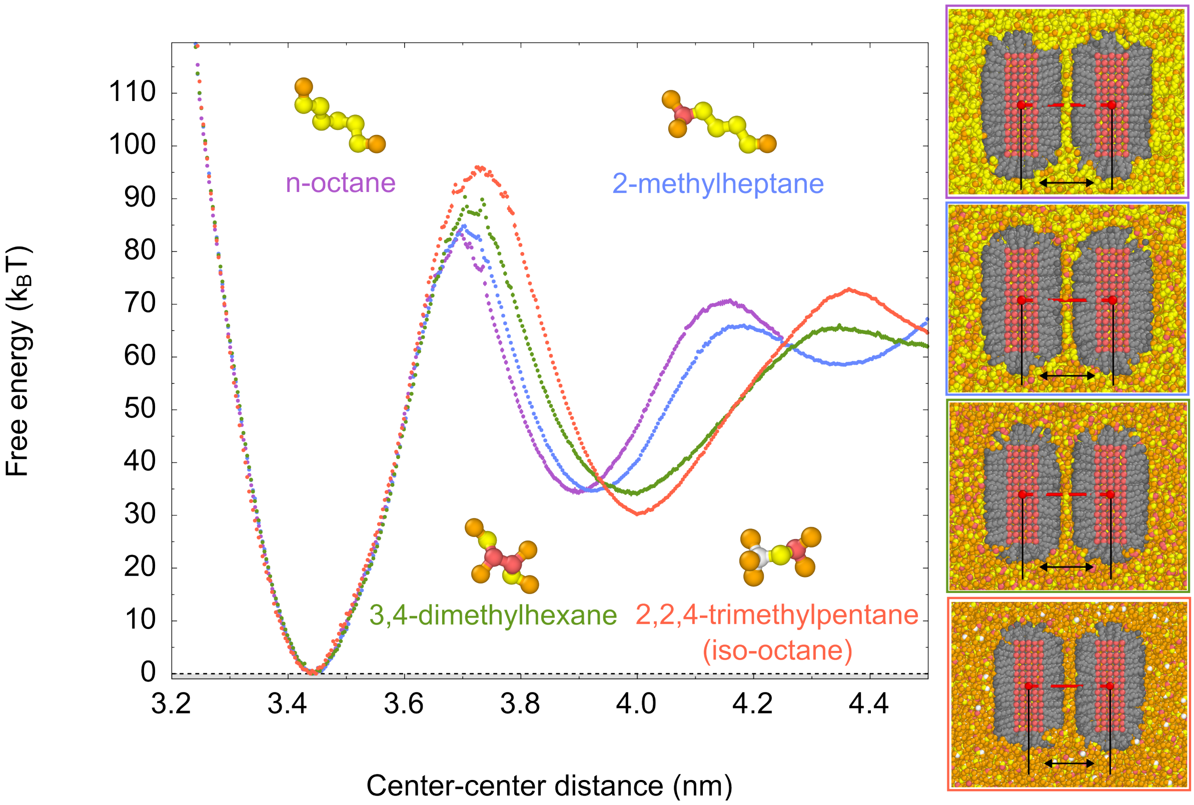

Figure 7.23: Isomers of octane. Shown is the face-to-face interaction. The TraPPE-UA setup is used. On the right, cross-sectional snapshots of the setups are displayed. Shown are snapshots from an umbrella window close to the 2nd minima. The bead colors correspond to the different bead types: CH_3 is shown in orange, CH_2 in yellow, CH_1 in red, and CH_0 in white.

the spacing between the extrema of the free energy oscillation and the amplitudes of the oscillation depends on the octane isomer.

It is striking that regardless of the solvent, the 1st minimum is always at ~3.44 nm and the free energy curves are nearly identical up to a separation of ~3.65 nm. In Figure 7.24, we show the ligand and solvent densities away from and between the base facets at the 1st and 2nd free energy minima. Regardless of the octane isomer, the ligand densities are nearly identical at the 1st minimum. Furthermore, the solvent density between the ligand shells is nearly zero. Therefore, there is no difference in the course of the free energy curves at short distances.

Near the 1st maximum, the free energy curves split. With increasing branching of the solvent molecules, the peak of the 1st maximum shifts to larger distances, and the maximum free energy value increases. We attribute both changes to the increasing cross-section of the solvent molecules.

Let us consider a simplified model. Consider two hard, flat facets without ligands and hard spherical solvent molecules. As the facets move away from each other, a certain distance must be reached before the spheres can get between the facets (see sketch in

Figure 7.25). As the distance increases, the excluded volume increases and the free energy increases accordingly. For spheres with larger diameters, the facets must be further apart before the spheres can get between the facets. Accordingly, the free energy of the maximum increases and the maximum peaks shift to larger distances for larger spheres.

Of course, this is a very simplified picture. In particular, it neglects the softness of the ligand shell, the flexibility of the solvent molecules, and that the interactions of the molecules change dependent on the solvent type. For example, the solvent molecules will not penetrate all at once into the volume between the facets. They will enter continuously (compare with results in Subsection 7.2.3). However, the model illustrates why the maximum free energy values increase.

The positions and free energy values of the 2nd minima also depend on the octane isomer. With increasing branching, the minima shift to larger distances due to the thicker solvent layers. This is also visible in the solvent densities in Figure 7.24. In each system, there is a solvent density peak between the nanoplatelets at the 2nd minimum. The peaks shrink and broaden with increasing branching. The broadening is consistent with the changes in the spacing between the extrema in the free energy curves. However, there is no simple connection between the free energy values of the 2nd minima and the density curves. This becomes clear when comparing 3,4-dimethylhexane and 2,2,4-trimethylheptane. Their ligand and solvent density curves are nearly identical at the 1st and 2nd minimum. Still, the free energy values are different. This illustrates that the free energy curves are determined not only by the densities, but also by the interactions between the ligand and solvent molecules, which change with the solvent type.

These results show how difficult it is to predict how the isomers of a solvent affect the interaction between the nanoplatelets. We do not find a clear trend. Therefore, it is probably easier to use n-alkanes with different lengths to tune the nanoplatelet interaction. Nevertheless, these results show that the use of isomers for the tuning of the interaction is also possible.

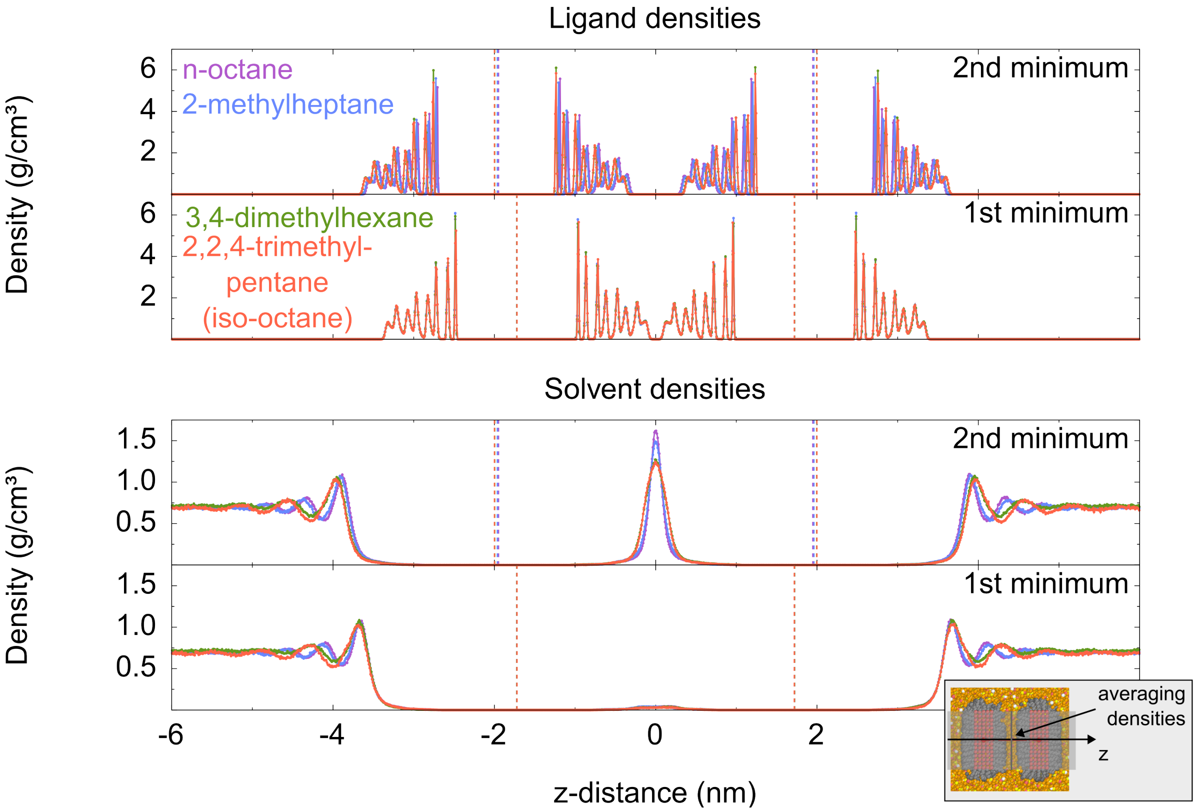

Figure 7.24: Ligand and solvent densities at the first and second free energy minimum. The solvent is varied between different isomers of octane. The center positions of the nanoplatelets are marked with doted lines.

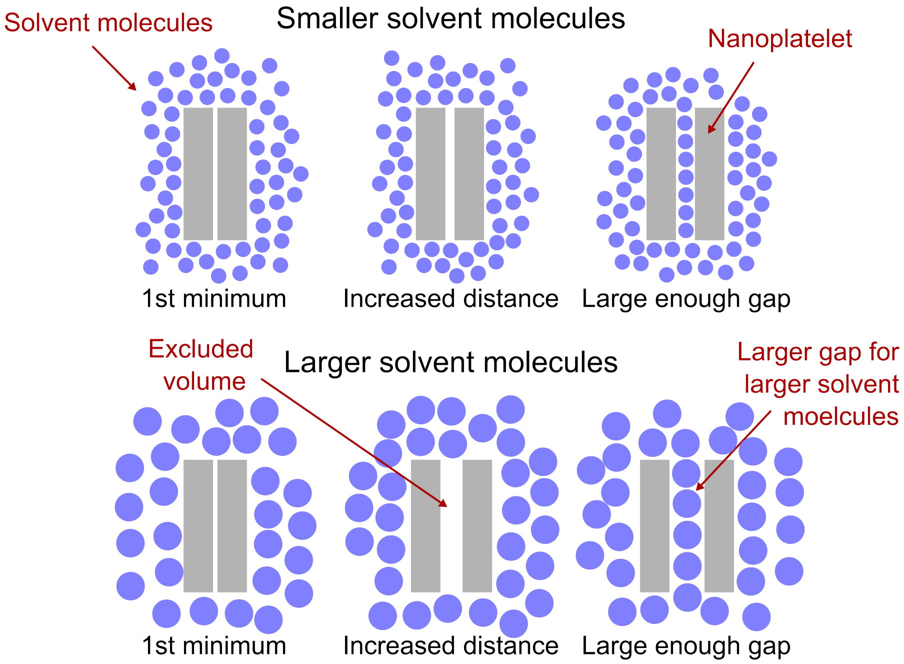

Figure 7.25: Simplified hard particle model to illustrate the effect of solvent molecule size

7.3 Summary and discussion

In summary, we find in this chapter that the interplay between the properties of the ligand shell, the solvent restructuring, and the solvent type dictates the free energy of the interaction of ligand passivated CdSe nanoplatelets. Thereby, the shape of interaction depends on the approach path. We find a strong free energy oscillation when two nanoplatelets approach/separate face-to-face, because of the solvent layering between the base facets. The separation dependent solvent layering causes strong solvation forces that are reflected in the free energy oscillation. In contrast, we find no free energy oscillation when the nanoplatelets approach/separate in a lateral side-shift, since the solvent does not layer.

We observe several trends. The solvent restructuring at a ligand shell depends on the ligand packing density, and the structure of the ligand-solvent interface. Accordingly, we find that the strength of the face-to-face interaction increases with the grafting density, and decreases with the ligand length. Furthermore, we find that the structure and packing density of the ligand shell depends on the facet area. The ligands at the edges of a facet have more space than the ligands in the center of a facet. Therefore, the ligand packing density away from the center of a facet is larger, as well as the solvent restructuring. We observe that this effect is particularly strong for small nanoplatelets/ facets. For larger nanoplatelets, we find that the strength of the interaction increases nearly linear with the facet area. We find that the linear trend corresponds to very similar densities away from the facets between the systems. However, we observe that the densities slowly change with the facet area. Therefore, we expect for very large facet area changes a stronger than linear increase in the strength of the interaction. Surprisingly, we find that also the thickness of the nanoplatelets has an effect on the face-to-face interaction. As we increase the interaction, we increase the ligand density and the solvent restructuring away from the side facets. We observe that the changes in the edges between the side facets and the base facets have a significant effect on the attraction between the nanoplatelets.

We also consider different solvent types. We find that the attraction between nanoplatelets in n-alkanes increases with the chain length. Furthermore, we compare different isomers of octane. We find that the spacing between the extrema of the free energy oscillation can be tuned, as well as the amplitudes.

Overall, we can state that solvation forces dominate the interaction between ligand passivated CdSe nanoplatelets in pure apolar solvents. Therefore, we can most effectively control the interaction and steric stability of CdSe nanoplatelets by tuning the solvation forces.

Chapter 8

Experimental validation

The results shown in this chapter are part of a joint project with our colleagues Shuai Chen and Hai Wang. The experiments were carried out by them. We participated in the directed design of the experiments, as well as in the interpretation, which is based on our simulation results. These results are also included in the PhD thesis of Shuai Chen [130]. A joint publication is under preparation.

Our simulation results suggest that solvation forces dominate the interaction of CdSe nanoplatelets, and are the main cause of nanoplatelet stack formation. However, even though previous studies are in agreement with our results [45, 46, 37], experimental results that distinguish the effect of solvation forces from the other interaction forces are desirable.

Our approach is to look at the self-assembling process in solution of nanoplatelets with different properties, and thus differentiate the influence of the interactions. Jana *et al.*, as well as Momper *et al.*, confirmed by small-angle X-ray scattering (SAXS) experiments that CdSe nanoplatelet can form stacks in n-alkane solvents [45, 37]. However, this method is quite unprecise. It can only be used to detect larger stacks.

Our setup allows us to determine the CdSe nanoplatelet concentration at which the self-assembling process begins. To do so, we exploit the specific optical, and electrical properties of CdSe nanoplatelets. We induce (exciton dominated) charge species in the nanoplatelets with a laser pulse. When the nanoplatelets form dimers or stacks, the electronic coupling between the nanoplatelets increases. Enhanced inter-nanoplatelet charge separation causes free charge carrier generation. Additionally, we expect that the mobility of the free charge carriers increases, as the nanoplatelets assemble. As a result, the photoconductivity increases as CdSe nanoplatelets self-assemble. The change in the photoconductivity can be measured with optical-pump terahertz-probe spectroscopy (OPTP) [37]. We exploit this effect to measure the saturation concentration at which the CdSe nanoplatelets start self-assembling. We vary the base facet area, as well as the solvent type. The altered saturation concentrations allow us to draw conclusions about the interactions.

8.1 Synthesis

We synthesize CdSe nanoplatelets with four Cd monolayers (see Chapter 3.1) [131, 130]. This corresponds to a nanoplatelet thickness of 1.4 nm. By varying the reaction time, we produce samples with four different average base facet areas: 24 nm^2, 119 nm^2, 215 nm^2, and 420 nm^2. In Figure 8.1a-d, we show transmission electron microscopy (TEM) images of the samples. While the thickness is controlled with atomic precision, there is a variation in the lateral dimensions. Most of the nanoplatelet base facets are rectangular. However, some nanoplatelets, especially those with around 420 nm^2 facet area, deviate from the rectangle shape.

To characterize the nanoplatelets, we measure the absorption and emission spectra of the nanoplatelets. We find sharp absorption peaks at around 480 nm, and 512 nm, as well as a sharp emission peak at 512 nm. For the sample with 24 nm base facet area, we find a minor spectral shift of ∼7 nm. We do not find such a shift for the larger nanoplatelets. This result is in agreement with the expectation, that the electronic structure mainly depends on the thickness of the nanoplatelets (see Section 3.2). The lateral dimensions of the larger nanoplatelets with 119 nm^2, 215 nm^2, and 420 nm^2 base facet area are much larger than the bulk CdSe exciton Bohr radius of (4-6) nm, while the thickness of 1.4 nm is smaller [86, 87]. Therefore, the quantum confinement effect occurs only in the thickness. Regardless of the base facet area, the spectra do not change. The only exception is the sample with 24 nm^2 base facet area. In this sample, the base facet side length of around ∼ 5 nm is similar to the bulk CdSe exciton Bohr radius of (4-6) nm. Hence, the quantum confinement in the lateral dimensions influences the spectrum in this sample.

For the three samples with larger base facets, we measure the absorption spectra for different nanoplatelet concentrations (Figure A.15). Furthermore, we show the absorption spectra of the sample with 119 nm base facet area in different solvents in Figure A.16. The wavelength of the peaks do not change.

8.2 Method: optical-pump terahertz-probe spectroscopy

We apply optical-pump terahertz-probe spectroscopy (OPTP), to measure the photoconductivity. A sketch of the setup is shown in Figure 8.2. We use an ultrafast laser pulse (∼100 fs, 400 nm, 3.1 eV). With the pulse, we optically promote electrons from the valence band to the conduction band. This leads to a change in the conductivity ($\Delta\sigma$), which we measure by a terahertz (THz) pulse with a duration of 1 ps. Thereby, $\Delta\sigma = \Delta\sigma_\mathrm{R} + i\Delta\sigma_\mathrm{I}$ is a complex quantity. The electrical field of the terahertz pulse (E) accelerates free charge carriers, which in turn leads to the attenuation ΔE of the pulse. The attenuation is linearly proportional to the real part of the conductivity ($\Delta E \propto \Delta\sigma_\mathrm{R}$). Excitons, which are in total charge neutral, induce mainly a phase shift Δt in the terahertz pulse. This phase shift is associated with the polarizability of the excitons. It is proportional to the imaginary part of the conductivity $\Delta\sigma_\mathrm{I}$.

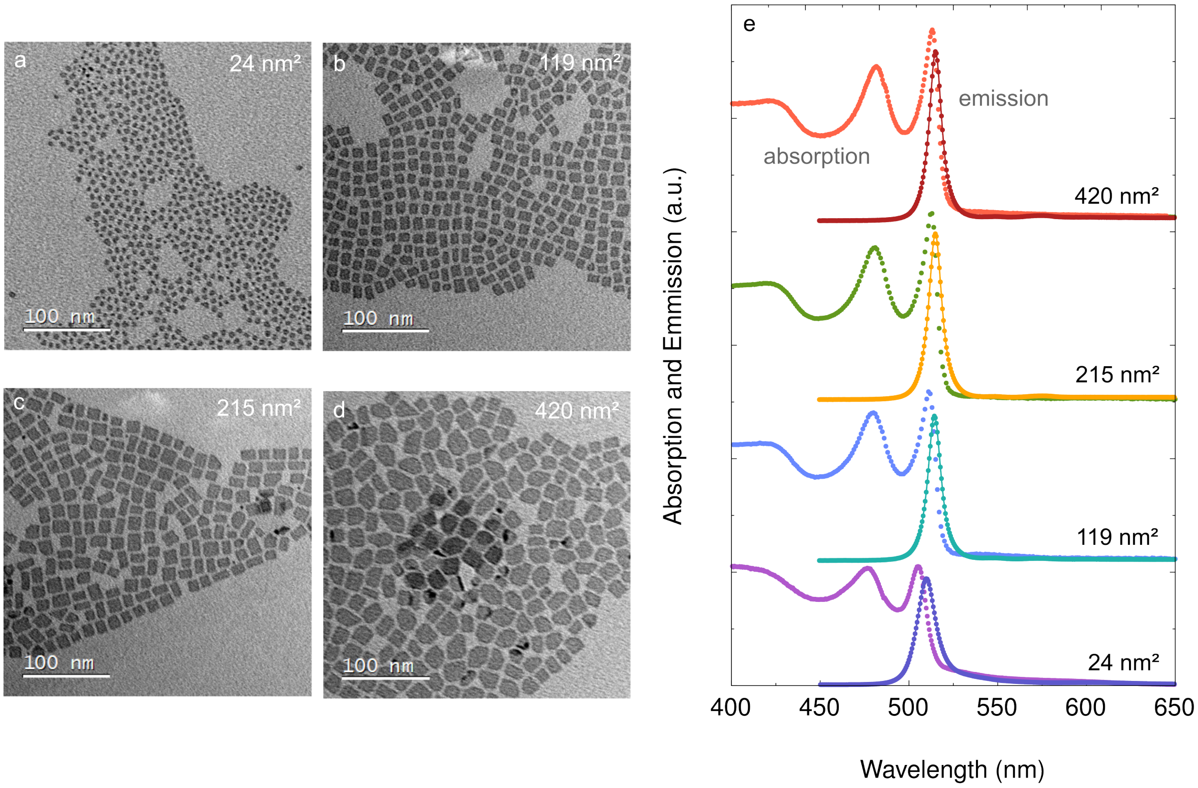

Figure 8.1: TEM images of synthesized CdSe nanoplatelets (**panel a-d**). The facet areas are 24 nm^2 (**panel a**), 119 nm^2 (**panel b**), 215 nm^2 (**panel c**), and 420 nm^2 (**panel d**). **Panel e**, shows the corresponding absorption spectra (dots), as well as the emission spectra (lines with dots).

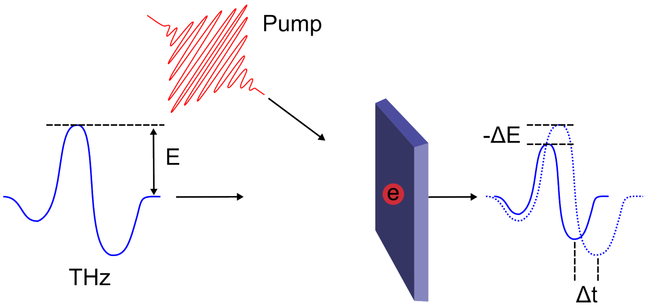

Figure 8.2: Setup of the optical-pump terahertz-probe spectroscopy (OPTP). A pump pulse promotes electrons to the valence band. The change in the conductivity is measured by a terahertz pulse. The components of the complex conductivity are proportional to the phase shift Δt and the change of the amplitude of the electric field $-\Delta E$.

8.3 Results

In the first series of experiments, we vary the base facet area. For each base facet area, we disperse the CdSe nanoplatelets in n-hexane (Figure 8.1a-d), and carry out OPTP measurements. We measure the attenuation of the electric field of the THz signal ΔE. For the comparability of the photoconductivity in different nanoplatelets concentrations, we normalize ΔE by the absorbed photon density N_{abs}. The photoconductivity $\Delta\sigma$ is linearly proportional to $\Delta E/N_{\text{abs}}$.

We find that the photoconductivity depends on the base facet area. In the sample with 24 nm^2 base facet area, we find a purely excitonic response. The real part of the measured photoconductivity is zero, while we obtain a strong imaginary component. Even at very high nanoplatelet concentrations, this does not change (see Figure A.14 in the Appendix). The most obvious explanation is that the majority, if not all, of the charge carriers are in an exciton state. The bulk CdSe exciton radius is around 5.4 nm [87]. The side length of the base facet area is smaller. Therefore, even high-energy charge carriers have no chance to flee the exciton configuration within a single nanoplatelet. Evidence of this is also provided by the spectral shift in the absorption spectrum (Figure 8.1e), which indicates a lateral quantum confinement effect. For completeness, we should note that Brumberg *et al.* have observed that the in-plane radius of excitons in CdSe nanoplatelets is in the range of 1-2 nm [87]. Therefore, not all questions are clarified here. It would be interesting to analyze this in more detail. Anyway, we can conclude that we cannot make a statement about whether the nanoplatelets with 24 nm^2 facet area form stacks or not.

Fortunately, we can make more definite statements for larger nanoplatelets. The photoconductivity of the larger nanoplatelets also has a large imaginary component, which again indicates excitons (see Figure A.15e-f). However, free charge carriers also occur here, which leads to a real component in the photoconductivity. In Figure 8.3a, we plot the real component of the photoconductivity for the sample with 420 nm^2 facet area. Following the optical excitation, the conductivity increases. First there is a peak, then the conductivity drops to a metastable level. The conductivity strength depends on the nanoplatelet concentration. For several concentrations, we average the conductivity between 1.5 ps and 2.0 ps. In Figure 8.3b, we plot the resulting curve. The curve shows a sigmoidal transition. Our interpretation is that this transition in photoconductivity is due to the self-assembling of the nanoplatelets. As already described in the introduction of this chapter, the electronic coupling between the nanoplatelets increases when they self-assemble. The enhanced inter-nanoplatelet charge separation increases the number of free charge carriers. Additionally, we expect that the mobility of the free charge carriers increases. Both effects contribute to the increase in the photoconductivity.

That the self-assembling of the CdSe nanoplatelets depends on the concentration is straightforward. If the platelets assemble, or not, depends on the balance between the different free energy terms (see Chapter 2, and Section 3.4). Some terms, such as the core-core van der Waals attraction, and the solvation forces favor the assembly of nanoplatelets, while other terms, such as the rotational entropy, and the translational entropy favor the dispersed state.

The nanoplatelet concentrations c in our experiments are relatively small, and the volume fraction of the nanoplatelets is $< 1\%$. Therefore, we can assume that most of the terms contributing to the free energy of the system will not significantly change within the concentrations range. However, the translational entropy of a nanoplatelet depends directly on the accessible volume, and therefore on the nanoplatelet concentration. It contributes to the free energy by:

$$G_{\mathrm{trans}} = k_{\mathrm{B}} T \log(c). \tag{8.1}$$

As we increase the concentration, we increase the free energy G_{trans}, and shift the balance of the free energy terms towards assembly. At the saturation concentration, the balance has shifted to the point where the nanoplatelets begin to assemble.

In Figure 8.3b, the curves for the other facet sizes are also shown. As already discussed, we do not measure a photoconductivity in the sample with $24\,\mathrm{nm}^2$ facet area. For the other samples, we find a clear trend. The larger the facet area, the lower the saturation concentration. This is in agreement with our simulations, where we have found that the attraction increases with the facet area (see Section 7.2.6). A higher attraction between the nanoplatelets shifts the balance towards assembling. Anyway, we would see this trend in the other interactions as well. The core-core van der Waals interaction also increases with facet area (Section 3.4), as it is expected for the dipole-dipole interaction. Measurements on CdSe nanorods have shown that the dipolar moments scale linearly with the nanocrystal volume [132, 52].

Therefore, in the next step, we consider different n-alkanes solvents. Here, our simulations show that the attraction due to the solvation forces increases with the chain length (see Section 7.2.9). In contrast, the core-core van der Waals interaction decreases with the chain length (Section 3.4). Similarly, we expect the dipole-dipole interaction to decrease with chain length. The different trends allow us to experimentally clarify which interaction dominates here.

We chose the sample with facet areas around $119\,\mathrm{nm}^2$, and consider n-hexane, n-octane, n-decane, and n-dodecane as solvents. In Figure 8.3c, we show the measured curves. For further details, see also Figure A.16 in the Appendix. We find that the saturation concentration decreases with the n-alkane chain length. The longer the n-alkane chain is, the smaller the concentration at which the nanoplatelets start to assemble. As discussed, we expect that the saturation concentration depends on the attraction between the CdSe nanoplatelets. We infer that the attraction between the nanoplatelets increases with the chain length. Therefore, the observed trend is consistent with our simulations. This result confirms our hypotheses that solvation forces play a crucial role in the interaction and steric stability of colloidal CdSe nanoplatelets. Indeed, it demonstrates that solvation forces can dominate the interaction.

Finally, the comparison of Figure 8.3b, and Figure 8.3c demonstrates that the interaction and the steric stability sensitively depends on various parameters. It is possible to precisely tune the interaction. For example, it is possible to set the same steric stability for different large nanoplatelets, just by tuning the solvent type.

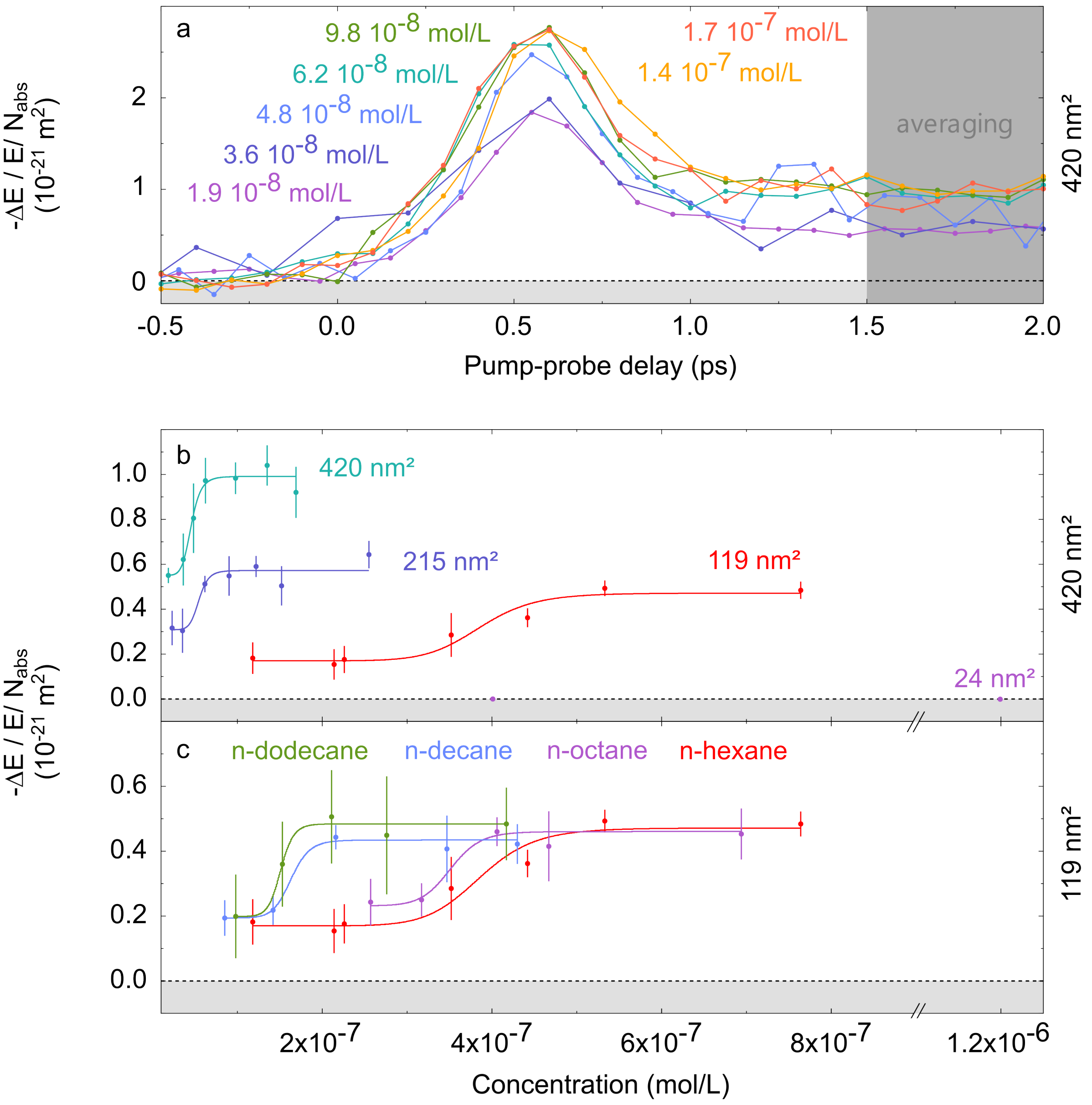

Figure 8.3: OPTP measurements. **Panel a** shows the measured real component of the photoconductivity before and after the pump pulse (0.0 ps). The CdSe nanoplatelets have base facet areas of around 420 nm^2. The solvent is n-hexane. The nanoplatelet concentration is varied. To guide the eyes, the points are connected with straight lines. For each nanoplatelet concentration, the conductivity is averaged in the interval between 1.5 ps and 2.0 ps. The averaged conductivities are plotted in **panel b** (teal data points, 420 nm^2). Furthermore, **panel b** shows the averaged conductivities for other base facet areas (215 nm^2, 119 nm^2, and 24 nm^2). **Panel c** shows the concentration dependent conductivities in different n-alkane solvents. The base facet area in **panel c** is around 119 nm^2. The lines in **panel b** and **c** are fits with sigmoidal curves.

8.4 Summary and discussion

We use OPTP measurements to evaluate the saturation concentration at which CdSe nanoplatelets start to assemble. The OPTP method takes advantage of the special optical and electronic properties of CdSe nanoplatelets. Its use is limited to systems in which the photoconductivity changes depending on the assembling. For example, we assume that this method could also be applied to study perovskite nanoparticles [39].

In general, the assembly of nanocrystals depends on the balance between different free energy terms (see Chapter 2). Therefore, we can draw conclusions about the interactions from the measured saturation concentrations. We find that the saturation concentration decreases with the facet area, which indicates that the attraction between the nanoplatelets increases. This observation is in accordance to our simulations, where the attraction increases with the facet area (see Section 7.2.6). This also applies to the results for n-alkanes of different lengths. The saturation concentration decreases with the length of the n-alkane chain. We infer that the attraction between the CdSe nanoplatelets increases with the n-alkane chain length. This result is in agreement with our simulation results. It confirms our hypothesis that solvation forces dominate the CdSe nanoplatelet interaction, since both the core-core van der Waals interaction, and the dipole-dipole interaction should decrease with the n-alkane chain length, while our simulations show that the attraction due to the solvation forces increases.

Chapter 9

Summary and outlook

In this thesis, we use molecular dynamics simulations to examine the interplay of the different interactions of ligand passivated CdSe nanoplatelets in apolar solvents and relate them to experimental observations.

Several contributions can influence the interaction between colloidal nanocrystals. Which interactions are important in a given colloidal system depends on the materials used and the discrete structure of the materials. Often, the van der Waals attraction between the nanocrystal cores dominates the interaction, particularly between metallic nanocrystals [21]. However, the core-core van der Waals attraction between CdSe nanoplatelets is very weak. We estimate the core-core van der Waals interaction energy with the Hamaker approach (see Section 3.4). Thereby, we compare different facet areas, distances, and solvent types. For example, we find that the interaction energy between nanoplatelets with a base facet area of $225\,\mathrm{nm}^2$ is less than $\leq 1\,\mathrm{k_B T}$ (see Section 3.4).

Some nanocrystals exhibit large permanent dipoles, which can also significantly influence the interaction, for example CdSe nanorods [55]. Dozov *et al.* have found large permanent dipoles in CdSe nanoplatelets with a facet area of about $180\,\mathrm{nm}^2$ [48]. They have estimated the maximal dipole-dipole interaction energy to be around $-3\,\mathrm{k_B T}$. However, Dozov *et al.* have calculated the interaction energy for the configuration of the dipoles that maximizes the attraction. They also have not considered thermal fluctuations. Therefore, the average attraction is probably smaller. It would be worthwhile to investigate this effect further. In particular, we wonder to what extent the permanent dipoles depend on nanoplatelet thickness and the lateral dimensions. However, for our considerations, it is sufficient to note that the dipole-dipole interaction is small for CdSe nanoplatelets.

We run simulations where we find that the collective interaction between the ligand and solvent molecules has a much stronger impact than the core-core van der Waals interaction and the dipole-dipole interaction (see Chapter 7). In particular, strong solvation forces occur. We find that the solvent restructures at the ligand-solvent interface of the nanoplatelets. The solvent molecules order into layers around single nanoplatelets. This structural change from the bulk solvent increases the free energy. As two nanoplatelets approach each other, the solvent structure changes. Depending on the arrangement of the solvent molecules in each separation, the free energy can increase or decrease. We calculate free energy curves to characterize the pair interaction of two CdSe nanoplatelets.

We find that the shape of the free energy curves depends sensitively on the assembling pathway, and the relative orientation of the nanoplatelets. For example, we find a strong free energy oscillation at close distances when two nanoplatelets approach/separate face-to-face with their base facets. This is because the solvent layering intensifies between the facets. The free energy minima are at separations, where we find an integer number of solvent layers in between. At the transition between states with well-defined solvent layers, we find free energy barriers. However, these barriers are smaller, or not present on other assembling trajectories, since the solvent restructuring depends on the relative orientation of the nanoplatelets.

A dispersion with ligand passivated CdSe nanoplatelets and an n-alkane solvent like n-hexane is metastable. Dependent on the concentration, the nanoplatelets form stacks and precipitate within minutes, hours, or days [45]. We infer that solvation forces are crucial for the attraction between the nanoplatelets, and cause the stack formation in pure n-alkane solvents [45, 46]. Both the dipole-dipole interaction and the core-core van der Waals interaction will also contribute to the stack formation. However, they are too weak to be the main attraction. Furthermore, we assume that one of the reasons why such a dispersion is metastable is that the free energy barriers arise due to the layer formation of the solvent. The free energy barriers prevent direct self-assembly of the CdSe nanoplatelets.

We find that the strength and shape of the solvation forces depend on several parameters of the colloidal system. The magnitude of the solvation forces depends on the nanoplatelet geometry, the ligand shell properties, the solvent type, and the temperature (see Figure 9.1, and Chapter 7). For example, we find that the attraction between CdSe nanoplatelets increases with the base facet area. Also, we find for n-alkane solvents that the attraction increases with the solvent molecule chain length. The experiments of our collaborators confirm these trends (see Chapter 8). Furthermore, we find that the solvation forces become weaker with increasing ligand length. This trend is in agreement with previous experiments of Jana *et al.* that have shown that the steric stability of CdSe nanoplatelets in n-hexane increases with the ligand length [45]. Based on our results, we attribute the change in steric stability to the change in attraction between the platelets.

The knowledge that solvation forces play the crucial role in the interaction and steric stabilization of colloidal CdSe nanoplatelets in pure alkane solvents opens a large space for variations and manipulations. For example, let us assume that we have a defined CdSe nanoplatelet size and want to tune the steric stability. Then we can just change the solvent type, or change the ligand length. On the other hand, let us assume that we need to use a specific ligand type. Then, we can just change the nanoplatelet dimensions or the solvent type. We anticipate that these options to tune the interaction will simplify the processing of CdSe nanoplatelets. This will contribute to the use of CdSe nanoplatelets in new innovative applications, such as in light-emitting devices [40], solar cells [41], field effect transistors [42], and lasers [43].

In many ways, colloidal CdSe nanoplatelets are an ideal model system to study solvation forces between ligand passivated nanocrystals. The dense ligand shell and large base facet areas favor strong pronounced solvation forces, while the weak core-core van der Waals and dipole-dipole interactions can be neglected. Therefore, we can also compare and

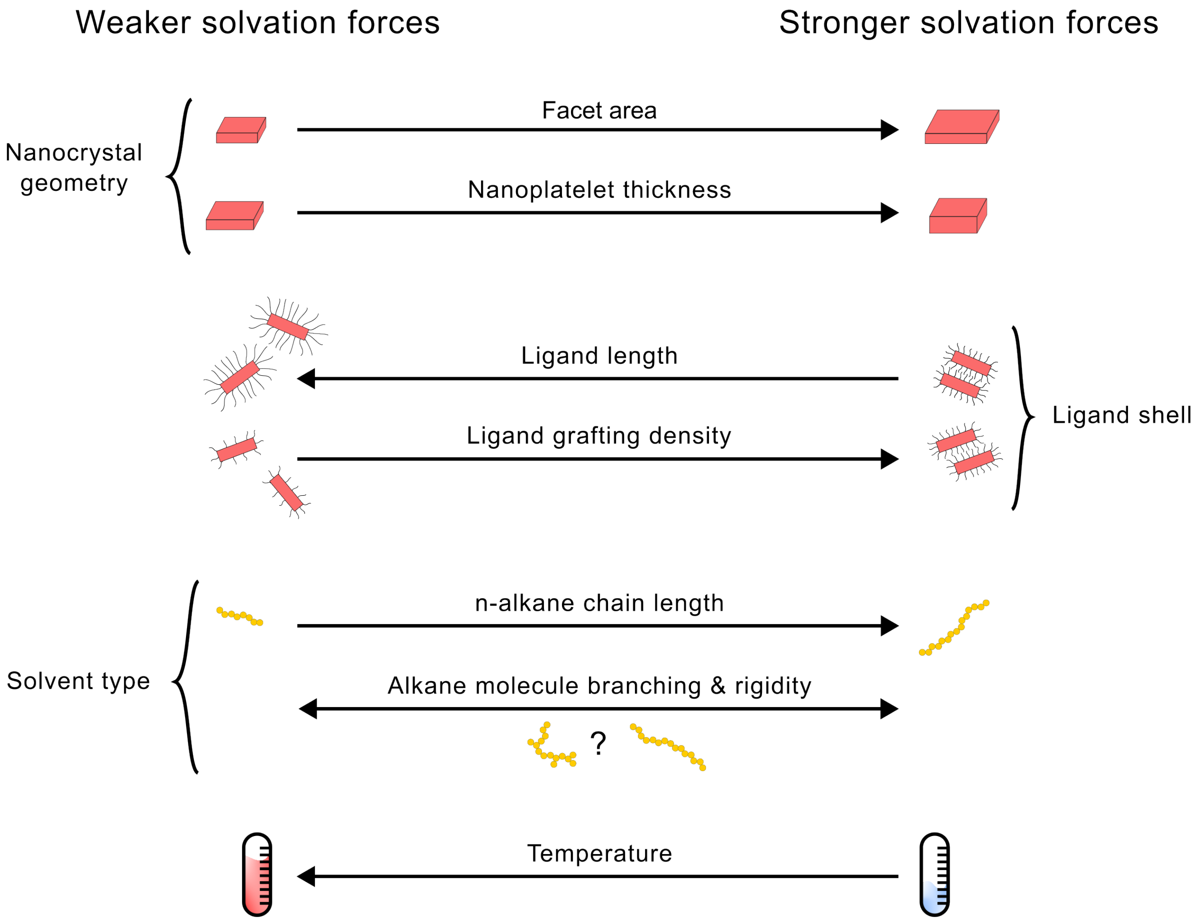

Figure 9.1: Solvation forces play a crucial role in the interaction of CdSe nanoplatelets. Several parameters influence the strength of the solvation forces. For example, the solvation forces increase with the facet area, while the solvation forces decrease with the ligand length. The trends that have been found are summarized in the figure.

transfer our findings to other apolar colloidal systems with ligand coated nanocrystals.

First, we should discuss systems where solvation forces are typically weak, and in most cases negligible. Spherical ligand passivated nanocrystals are the most obvious example. The ligand packing density depends sensitively on the curvature of the nanocrystal surface. The ligands can occupy more space away from a curved surface. Accordingly, the ligand packing density decreases away from the nanocrystal surface. Therefore, the ligand-solvent interface of spherical nanocrystals is usually not well-defined, and solvent restructuring is strongly reduced. Hence, solvation forces typically play a minor role in the interaction of spherical nanocrystals [31, 32, 30]. As our simulations indicate, this is also true for small nanocrystals, where the ligand length is larger, or close to the dimension of the nanocrystals (see Subsection 7.2.6).

We expect significant solvation forces for nanocrystals with extended facets and dense ligand shells. To our knowledge, ligand-passivated CdS nanorods are the only other apolar colloidal system with ligand passivated nanocrystals where strong solvation forces have been observed so far. Widmer-Cooper *et al.* have demonstrated that solvation forces strongly influence their interaction [33, 34]. There are two crucial differences to the CdSe nanoplatelets. Although the facet areas of the nanorods are also large, the side lengths of the rectangular facets are unequal. One side length is very long, while the other is short. In addition, the ligand grafting density is significantly lower at the nanorods than on the CdSe nanoplatelets. Therefore, the ligands have more space, and the solvent layering is less pronounced. As our analysis of the solvent restructuring suggests, these properties lead to a greater temperature effect (see Subsection 6.2.5). Widmer-Cooper *et al.* have found a temperature dependent order-disorder transition in the ligand shell. The ligand molecules form bundles at lower temperatures. These ligand bundles promote the solvent layering. At higher temperatures, the bundles disintegrate and the solvent layering becomes less pronounced. Accordingly, the attraction due to the solvation forces vanish at higher temperatures. With a larger ligand grafting density and with wider facets, the solvent layering would be less sensitive to the temperature, and the order-disorder transition would be weaker. This system illustrates that strong solvation forces can occur even when the ligand density and geometry actually indicate weak solvation forces.

Nanocrystals that behave very similar to CdSe nanoplatelets are $CsPbBr_3$ perovskite nanoplatelets [39]. Prabhakaran *et al.* have synthesized perovskite nanoplatelets with a facet area of around $168\,\mathrm{nm}^2$, and a thickness of around 3-4 nm. They have found that these platelets can also form stacks. Based on our results, we assume that solvation forces play a significant role here. However, we must consider the subtleties. Prabhakaran *et al.* have passivated the facets of the nanoplatelets with Cs- and Pb-oleate ($PbC_{18}H_{34}O_2$) and oleylammonium-Br ($C_{18}H_{38}BrN$). Furthermore, they have used toluene as the solvent. It would be very intriguing to find out how the two types of ligands influence each other, and how toluene behaves as a solvent. Of course, the effect of other interactions would also have to be considered in this system. However, probably because solvation forces between ligand passivated nanocrystals have not been in the focus of the scientific community, solvation forces have not been investigated for this system yet. Therefore, a closer look at the interactions in this system would be particularly interesting.

In general, we expect that solvation forces will play a crucial role in the interactions of nanocrystals with extended flat facets, well-defined and even ligand-solvent interfaces, and large ligand packing densities. It would be interesting to investigate further colloidal systems with the methods which we use here.

Appendix A

Additional results

In this part of the appendix, we present complementary results to different sections of the thesis. We name the sections according to the complemented chapters and sections.

A.1 Chapter 6: Solvent restructuring at ligand brushes

A.1.1 Infinite facets with the MARTINI model

In Chapter 6, we study how the solvent restructuring at the ligand-solvent interface depends on different parameters. For the ligand grafting density, the ligand length, and the n-alkane solvent length, we also run simulations with the MARTINI infinite facet setup (see Section 5.1 for a description of the setup). Here, we present these additional results.

The TraPPE-UA force field provides a representation that is very close to an atomistic description. Whereas, the resolution of the MARTINI force field is considerably reduced. While we observe similar trends with the MARTINI force field as with the TraPPE-UA force field, it is important to be aware of the differences. The most obvious difference between the force fields is that the C1 MARTINI beads are larger than the CH_x. The impact of this is particularly evident when comparing different ligand grafting densities (Figure A.1). Here, we find that the solvent restructuring increases from 2.7 ligands / nm^2 to 3.6 ligands / nm^2, similar to the trend in the united atom approach in Figure 6.3. However, the trend breaks for 4.2 ligands / nm^2. Here, the solvent restructuring is less pronounced, as for 3.6 ligands / nm^2. The reason is simple. Due to their size, the ligand beads have not enough space. Therefore, the ordering within the ligand shell changes. Some ligands shrink, while some extent. This is visible in the ligand density, where secondary maxima appear, and which extends further into the solvent. As a result, the surface of the ligand-solvent interface gets uneven, which disturbs the solvent layering.

In Figure A.3, we plot the densities for different ligand length. Similar to the result from the TraPPE-UA setup, we find that the solvent restructuring is less pronounced in the simulation with five ligand beads than in the simulation with four ligand beads (compare with Figure 6.4). However, there is a deviation from the trend for the simulation with three ligand beads. This we can attribute to the change that we find in the ligand density. Here, the peaks are less pronounced, and the ligand density reaches further into the solvent. Accordingly, we find more solvent molecules within the ligand shell. A reason

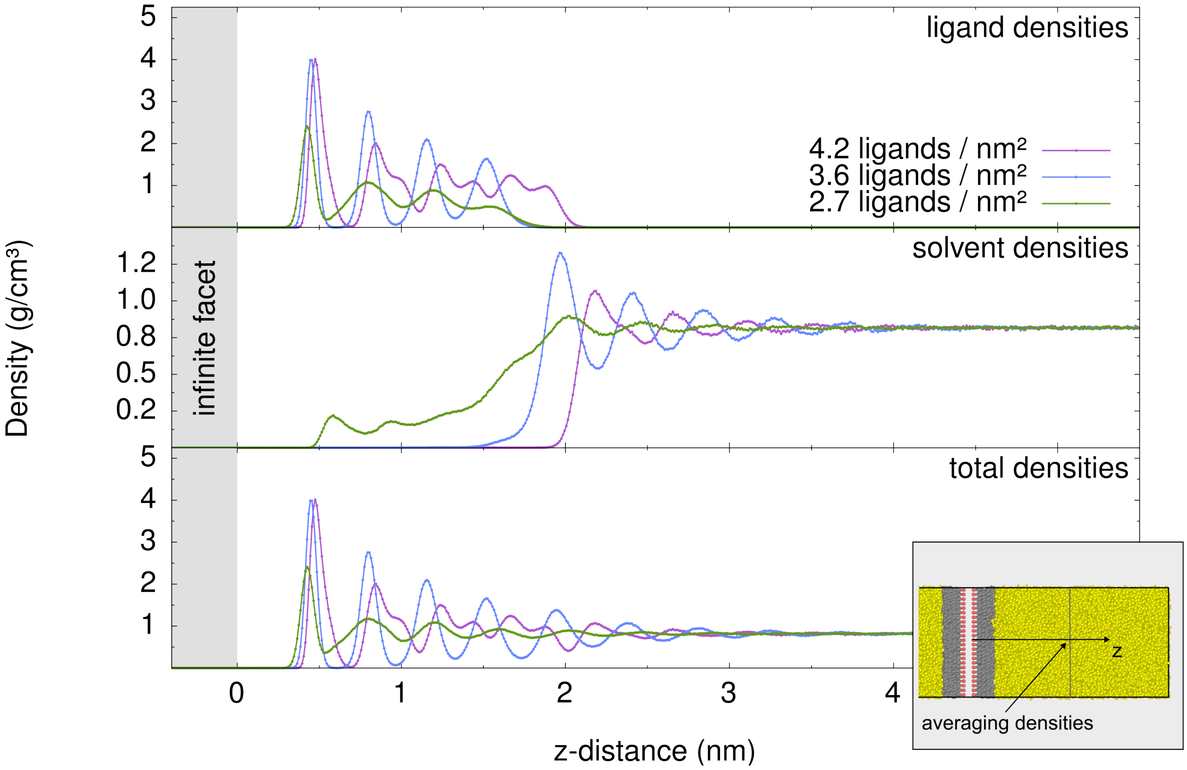

Figure A.1: Comparison of different ligand grafting densities in the infinite facet setup with the MARTINI force field. The top panel shows the ligand, the middle panel the solvent, and the bottom panel the total densities. As depicted in the inset, the densities at each distance z are averaged over the whole xy-plane, and time averaged. For clarity, the data points are connected with straight lines.

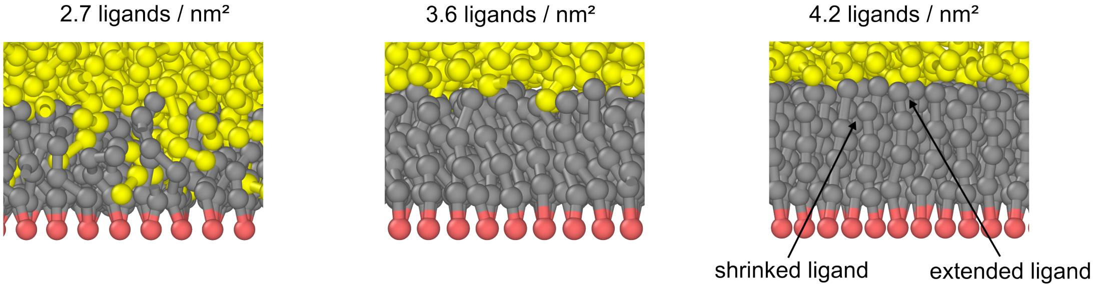

Figure A.2: Comparison of the ligand grafting density by cross-sectional snapshots of the infinite setup with the MARTINI model. The ligand shell with 2.7 ligands / nm^2 is softer than the ligand shell with 3.6 ligands / nm^2. The ligand shell with 4.2 ligands / nm^2 is so hard that some ligands shrink, while others extend. The result is an uneven surface.

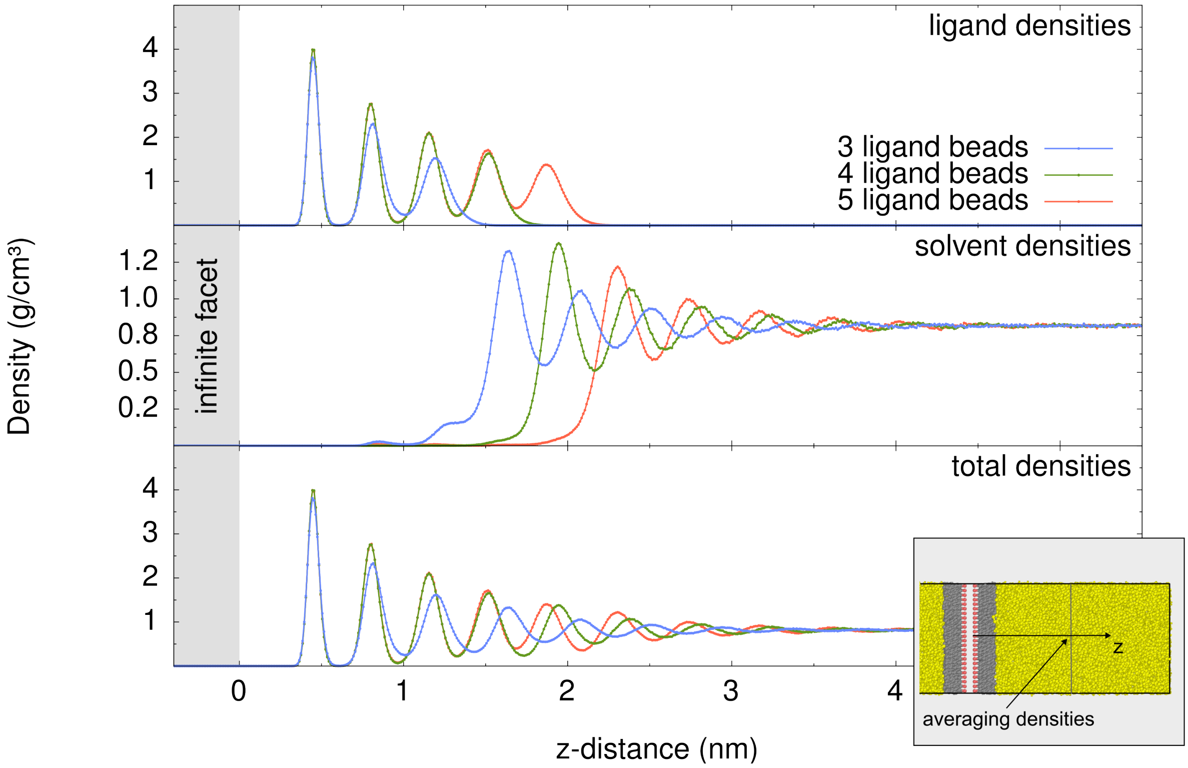

Figure A.3: Comparison of different ligand lengths in the infinite facet setup with the MARTINI force field. The top panel shows the ligand, the middle panel the solvent, and the bottom panel the total densities. As depicted in the inset, the densities at each distance z are averaged over the whole xy-plane, and time averaged. For clarity, the data points are connected with straight lines.

could be the surface potential, which has a cutoff of $r_{\text{cutoff}} = 2.5\sigma = 1.55\,\text{nm}$. Therefore, the solvent molecules come in its influence range. We should note that we do not find such a deviation in the densities of a finite nanoplatelet (see Figure 7.10).

We compare different solvent n-alkane chain lengths in Figure A.4. Similar to the results from the TraPPE-UA setup, we find that the solvent layering increases with the chain length (compare with Figure 6.5).

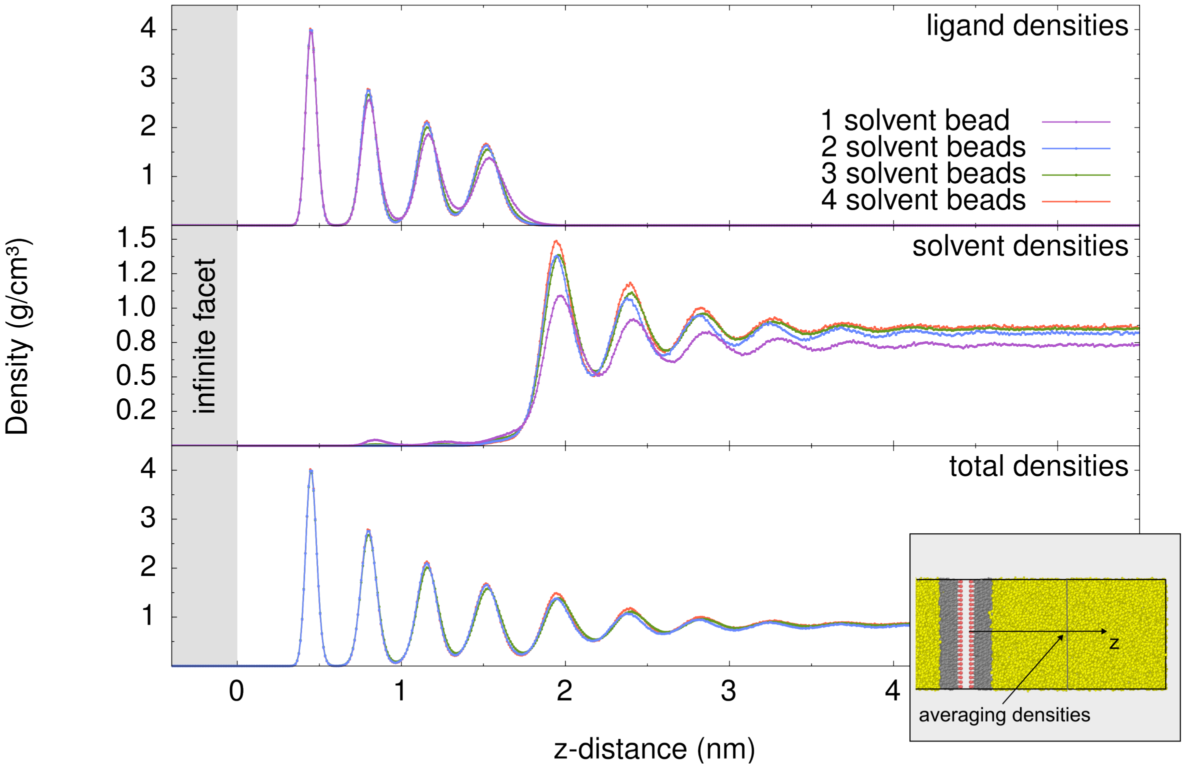

Figure A.4: Comparison of different solvent n-alkane chain lengths in the infinite facet setup with the MARTINI force field. The top panel shows the ligand, the middle panel the solvent, and the bottom panel the total densities. As depicted in the inset, the densities at each distance z are averaged over the whole xy-plane, and time averaged. For clarity, the data points are connected with straight lines.

A.2 Chapter 7: CdSe nanoplatelets pair interaction

A.2.1 Characterization of nanoplatelet stacks

In this section, we present additional results to Section 7.2.1.

A.2.1.1 Time series of the center-center distances in different setups

In Figure A.5, we show the time series of the center-center distances from the simulations with two nanoplatelets that are initiated in the not assembled state. We compare nanoplatelets with facet areas between 20.0 nm^2 and 55.7 nm^2, with a fixed thickness of 1.5 nm. Independent of the facet area, do not observe assembling of the nanoplatelets within the simulation time. The time series for 55.7 nm^2 differs from the others, since we use 350k solvent molecules instead of 100k solvent molecules in the simulation (see Table B.7). The simulation box is larger, and therefore the maximal possible distance between two nanoplatelets in the box (see dashed lines in Figure A.5).

For the simulations with three nanoplatelets that are initiated in the assembled stack state, we show the trajectories in Figure A.6. The stack consistent of nanoplatelets with 20 nm^2 base facet area disassembles fast (top panel), while the stack consistent of nanoplatelets with 45.1 nm^2 is stable (bottom panel). The trajectories of the simulations that are initiated in the not assembled state are plotted in Figure A.7. Again, we do not observe assembling.

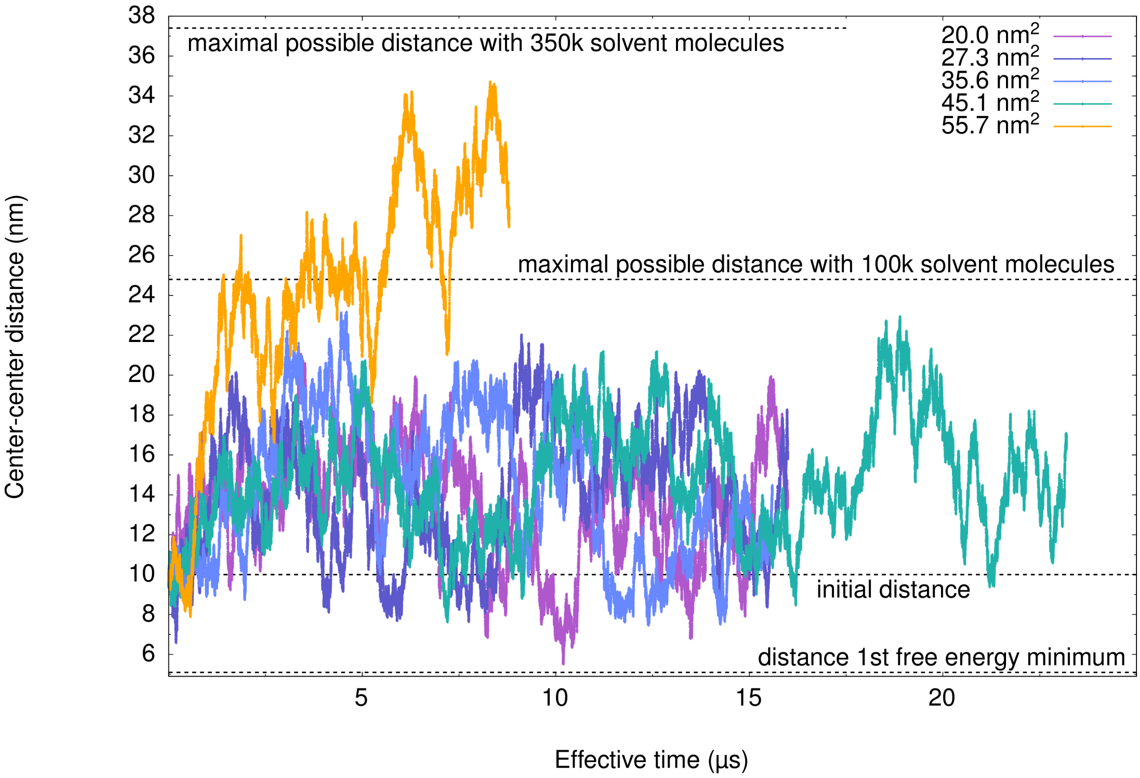

Figure A.5: Time series of the center-center distances from the simulations with two nanoplatelets that are initiated in the not assembled state [96]. The base facet area is varied between 20.0 nm^2, and 55.7 nm^2. In the simulation with 55.7 nm^2 base facet area, we include 350k solvent molecules, while we use only 100k in the other simulations (see Table B.7). Therefore, the simulation box is larger, as well as the theoretical maximal possible distance between the nanoplatelets. The noticeable difference in the time series between 55.7 nm^2 and the other facet sizes is due to this. We mark the initial distances, the distance of the 1st free energy minima, and the maximal possible distances with dashed lines.

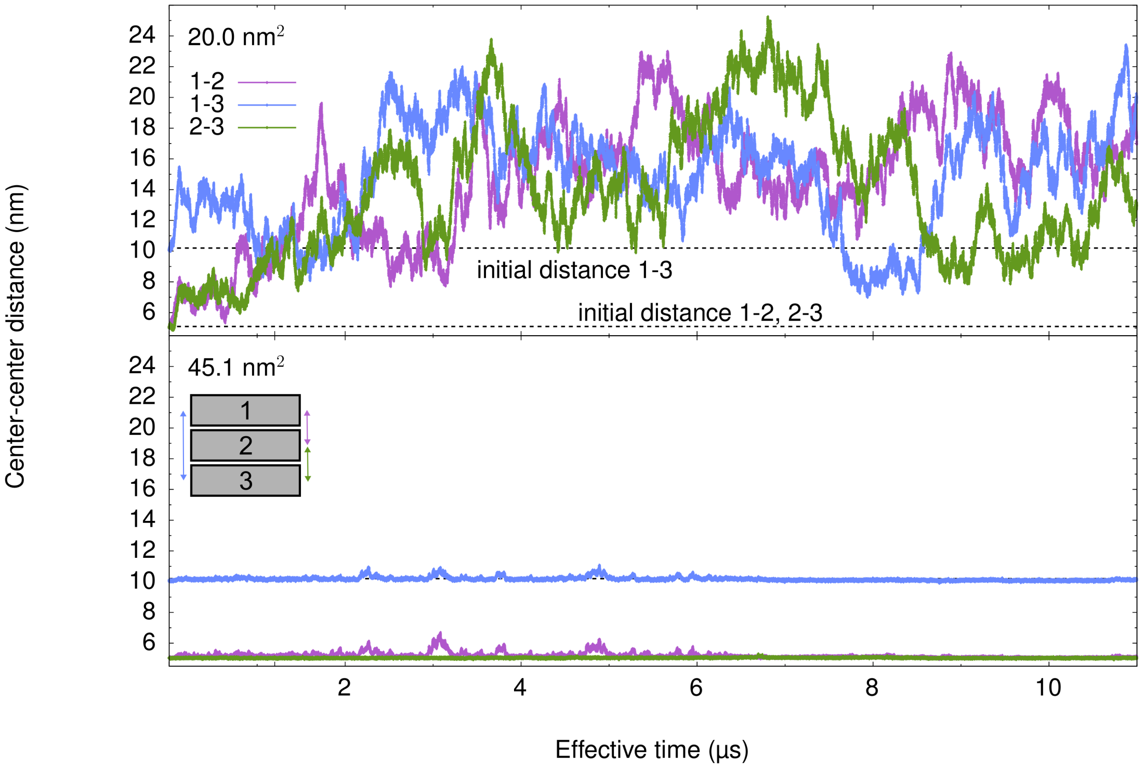

Figure A.6: Time series of the center-center distances for the simulations with three nanoplatelets that are initiated in the stack configuration [96]. The nanoplatelets are labeled as number 1, 2, and 3 (see key). 20.0 nm^2 base facet area **(top panel)** is compared to 45.1 nm^2 base facet area **(bottom panel)**.

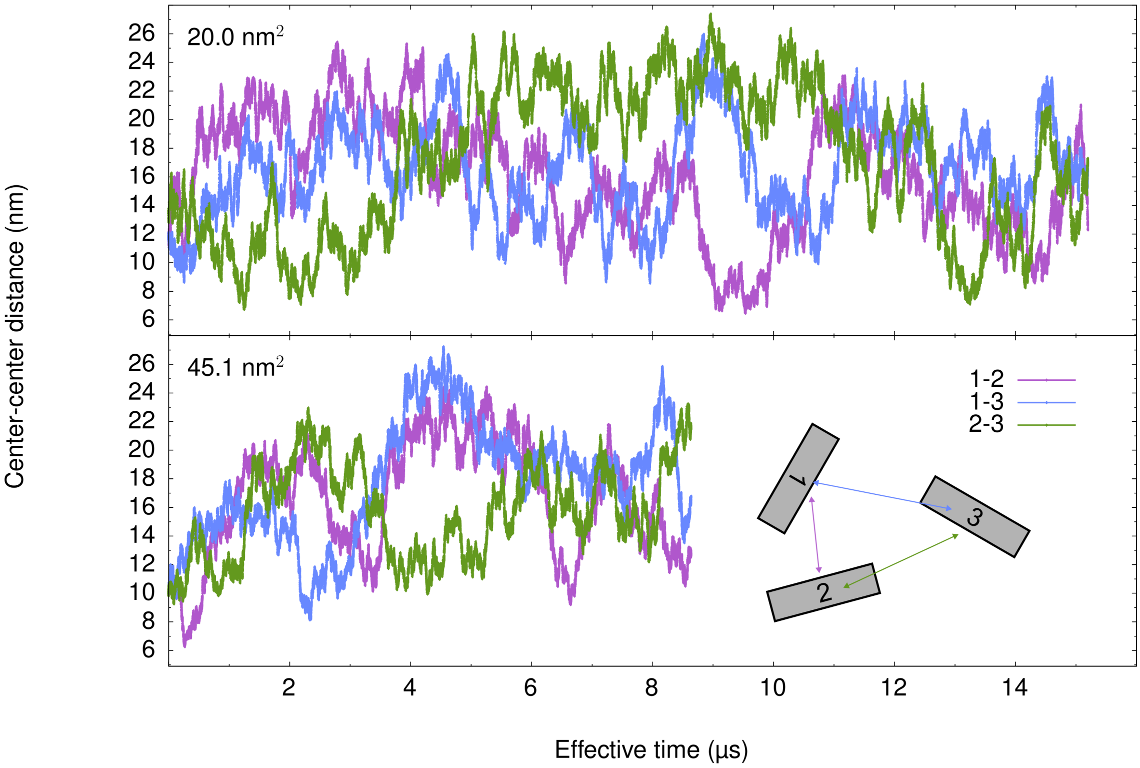

Figure A.7: Time series of the center-center distances for the simulations with three nanoplatelets that are initiated in the not assembled configuration. The nanoplatelets are labeled as number 1, 2, and 3 (see key). $20.0\,\mathrm{nm}^2$ base facet area **(top panel)** is compared to $45.1\,\mathrm{nm}^2$ base facet area **(bottom panel)**.

A.2.1.2 Mean square displacement

We calculate the mean square displacements (MSD) of simulations that are initiated in the not assembled configuration. As we have only a few nanoplatelets, we calculate the MSD by a time average:

$$\mathrm{MSD}(\tau) = \frac{1}{\#_{\mathrm{platelets}}} \sum_{j=1}^{\#_{\mathrm{platelets}}} \frac{1}{N} \sum_{i=1}^{N} \left(\vec{R}(t_i + \tau) - \vec{R}(t_i) \right)^2 . \tag{A.1}$$

Thereby, is $\#_{\mathrm{platelets}}$ the number of nanoplatelets, t_i a timestep, and τ the lag time. The number of reference frames taken into account N varies dependent on τ and the length of the trajectory.

For the simulations with two nanoplatelets, the MSDs are plotted in Figure A.8. The MSDs of the simulations with three nanoplatelets are shown in Figure A.9.

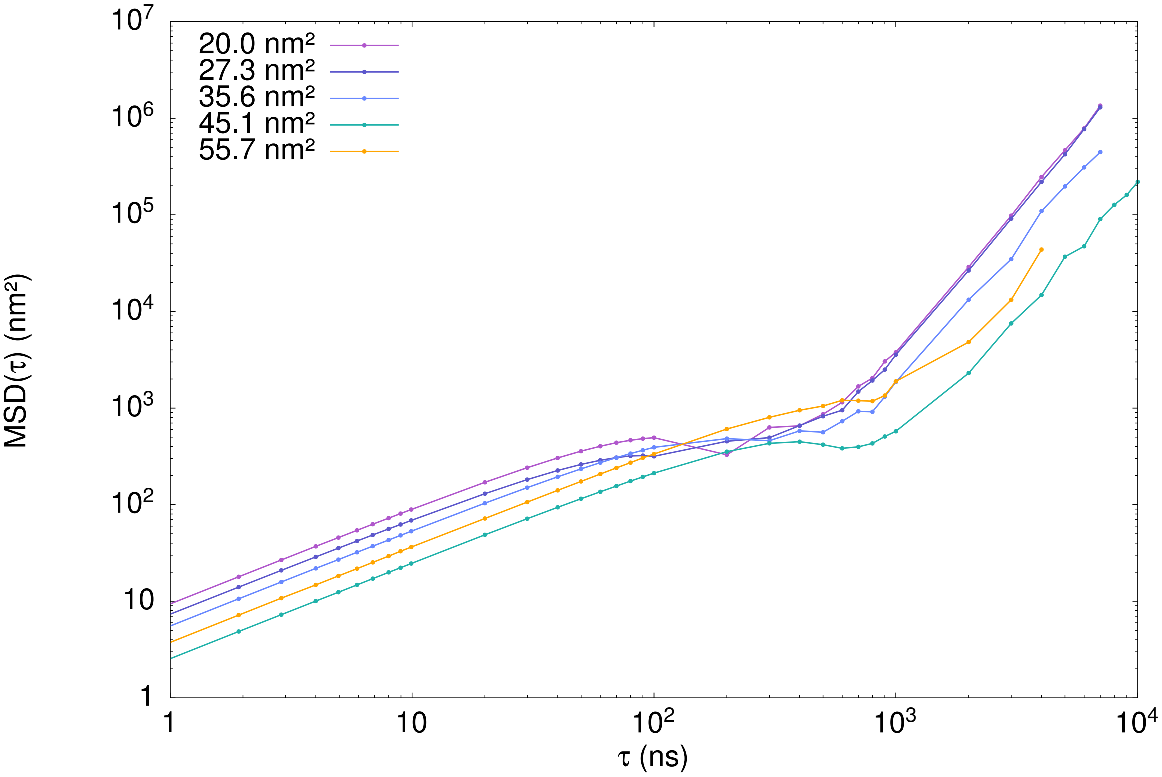

Figure A.8: Mean square displacement of the simulations with two nanoplatelets [96]. Simulations are initialized in the not assembled state.

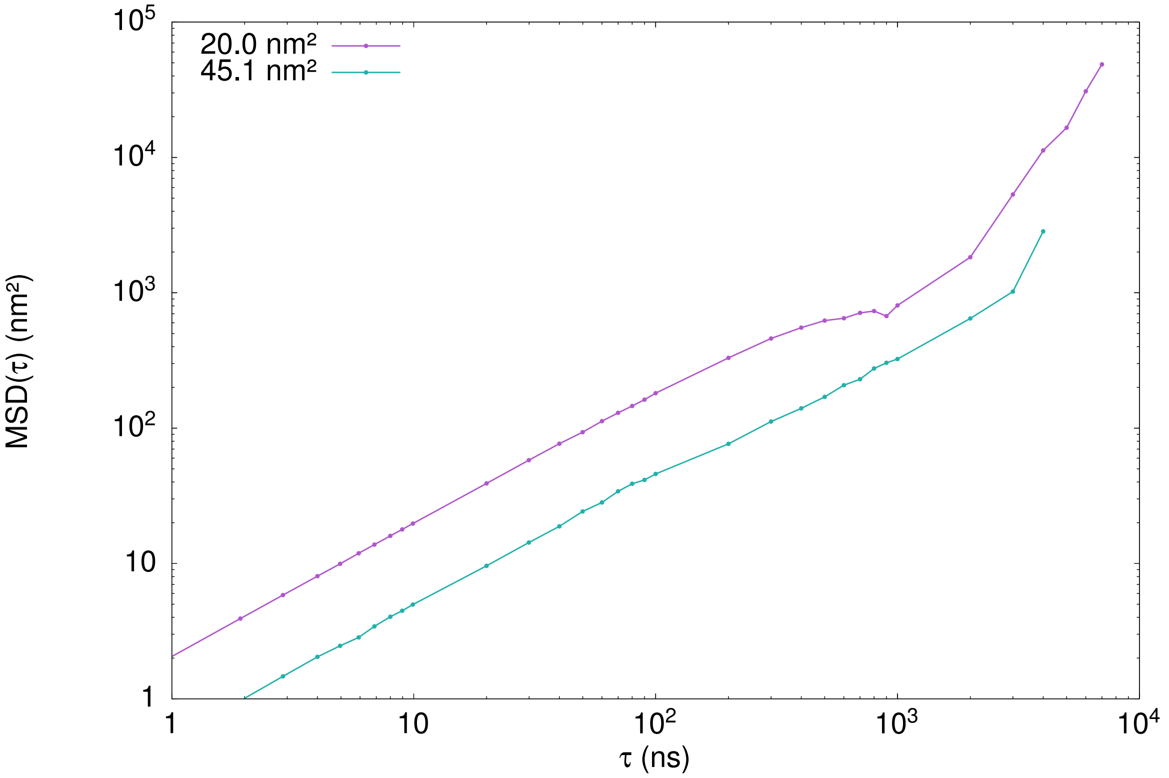

Figure A.9: Mean square displacement of the simulations with three nanoplatelets [96]. Simulations are initialized in the not assembled state.

A.2.2 Section 7.2.2: Interaction mechanism

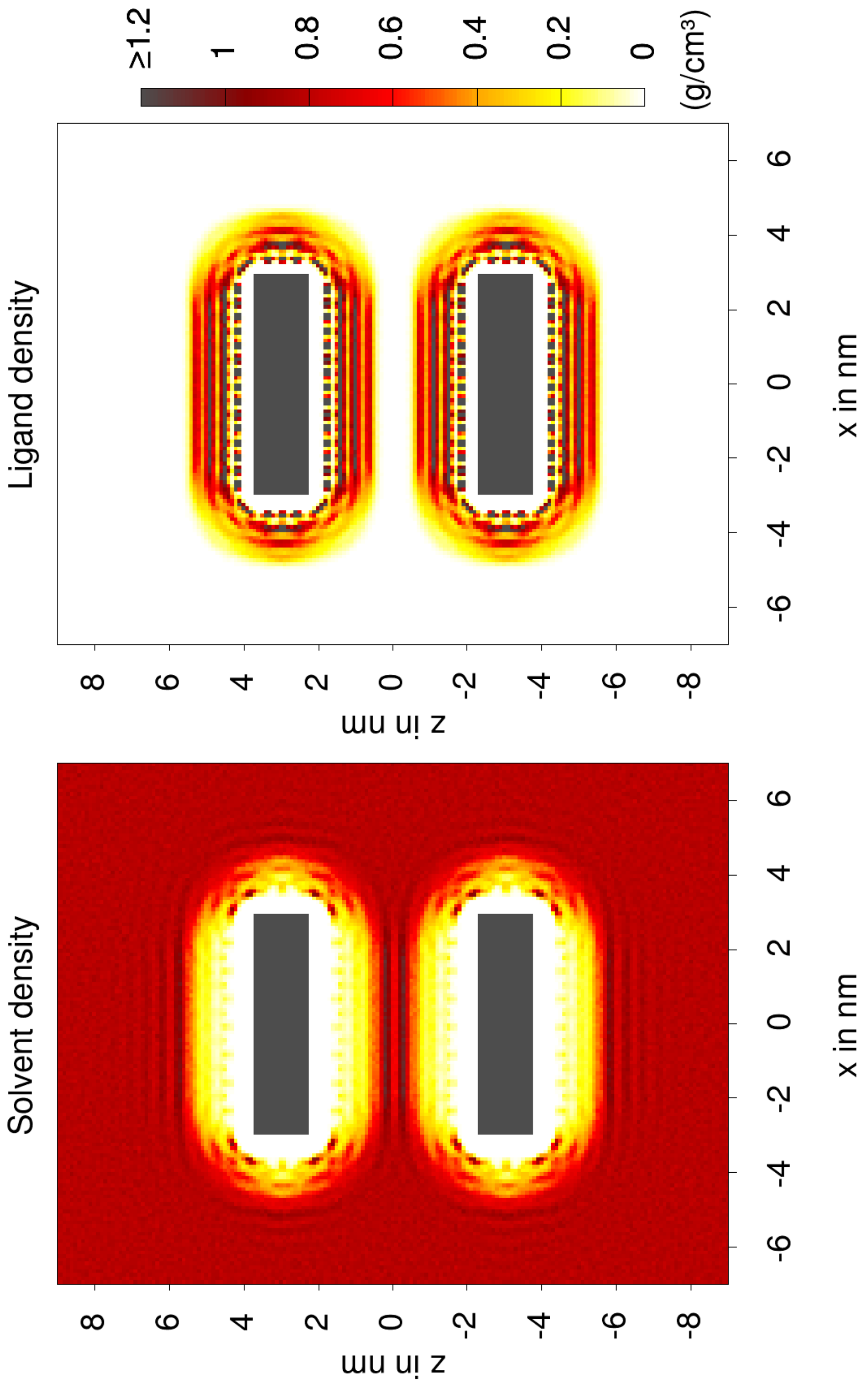

Figure A.10: Heatmaps of the solvent (left) and ligand (right) densities. Shown is the 3rd free energy minimum from the face-to-face approach (see Figure 7.3b, e).

A.2.3 Section 7.2.4: Ligand grafting density

Similar to Figure 7.12 in Section 7.2.6, we plot the free energy values of the first three minima, and the first two maxima over the ligand grafting density (Figure A.11). The free energy values at the extrema increase with the ligand grafting density.

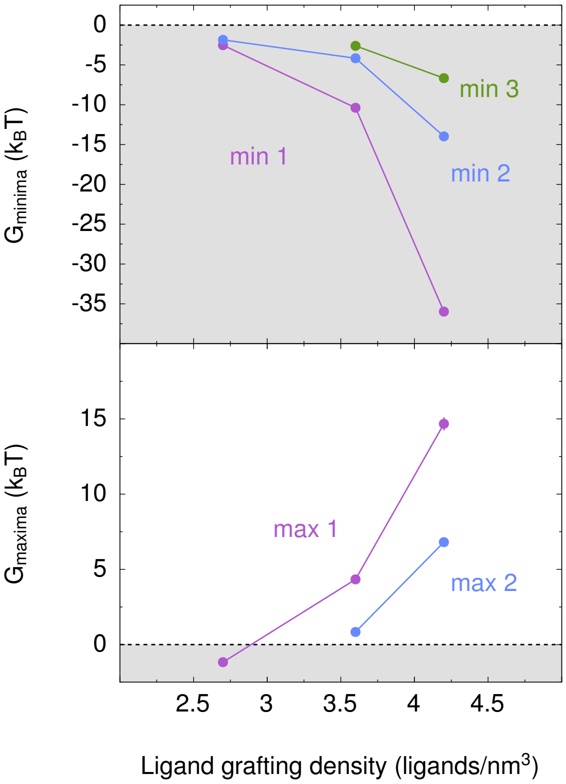

Figure A.11: The strength of the face-to-face interaction between two nanoplatelets depends on the ligand grafting density [96]. Free energy values of selected extrema are plotted over the ligand grafting density. The data points are connected with straight lines to guide the eyes.

A.2.4 Chapter 7.2.5: Ligand length

Also for the ligand length, we plot the free energy values of the first three minima, and the first two maxima (Figure A.12). The free energy values at the extrema decrease with the ligand length.

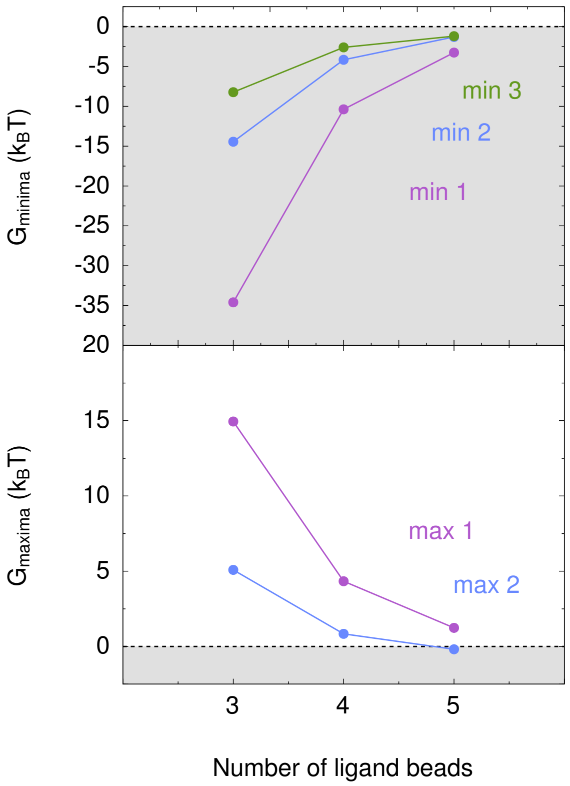

Figure A.12: The strength of the face-to-face interaction between two nanoplatelets depends on the ligand length [96]. Free energy values of selected extrema are plotted over the ligand length. The data points are connected with straight lines to guide the eyes.

A.2.5 Section 7.2.7: Nanoplatelet thickness

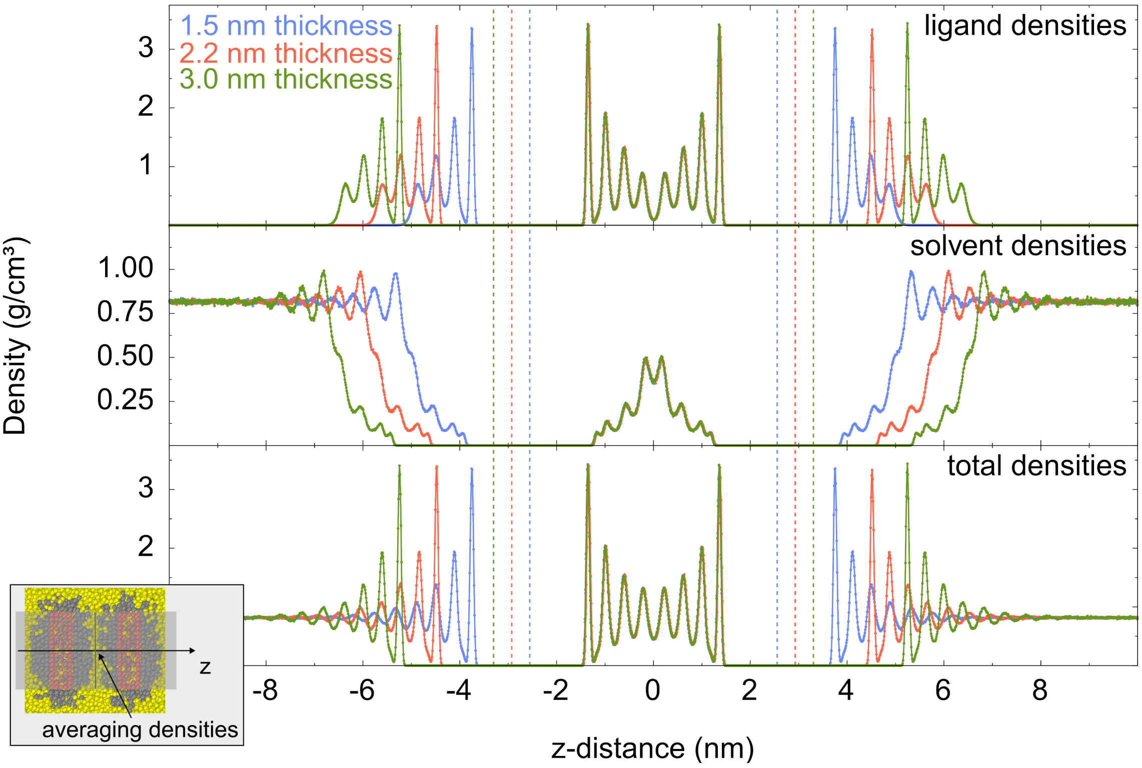

Figure A.13: Ligand and solvent densities at the first free energy minimum for nanoplatelets with 1.5 nm thickness, 2.2 nm thickness, and 3.0 nm thickness. The positions of the nanoplatelets are indicated with dashed lines in the corresponding color. The top panel shows the ligand, the middle panel the solvent, and the bottom panel the total densities. As depicted in the inset, the densities at each distance z are averaged over the whole base facet area in the corresponding xy-plane, and are time averaged. For clarity, the data points are connected with straight lines.

A.3 Chapter 8: Experimental validation

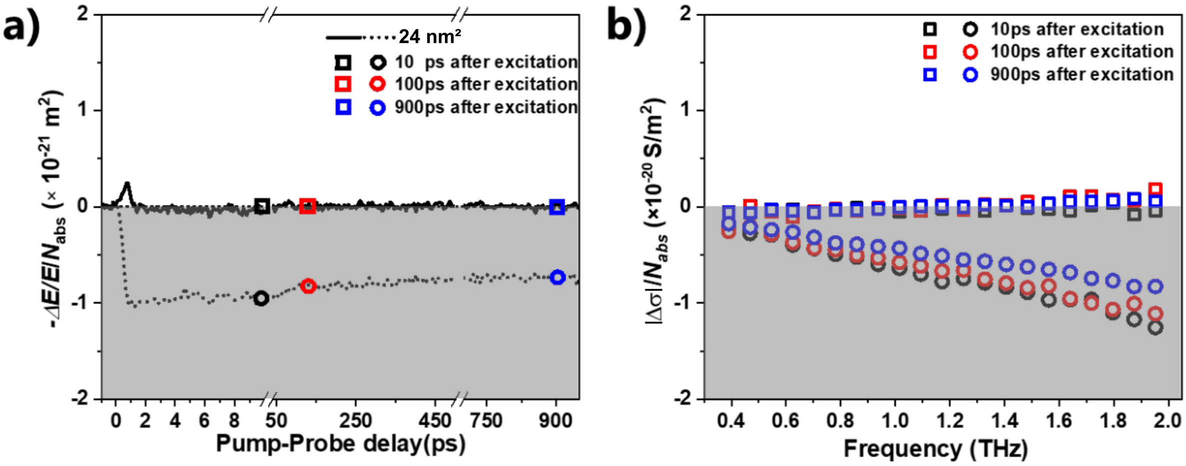

Figure A.14: Additional results. The base facet area is around 24 nm^2, and the solvent is n-hexane. **Panel a** shows the measured real and imaginary component of the photoconductivity before and after the pump pulse (0.0 ps), and **panel b** shows the frequency resolved imaginary component of the photoconductivity. The figure originates from Shuai Chen's dissertation and has been adapted [130].

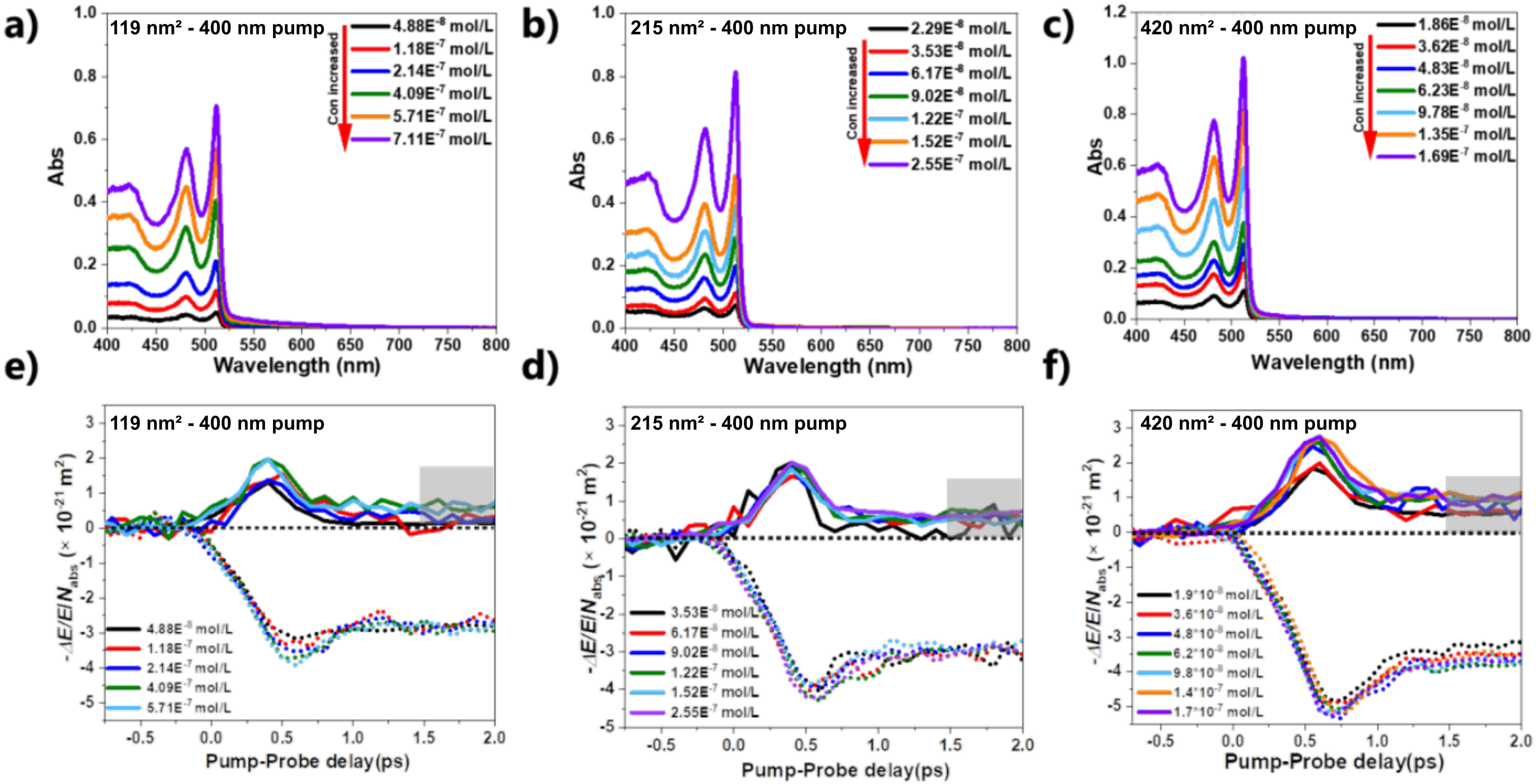

Figure A.15: Additional experimental data from the experiments with different base facet areas. The **panels a-c** show absorption spectra of nanoplatelets in n-hexane with base facet areas around 119 nm^2 (**panel a**), 215 nm^2 (**panel b**), and 420 nm^2 (**panel c**). The **panels d-f** shows the measured real component of the photoconductivity before and after the pump pulse (0.0 ps). The concentration is varied in all panels. The figure originates from Shuai Chen's dissertation and has been adapted [130].

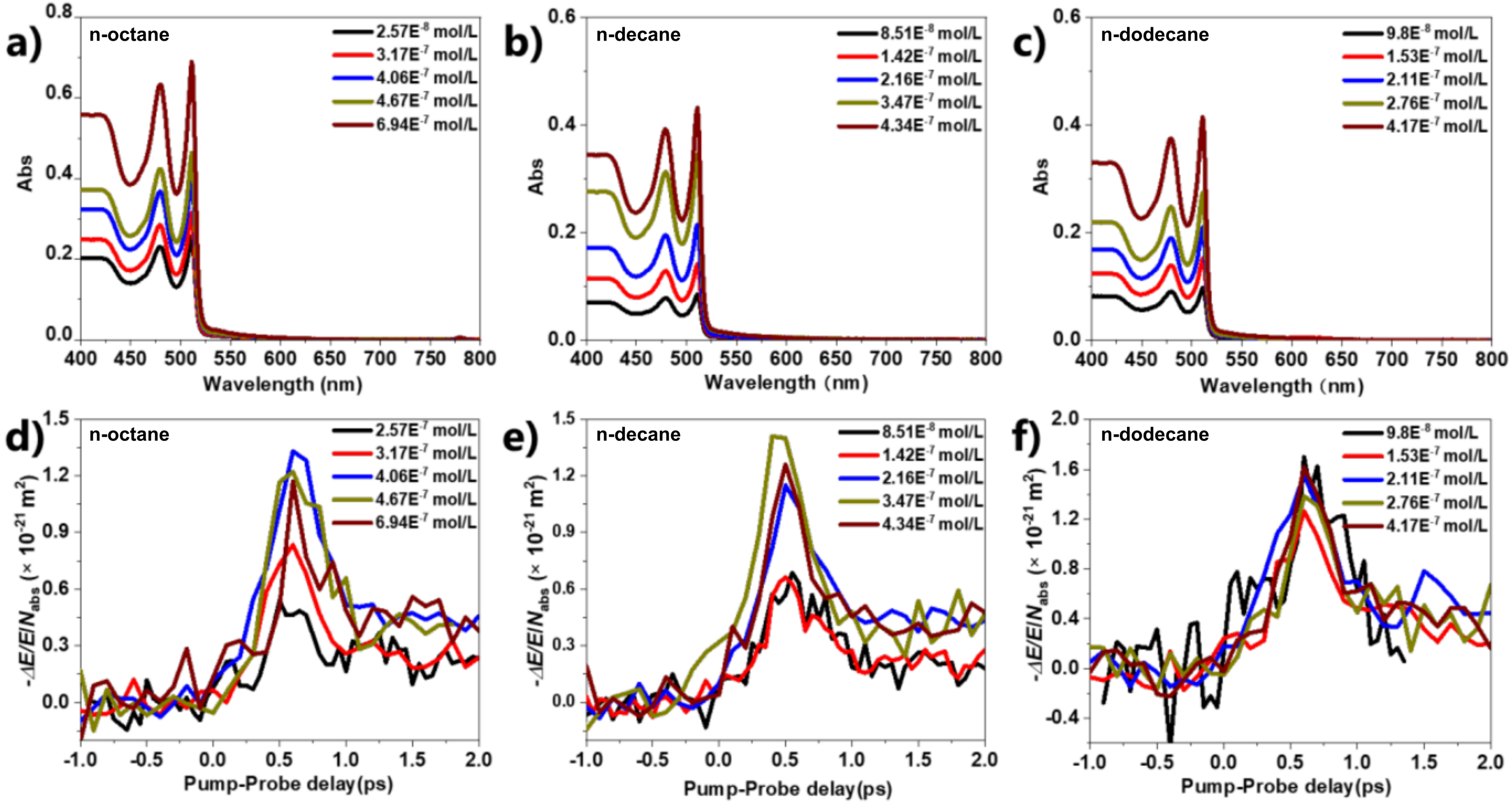

Figure A.16: Additional experimental data from the experiments with different n-alkane solvents. The **panels a-c** show absorption spectra of nanoplatelets in n-octane (**panel a**), n-decane (**panel b**), and n-dodecane (**panel c**). The **panels d-f** shows the measured real component of the photoconductivity before and after the pump pulse (0.0 ps). The concentration is varied in all panels. The figure originates from Shuai Chen's dissertation and has been adapted [130].

Appendix B

Simulation details and benchmarks

In this part of the appendix, we present complementary simulation details and benchmarks. We name the sections according to the complemented chapters and sections.

B.1 Chapter 6: Solvent restructuring at ligand brushes

B.1.1 Simulation details

In the Tables B.1-B.5, we list for each simulation in Chapter 6 the number of solvent molecules, and the side lengths of the simulation box.

The periodic simulation boxes of the simulations with the finite nanoplatelets are cubic ($x = y = z$, see Section 5.2). Here, we list the averaged z-side lengths. The periodic simulation boxes of the simulations with the infinite facets have a square base. The side lengths of the square base do not change during a simulation ($x = y =$ constant). The z-side length of the simulation boxes are varied to control the pressure (see Section 5.1). We list the constant x, y-side lengths, and the averaged z-side length.

Facet area (nm^2)	# of solvent molecules	x, y side length (nm)	Average z-side length (nm)
5.9	50k		24.0
9.2	50k		24.0
13.3	50k		24.0
18.1	50k		24.1
23.7	50k		24.1
29.9	50k		24.2
37.0	50k		24.2
infinite facet	6k	9.7	22.4

Table B.1: Details for the simulations with different facet areas in Section 6.2.1.

Facet area (nm^2)	Ligand grafting density (ligands/nm^2)	# of solvent molecules	x, y-side length (nm)	Average z side length (nm)
37.0	2.7	50k		34.6
37.0	3.5	50k		34.6
37.0	4.4	50k		34.7
37.0	5.4	50k		34.8
infinite facet	3.8	7k	10.2	22.4
infinite facet	4.7	6k	9.4	23.2
infinite facet	5.4	6k	9.7	22.4
infinite facet	6.7	6k	9.8	22.1

Table B.2: Details for the simulations with different ligand grafting densities in Section 6.2.2.

Facet area (nm^2)	# of ligand beads	# of solvent molecules	x, y side length (nm)	Average z side length (nm)
18.1	8	50k		34.3
18.1	12	50k		34.3
18.1	16	50k		34.4
18.1	20	50k		34.5
infinite facet	8	6k	9.7	20.4
infinite facet	12	6k	9.7	21.4
infinite facet	16	6k	9.7	22.4
infinite facet	20	6k	9.7	23.4

Table B.3: Details for the simulations with different ligand lengths in Section 6.2.3.

Solvent type	# of solvent molecules	x, y side length (nm)	Average z side length (nm)
n-hexane	2k	4.9	23.8
n-heptane	1.5k	4.9	20.7
n-octane	6k	9.7	22.4
n-nonane	1.5k	4.9	24.1
n-decane	1.5k	4.9	25.7
n-undecane	1.5k	4.9	27.4
n-dodecane	1.5k	4.9	29.1
n-tridecane	1.5k	4.9	30.8
n-tetradecane	1.5k	4.9	32.5
2-methylheptane	1.5k	4.9	22.6
3,4-dimethylhexane	1.5k	4.9	22.0
2,2,4-trimethylpentane	1.5k	4.9	22.8
1-octene	1.5k	4.9	20.5
1,7-octene	1.5k	4.9	20.1

Table B.4: Details for the simulations with different solvent types in Section 6.2.4.

Facet area (nm^2)	Temperature (K)	# of solvent molecules	x, y side length (nm)	Average z side length (nm)
18.1	280	50k		33.6
18.1	300	50k		34.4
18.1	320	50k		35.3
18.1	340	50k		36.3
18.1	360	50k		37.3
infinite facet	280	6k	9.7	22.0
infinite facet	300	6k	9.7	22.4
infinite facet	320	6k	9.7	22.8
infinite facet	340	6k	9.7	23.3
infinite facet	360	6k	9.7	23.8

Table B.5: Details for the simulations with different temperatures in Section 6.2.5.

B.1.2 Effect of the bin size in the density calculations

We check which bin size is suitable to calculate the densities in the TraPPE-UA setup. Our results for an infinite facet in n-hexane are shown in Figure B.1. A bin size of 0.01 nm is accurate enough to reproduce the important features of the densities. We use it in all further density calculations in the TraPPE-UA setups, and in the MARTINI setups.

It is worth noting that at high accuracy (small bin size), the density of the ligand shell oscillates. This is due to the limited flexibility of the ligand beads, especially close to the platelet facet surface. However, at low accuracy, the mean ligand density is constant within the ligand shell. Therefore, our results are consistent with the approximation that the ligand density inside the shell is constant [27]:

$$\delta_{\mathrm{lig}}(z) = \delta_0. \tag{B.1}$$

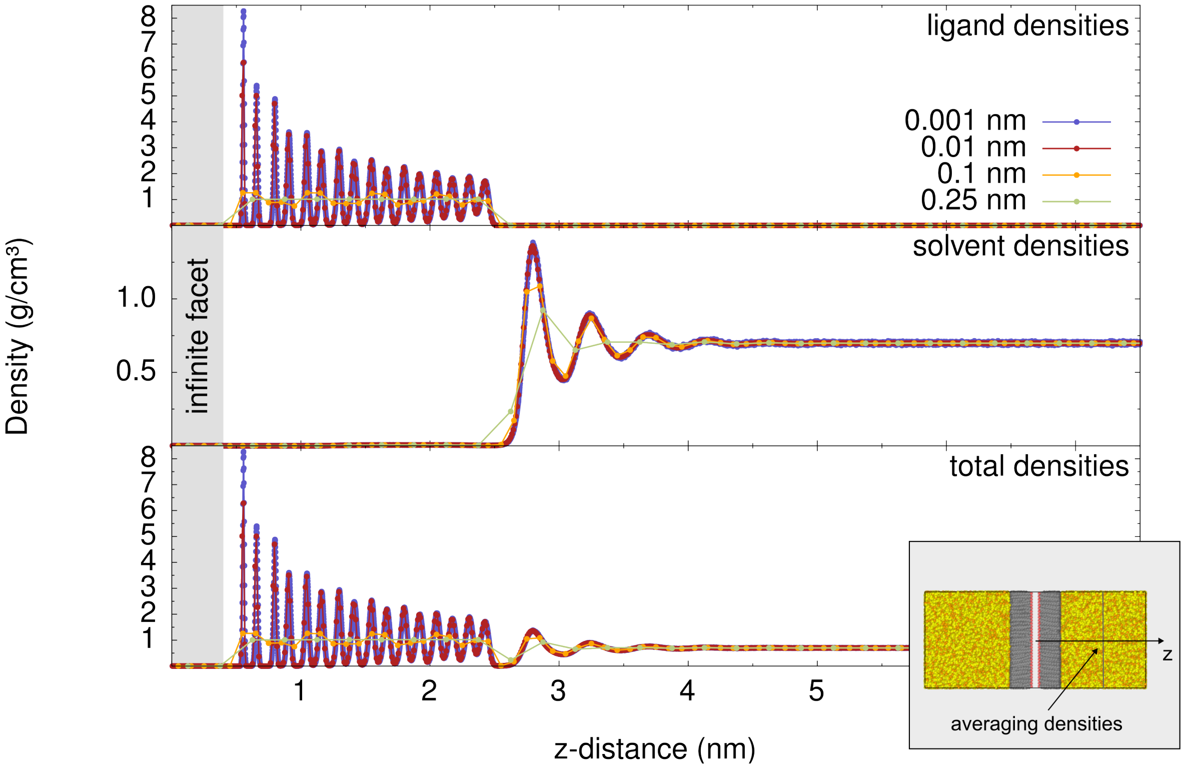

Figure B.1: Effect of bin size. The densities are calculated with different bin sizes: 0.001 nm, 0.01 nm, 0.1 nm, and 0.25 nm. The solvent is n-hexane. The top panel shows the ligand, the middle panel the solvent, and the bottom panel the total densities. As depicted in the inset, the densities at each distance in the z-direction result from the averaging over the entire xy-plane, and from time averaging. For clarity, the data points are connected with straight lines.

B.2 Chapter 7: CdSe nanoplatelets pair interaction

B.2.1 Parameter tests free energy curves

We test different parameters that influence the calculation of the free energy curves.

B.2.1.1 WHAM parameter tests

We use the WHAM code of Daniel Bauer [124] to calculate the free energy curves in Chapter 7. However, the accuracy of the free energy curves depends on the chosen parameters in the WHAM calculation. Therefore, we perform test calculations in the MARTINI setup for the number of bins, the tolerance, and the number of bootstrapping runs. In the Figures B.2-B.4, we show examples of the tests (face-to-face approach, 27.3 nm^2, 100k solvent molecules).

In Figure B.2, we show an example of the effect of the number of bins. We find that a too high number of bins leads to a high fluctuation, while a too low value creates a shift in the free energy curve. We chose 305 bins/nm for all further WHAM calculations. An example of the test of the tolerance is shown in Figure B.3. Here, we find that for tolerances smaller than 1e-06 kJ/mol the changes in the free energy are little. Therefore, we chose this value for all further WHAM calculations. In Figure B.4, we show an example for the test of different numbers of bootstrapping runs (bt). We find that the differences in the error bars are small. We chose to use ten bootstrapping runs to evaluate the errors in our free energy calculations.

We list the parameters we use for the calculation of the free energy curves in Table B.6.

Number of bins	Tolerance	Bootstrapping steps (bt)
305 bins / nm	1e-06 kJ/mol	10

Table B.6: WHAM parameters for the calculation of the free energy curves in Chapter 7.

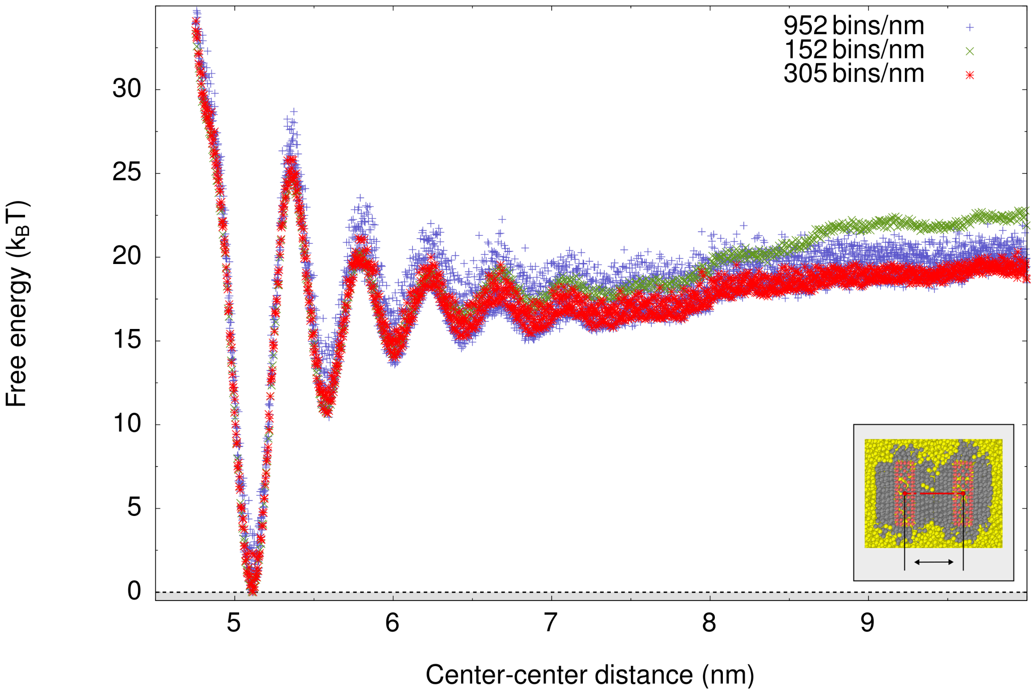

Figure B.2: Comparison of free energy curves that result from WHAM calculations with different numbers of bins [96].

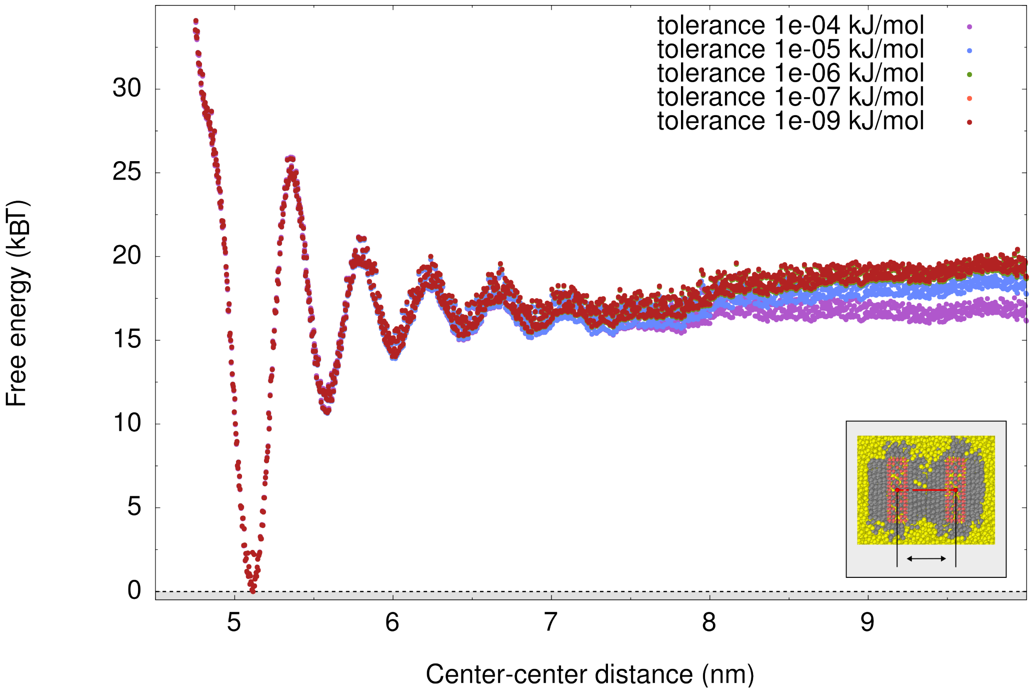

Figure B.3: Comparison of free energy curves that result from WHAM calculations with different tolerances [96].

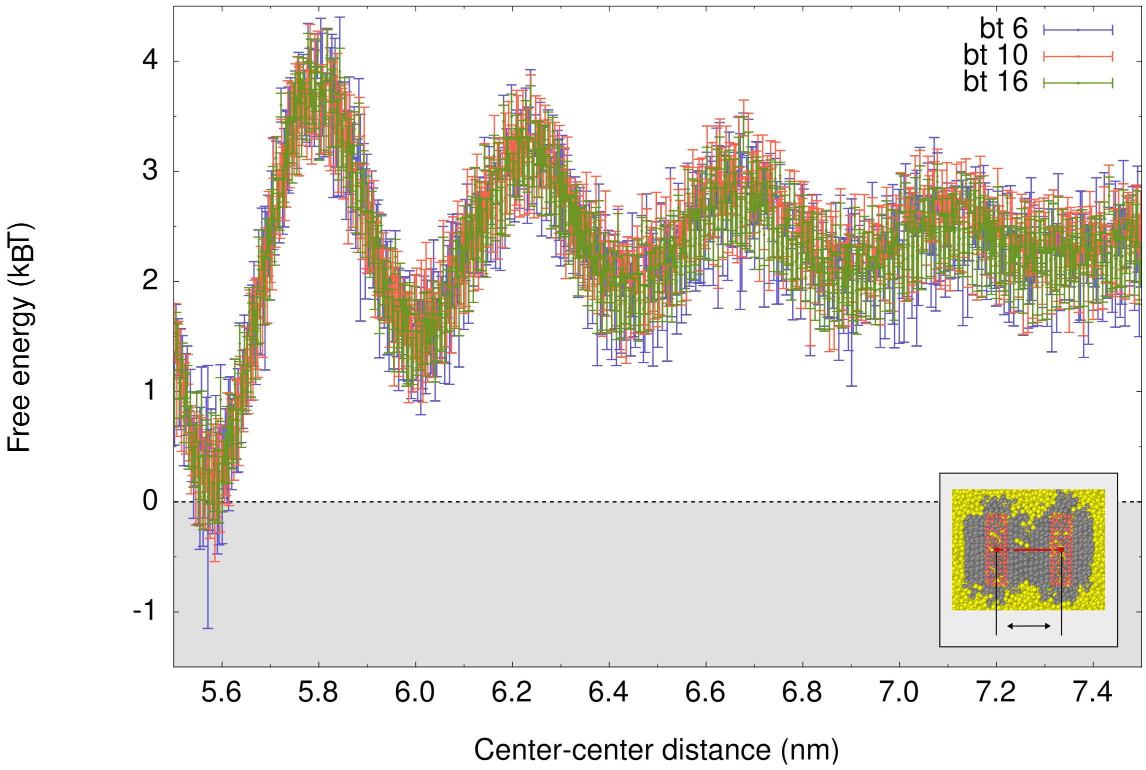

Figure B.4: Comparison of different numbers of bootstrapping runs (bt) [96].

B.2.1.2 Directional dependence of umbrella simulations

In Chapter 7, we start the umbrella sampling calculations always from an initial configuration, where the nanoplatelets have a small separation. We then move to larger distances. We describe the procedure in Section 5.5. If the outcome of Umbrella sampling is affected by the initial conditions, it may indicate that the simulations are not sufficiently converged [126]. To validate our free energy curves, we perform for selected systems umbrella simulations with an initial configuration, where the nanoplatelets have 10 nm center-center separation. In these test calculations, we move from large to small distances. We find no significant differences (Figure B.5).

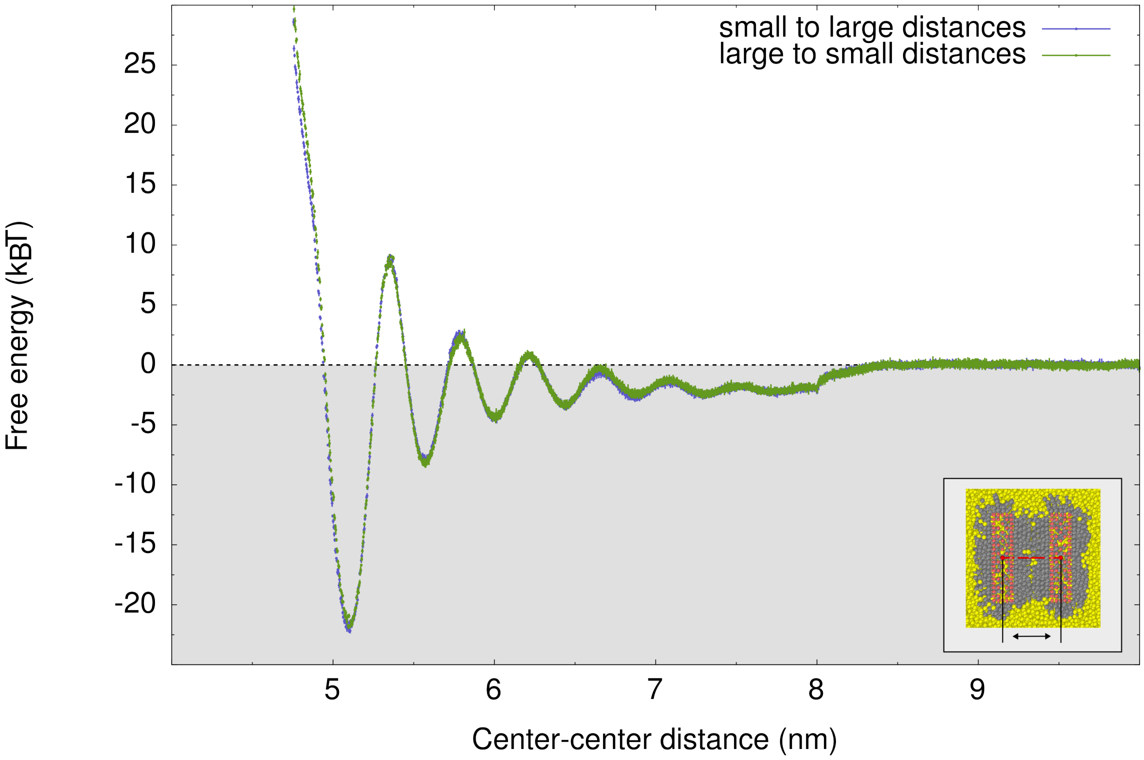

Figure B.5: Example free energy curves for the test of the directionality of the umbrella simulations [96]. We show the result from the system with the largest facet area (55.7 nm^2). The first free energy curve is calculated starting from an initial configuration, where the nanoplatelets have a center-center separation of 4.1 nm **(small to large distances)**. The second free energy curve is calculated starting from an initial configuration, where the nanoplatelets have a center-center separation of 10 nm **(large to small distances)**.

B.2.1.3 Box size

The periodic cubic simulation box must be large enough to avoid finite size effects. The required simulation box size depends on the nanoplatelet size as well as the solvent. In Figure B.6, we compare the box size for a nanoplatelet with 35.6 nm^2 facet area, and 1.5 nm thickness in n-octane. Here, the differences in the free energy curve are small. Therefore, for other simulations with nanoplatelets smaller or equal to this size in n-octane, we use 100k solvent molecules. However, for larger nanoplatelets, we have to increase the box size. In Figure B.7, we show the dependence of the box size for the free energy calculation with nanoplatelets with 3.0 nm thickness. Here, a too small simulation box significantly influences the free energy curve at larger separations. In general, we use larger simulation boxes with more solvent molecules in simulations with larger nanoplatelets, and longer solvent molecules (see Tables in Section B.2.2).

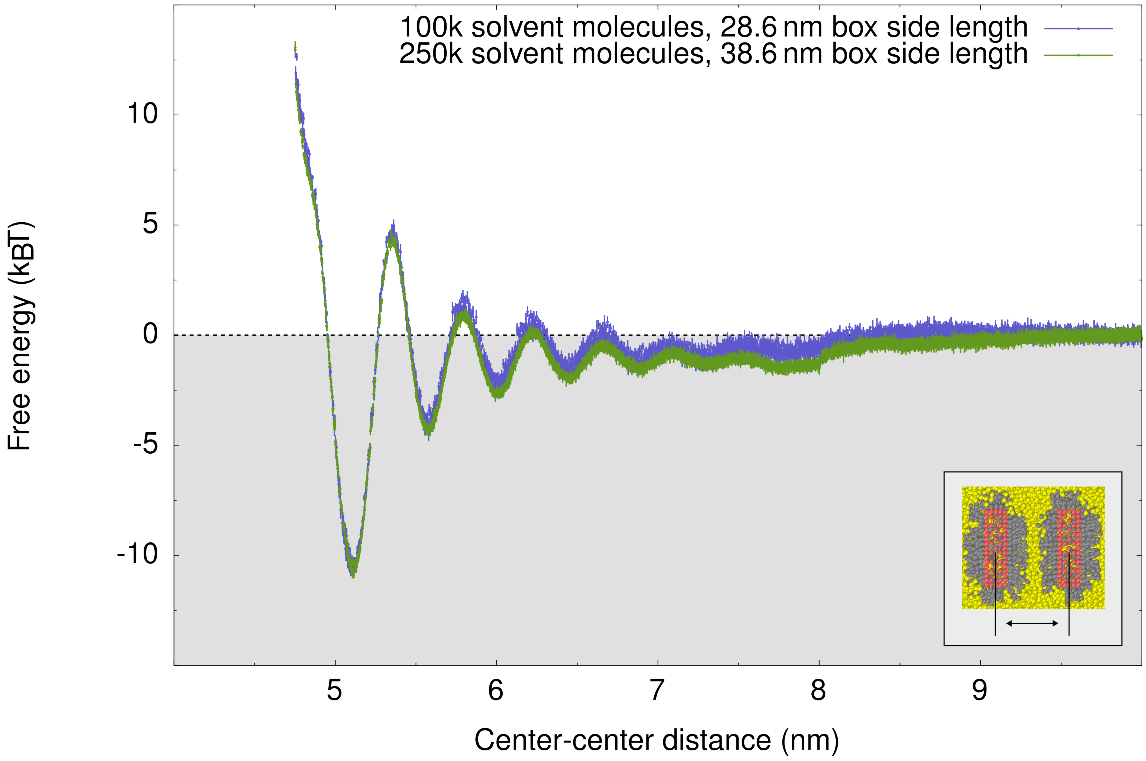

Figure B.6: Test of the box size, and number of solvent molecules for a nanoplatelet with 35.6 nm^2 facet area. In the simulation with 100k solvent molecules, the change in the equilibrium position between windows is $\Delta\lambda^{\text{ref}} = 0.005$ nm, while it is $\Delta\lambda^{\text{ref}} = 0.0025$ nm in the second system. For nanoplatelets with a thickness of 1.5 nm, and a facet area of ≤ 35.6 nm^2, 100k solvent molecules are sufficient. For larger nanoplatelets, more solvent molecules, and larger simulation boxes are required.

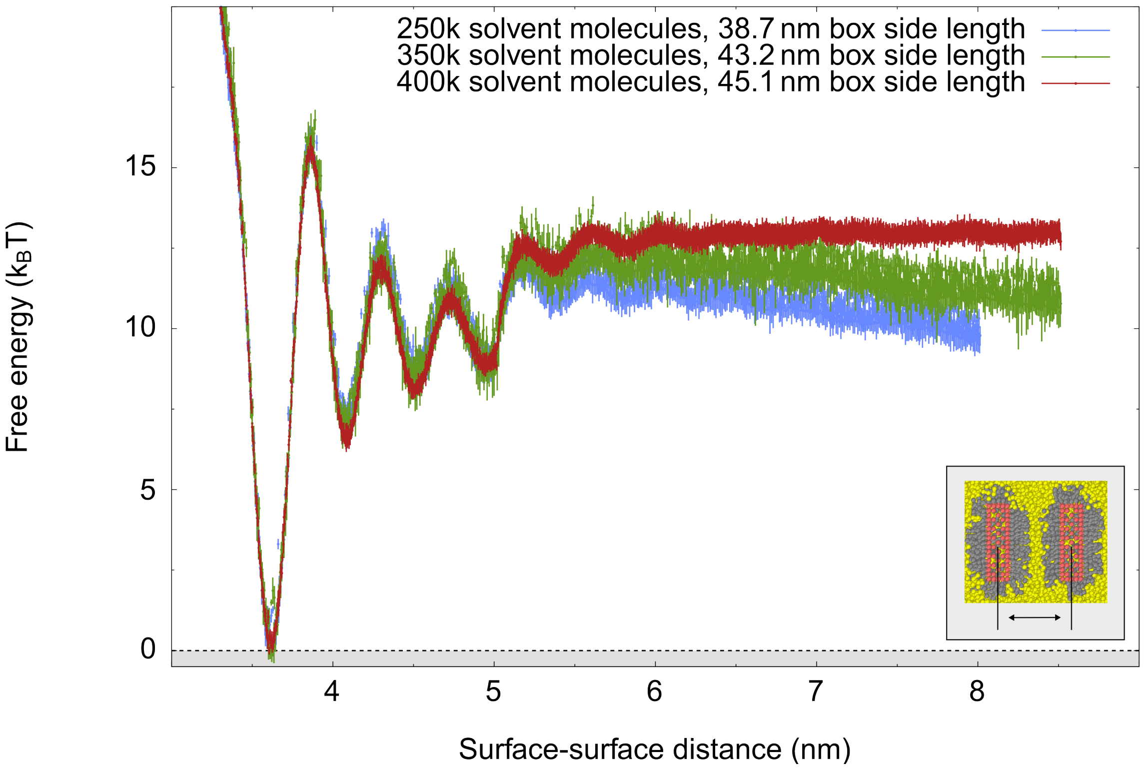

Figure B.7: Box size effect for 3.0 nm thick nanoplatelets. Again, the facet area 35.6 nm^2. In the simulations with 250k and 350k solvent molecules, the change in the equilibrium position between windows is $\Delta\lambda^{\mathrm{ref}} = 0.005$ nm, while it is $\Delta\lambda^{\mathrm{ref}} = 0.0025$ nm in the system with 400k solvent molecules. For comparison, the zero point of the free energy is placed in the 1st free energy minimum. Due to the larger thickness, a larger simulation box with more solvent molecules is required.

B.2.1.4 Compare number of snapshots

The sampling must be sufficient in the calculation of the free energy curves with WHAM. In Figure B.8, we compare free energy curves calculated with the MARTINI force field. We extract the center distances from 60, 125, and 250 snapshots from the end of the production run, and calculate with each dataset the free energy curve. The differences are small. We choose in all free energy calculations with the MARTINI force field 250 snapshots, except the calculations with three and four solvent beads. For three and four beads, we use the distances from 500 snapshots.

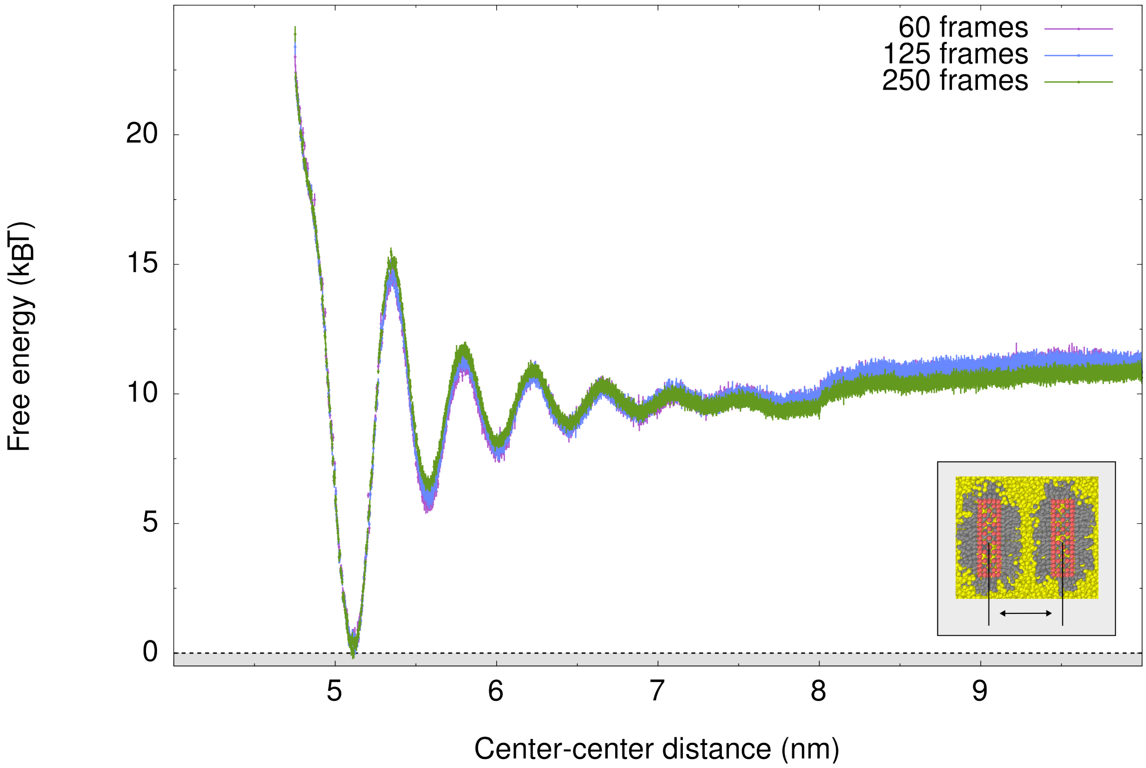

Figure B.8: Test of included number of snapshots in the WHAM free energy calculation. The nanoplatelets have 35.6 nm^2 facet area, and a thickness of 1.5 nm. The solvent is n-octane.

B.2.1.5 Convergence of the free energy curves with three and four solvent beads

The longer the n-alkane, the higher is the viscosity. In our simulations, we find that equilibrating of the simulation windows takes longer. Since the nanoplatelets move slower, we consider the distances from 500 snapshots from a period of 80 ns for the calculation of the free energy curves. In Figure B.9 and B.10, we show the convergence of the free energy curves for the calculations with three and four solvent beads. From each set of free energy curves, we use the most converged curves in Section 7.2.9 (500-1000 snapshots).

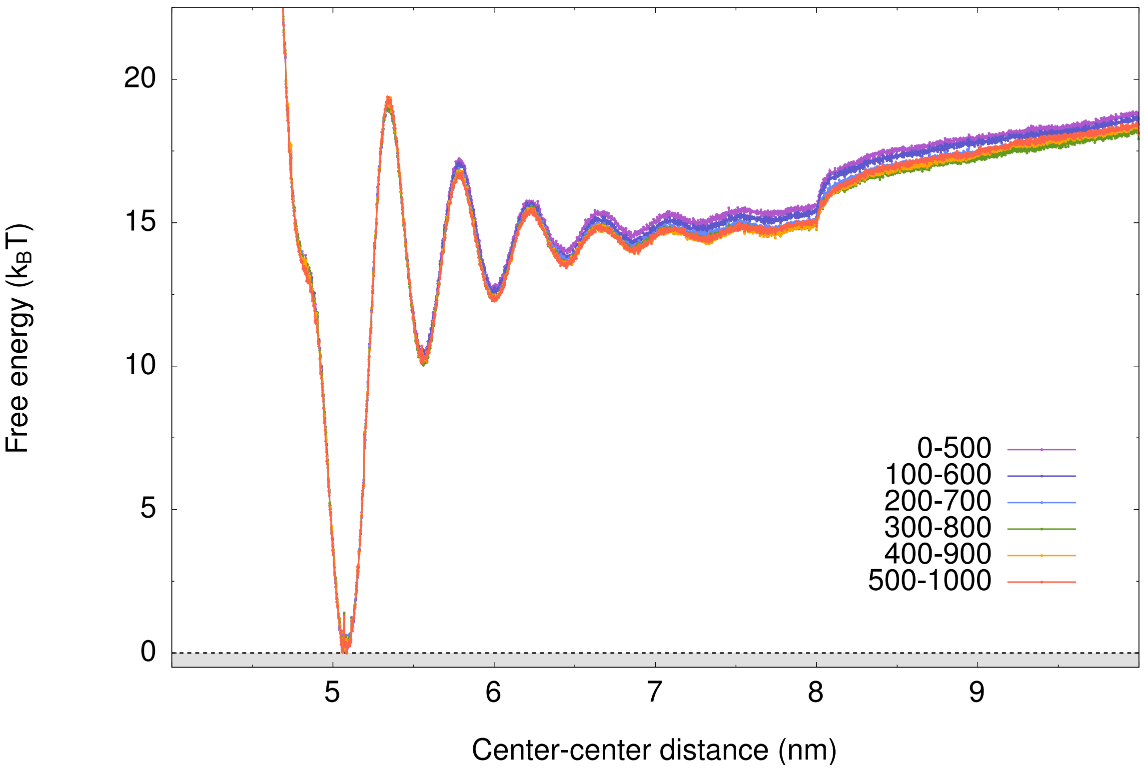

Figure B.9: Convergence of the free energy curve with three solvent beads (without error bars). The legend shows the simulation steps of the production run by which the respective free energy curve was calculated (see Section 5.5). 500 time steps correspond to 80 ns.

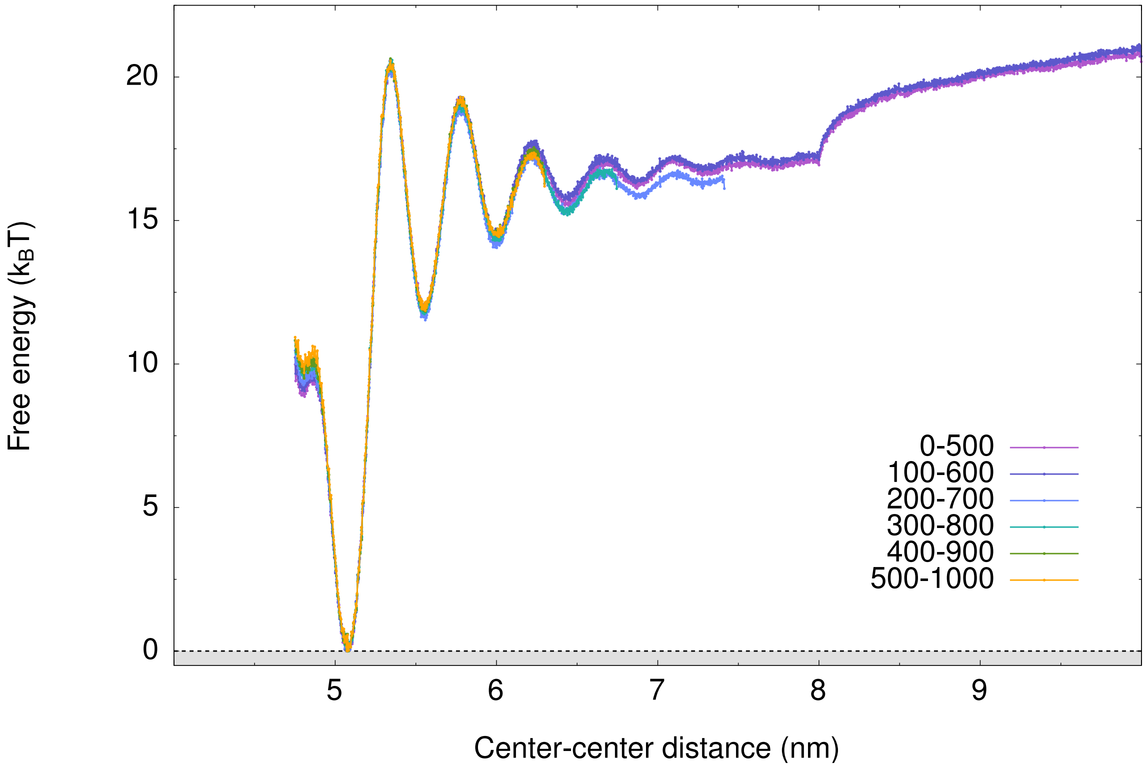

Figure B.10: Convergence of the free energy curve with four solvent beads (without error bars). The legend shows the simulation steps of the production run by which the respective free energy curve was calculated (see Section 5.5). 500 time steps correspond to 80 ns. The first part of the curve is converged. We use the free energy curve that includes the simulation steps 500-1000.

B.2.2 Simulation details

In Table B.7 to B.18, we list details for the simulations from Chapter 7. Among other parameters, we list the base facet area, the number of solvent molecules, the average simulation box side length, and the distance between two windows $\Delta\lambda^{\mathrm{ref}}$ of the umbrella sampling. For free energy calculations, the size of the simulation box is determined in the window with the largest distance between the nanoplatelets, typically at around 10 nm [96].

Base facet area (nm^2)	# of solvent molecules	Average simulation box side length (nm)
20.0	100k	28.5
27.3	100k	28.5
35.6	100k	28.6
45.1	100k	28.6
55.7	350k	43.2

Table B.7: Details for the unconstrained simulations with two nanoplatelets in Section 7.2.1.

Base facet area (nm^2)	# of solvent molecules	Average simulation box side length (nm)
20.0	150k	32.6
45.1	250k	38.7

Table B.8: Details for the unconstrained simulations with three nanoplatelets in Section 7.2.1.

	Base facet area (nm^2)	# of solvent molecules	Average simulation box side length (nm)	$\Delta\lambda^{\mathrm{ref}}$ (nm)
face-to-face	35.6	250k	38.6	0.0025
side-to-side	35.6	250k	38.6	0.0025
side shift	35.6	250k	38.6	0.0025

Table B.9: Simulation details for the analysis of the interaction mechanism in Section 7.2.2.

	Base facet area (nm^2)	# of solvent molecules	Average simulation box side length (nm)	$\Delta\lambda^{\mathrm{ref}}$ (nm)
without ligand shell	35.6	100k	28.5	0.0025
with ligand shell	35.6	250k	38.6	0.0025

Table B.10: Simulation details for comparison of a nanoplatelet without and with a ligand shell in Section 7.2.3.

Ligand density	Base facet area (nm^2)	# of solvent molecules	Average simulation box side length (nm)	$\Delta\lambda^{\mathrm{ref}}$ (nm)
2.7	27.3	100k	28.5	0.005
3.6	27.3	100k	28.5	0.005
4.2	27.3	100k	28.5	0.005

Table B.11: Simulation details for the analysis of the effect of the ligand grafting density in Section 7.2.4.

Ligand length	Base facet area (nm^2)	# of solvent molecules	Average simulation box side length (nm)	$\Delta\lambda^{\mathrm{ref}}$ (nm)
3	35.6	100k	28.5	0.005
4	35.6	250k	38.6	0.0025
5	35.6	100k	28.6	0.005

Table B.12: Simulation details for the analysis of the effect of the ligand length in Section 7.2.5.

Base facet area (nm^2)	# of solvent molecules	Average simulation box side length (nm)	$\Delta\lambda^{\mathrm{ref}}$ (nm)
2.2	100k	28.4	0.005
5.0	100k	28.4	0.005
8.9	100k	28.4	0.005
13.9	100k	28.5	0.005
20.0	100k	28.5	0.005
27.3	100k	28.5	0.005
35.6	250k	38.6	0.0025
45.1	250k	38.6	0.0025
55.7	350k	43.2	0.0025

Table B.13: Simulation details for the analysis of the base facet area in Section 7.2.6.

Thickness (nm)	Base facet area (nm^2)	# of solvent molecules	Average simulation box side length (nm)	$\Delta\lambda^{\mathrm{ref}}$ (nm)
1.5	35.6	250k	38.6	0.0025
2.2	35.6	400k	45.1	0.0025
3.0	35.6	400k	45.1	0.0025

Table B.14: Simulation details for the analysis of the platelet thickness in Section 7.2.7.

Temperature (K)	Base facet area (nm^2)	# of solvent molecules	Average simulation box side length (nm)	$\Delta\lambda^{\mathrm{ref}}$ (nm)
280	35.6	250k	?	0.005
300	35.6	250k	38.6	0.0025
320	35.6	400k	45.4	0.0025
340	35.6	400k	45.7	0.0025

Table B.15: Simulation details for the analysis of the temperature dependence in the MARTINI setup in Subsection 7.2.8.1.

Temperature (K)	Base facet area (nm^2)	# of solvent molecules	Average box side length (nm)	$\Delta\lambda^{\mathrm{ref}}$ (nm)
280	18.1	100k	29.5	0.005
300	18.1	100k	30.1	0.005
340	18.1	100k	31.7	0.005

Table B.16: Simulation details for the analysis of the temperature dependence in the TraPPE-UA setup in Subsection 7.2.8.2.

# of solvent beads in one molecule	Base facet area (nm^2)	# of solvent molecules	Average simulation box side length (nm)	$\Delta\lambda^{\mathrm{ref}}$ (nm)
1	35.6	200k	29.6	0.0025
2	35.6	250k	38.6	0.0025
3	35.6	450k	53.0	0.0025
4	35.6	500k	60.0	0.0025

Table B.17: Simulation details for the analysis of different n-alkane solvent lengths in Section 7.2.9.

Solvent type	Base facet area (nm^2)	# of solvent molecules	Average box side length (nm)	$\Delta\lambda^{\mathrm{ref}}$ (nm)
n-octane	18.1	100k	30.1	0.005
2-methylheptane	18.1	100k	30.2	0.005
3,4-dimethylhexane	18.1	100k	29.9	0.005
2,2,4-trimethylpentane	18.1	100k	30.3	0.005

Table B.18: Details for the simulations with different octane isomers in Section 7.2.10.

Bibliography

[1] B. Karthick and Ramesh Maheshwari: *Lotus-inspired nanotechnology applications.* Resonance, 13:1141–1145, December 2008. `https://doi.org/10.1007/s12045-008-0113-y`.

[2] Ali K. Yetisen, Hang Qu, Amir Manbachi, Haider Butt, Mehmet R. Dokmeci, Juan P. Hinestroza, Maksim Skorobogatiy, Ali Khademhosseini, and Seok Hyun Yun: *Nanotechnology in Textiles.* ACS Nano, 10(3):3042–3068, 2016. `https://doi.org/10.1021/acsnano.5b08176`.

[3] Katherine Bourzac: *Quantum dots go on display.* Nature, 493:283, January 2013. `https://doi.org/10.1038/493283a`.

[4] Zhen Luo, Zhuoqing Li, Zhe Xie, Inna M. Sokolova, Lan Song, Willie J. G. M. Peijnenburg, Menghong Hu, and Youji Wang: *Rethinking Nano-TiO_2 Safety: Overview of Toxic Effects in Humans and Aquatic Animals.* Small, 16(36):2002019, 2020. `https://doi.org/10.1002/smll.202002019`.

[5] Jeremy T. Gidney, Martyn V. Twigg, and David B. Kittelson: *Effect of Organometallic Fuel Additives on Nanoparticle Emissions from a Gasoline Passenger Car.* Environmental Science & Technology, 44(7):2562–2569, 2010. `https://doi.org/10.1021/es901868c`.

[6] Federico Montanarella and Maksym V. Kovalenko: *Three Millennia of Nanocrystals.* ACS Nano, 16(4):5085–5102, 2022. `https://doi.org/10.1021/acsnano.1c11159`.

[7] Giora Rytwo: *Clay Minerals as an Ancient Nanotechnology: Historical Uses of Clay Organic Interactions, and Future Possible Perspectives.* Macla, 9:15–17, 2008.

[8] Antonio Doménech, María Teresa Doménech-Carbó, and María Luisa Vázquez de Agredos-Pascual: *From Maya Blue to "Maya Yellow": A Connection between Ancient Nanostructured Materials from the Voltammetry of Microparticles.* Angewandte Chemie International Edition, 50(25):5741–5744, 2011. `https://doi.org/10.1002/anie.201100921`.

[9] M. Reibold, P. Paufler, A. A. Levin, W. Kochmann, N. Pätzke, and D. C. Meyer: *Carbon nanotubes in an ancient Damascus sabre.* Nature, 444:286, November 2006. `https://doi.org/10.1038/444286a`.

[10] Marianne Reibold, Peter Paufler, Aleksandr A. Levin, Werner Kochmann, Nora Pätzke, and Dirk C. Meyer: *Discovery of Nanotubes in Ancient Damascus Steel.* In Do Tran Cat, Annemarie Pucci, and Klaus Wandelt (editors): *Physics and Engineering of New Materials*, pages 305–310. Springer Berlin Heidelberg, 2009. `https://link.springer.com/chapter/10.1007/978-3-540-88201-5_35`.

[11] Ivana Angelini, Gilberto Artioli, Paolo Bellintani, Valeria Diella, Mauro Gemmi, Angela Polla, and Antonella Rossi: *Chemical analyses of Bronze Age glasses from Frattesina di Rovigo, Northern Italy.* Journal of Archaeological Science, 31(8):1175–1184, 2004. `https://doi.org/10.1016/j.jas.2004.02.015`.

[12] Philippe Colomban: *The Use of Metal Nanoparticles to Produce Yellow, Red and Iridescent Colour, from Bronze Age to Present Times in Lustre Pottery and Glass: Solid State Chemistry, Spectroscopy and Nanostructure.* Journal of Nano Research, 8:109–132, October 2009. `https://doi.org/10.4028/www.scientific.net/JNanoR.8.109`.

[13] Ulf Leonhardt: *Invisibility cup.* Nature Photonics, 1:207–208, April 2007. `https://doi.org/10.1038/nphoton.2007.38`.

[14] Andrey Drozdov, Maxim Andreev, Maxim Kozlov, Dmitriy Petukhov, Sergey Klimonsky, and Claudio Pettinari: *Lycurgus cup: the nature of dichroism in a replica glass having similar composition.* Journal of Cultural Heritage, 51:71–78, 2021. `https://doi.org/10.1016/j.culher.2021.07.002`.

[15] Alexander L. Efros and Louis E. Brus: *Nanocrystal quantum dots: From discovery to modern development.* ACS Nano, 15(4):6192–6210, 2021. `https://doi.org/10.1021/acsnano.1c01399`.

[16] A. P. Alivisatos: *Perspectives on the Physical Chemistry of Semiconductor Nanocrystals.* The Journal of Physical Chemistry, 100(31):13226–13239, 1996. `https://doi.org/10.1021/jp9535506`.

[17] Kui Yu and Kirk S. Schanze: *Commemorating the nobel prize in chemistry 2023 for the discovery and synthesis of quantum dots.* ACS Central Science, 9(11):1989–1992, 2023. `https://doi.org/10.1021/acscentsci.3c01296`.

[18] Maksym V. Kovalenko, Liberato Manna, Andreu Cabot, Zeger Hens, Dmitri V. Talapin, Cherie R. Kagan, Victor I. Klimov, Andrey L. Rogach, Peter Reiss, Delia J. Milliron, Philippe Guyot-Sionnnest, Gerasimos Konstantatos, Wolfgang J. Parak, Taeghwan Hyeon, Brian A. Korgel, Christopher B. Murray, and Wolfgang Heiss: *Prospects of Nanoscience with Nanocrystals.* ACS Nano, 9(2):1012–1057, 2015. `https://doi.org/10.1021/nn506223h`.

[19] Thomas A. Witten and Philip A. Pincus: *Structured fluids Polymers, Colloids, Surfactants.* Oxford University Press, 2004.

[20] Jacob Israelachvili: *Intermolecular and Surface Forces (3. Edition).* Academic Press, July 2011. `https://doi.org/10.1016/C2009-0-21560-1`.

[21] Siddique J. Khan, F. Pierce, C. M. Sorensen, and A. Chakrabarti: *Self-Assembly of Ligated Gold Nanoparticles: Phenomenological Modeling and Computer Simulations.* Langmuir, 25(24):13861–13868, 2009. `https://doi.org/10.1021/la9008202`.

[22] Carlos A. Silvera Batista, Ronald G. Larson, and Nicholas A. Kotov: *Nonadditivity of nanoparticle interactions.* Science, 350(6257):1242477, 2015. `https://doi.org/10.1126/science.1242477`.

[23] Zhun Liu, Hu Zhou, Young S. Lim, Jung Hoon Song, Longhai Piao, and Sang Ho Kim: *Synthesis of Silver Nanoplates by Two-Dimensional Oriented Attachment.* Langmuir, 28(25):9244–9249, 2012. `https://doi.org/10.1021/la301721y`.

[24] Mun Ho Kim, Dong Ki Yoon, and Sang Hyuk Im: *Growth pathways of silver nanoplates in kinetically controlled synthesis: bimodal versus unimodal growth.* RSC Adv., 5:14266–14272, 2015. `http://dx.doi.org/10.1039/C4RA12818D`.

[25] Tonnam Balankura, Tianyu Yan, Omid Jahanmahin, Jenwarin Narukatpichai, Alan Ng, and Kristen A. Fichthorn: *Oriented attachment mechanism of triangular Ag nanoplates: a molecular dynamics study.* Nanoscale Adv., 2:2265–2270, 2020. `http://dx.doi.org/10.1039/D0NA00124D`.

[26] Tuan A. Ho, Kevin M. Rosso, and Louise J. Criscenti: *Atomistic Mismatch Defines Energy–Structure Relationships during Oriented Attachment of Nanoparticles.* The Journal of Physical Chemistry Letters, 13(40):9339–9347, 2022. `https://doi.org/10.1021/acs.jpclett.2c02511`.

[27] Dahin Kim and Doh C. Lee: *Surface Ligands as Permeation Barrier in the Growth and Assembly of Anisotropic Semiconductor Nanocrystals.* The Journal of Physical Chemistry Letters, 11(7):2647–2657, 2020. `https://doi.org/10.1021/acs.jpclett.9b03052`.

[28] Michael A. Boles, Michael Engel, and Dmitri V. Talapin: *Self-Assembly of Colloidal Nanocrystals: From Intricate Structures to Functional Materials.* Chemical Reviews, 116(18):11220–11289, 2016. `https://doi.org/10.1021/acs.chemrev.6b00196`.

[29] D.H Napper: *Steric stabilization.* Journal of Colloid and Interface Science, 58(2):390–407, 1977. `https://doi.org/10.1016/0021-9797(77)90150-3`.

[30] Thomas Kister, Debora Monego, Paul Mulvaney, Asaph Widmer-Cooper, and Tobias Kraus: *Colloidal Stability of Apolar Nanoparticles: The Role of Particle Size and Ligand Shell Structure.* ACS Nano, 12(6):5969–5977, 2018. `https://doi.org/10.1021/acsnano.8b02202`.

[31] Debora Monego, Thomas Kister, Nicholas Kirkwood, Paul Mulvaney, Asaph Widmer-Cooper, and Tobias Kraus: *Colloidal Stability of Apolar Nanoparticles: Role of Ligand Length.* Langmuir, 34(43):12982–12989, 2018. `https://doi.org/10.1021/acs.langmuir.8b02883`.

[32] Debora Monego, Thomas Kister, Nicholas Kirkwood, David Doblas, Paul Mulvaney, Tobias Kraus, and Asaph Widmer-Cooper: *When Like Destabilizes Like: Inverted Solvent Effects in Apolar Nanoparticle Dispersions.* ACS Nano, 14(5):5278–5287, 2020. `https://doi.org/10.1021/acsnano.9b03552`.

[33] Asaph Widmer-Cooper and Phillip Geissler: *Orientational Ordering of Passivating Ligands on CdS Nanorods in Solution Generates Strong Rod–Rod Interactions.* Nano Letters, 14(1):57–65, 2014. `https://doi.org/10.1021/nl403067p`.

[34] Asaph Widmer-Cooper and Phillip L. Geissler: *Ligand-Mediated Interactions between Nanoscale Surfaces Depend Sensitively and Nonlinearly on Temperature, Facet Dimensions, and Ligand Coverage.* ACS Nano, 10(2):1877–1887, 2016. `https://doi.org/10.1021/acsnano.5b05569`.

[35] Aydan Yeltik, Savas Delikanli, Murat Olutas, Yusuf Kelestemur, Burak Guzelturk, and Hilmi Volkan Demir: *Experimental Determination of the Absorption Cross-Section and Molar Extinction Coefficient of Colloidal CdSe Nanoplatelets.* The Journal of Physical Chemistry C, 119(47):26768–26775, 2015. `https://doi.org/10.1021/acs.jpcc.5b09275`.

[36] Henry Halim, Johanna Simon, Ingo Lieberwirth, Volker Mailänder, Kaloian Koynov, and Andreas Riedinger: *Water-dispersed semiconductor nanoplatelets with high fluorescence brightness, chemical and colloidal stability.* J. Mater. Chem. B, 8:146–154, 2020. `http://dx.doi.org/10.1039/C9TB02377A`.

[37] Rebecca Momper, Heng Zhang, Shuai Chen, Henry Halim, Ewald Johannes, Stoyan Yordanov, Daniele Braga, Balthasar Blülle, David Doblas, Tobias Kraus, Mischa Bonn, Hai I. Wang, and Andreas Riedinger: *Kinetic Control over Self-Assembly of Semiconductor Nanoplatelets.* Nano Letters, 20(6):4102–4110, 2020. `https://doi.org/10.1021/acs.nanolett.9b05270`.

[38] Rebecca Momper, Antonio Ibanez Landeta, Long Yang, Henry Halim, Heloise Therien-Aubin, Eberhard Bodenschatz, Katharina Landfester, and Andreas Riedinger: *Plasmonic and Semiconductor Nanoparticles Interfere with Stereolithographic 3D Printing.* ACS Applied Materials & Interfaces, 12(45):50834–50843, 2020. `https://doi.org/10.1021/acsami.0c14546`.

[39] Aarya Prabhakaran, Zhiya Dang, Rohan Dhall, Fabrizio Camerin, Susana Marín-Aguilar, Balaji Dhanabalan, Andrea Castelli, Rosaria Brescia, Liberato Manna, Marjolein Dijkstra, and Milena P. Arciniegas: *Real-Time In Situ Observation of $CsPbBr_3$ Perovskite Nanoplatelets Transforming into Nanosheets.* ACS Nano, 17(14):13648–13658, 2023. `https://doi.org/10.1021/acsnano.3c02477`.

[40] Zhuoying Chen, Brice Nadal, Benoit Mahler, Hervé Aubin, and Benoit Dubertret: *Quasi-2D Colloidal Semiconductor Nanoplatelets for Narrow Electroluminescence.* Advanced Functional Materials, 24(3):295–302, 2014. `https://doi.org/10.1002/adfm.201301711`.

[41] Clare E. Rowland, Igor Fedin, Hui Zhang, Stephen K. Gray, Alexander O. Govorov, Dmitri V. Talapin, and Richard D. Schaller: *Picosecond energy transfer and multiexciton transfer outpaces Auger recombination in binary CdSe nanoplatelet solids.* Nature Materials, 14:484–489, March 2015. `https://doi.org/10.1038/nmat4231`.

[42] Emmanuel Lhuillier, Silvia Pedetti, Sandrine Ithurria, Hadrien Heuclin, Brice Nadal, Adrien Robin, Gilles Patriarche, Nicolas Lequeux, and Benoit Dubertret: *Electrolyte-Gated Field Effect Transistor to Probe the Surface Defects and Morphology in Films of Thick CdSe Colloidal Nanoplatelets.* ACS Nano, 8(4):3813–3820, 2014. `https://doi.org/10.1021/nn500538n`.

[43] Joel Q. Grim, Sotirios Christodoulou, Francesco Di Stasio, Roman Krahne, Roberto Cingolani, Liberato Manna, and Iwan Moreels: *Continuous-wave biexciton lasing at room temperature using solution-processed quantum wells.* Nature Nanotechnology, 9:891–895, October 2014. `https://doi.org/10.1038/nnano.2014.213`.

[44] Sandrine Ithurria and Benoit Dubertret: *Quasi 2D Colloidal CdSe Platelets with Thicknesses Controlled at the Atomic Level.* Journal of the American Chemical Society, 130:16504–16505, December 2008. `https://doi.org/10.1021/ja807724e`.

[45] Santanu Jana, Trang N. T. Phan, Cécile Bouet, Mickael D. Tessier, Patrick Davidson, Benoit Dubertret, and Benjamin Abécassis: *Stacking and Colloidal Stability of CdSe Nanoplatelets.* Langmuir, 31(38):10532–10539, 2015. `https://doi.org/10.1021/acs.langmuir.5b02152`.

[46] Santanu Jana, Patrick Davidson, and Benjamin Abécassis: *CdSe Nanoplatelets: Living Polymers.* Angewandte Chemie International Edition, 55(32):9371–9374, 2016. `https://doi.org/10.1002/anie.201603880`.

[47] Aaron E. Saunders, Ali Ghezelbash, Detlef M. Smilgies, Michael B. Sigman, and Brian A. Korgel: *Columnar Self-Assembly of Colloidal Nanodisks.* Nano Letters, 6(12):2959–2963, 2006. `https://doi.org/10.1021/nl062419e`.

[48] Ivan Dozov, Claire Goldmann, Patrick Davidson, and Benjamin Abécassis: *Probing permanent dipoles in CdSe nanoplatelets with transient electric birefringence.* Nanoscale, 12:11040–11054, 2020. `http://dx.doi.org/10.1039/D0NR00884B`.

[49] Jun Zhang, Haibing Zhang, Weicheng Cao, Zhenfeng Pang, Jiongzhao Li, Yufei Shu, Chenqi Zhu, Xueqian Kong, Linjun Wang, and Xiaogang Peng: *Identification of Facet-Dependent Coordination Structures of Carboxylate Ligands on CdSe Nanocrystals.* Journal of the American Chemical Society, 141(39):15675–15683, 2019. `https://doi.org/10.1021/jacs.9b07836`.

[50] Lilian Guillemeney, Laurent Lermusiaux, Guillaume Landaburu, Benoit Wagnon, and Benjamin Abécassis: *Curvature and self-assembly of semi-conducting nanoplatelets.* Communications Chemistry, 5:1–11, 2022. `https://doi.org/10.1038/s42004-021-00621-z`.

[51] Ian D. Morrison: *Electrical charges in nonaqueous media.* Colloids and Surfaces A: Physicochemical and Engineering Aspects, 71(1):1–37, 1993. `https://doi.org/10.1016/0927-7757(93)80026-B`.

[52] Benjamin Abécassis: *Three-Dimensional Self Assembly of Semiconducting Colloidal Nanocrystals: From Fundamental Forces to Collective Optical Properties.* ChemPhysChem, 17(5):618–631, 2016. `https://doi.org/10.1002/cphc.201500856`.

[53] Dieter Meschede: *Gerthsen physik.* 2015. `https://doi.org/10.1007/978-3-662-45977-5`.

[54] Moonsub Shim and Philippe Guyot-Sionnest: *Permanent dipole moment and charges in colloidal semiconductor quantum dots.* The Journal of Chemical Physics, 111(15):6955–6964, October 1999. `https://doi.org/10.1063/1.479988`.

[55] Liang shi Li and A. Paul Alivisatos: *Origin and Scaling of the Permanent Dipole Moment in CdSe Nanorods.* Physical Review Letters, 90:097402, Mar 2003. `https://doi.org/10.1103/PhysRevLett.90.097402`.

[56] Robert D. Gunning, Catriona O'Sullivan, and Kevin M. Ryan: *A multi-rate kinetic model for spontaneous oriented attachment of CdS nanorods.* Physical Chemistry Chemical Physics, 12:12430–12435, 2010. `http://dx.doi.org/10.1039/C0CP00196A`.

[57] Weiqiang Lv, Weidong He, Xiaoning Wang, Yinghua Niu, Huanqi Cao, James H. Dickerson, and Zhiguo Wang: *Understanding the oriented-attachment growth of nanocrystals from an energy point of view: a review.* Nanoscale, 6:2531–2547, 2014. `http://dx.doi.org/10.1039/C3NR04717B`.

[58] Kyle J. M. Bishop, Christopher E. Wilmer, Siowling Soh, and Bartosz A. Grzybowski: *Nanoscale Forces and Their Uses in Self-Assembly.* Small, 5(14):1600–1630, 2009. `https://doi.org/10.1002/smll.200900358`.

[59] H.C. Hamaker: *The London—van der Waals attraction between spherical particles.* Physica, 4(10):1058–1072, 1937. `https://doi.org/10.1016/S0031-8914(37)80203-7`.

[60] Jia Qi Lin, Hong Wu Zhang, Zhen Chen, Yong Gang Zheng, Zhong Qiang Zhang, and Hong Fei Ye: *Simulation Study of Aggregations of Monolayer-Protected Gold Nanoparticles in Solvents.* The Journal of Physical Chemistry C, 115(39):18991–18998, 2011. `https://doi.org/10.1021/jp204735d`.

[61] R. Evans, J. B. Smitham, and D. H. Napper: *Theoretical prediction of the elastic contribution to steric stabilization.* Colloid and Polymer Science, 255:161–167, 1977. `https://doi.org/10.1007/BF01777275`.

[62] Katherine C. Elbert, Thi Vo, Nadia M. Krook, William Zygmunt, Jungmi Park, Kevin G. Yager, Russell J. Composto, Sharon C. Glotzer, and Christopher B. Murray: *Dendrimer Ligand Directed Nanoplate Assembly.* ACS Nano, 13(12):14241–14251, 2019. `https://doi.org/10.1021/acsnano.9b07348`.

[63] Hendrik Heinz, Chandrani Pramanik, Ozge Heinz, Yifu Ding, Ratan K. Mishra, Delphine Marchon, Robert J. Flatt, Irina Estrela-Lopis, Jordi Llop, Sergio Moya, and Ronald F. Ziolo: *Nanoparticle decoration with surfactants: Molecular interactions, assembly, and applications.* Surface Science Reports, 72(1):1–58, 2017. `https://doi.org/10.1016/j.surfrep.2017.02.001`.

[64] Antonella Badia, Louis Cuccia, Linette Demers, Fred Morin, and R. Bruce Lennox: *Structure and Dynamics in Alkanethiolate Monolayers Self-Assembled on Gold Nanoparticles: A DSC, FT-IR, and Deuterium NMR Study.* Journal of the American Chemical Society, 119(11):2682–2692, 1997. `https://doi.org/10.1021/ja963571t`.

[65] Lionel Salem: *Attractive Forces between Long Saturated Chains at Short Distances.* The Journal of Chemical Physics, 37(9):2100–2113, July 2004. `https://doi.org/10.1063/1.1733431`.

[66] Uzi Landman and W. D. Luedtke: *Small is different: energetic, structural, thermal, and mechanical properties of passivated nanocluster assemblies.* Faraday Discussions, 125:1–22, 2004. `http://dx.doi.org/10.1039/B312640B`.

[67] Philipp Schapotschnikow and Thijs J. H. Vlugt: *Understanding interactions between capped nanocrystals: Three-body and chain packing effects.* The Journal of Chemical Physics, 131(12):124705, September 2009. `https://doi.org/10.1063/1.3227043`.

[68] A. Travesset: *Topological structure prediction in binary nanoparticle superlattices.* Soft Matter, 13:147–157, 2017. `http://dx.doi.org/10.1039/C6SM00713A`.

[69] Curt Waltmann, Nathan Horst, and Alex Travesset: *Capping Ligand Vortices as "Atomic Orbitals" in Nanocrystal Self-Assembly.* ACS Nano, 11(11):11273–11282, 2017. `https://doi.org/10.1021/acsnano.7b05694`.

[70] Bharat Bhushan: *Springer Handbook of Nanotechnology.* Springer Berlin Heidelberg, 4th edition, 2017. `https://doi.org/10.1007/978-3-662-54357-3`.

[71] Hugo K. Christenson: *Experimental measurements of solvation forces in nonpolar liquids.* The Journal of Chemical Physics, 78(11):6906–6913, June 1983, ISSN 0021-9606. `https://doi.org/10.1063/1.444639`.

[72] Hugo K. Christenson: *Experimental measurements of solvation forces in nonpolar liquids.* The Journal of Chemical Physics, 78(11):6906–6913, June 1983. `https://doi.org/10.1063/1.444639`.

[73] Jee Ching Wang and Kristen A. Fichthorn: *Molecular dynamics studies of the effects of chain branching on the properties of confined alkanes.* The Journal of Chemical Physics, 116(1):410–417, January 2002. `https://doi.org/10.1063/1.1419258`.

[74] Patricia M. McGuiggan and Jacob N. Israelachvili: *Adhesion and short-range forces between surfaces. Part II: Effects of surface lattice mismatch.* Journal of Materials Research, 5(10):2232–2243, 1990. `https://doi.org/10.1557/JMR.1990.2232`.

[75] Yong Qin and Kristen A. Fichthorn: *Molecular-dynamics simulation of forces between nanoparticles in a Lennard-Jones liquid.* The Journal of Chemical Physics, 119(18):9745–9754, October 2003. `https://doi.org/10.1063/1.1615493`.

[76] Jens Laube, Samir Salameh, Michael Kappl, Lutz Mädler, and Lucio Colombi Ciacchi: *Contact Forces between TiO2 Nanoparticles Governed by an Interplay of Adsorbed Water Layers and Roughness.* Langmuir, 31(41):11288–11295, 2015. `https://doi.org/10.1021/acs.langmuir.5b02989`.

[77] Utkarsh Anand, Jingyu Lu, Duane Loh, Zainul Aabdin, and Utkur Mirsaidov: *Hydration Layer-Mediated Pairwise Interaction of Nanoparticles.* Nano Letters, 16(1):786–790, 2016. `https://doi.org/10.1021/acs.nanolett.5b04808`.

[78] Xinyi Shen and Ian C. Bourg: *Molecular dynamics simulations of the colloidal interaction between smectite clay nanoparticles in liquid water.* Journal of Colloid and Interface Science, 584:610–621, 2021. `https://doi.org/10.1016/j.jcis.2020.10.029`.

[79] Sho Asakura and Fumio Oosawa: *Interaction between particles suspended in solutions of macromolecules.* Journal of Polymer Science, 33(126):183–192, 1958. `https://doi.org/10.1002/pol.1958.1203312618`.

[80] J. C. Crocker, J. A. Matteo, A. D. Dinsmore, and A. G. Yodh: *Entropic Attraction and Repulsion in Binary Colloids Probed with a Line Optical Tweezer.* Physical Review Letters, 82:4352–4355, May 1999. `https://doi.org/10.1103/PhysRevLett.82.4352`.

[81] T. G. Mason: *Osmotically driven shape-dependent colloidal separations.* Physical Review E, 66:060402, Dec 2002. `https://doi.org/10.1103/PhysRevE.66.060402`.

[82] Andreas Riedinger, Florian D. Ott, Aniket Mule, Sergio Mazzotti, Philippe N. Knüsel, Stephan J.P. Kress, Ferry Prins, Steven C. Erwin, and David J. Norris: *An intrinsic growth instability in isotropic materials leads to quasi-two-dimensional nanoplatelets.* Nature Materials, 16:743–748, 2017. `https://doi.org/10.1038/nmat4889`.

[83] Celso de Mello Donegá: *Synthesis and properties of colloidal heteronanocrystals.* Chemical Society Reviews, 40:1512–1546, 2011. `http://dx.doi.org/10.1039/C0CS00055H`.

[84] Rolf Koole, Esther Groeneveld, Daniel Vanmaekelbergh, Andries Meijerink, and Celso de Mello Donegá: *Size Effects on Semiconductor Nanoparticles.* In Celso de Mello Donegá (editor): *Nanoparticles: Workhorses of Nanoscience*, pages 13–51. Springer Berlin Heidelberg, 2014. `https://doi.org/10.1007/978-3-662-44823-6_2`.

[85] Neil W. Ashcroft and N. David Mermin: *Solid State Physics.* CBS publishing asia LTD., 1976.

[86] Todd D. Krauss and Jeffrey J. Peterson: *Electronic structure and optical transitions in colloidal semiconductor nanocrystals.* In Gerasimos Konstantatos and Edward H.Editors Sargent (editors): *Colloidal Quantum Dot Optoelectronics and Photovoltaics*, page 59–86. Cambridge University Press, 2013. `https://doi.org/10.1017/CBO9781139022750.004`.

[87] Alexandra Brumberg, Samantha M. Harvey, John P. Philbin, Benjamin T. Diroll, Byeongdu Lee, Scott A. Crooker, Michael R. Wasielewski, Eran Rabani, and Richard D. Schaller: *Determination of the In-Plane Exciton Radius in 2D CdSe Nanoplatelets via Magneto-optical Spectroscopy.* ACS Nano, 13(8):8589–8596, 2019. `https://doi.org/10.1021/acsnano.9b02008`.

[88] Arkaprava Bhattacharyya and Vijay K. Arora: *Quantum Nanoengineering.* In Amretashis Sengupta and Chandan Kumar Sarkar (editors): *Introduction to Nano: Basics to Nanoscience and Nanotechnology*, pages 59–71, Berlin, Heidelberg, 2015. Springer Berlin Heidelberg. `https://doi.org/10.1007/978-3-662-47314-6_4`.

[89] Wen Zhang: *Nanoparticle Aggregation: Principles and Modeling.* In David G. Capco and Yongsheng Chen (editors): *Nanomaterial: Impacts on Cell Biology and Medicine*, pages 19–43, Dordrecht, 2014. Springer Netherlands. `https://doi.org/10.1007/978-94-017-8739-0_2`.

[90] Patricia Taboada-Serrano, Chin Ju Chin, Sotira Yiacoumi, and Costas Tsouris: *Modeling aggregation of colloidal particles.* Current Opinion in Colloid & Interface Science, 10(3):123–132, 2005. `https://doi.org/10.1016/j.cocis.2005.07.003`.

[91] Robert B Grubbs and Robert H Grubbs: *50th Anniversary Perspective: Living Polymerization—Emphasizing the Molecule in Macromolecules.* Macromolecules, 50(18):6979–6997, 2017. `https://doi.org/10.1021/acs.macromol.7b01440`.

[92] Mengxin Gu, Xiaodong Ma, Liangshun Zhang, and Jiaping Lin: *Reversible Polymerization-like Kinetics for Programmable Self-Assembly of DNA-Encoded Nanoparticles with Limited Valence.* Journal of the American Chemical Society, 141(41):16408–16415, 2019. `https://doi.org/10.1021/jacs.9b07919`.

[93] Benjamin Abécassis, Mickael D. Tessier, Patrick Davidson, and Benoit Dubertret: *Self-Assembly of CdSe Nanoplatelets into Giant Micrometer-Scale Needles Emitting Polarized Light.* Nano Letters, 14(2):710–715, 2014. `https://doi.org/10.1021/nl4039746`.

[94] Eran Rabani: *An interatomic pair potential for cadmium selenide.* The Journal of Chemical Physics, 116(1):258–262, January 2002. `https://doi.org/10.1063/1.1424321`.

[95] David B. Hough and Lee R. White: *The calculation of hamaker constants from liftshitz theory with applications to wetting phenomena.* Advances in Colloid and Interface Science, 14(1):3–41, 1980. `https://doi.org/10.1016/0001-8686(80)80006-6`.

[96] Nanning Petersen, Martin Girard, Andreas Riedinger, and Omar Valsson: *The Crucial Role of Solvation Forces in the Steric Stabilization of Nanoplatelets.* Nano Letters, 22(24):9847–9853, 2022. `https://doi.org/10.1021/acs.nanolett.2c02848`.

[97] K Jiang and P Pinchuk: *Temperature and size-dependent Hamaker constants for metal nanoparticles.* Nanotechnology, 27(34):345710, 2016. `https://dx.doi.org/10.1088/0957-4484/27/34/345710`.

[98] Daan Frenkel and Berend Smit: *Understanding Molecular Simulation (Second Edition).* Academic Press, San Diego, 2002. `https://doi.org/10.1016/B978-0-12-267351-1.X5000-7`.

[99] Mark E. Tuckerman: *Statistical Mechanics: Theory and Molecular Simulation.* Oxford University Press, 2011. `https://doi.org/10.1002/anie.201105752`.

[100] H. J. C. Berendsen, J. P. M. Postma, W. F. van Gunsteren, A. DiNola, and J. R. Haak: *Molecular dynamics with coupling to an external bath.* The Journal of Chemical Physics, 81(8):3684–3690, October 1984. `https://doi.org/10.1063/1.448118`.

[101] Herman J. C. Berendsen: *Simulating the Physical World: Hierarchical Modeling from Quantum Mechanics to Fluid Dynamics.* Cambridge University Press, 2007. `https://doi.org/10.1017/CBO9780511815348`.

[102] González, M.A.: *Force fields and molecular dynamics simulations.* JDN, 12:169–200, 2011. `https://doi.org/10.1051/sfn/201112009`.

[103] Glenn J. Martyna, Douglas J. Tobias, and Michael L. Klein: *Constant pressure molecular dynamics algorithms.* The Journal of Chemical Physics, 101(5):4177–4189, September 1994. `https://doi.org/10.1063/1.467468`.

[104] P. Español and P. Warren: *Statistical Mechanics of Dissipative Particle Dynamics.* Europhysics Letters, 30(4):191, may 1995. `https://dx.doi.org/10.1209/0295-5075/30/4/001`.

[105] V. Brázdová and D.R. Bowler: *Atomistic Computer Simulations: A Practical Guide.* John Wiley & Sons, Ltd, 2013. `https://doi.org/10.1002/9783527671816`.

[106] M.P. Allen and D.J. Tildesley: *Computer Simulation of Liquids.* Oxford University Press, 2009.

[107] Marcus G. Martin and J. Ilja Siepmann: *Transferable Potentials for Phase Equilibria. 1. United-Atom Description of n-Alkanes.* The Journal of Physical Chemistry B, 102(14):2569–2577, 1998. `https://doi.org/10.1021/jp972543+`.

[108] Jaehyeok Jin, Alexander J. Pak, Aleksander E. P. Durumeric, Timothy D. Loose, and Gregory A. Voth: *Bottom-up coarse-graining: Principles and perspectives.* Journal of Chemical Theory and Computation, 18(10):5759–5791, 2022. `https://doi.org/10.1021/acs.jctc.2c00643`.

[109] Siewert J. Marrink, H. Jelger Risselada, Serge Yefimov, D. Peter Tieleman, and Alex H. de Vries: *The MARTINI Force Field: Coarse Grained Model for Biomolecular Simulations.* The Journal of Physical Chemistry B, 111(27):7812–7824, 2007. `https://doi.org/10.1021/jp071097f`.

[110] Riccardo Alessandri, Fabian Grünewald, and Siewert J. Marrink: *The Martini Model in Materials Science.* Advanced Materials, 33(24):2008635, 2021. `https://doi.org/10.1002/adma.202008635`.

[111] *TraPPE: Transferable Potentials for Phase Equilibria Force Field.* `http://trappe.oit.umn.edu/`, Accessed: 2023-10-16.

[112] Shyamal K. Nath, Fernando A. Escobedo, and Juan J. de Pablo: *On the simulation of vapor–liquid equilibria for alkanes.* The Journal of Chemical Physics, 108(23):9905–9911, June 1998. `https://doi.org/10.1063/1.476429`.

[113] Johannes Kästner: *Umbrella sampling.* WIREs Computational Molecular Science, 1(6):932–942, 2011. `https://doi.org/10.1002/wcms.66`.

[114] Jae Hyeon Ko, Dongsuk Yoo, and Yong Hyun Kim: *Atomic models for anionic ligand passivation of cation-rich surfaces of IV–VI, II–VI, and III–V colloidal quantum dots.* Chemical Communications, 53:388–391, 2017. `http://dx.doi.org/10.1039/C6CC07933D`.

[115] Joshua A. Anderson, Chris D. Lorenz, and A. Travesset: *General purpose molecular dynamics simulations fully implemented on graphics processing units.* Journal of Computational Physics, 227(10):5342–5359, 2008. `https://doi.org/10.1016/j.jcp.2008.01.047`.

[116] Jens Glaser, Trung Dac Nguyen, Joshua A. Anderson, Pak Lui, Filippo Spiga, Jaime A. Millan, David C. Morse, and Sharon C. Glotzer: *Strong scaling of general-purpose molecular dynamics simulations on GPUs.* Computer Physics Communications, 192:97–107, 2015. `https://doi.org/10.1016/j.cpc.2015.02.028`.

[117] Joshua A. Anderson, Jens Glaser, and Sharon C. Glotzer: *HOOMD-blue: A Python package for high-performance molecular dynamics and hard particle Monte Carlo simulations.* Computational Materials Science, 173:109363, 2020. `https://doi.org/10.1016/j.commatsci.2019.109363`.

[118] Carolyn L. Phillips, Joshua A. Anderson, and Sharon C. Glotzer: *Pseudo-random number generation for Brownian Dynamics and Dissipative Particle Dynamics simulations on GPU devices.* Journal of Computational Physics, 230(19):7191–7201, 2011. `https://doi.org/10.1016/j.jcp.2011.05.021`.

[119] Martin Girard, Ali Ehlen, Anisha Shakya, Tristan Bereau, and Monica Olvera de la Cruz: *Hoobas: A highly object-oriented builder for molecular dynamics.* Computational Materials Science, 167:25–33, 2019. `https://doi.org/10.1016/j.commatsci.2019.05.003`.

[120] Mark E Tuckerman, José Alejandre, Roberto López-Rendón, Andrea L Jochim, and Glenn J Martyna: *A Liouville-operator derived measure-preserving integrator for molecular dynamics simulations in the isothermal–isobaric ensemble.* Journal of Physics A: Mathematical and General, 39(19):5629, 2006. `https://dx.doi.org/10.1088/0305-4470/39/19/S18`.

[121] Tang Qing Yu, José Alejandre, Roberto López-Rendón, Glenn J. Martyna, and Mark E. Tuckerman: *Measure-preserving integrators for molecular dynamics in the isothermal–isobaric ensemble derived from the Liouville operator.* Chemical Physics, 370(1):294–305, 2010. `https://doi.org/10.1016/j.chemphys.2010.02.0145`.

[122] Shankar Kumar, John M. Rosenberg, Djamal Bouzida, Robert H. Swendsen, and Peter A. Kollman: *THE weighted histogram analysis method for free-energy calculations on biomolecules. I. The method.* Journal of Computational Chemistry, 13(8):1011–1021, 1992. `https://doi.org/10.1002/jcc.540130812`.

[123] Marc Souaille and Benoît Roux: *Extension to the weighted histogram analysis method: combining umbrella sampling with free energy calculations.* Computer Physics Communications, 135(1):40–57, 2001. `https://doi.org/10.1016/S0010-4655(00)00215-0`.

[124] Daniel Bauer: *WHAM - An efficient weighted histogram analysis implementation written in Rust. (v1.1.3) [Software]. Zenodo*, July 2021. `https://doi.org/10.5281/zenodo.5121486`.

[125] Jochen S. Hub, Bert L. de Groot, and David van der Spoel: *g_wham—A Free Weighted Histogram Analysis Implementation Including Robust Error and Autocorrelation Estimates.* Journal of Chemical Theory and Computation, 6(12):3713–3720, 2010. `https://doi.org/10.1021/ct100494z`.

[126] F. Di Palma, S. Bottaro, and G. Bussi: *Kissing loop interaction in adenine riboswitch: insights from umbrella sampling simulations.* BMC Bioinformatics, 16(Suppl 9):S6, 2015. `https://doi.org/10.1186/1471-2105-16-S9-S6`.

[127] Mirijam Zobel, Reinhard B. Neder, and Simon A. J. Kimber: *Universal solvent restructuring induced by colloidal nanoparticles.* Science, 347(6219):292–294, 2015. `https://doi.org/10.1126/science.1261412`.

[128] Sabrina L J Thomä, Sebastian W Krauss, Mirco Eckardt, Phil Chater, and Mirijam Zobel: *Atomic insight into hydration shells around facetted nanoparticles.* Nature Communications, 10:995, 2019. `https://doi.org/10.1038/s41467-019-09007-1`.

[129] Jee Ching Wang and Kristen A. Fichthorn: *Molecular dynamics studies of the effects of chain branching on the properties of confined alkanes.* The Journal of Chemical Physics, 116(1):410–417, January 2002. `https://doi.org/10.1063/1.1419258`.

[130] Shuai Chen: *Semiconducting Nanocrystals: Synthesis, Colloidal Stability, and Charge Carrier Dynamics*, 2023. `https://hdl.handle.net/21.11116/0000-000D-99F4-3`, PhD thesis, Johannes Gutenberg-Universität, Mainz.

[131] Sandrine Ithurria and Benoit Dubertret: *Quasi 2D Colloidal CdSe Platelets with Thicknesses Controlled at the Atomic Level.* Journal of the American Chemical Society, 130(49):16504–16505, 2008. `https://doi.org/10.1021/ja807724e`.

[132] Thomas Nann and Jürgen Schneider: *Origin of permanent electric dipole moments in wurtzite nanocrystals.* Chemical Physics Letters, 384(1):150–152, 2004. `https://doi.org/10.1016/j.cplett.2003.12.017`.

[133] Alexander Stukowski: *Visualization and analysis of atomistic simulation data with OVITO–the Open Visualization Tool.* Modelling and Simulation in Materials Science and Engineering, 18(1):015012, dec 2009. `https://dx.doi.org/10.1088/0965-0393/18/1/015012`.

[134] Inkscape-Entwicklerteam: *Inkscape (v1.3.1) [Software].* `https://inkscape.org`.

[135] Thomas Williams, Colin Kelley *et al.*: *Gnuplot (v5.2) [software].* `http://www.gnuplot.info`.

[136] TeX Users Groups: *TeX Live (v2022.1) [Software].* `https://www.tug.org/texlive/`.

[137] Overleaf: *Overleaf [Software].* `https://www.overleaf.com`, 23-11-2023.

[138] DeepL SE: *DeepL [Software].* `https://www.deepl.com/`, 23-11-2023.

[139] LanguageTooler GmbH: *LanguageTool [Software].* `https://languagetool.org/de`, 23-11-2023.

Software

- System setup: Hoobas [119]
- Molecular dynamics simulations: HOOMD [117]
- Free energy calculation: WHAM as implemented by Daniel Bauer [124]
- Simulation snapshots: Ovito [133]
- Graphics production: Inkscape [134], Gnuplot [135]
- Document generation: LaTeX[136] in Overleaf [137]
- Translation: DeepL [138]
- Spelling and grammar correction: LanguageTool [139]

Acknowledgement

First and foremost, I would like to thank [redacted] for giving me the opportunity to do my PhD in his department, and to work in the colorful, international, and interdisciplinary working environment of the Max-Planck Institute for Polymer Research (MPI-P).

My special thanks go to my daily supervisors [redacted], [redacted] and [redacted]. I would like to thank them very much for their great support. The last few years have been extraordinary in many ways, and without their support this work would not have been possible. In particular, I would like to thank [redacted] for his excellent supervision. From the beginning of my PhD, our collaboration has been close and fruitful. In particular, I would like to thank him for his continued support after he became an assistant professor at the University of North Texas. I will always look back happily on our cross-continental collaboration, and I am grateful for the extraordinary support.

I would like to thank [redacted] for a pleasant and fruitful collaboration. He gave me an excellent insight into the experimental perspective of our project in his group. I have fond memories of the great weekly group meetings, engaging discussions, and enjoyable social activities.

I am very grateful to [redacted] for his support. From the start of my project, I benefited greatly from his outstanding professional and technical knowledge. After the promotion of [redacted] became a new group leader in the MPI-P, and my direct supervisor within the institute. We continued our fruitful collaboration and Martin proved to be an excellent group leader. I would like to thank him very much for his awesome support.

We closely worked together with [redacted] and [redacted]. [redacted] performed a series of experiments to validate our results. My special thanks go to him and his supervisor, [redacted]. I have thoroughly enjoyed our collaboration.

The MPI-P is a vibrant, and energetic place. I am grateful to all members of the MPI-P and of the AK [redacted]. In those fantastic years, I made friendship with many of you, and I will miss you greatly.

I would like to thank all my friends who have supported me over the last years. My special thanks go to my childhood friend [redacted].

Finally, I would like to thank my family. Without their continuous and unconditional support, this work would not have been possible.